COMPACT ULTRAVIOLET LASER

Brian Walter Baird
B.S., University of Oregon, 1980
M.S., University of Washington, 1984

A dissertation presented to the faculty of the
Oregon Graduate Institute of Science and Technology
in partial fulfillment of the
requirements for the degree
Doctor of Philosophy
in
Applied Physics

April, 1997

The dissertation "Compact Ultraviolet Laser" by Brian Baird has been examined and approved by the following Examination Committee:

Richard K. DeFreez, Dissertation Advisor
Associate Professor

Anthony E. Bell
Associate Professor

Reinhart Engelmann
Professor

Gary A. Evans
Professor, Southern Methodist University

DEDICATION

This dissertation is dedicated to my loving wife, Georgette. Her strong support and dedication helped me immeasurably throughout my studies and research and was instrumental in supporting the completion of this dissertation.

ACKNOWLEDGEMENTS

I am deeply thankful for the powerful support and constant encouragement that Professor Richard DeFreez has offered to me throughout my studies, research, and during the completion of this dissertation. I have learned immeasurably from his example as a scientist and educator.

I wish to extend my gratitude to the other members of my committee, Professor Anthony Bell, Professor Reinhart Engelmann, and Professor Gary Evans for assisting my research, offering many constructive comments, and supporting my dissertation efforts.

I would like to thank Peter Carlson and Dr. Zhouyu Bao for teaching me how to follow in their footseps and understand the intricacies of how to fabricate unstable resonator semiconductor lasers by focused-ion-beam micromachining. From each of them, I learned many valuble lab skills.

I would like to thank Dr. John Bierlein, Dr. Mark Roelofs, Brian Brown, Robert Tamosaitis, and Len Conlin of Du Pont Central Research and Development Department who supported my research towards a compact ultraviolet laser over many years and who supplied the KTP waveguides used in this research. During the completion of this dissertation, Dr. Bierlein passed away. His loss is deeply felt.

I would like to thank Jay Kirk of Southern Methodist University for his work in processing the AlGaAs wafer material from which I micromachined the URSLs discussed in this dissertation. I also wish to thank Rich Toohey, Frank Hawrylo, and Larry Cramer of Laser Diode Inc. for their invaluble assistance in coating and packaging the URSLs.

I extend my appreciation to Professors Fred Holmes, Jim Parsons, and Rao Gudimetla, and Scott Prahl for their assistance during my studies at OGI. I also wish to thank John Hunt and Bev Kyler for their help.

During my many hours working at Linfield Research Institute, I was often helped by Professor Bill Mackie, Gary Cabe and Mark Hinrichs. Their assistance is greatly appreciated.

I want to acknowledge the help I received from the Oregon Medical Laser Center and its staff, including Dr. Kenton Gregory and Lisa Buckley. I also want to thank Illumenex Corporation and its President, Mr. Charles Hadley for the financial support of this research which it extended through my employer, ESI.

Many thanks go to Tom Haw for helping me keep the Ti:Sapphire laser aligned and operating.

It is a pleasure to acknowledge the many people at ESI who have helped me throughout my studies and research. My thanks to Dick Harris, Ed Swenson, Tom Richardson, Brady Nilsen, David Lo, Fred Mattern, Don Warfield, Chhy Aing, Carey Pico and Hoss Reynolds. I wish to especially thank my fellow student Yunlong Sun for his constant support and encouragement during my research.

TABLE OF CONTENTS

DEDICATION iii
ACKNOWLEDGEMENTS iv
TABLE OF CONTENTS vi
LIST OF FIGURES ix
LIST OF TABLES xii
LIST OF SYMBOLS xiii
LIST OF ACRONYMS xv
ABSTRACT xvi
1. INTRODUCTION 1
2. COMPACT ULTRAVIOLET LASERS 6
2.1 EMERGING APPLICATIONS FOR COMPACT ULTRAVIOLET LASER 6
2.2 OVERVIEW OF COMPACT ULTRAVIOLET LASERS 11
2.3 SEMICONDUCTOR LASERS 12
2.4 FREQUENCY CONVERSION 14
2.4.1 FREQUENCY CONVERSION FUNDAMENTALS 14
2.4.2 SINGLE-PASS FREQUENCY CONVERSION OF DIODE DIODE LASER OUTPUT IN BULK MATERIALS 18
2.4.3 FREQUENCY CONVERSION OF DIODE LASER OUTPUT IN EXTERNAL RESONANT CAVITIES 18
2.4.4 FREQUENCY CONVERSION OF DIODE-PUMPED SOLID STATE LASERS 19
2.4.5 FREQUENCY CONVERSION OF DIODE LASER OUTPUT USING NONLINEAR OPTICAL WAVEGUIDES 21

2.5 DISCUSSION 32
3. DESIGN CONSIDERATIONS FOR URSL-PUMPED KTP WAVEGUIDE LASERS 34
3.1 KTP WAVEGUIDE PROCESS AND WAFER CONSIDERATIONS FOR NUV OPERATION 36
3.2 KTP WAVEGUIDE SPECTRAL CHARACTERISTICS 38
3.3 SPATIAL MODE CONSIDERATIONS 41
3.4 DIODE LASER REQUIREMENTS 44
3.5 DISCUSSION 50
4. MODELING OF SPATIAL MODES OF NONLINEAR WAVEGUIDES 52
4.1 INTRODUCTION 52
4.2 DERIVATION OF IMPROVED EXPRESSION FOR NORMALIZED CONVERSION EFFICIENCY 60
4.2.1 EVALUATION OF η_{norm} FOR CASE OF 2-D KTP CHANNEL WAVEGUIDE 65
4.2.2 DISCUSSION OF RESULTS 66
4.3 EFFECTIVE INDEX METHOD MODELING METHODS AND RESULTS 67
4.4 BEAM PROPAGATION METHOD MODEL AND RESULTS 79
4.5 DISCUSSION 97
5. BEAM PROPAGATION MODELING OF SECOND HARMONIC GENERATION IN NONLINEAR WAVEGUIDES 98
5.1 INTRODUCTION 98
5.2 DEVELOPMENT OF BPMSHG 100
5.3 BPMSHG RESULTS FOR KTP PERIODICALLY SEGMENTED WAVEGUIDES 104
5.4 DISCUSSION 112

6. EXPERIMENTAL CHARACTERIZATION OF KTP NONLINEAR WAVEGUIDES 113
6.1 ARGON-ION PUMPED Ti:SAPPHIRE LASER CHARACTERIZATION 113
6.2 NEAR ULTRAVIOLET SPECTRAL CHARACTERIZATION OF HYDROTHERMAL KTP WAVEGUIDES 122
6.3 NEAR ULTRAVIOLET SPATIAL MODE CHARACTERIZATION OF HYDROTHERMAL KTP WAVEGUIDES 134
6.4 DISCUSSION 138
7. FABRICATION AND TESTING OF UNSTABLE RESONATOR SEMICONDUCTOR LASERS 140
7.1 INTRODUCTION 140
7.2 URSL STRUCTURE PROCESSING AND EVALUATION 142
7.3 FIBM PROCESSING OF 770 nm URSLs 147
7.4 PERFORMANCE TESTING OF URSLS 154
7.5 DISCUSSION 155
8. URSL-PUMPED WAVEGUIDE LASER INTEGRATION AND TESTING 161
8.1 INTRODUCTION 161
8.2 UPWL INTEGRATION AND TESTING 162
8.3 DISCUSSION 168
9. SUGGESTIONS FOR FUTURE WORK 171
9.1 SUMMARY AND CONCLUSIONS 171
9.2 SUGGESTIONS FOR FUTURE WORK 177
REFERENCES 179
APPENDIX A 195
BIOGRAPHICAL SKETCH 229

LIST OF FIGURES

2.1 Conceptual diagram of laser source for blue compact disc system 7

2.2 Artist's rendering of light delivery system for PUVA 7

2.3 DNA photo adduct structure showing psoralen interpolation 9

2.4 UV-laser-based AA system for deposition process monitoring and control 10

2.5 Schematic view of KTP PSW 24

3.1 Power spectrum of Sony 303XT AlGaAs 0.5 W laser diode 47

3.2 Frequency-selective laser diode structures 49

4.1 Transverse TM_0 and TM_1 spatial mode profiles 56

4.2 Electric field distributions for $\Delta n_{surf} = 0.010$ 57

4.3 Planar wavefront propagated through one waveguide period 58

4.4 Channel waveguide structure 66

4.5 KTP PSW structure employed for EIM modeling 69

4.6 KTP refractive index vs. wavelength: fundamental 70

4.7 Transverse TM_0 spatial mode profiles for KTP PSW 74

4.8 Fundamental lateral TM_0 spatial mode profiles for KTP PSW 75

4.9 TM_0 spatial mode profile at 770 nm 77

4.10 TM_0 spatial mode profile at 385 nm 78

4.11 2-D surface plot of fundamental intensity for PSW for Δn=0.010 87

4.12 2-D surface plot of SH intensity for PSW for Δn=0.010 88

4.13 On-axis fundamental intensity vs. propagation distance for Δn=0.010 89

4.14 On-axis SH intensity vs. propagation distance for Δn=0.010 90

4.15 2-D surface plot of fundamental intensity for channel waveguide 91

4.16 2-D surface plot of SH intensity for channel waveguide 92

4.17 2-D surface plot of fundamental intensity for PSW for Δn=0.015 93

4.18 On-axis fundamental intensity vs. propagation distance for Δn=0.015 94

4.19 2-D surface plot of SH intensity for PSW for Δn=0.015 95
4.20 On-axis SH intensity vs. propagation distance for Δn=0.015 96
5.1 2-D surface intensity plot for λ=0.7512 μm 102
5.2 2-D surface intensity plot for λ=0.3756 μm 103
5.3 SHG power vs. propagation distance 105
5.4 2-D surface intensity plot at λ_f=0.75447 μm 108
5.5 On-axis intensity vs. propagation distance at λ_f=0.75447 μm 109
5.6 2-D surface intensity plot at λ_{SH}=0.37723 μm 110
5.7 On-axis intensity vs. propagation distance at λ_{SH}=0.37723 μm 111
6.1 Power spectrum of Sony 304XT AlGaAs laser diode 115
6.2 Ti:Sapphire wavelength vs. etalon micrometer position 116
6.3 Ti:Sapphire wavelength vs. etalon micrometer position fit 117
6.4 Ti:Sapphire beam diameter vs. propagation distance 119
6.5 Near-field expanded Ti:Sapphire beam diameter vs. propagation distance 121
6.6 Far-field expanded Ti:Sapphire beam diameter vs. propagation distance 121
6.7 Experimental set-up for SHG characterization of KTP PSWs 126
6.8 Layout of waveguide positions 127
6.9 SHG power vs. wavelength: TM_0 128
6.10 SHG power vs. wavelength: TM_1 130
6.11 SHG power vs. wavelength: TM_2 131
6.12 Modal SHG power vs. wavelength 132
6.13 SHG wavelength vs. temperature 133
6.14 SH TM_0 spatial mode profile for C9 135
6.15 SH TM_0 spatial mode profile for C12 136
6.16 SH TM_0 spatial mode profile for C11 136
6.17 SH TM_1 spatial mode profile for C10 137
6.18 SH TM_2 spatial mode profile for C11 137
7.1 Schematic illustration of the original wafer pattern and geometrical structure

of a FIBM half-symmetric URSL 145
7.2 Metallization patterns for 770 nm URSLs 146
7.3 Double mirror pulsed output power for tapered device 148
7.4 Double mirror pulsed output power for non-tapered device 149
7.5 Ln(I_{th}) vs. temperature for non-tapered device 150
7.6 Microphotograph of FIBM 80-40 GRINSCH URSL with core grating 152
7.7 L-I curves of URSL device I-4 157
7.8 Wavelength spectrum for tapered URSL 158
7.9 Wavelength spectrum for non-tapered core-grating URSL 159
7.10 Lateral intensity profile for non-tapered core-grating URSL 160
8.1a Transverse intensity profile of astigmatism corrected URSL 164
8.1b Lateral intensity profile of astigmatism corrected URSL 164
8.2 Experimental set-up for URSL-pumped KTP waveguide laser 165
8.3 Power spectrum of URSL with Bragg feedback from KTP PSW 167

LIST OF TABLES

3.1 Preliminary design requirements for diode-pumped KTP waveguide laser.....35

3.2 KTP waveguide performance summary.....37

4.1 Computed values of η_{norm}.....66

4.2 770 nm refractive index construction and effective index data.....72

4.3 385 nm refractive index construction and effective index data.....73

4.4 Principal data parameters for BPMG7 analysis.....85

6.1 Hydrothermal KTP PSW characteristics.....124

7.1 Basic epitaxial laser structure specifications for 770 nm URSL.....144

7.2 FIBM processing parameters for 770 nm URSLs.....153

7.3 Summary of packaged device characteristics.....153

LIST OF FREQUENTLY USED SYMBOLS

Symbol	Description
ω	Optical angular frequency in vacuum
λ	Optical wavelength in vacuum
Λ	Period length of periodically segmented waveguide
ρ	Spatial mode number supported by asymmetric slab waveguide
λ_{Bragg}	Bragg optical wavelength in vacuum
η_{eff}	Normalized conversion efficiency
$\lambda_{f,SH}$	Fundamental and second harmonic optical wavelength in vacuum
ϕ_n	Fourier expansion coefficients
Δn	Refractive index contrast in waveguide
Δn_{surf}	Refractive index contrast at waveguide surface
λ_{QPM}	Quasi-phase-matching fundamental optical wavelength in vacuum
c	Speed of light in vacuum
d_{eff}	Effective nonlinear d coefficient
d_{ijk}	Nonlinear susceptibility tensor
E(x,y,z,t)	Electric field
F_n	Fresnel number
J_{th}	Threshold current density for semiconductor laser
k (k_0)	Wavevector in material (in vacuum)
$l_{1,2}$	Segment length of diffused and undiffused waveguide segments
l_c	Quasi-phase-matching coherence length
m	Quasi-phase-matching order
M	Resonator magnification
$N_{d,a}$	Dopant ion densities (donor, acceptor)
P(x,y,z,t)	Electric polarization

LIST OF FIGURES

2.1 Conceptual diagram of laser source for blue compact disc system 7

2.2 Artist's rendering of light delivery system for PUVA 7

2.3 DNA photo adduct structure showing psoralen interpolation 9

2.4 UV-laser-based AA system for deposition process monitoring and control 10

2.5 Schematic view of KTP PSW 24

3.1 Power spectrum of Sony 303XT AlGaAs 0.5 W laser diode 47

3.2 Frequency-selective laser diode structures 49

4.1 Transverse TM_0 and TM_1 spatial mode profiles 56

4.2 Electric field distributions for $\Delta n_{surf} = 0.010$ 57

4.3 Planar wavefront propagated through one waveguide period 58

4.4 Channel waveguide structure 66

4.5 KTP PSW structure employed for EIM modeling 69

4.6 KTP refractive index vs. wavelength 70

4.7 Transverse TM_0 spatial mode profiles for KTP PSW 74

4.8 Fundamental lateral TM_0 spatial mode profiles for KTP PSW 75

4.9 TM_0 spatial mode profile at 770 nm 77

4.10 TM_0 spatial mode profile at 385 nm 78

4.11 2-D surface plot of fundamental intensity for PSW for Δn=0.010 87

4.12 2-D surface plot of SH intensity for PSW for Δn=0.010 88

4.13 On-axis fundamental intensity vs. propagation distance for Δn=0.010 89

4.14 On-axis SH intensity vs. propagation distance for Δn=0.010 90

4.15 2-D surface plot of fundamental intensity for channel waveguide 91

4.16 2-D surface plot of SH intensity for channel waveguide 92

4.17 2-D surface plot of fundamental intensity for PSW for Δn=0.015 93

4.18 On-axis fundamental intensity vs. propagation distance for Δn=0.015 94

4.19 2-D surface plot of SH intensity for PSW for Δn=0.015 95
4.20 On-axis SH intensity vs. propagation distance for Δn=0.015 96
5.1 2-D surface intensity plot for λ=0.7512 μm 102
5.2 2-D surface intensity plot for λ=0.3756 μm 103
5.3 SHG power vs. propagation distance 105
5.4 2-D surface intensity plot at λ_f=0.75447 μm 108
5.5 On-axis intensity vs. propagation distance at λ_f=0.75447 μm 109
5.6 2-D surface intensity plot at λ_{SH}=0.37723 μm 110
5.7 On-axis intensity vs. propagation distance at λ_{SH}=0.37723 μm 111
6.1 Power spectrum of Sony 304XT AlGaAs laser diode 115
6.2 Ti:Sapphire wavelength vs. etalon micrometer position 116
6.3 Ti:Sapphire wavelength vs. etalon micrometer position fit 117
6.4 Ti:Sapphire beam diameter vs. propagation distance 119
6.5 Near-field expanded Ti:Sapphire beam diameter vs. propagation distance 121
6.6 Far-field expanded Ti:Sapphire beam diameter vs. propagation distance 121
6.7 Experimental set-up for SHG characterization of KTP PSWs 126
6.8 Layout of waveguide positions 127
6.9 SHG power vs. wavelength: TM_0 128
6.10 SHG power vs. wavelength: TM_1 130
6.11 SHG power vs. wavelength: TM_2 131
6.12 Modal SHG power vs. wavelength 132
6.13 SHG wavelength vs. temperature 133
6.14 SH TM_0 spatial mode profile for C9 135
6.15 SH TM_0 spatial mode profile for C12 136
6.16 SH TM_0 spatial mode profile for C11 136
6.17 SH TM_1 spatial mode profile for C10 137
6.18 SH TM_2 spatial mode profile for C11 137
7.1 Schematic illustration of the original wafer pattern and geometrical structure

of a FIBM half-symmetric URSL 145
7.2 Metalization patterns for 770 nm URSLs 146
7.3 Double mirror pulsed output power for tapered device 148
7.4 Double mirror pulsed output power for non-tapered device 149
7.5 $\ln(I_{th})$ vs. temperature for non-tapered device 150
7.6 Microphotograph of FIBM 80-40 GRINSCH URSL with core grating 152
7.7 L-I curves of URSL device I-4 157
7.8 Wavelength spectrum for tapered URSL 158
7.9 Wavelength spectrum for non-tapered core-grating URSL 159
7.10 Lateral intensity profile for non-tapered core-grating URSL 160
8.1a Transverse intensity profile of astigmatism corrected URSL 164
8.1b Lateral intensity profile of astigmatism corrected URSL 164
8.2 Experimental set-up for URSL-pumped KTP waveguide laser 165
8.3 Power spectrum of URSL with Bragg feedback from KTP PSW 167

LIST OF TABLES

3.1 Preliminary design requirements for diode-pumped KTP waveguide laser.....35

3.2 KTP waveguide performance summary.....37

4.1 Computed values of η_{norm}.....66

4.2 770 nm refractive index construction and effective index data.....72

4.3 385 nm refractive index construction and effective index data.....73

4.4 Principal data parameters for BPMG7 analysis.....85

6.1 Hydrothermal KTP PSW characteristics.....124

7.1 Basic epitaxial laser structure specifications for 770 nm URSL.....144

7.2 FIBM processing parameters for 770 nm URSLs.....153

7.3 Summary of packaged device characteristics.....153

LIST OF FREQUENTLY USED SYMBOLS

Symbol	Description
ω	Optical angular frequency in vacuum
λ	Optical wavelength in vacuum
Λ	Period length of periodically segmented waveguide
ρ	Spatial mode number supported by asymmetric slab waveguide
λ_{Bragg}	Bragg optical wavelength in vacuum
η_{eff}	Normalized conversion efficiency
$\lambda_{f,SH}$	Fundamental and second harmonic optical wavelength in vacuum
ϕ_n	Fourier expansion coefficients
Δn	Refractive index contrast in waveguide
Δn_{surf}	Refractive index contrast at waveguide surface
λ_{QPM}	Quasi-phase-matching fundamental optical wavelength in vacuum
c	Speed of light in vacuum
d_{eff}	Effective nonlinear d coefficient
d_{ijk}	Nonlinear susceptibility tensor
E(x,y,z,t)	Electric field
F_n	Fresnel number
J_{th}	Threshold current density for semiconductor laser
k (k_0)	Wavevector in material (in vacuum)
$l_{1,2}$	Segment length of diffused and undiffused waveguide segments
l_c	Quasi-phase-matching coherence length
m	Quasi-phase-matching order
M	Resonator magnification
$N_{d,a}$	Dopant ion densities (donor, acceptor)
P(x,y,z,t)	Electric polarization

q	Quasi-phase-matching condition

LIST OF FREQUENTLY USED ACRONYMS

Acronym	Full Name
BPM	Beam propagation method
CW	Continuous wave
DFB	Distributed feedback
DPSSL	Diode-pumped solid state laser
EIM	Effective index model
FD	Finite difference
FFT	Fast Fourier transform
FIBM	Focused-ion-beam micromachining
FWHM	Full width at half maximum
GRINSCH	Graded-index separate confinement heterostructure
KTP	Potassium titanyl phosphate
MOPA	Master oscillator power amplifier
NUV	Near ultraviolet
PSW	Periodically segmented waveguide
PUVA	Psoralen activation by ultraviolet-A
QPM	Quasi-phase-matching
SH	Second harmonic
SHG	Second harmonic generation
SQW	Single quantum well
URSL	Unstable resonator semiconductor laser

ABSTRACT

Compact Ultraviolet Laser

Brian Walter Baird, Ph.D.

Oregon Graduate Institute of Science & Technology

Supervising Professor: Richard K. DeFreez

This dissertation presents theoretical analysis and experimental investigation of a compact ultraviolet laser, comprising an unstable resonator semiconductor (URSL) laser-pumped potassium titanyl phosphate (KTP) periodically segmented waveguide (PSW) laser.

A comprehensive survey of existing short wavelength visible and near ultraviolet laser technologies suitable for the development of compact ultraviolet lasers is presented. This survey establishes the suitability of a diode-pumped KTP PSW laser as an attractive approach for developing a compact ultraviolet laser. Requirements for an efficient diode-pumped KTP PSW laser are given, leading to the selection of a frequency-stabilized URSL and hydrothermal KTP PSWs as the component technologies to be developed and integrated.

Since the design requirements for the URSL and KTP PSW are critically dependent on a thorough understanding of the spatial mode properties of KTP PSWs, analyses and modeling of the spatial mode properties of these devices is presented using

effective index method (EIM) and beam propagation method (BPM) models. In addition, a new expression for the normalized conversion efficiency is presented which explicitly incorporates the dependence of this important parameter on the lateral variation of the refractive index and d coefficient.

To assess the theoretical performance of an URSL-pumped KTP PSW, the BPM model was extended to incorporate second harmonic generation. This represents an important contribution to the development of numerical methods for modeling nonlinear waveguides, in general, and provides important information on the cooperative effects of diffraction and spatial mode beating on the SHG output from KTP PSWs.

Extensive optical characterization of NUV SHG in hydrothermal KTP PSWs using an argon-ion laser-pumped Ti:Sapphire laser as the infrared laser pump source is presented. Spectral characterization, spatial mode characterization, and the temperature dependence of the QPM wavelength are presented. *This work includes results for the highest cw output powers reported for NUV SHG output from a laser-pumped KTP PSW.*

In an important step towards demonstration of an URSL-pumped KTP PSW laser, fabrication methods and test results are reported for half-symmetric, low magnification SQW AlGaAs URSLs emitting at 770 nm and designed for use as diode pump sources for hydrothermal KTP PSWs. These devices utilize a 200 μm x 500 μm active region profile and were focused-ion-beam micromachined to achieve a total resonator magnification of 2.9. *The first demonstration of high brightness, single-longitudinal mode operation from a core grating URSL is reported.*

This dissertation concludes with results for the the first demonstration of an URSL-pumped KTP waveguide laser. This compact ultraviolet laser represents a pioneering effort to take advantage of the high cw output powers available from high brightness URSLs to increase the SH output powers obtainable from diode-pumped nonlinear waveguide lasers and to extend the useful spectral range from these sources into the near ultraviolet.

CHAPTER 1
INTRODUCTION

In 1916, Albert Einstein recognized that an atom in an excited state when acted upon by radiation corresponding to one of its natural frequencies may produce stimulated emission.[1] The existence of stimulated emission was found to be required to account for the equilibrium distribution of energy states of atoms interacting with electromagnetic radiation. Nearly forty years later, in 1954, a group led by C. H. Townes at Columbia University constructed and demonstrated the first maser (an acronym for microwave amplification by stimulated emission of radiation).[2] They worked with the ammonia molecule NH_3 to produce monochromatic output at 23.870 MHz. Townes collaborated with A. L. Schalow to extend the principles of the maser to optical frequencies.[3] In 1960, the first optical maser, or laser, was demonstrated by T. H. Maiman.[4] Maiman used a xenon-filled quartz flash tube filtered to irradiate a ruby crystal with green light. The coherent pulses of 694.3 nm monochromatic radiation obtained by Maiman from his ruby laser were soon followed by laser light generated in a host of laboratories world-wide.

A 'golden age' in optical spectroscopy has ensued since the pioneering work of Townes, Schalow, and Maiman culminated in the demonstration of the first laser. The uses of lasers span a vast range of applications from remote sensing of the atmosphere to processing of advanced semiconductor integrated circuits. It is the unique combination of monochromaticity, spatial coherence, and wide range of intensities that modern lasers can achieve that has made them the indispensable light sources of science, medicine, and industry.

Contemporary problems in the development of advanced laser sources include extending the range of laser wavelengths, improving the efficiency by which lasers convert input energy into useful laser output, improving the spatial and spectral

coherence of lasers, and decreasing the size of lasers to allow greater flexibility in experimental and commercial applications. Each of these problems presents a unique set of challenges to the laser physicist depending on the choice of: optical material, pumping means, and resonator configuration. When efficiency and a compact package are paramount, semiconductor lasers and semiconductor laser-pumped solid state lasers, more commonly referred to as diode-pumped solid state lasers, are often the preferred solution.

Semiconductor lasers have been fabricated from a broad variety of materials. Commercially available semiconductor lasers utilize AlGaInP/GaAs as the active material for operating wavelengths from 610-690 nm; AlGaAs/GaAs from 760-880 nm; InGaAs/GaAs from 880-1100 nm; InGaAsP/InP from 1100-1700 nm; antinomide and Pb-salt for operation above 2500 nm. Tremendous effort is currently ongoing to produce blue-green semiconductor lasers. Current research has concentrated on high-bandgap materials including ZnCdSeS and AlGaInN.

Concurrent with the effort to widen the spectral range, researchers have endeavored to increase the spatially coherent output power available from semiconductor lasers. This has proven to be a particularly difficult problem owing to the tendency of semiconductor lasers when operated above about 200 mW to operate in several higher-order lateral modes or multiple filaments which maintain only partial spatial coherence with respects to the others. Recently, two methods of obtaining high-power spatially coherent output from semiconductor lasers have been shown. The flared monolithic master-oscillator/power-amplifier (FM-MOPA) has produced 5.0 W of coherent 980 nm output.[5] The FM-MOPA is complex, integrating a distributed-Bragg-reflector (DBR) master oscillator with a flared amplifier. In contrast, the unstable resonator semiconductor laser (URSL) has demonstrated comparable power and spatial coherence levels utilizing an elegantly simple construction.[6] An URSL is fabricated from a broad-area Fabry-Perot semiconductor laser by focused-ion-beam micromachining a cylinder mirror on one or both of the mirror facets, creating an unstable resonator configuration.

This approach, in principle, is applicable to any material system. Indeed, fabrication and operation of URSLs in a wide variety of material systems have recently been reported.[7]

Despite the many compelling attributes of semiconductor lasers, for applications demanding a compact laser with very high peak powers or diffraction-limited focused spot sizes with high continuous wave (CW) intensities, solid state lasers often offer superior performance in comparison. This superior performance is typically attributable to two fundamental differences between solid state lasers and semiconductor lasers. First, a solid state laser is typically constructed using a spherical mirror resonator that supports TEM_{mn} modes. The lowest order mode TEM_{00} propagates with a radially symmetric gaussian intensity distribution according to the classic formulation derived by Fox and Li.[8] In contrast, a typical semiconductor laser supports guided modes characteristic of a multiple-layer slab waveguide. These TE and TM spatial modes are generally asymmetric and the lowest order modes generally exhibit astigmatic beam propagation characteristics owing to the gain guiding in a stripe implementation of these devices. Second, the time constants for excited states differ greatly between the solid state lasers and semiconductor lasers. For a typical solid state laser material, Nd:YAG, the fluorescence lifetime of an Nd ion excited to the $^4F_{3/2}$ metastable level is 230 μs.[9] In comparison the carrier recombination lifetime for AlGaAs is about 1 ns.[10] This five order of magnitude difference in the relative excited state lifetimes for these optical materials explains why Q-switched solid state laser are far more commonly employed for applications requiring high peak powers. In addition, solid state lasers employ mode volumes whose cross-sectional area is far larger than employed in semiconductor lasers. This allows higher circulating powers to be generated within the resonator before the onset of catastrophic optical damage.

With the advent of commercially available semiconductor lasers capable of producing greater than 100 mW of CW power in the early 1980s, researchers began concerted efforts on development of diode-pumped solid state lasers. Early work focused on using AlGaAs semiconductor lasers to optically pump Nd:YAG and Nd:YLF.[11,12]

This work has since led to an explosion in the number and complexity of diode-pumped lasers. Baer demonstrated an AlGaAs diode-pumped Nd:YLF laser incorporating intracavity KTP for SHG emission in the green.[13] The development of AlGaInP semiconductor lasers together with the development of chromium-doped colquirites led to the demonstration of AlGaInP-pumped Cr:LiCAF lasers by Scheps.[14] The output power of these early diode-pumped solid state lasers were all limited by the available CW output power of the single-stripe diode pump sources. The development of much higher power diode laser arrays has spurred the development of diode-pumped solid state lasers capable of producing 1 W of CW output power at 266 nm[15] or more than 7 W of Q-switched 1064 nm average power output at 20 KHz.[16] The prospects for higher power output are excellent. Indeed, conceptual designs for using diode-pumped solid state lasers as ignition sources for laser fusion have been recently reported.[17]

Despite these advances in the development of compact semiconductor lasers and compact diode-pumped solid state lasers, reliable compact laser sources are unavailable over large ranges of the visible spectrum, particularly in the blue and violet ranges, and for virtually all of the ultraviolet spectrum. Compact laser sources in these wavelength ranges are required for advanced compact disc players and other optical recording applications.[18] Another important emerging application for short wavelength lasers is as monochromatic, spatially coherent light sources for photodynamic therapies in medicine.[19] In these applications, laser light is utilized to locally activate pharmaceutical agents.

To meet these emerging short wavelength requirements for compact lasers, various techniques for frequency conversion of semiconductor lasers have been demonstrated. These techniques, which will be reviewed in Chapter 2, include frequency conversion of diode lasers in bulk nonlinear crystals, using resonant cavity configurations, nonlinear waveguides, upconversion schemes, and frequency-doubled diode-pumped lasers. Further progress, however, will require more efficient

semiconductor laser sources and a more detailed understanding of the processes that influence the SHG conversion efficiencies.

The work presented in this thesis details the effort to analytically model and experimentally demonstrate the operation of a compact near ultraviolet laser. In Chapter 2, various approaches for realizing a compact near ultraviolet laser are discussed. Chapter 3 explores the design considerations for an URSL-pumped KTP waveguide laser. In Chapter 4, a new derivation of the normalized conversion efficiency (η_{eff}) for nonlinear waveguides is presented. Detailed analytical models and results for the spatial modes of channel and periodically segmented KTP nonlinear waveguides using effective index method and beam propagation method models are given. Chapter 5 discusses the development of BPMSHG, a beam propagation method computer model which explicitly incorporates second harmonic generation and back conversion, and the predictions this model makes for SHG generation in periodically segmented KTP nonlinear waveguides. In Chapter 6, experimental measurements of the NUV power spectrum, NUV and NIR spatial modes, and conversion efficiencies of flux-gown and hydrothermal KTP waveguides pumped by a Ti:Sapphire laser are given. Chapter 7 describes the fabrication and testing of the URSLs designed for use as diode pump sources for KTP waveguides. Chapter 8 presents the first experimental results for a diode-pumped KTP waveguide laser emitting in the NUV. Conclusions and suggestions for future work are given in Chapter 9.

CHAPTER 2
COMPACT ULTRAVIOLET LASERS

2.1 Emerging Applications for Compact Ultraviolet Lasers

Development of compact near ultraviolet laser sources is required for many emerging technologies, including high density optical recording[18], photodynamic therapies in medicine[19], and for atomic absorption monitors.[20] For these applications, the laser is typically required to emit in continuous wave (CW) operation as opposed to pulsed operation. The CW power required varies with each application. Optical recording applications typically require 1-5 mW[18] while photodynamic therapy may require a laser source emitting more than 25 mW.[20]

The beam propagation characteristics required for a compact near ultraviolet laser are particularly severe for high density optical recording.[18] The density of data that can be stored is proportional to λ^2. Accordingly, an optical disc recording system operating at 390 nm could store four times more than the amount of data storable by currently available commercial AlGaAs laser diode-based systems that operate at 780 nm. Figure 2.1 shows a conceptual diagram of a laser source for an advanced compact disc system designed for 425 nm. In this application, the required focused spot size diameter is 500 nm at 425 nm, which is near the diffraction limit for a blue laser source.

In contrast, the beam propagation characteristics required by photodynamic therapies can be significantly less severe. In the photodynamic therapy of restenosis[21], also known as PUVA, the laser output is coupled into a fiber, which is part of an optical catheter. Figure 2.2 shows a conceptual rendering of a light delivery system for PUVA, utilizing a compact ultraviolet laser source.

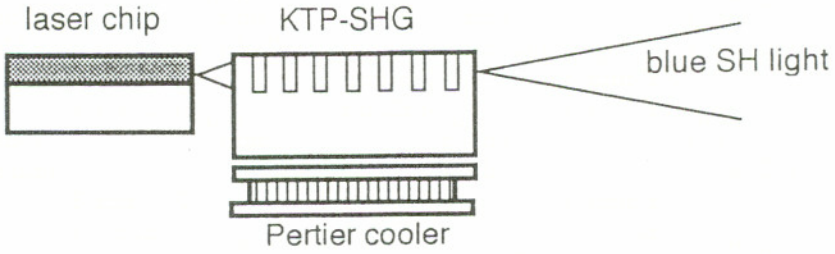

Figure 2.1 Conceptual diagram of laser source for blue compact disc system

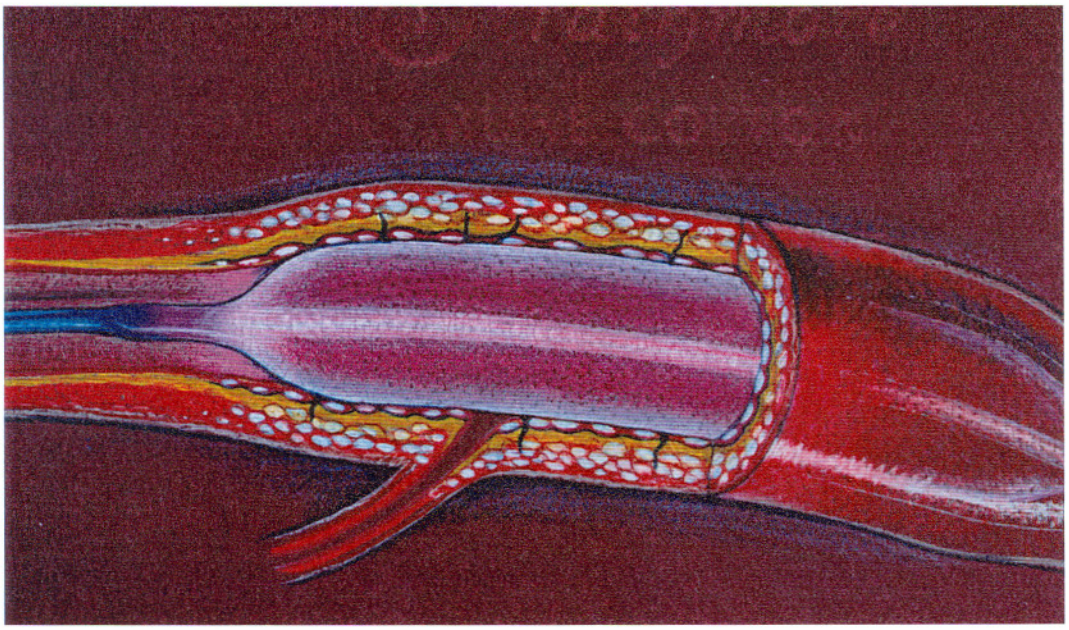

Figure 2.2 Artist's rendering of light delivery system for PUVA

The fiber core diameter is 500 microns and has an NA of 0.5. PUVA is intended as a preventive therapy for all patients undergoing invasive cardiac surgery, including heart bypass and angioplasty operations. A patient who is to receive such an operation will also be given psoralen, a pharmaceutical agent which can be locally activated by exposure to 365-390 nm radiation. Psoralen acts to prevent restenosis of the treated heart vessels by interfering with cell replication. Figure 2.3 shows schematically how psoralen interpolates between the paired receptor sites in DNA. Depending on the wavelength selected, psoralen acts to produce either monoadducts or cross-links within the DNA of the treated cell nucleus. Shorter near ultraviolet wavelengths, such as 365 nm, favor production of highly mutagenic cross-links. At longer wavelengths, the ratio of monoadducts to cross-links increases substantially. Studies have shown[21] that use of a longer wavelength, such as 385 nm, to increase the ratio of monoadducts contributing to the therapeutical effect would require a substantial increase in the required CW power from the laser source. The estimates of CW power at 385 nm at the laser source output prior to fiber coupling required for PUVA range from 20-50 mW.[22]

Recently, Wang and co-workers[20] have reported on the use of compact ultraviolet lasers as sources for an atomic absorption (AA) monitor for physical vapor deposition. This system was designed to be meet the AA monitoring requirements for the commercially important elements having strong absorption lines in the blue-ultraviolet, including tungsten (385 nm), titanium (391 nm), aluminum (394 nm), gallium (403 nm), and yttrium (408 nm). Current III-V laser diode sources cannot excite these lines. Figure 2.4 shows a block diagram of the UV-laser based system described by Wang. The system was demonstrated to be useful for controlling both evaporation and sputtering processes. Evaporation process monitoring and control were performed using derivative spectroscopy in which the frequency of the UV laser was dithered at a frequency f and the 2-f output from a lock-in amplifier was used to extract the absorption signal. The output power from the UV source laser was reported to be 3 μW.

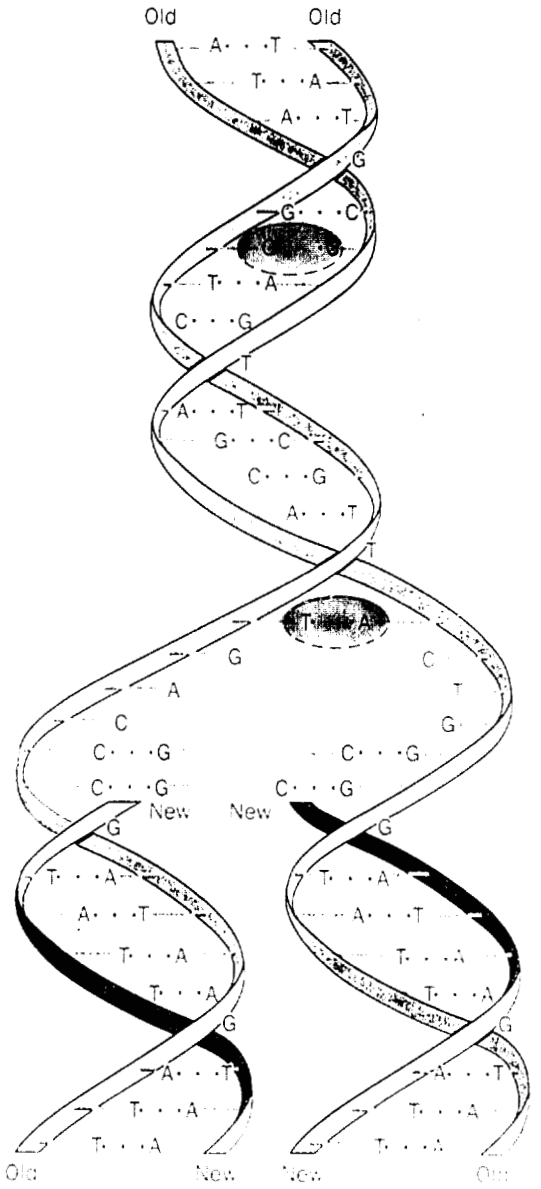

Figure 2.3 DNA photo adduct structure showing psoralen interpolation

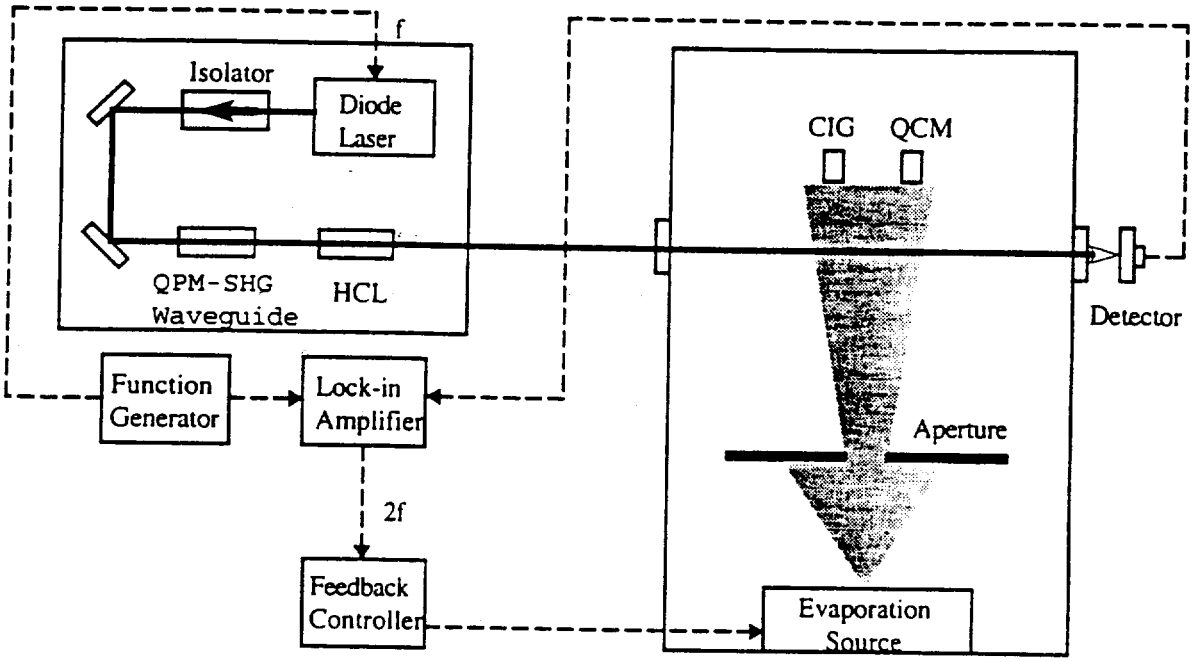

Figure 2.4 UV-laser based AA system for deposition process monitoring and control (After Wang et. al., ref. 20)

Together, the emerging optical recording, medical, and process control applications present a sophisticated challenge to developers of compact near ultraviolet lasers. The wide range in wavelengths (365-410 nm) required by these applications places severe material system limits on the development approaches. The requirement for excellent beam quality requires careful consideration of resonator and waveguiding performance. To meet the power requirements for the PUVA therapy applications, the laser source needs to be efficient and capable of operating over a modest range of CW power levels. Each of these emerging applications demands a compact laser source exhibiting high reliability.

2.2 Overview of Compact Ultraviolet Lasers

Development of compact ultraviolet laser sources share many comparable technological approaches with the more mature effort to develop compact blue-green lasers. The development of II-VI and/or III-V wide band-gap laser diodes is widely viewed as the approach which will meet the broad commercial requirements for future laser sources from the green and into the ultraviolet. Nonlinear frequency conversion of infrared InGaAs and AlGaAs laser diodes, including frequency-doubled solid state lasers, is a second approach that has demonstrated considerable promise for the realization of compact visible and near ultraviolet lasers. For certain applications, it is possible that diode-pumped upconversion lasers may meet the requirements for high-power applications where wavelength tunability is not required.

Each of these approaches was studied for suitability to develop a single spatial mode, 1-50 mW compact laser source capable of being constructed from a common material system set to operate over the 370-390 nm spectral range. This spectral range requirement was considered inclusive of the applications for advanced optical recording, photodynamic therapy of restenosis, and materials processing.

2.3 Semiconductor Lasers

A continuing challenge of semiconductor laser physics is the development of room-temperature, short visible and near ultraviolet semiconductor lasers. To meet this challenge, researchers have focused on ZnSe and related II-VI alloys systems[23,28-35] and GaN and related III-V alloy systems.[24-27,37,38] Each of these wide band-gap semiconductor alloy systems have been extensively studied since the mid-1980s. Room-temperature blue lasing action in optically-pumped ZnCdSe/ZnSe multiple quantum well structures was reported by Jeon et al. in 1990.[23] Similarly, in 1990, room-temperature optically-pumped stimulated emission was observed by Amano et al. in a GaN film with an AlN buffer layer.[24]

Efforts to develop diode lasers in these materials systems were hampered by the difficulty in fabricating structures with the required electrical properties for carrier confinement. GaN films are usually n-type[25] and low-resistivity p-type GaN films were difficult to obtain until Amano described a method for producing p-type GaN films by treating Mg-doped GaN films with low energy electron beam irradiation.[26] Amano et al. fabricated a double heterostructure GaN structure in 1992.[27] Blue and UV emission were reported from this device under high pulsed current density operation.

A similar problem stymied workers in the ZnSe alloy systems until the development of a low contact resistance p-type ZnSe was solved through the use of nitrogen doping.[28] This breakthrough led to the first demonstration of blue-green injection lasing in a wide band-gap II-VI alloy system by Haase and co-workers in April, 1991.[29] This system was reported to produce 490-512 nm output at 77 °K and 508-535 nm at room temperature from a ZnCdSe/ZnSe quantum well structure. Jeon et al., also in 1991, reported injection lasing action near 480 nm at 77 °K from a ZnCdSe/ZnSe quantum well structure.[30] This seminal work shortly led to a large number of reports of injection lasing in II-VI semiconductor laser devices.[31-35]

Work in II-VI diode lasers after these initial demonstrations quickly outpaced efforts in the wide band-gap III-V systems. In 1993, the 3M group of Haase, Walker, DePuydt, Qiu, and Cheng reported that they had achieved up to 1 hour of CW operation[31] from their best ZnCdSe/ZnSe quantum well device when operated at 80 °K. The CW output was 1-3 mW with emission in the 490-512 nm range and with threshold current densities of about 100 A/cm^2. Also in 1993, researchers from Sony described CW laser operation near 448 nm at 77 °K from a II-VI quaternary alloy using a ZnMgSeS quantum well structure. The threshold current density was reported to be 230 A/cm^2.[32] P-type doping was achieved using nitrogen plasma. N-type doping was accomplished with chlorine as the dopant, using $ZnCl_2$ as the dopant source. This choice of dopants is common to the approach taken by Jeon.[30] Sony reported in March, 1996 that they had maintained room-temperature CW operation at the 1 mW level in a II-VI ZnSe alloy system diode laser for 100 hours.[33] The problems with the lifetime of these devices appears to originate from crystal defects which spread into the quantum well active region under forward bias, leading to a quenching effect on laser power.[34]

The continuing difficulties in improving the lifetime for CW operation at low power in wide band-gap II-VI devices has led some observers to believe that the III-V materials based on GaN may be the optimum choice for producing diode lasers in the green-near ultraviolet wavelength range.[35,36] This view was certainly boosted when researchers from Nichia Chemical reported in January, 1996 that they observed pulsed stimulated emission at 300 °K from a current-injected surface-emitting InGaN MQW structure.[37] This device was observed to have strong emission at 417 nm and produced 215 mW under pulsed conditions at a drive current of 2.3 A. The laser threshold density was reported to be 4 kA/cm^2. Researchers at Matsushita have theoretically studied the high threshold current density for GaN/AlGaN QW diode lasers and concluded that the presence of nitrogen in these structures yield much heavier effective masses in the QW, resulting in a higher threshold current density relative to those observed in AlGaAs devices.[38]

2.4 Frequency Conversion

Four principal techniques exist for frequency conversion of infrared laser diode output to the visible and near ultraviolet spectral range (360-540 nm). These techniques are: direct single-pass frequency conversion of infrared laser diode output using second harmonic generation in bulk nonlinear crystals, frequency conversion of infrared laser diode output using second harmonic generation by placing the nonlinear crystal in a resonant cavity, frequency conversion of the output of diode-pumped solid state laser, and frequency conversion of infrared laser diode output using second harmonic generation in a nonlinear waveguide.

2.4.1 Frequency conversion fundamentals

Optical frequency conversion using the process of second harmonic generation in nonlinear optical materials was first described by Bloembergen et al.[39] and Franken et al.[40]

In a nonlinear optical material, coupling between two optical fields having respective frequencies ω_1 and ω_2 can produce polarizations at frequencies $n\omega_1$ and $m\omega_2$, where n and m are any positive integers.

Let the first optical field be a time dependent electric field with monochromatic frequency ω_1 and expressed by

$$\vec{E}_1(\vec{r},t) = \frac{1}{2}\left(\vec{E}_1 e^{\left[i\left(\vec{k}_1 \bullet \vec{r} - \omega_1 t\right)\right]} + \text{c.c.}\right) \tag{2.1}$$

and similarly for the second field at frequency ω_2

$$\vec{E}_2(\vec{r},t) = \frac{1}{2}\left(\vec{E}_2 e^{\left[i\left(\vec{k}_2 \bullet \vec{r} - \omega_2 t\right)\right]} + \text{c.c.}\right) \tag{2.2}$$

Then the vector components of the electric polarization at the sum frequency $\omega_3 = \omega_1 + \omega_2$ is given by

$$P_3^i(\vec{r},t) = \sum_{j,k=1}^{3} \varepsilon_0 d_{ijk} E_1^j(\vec{r},t) E_2^k(\vec{r},t) \tag{2.3}$$

and the nonlinear susceptibility tensor d_{ijk} for the harmonic frequency $\omega_3 = \omega_1 + \omega_2$ is defined as

$$P_3^i = 2 d_{ijk} E_1^i E_2^j \tag{2.4}$$

It is important to note that only noncentrosymmetric crystals can possess a nonvanishing d_{ijk} tensor. In centrosymmetric crystals, it can be shown by a simple mathematical argument[41] that the requirement that a reversal in signs of the electric fields also results in a reversal of sign for P forces $d_{ijk} \equiv 0$. The lack of an inversion symmetry is also a required characteristic of piezoelectric crystals.

The phasematching conditions for SHG in bulk crystals can be derived using the electromagnetic formulation of the nonlinear interaction presented by Yariv[41] and beginning with Maxwell's equations in a form which explicitly includes the polarization

$$\vec{\nabla} x \vec{H} = \sigma \vec{E} + \frac{\partial \vec{D}}{\partial t} \tag{2.5}$$

$$\vec{\nabla} x \vec{E} = -\mu \frac{\partial \vec{H}}{\partial t} \tag{2.6}$$

$$\vec{D} = \varepsilon_0 \vec{E} + \vec{P} \tag{2.7}$$

where σ is the conductivity and $\varepsilon = \varepsilon_0(1 + \chi_L)$. Now, expressing the total polarization as a sum of its linear and nonlinear components

$$\vec{P} = \varepsilon_0 \chi_L \vec{E} + \vec{P}_{NL} \tag{2.8}$$

Equation (2.5) becomes

$$\vec{\nabla} x \vec{H} = \sigma \vec{E} + \varepsilon \frac{\partial \vec{E}}{\partial t} + \frac{\partial}{\partial t} \vec{P}_{NL} \tag{2.9}$$

By taking the curl of both sides of Equation (2.6) and using the vector identity

$$\vec{\nabla} x \vec{\nabla} x \vec{E} = \vec{\nabla} \vec{\nabla} \cdot \vec{E} - \nabla^2 \vec{E} \tag{2.10}$$

we obtain

$$\vec{\nabla}^2\vec{E} = \mu_0\sigma\frac{\partial\vec{E}}{\partial t}\mu_0\varepsilon\frac{\partial^2\vec{E}}{\partial t^2} + \mu_0\frac{\partial^2 P_{NL}}{\partial t^2} \tag{2.11}$$

Considering the limiting case where we have three monochromatic plane waves with respective frequencies ω_1, ω_2, and ω_3 propagating in the z-direction according to

$$E_1(z,t) = \frac{1}{2}\left(E_1 e^{[i(w_1 t - k_1 z)]} + c.c.\right) \tag{2.12}$$

$$E_2(z,t) = \frac{1}{2}\left(E_2 e^{[i(w_2 t - k_2 z)]} + c.c.\right) \tag{2.13}$$

$$E_3(z,t) = \frac{1}{2}\left(E_3 e^{[i(w_3 t - k_3 z)]} + c.c.\right) \tag{2.14}$$

then for the special case for which $\omega_3 = \omega_1 + \omega_2$ it can be shown that the wave equation (2.11) yields

$$\frac{dE_1}{dz} = -\frac{\sigma_1}{2}\sqrt{\frac{\mu}{\varepsilon_1}}E_1 - \frac{i\omega_1}{2}\sqrt{\frac{\mu_0}{\varepsilon_1}}dE_3E_2^* e^{-i(k_3 - k_2 - k_1)z} \tag{2.15}$$

$$\frac{dE_2^*}{dz} = -\frac{\sigma_2}{2}\sqrt{\frac{\mu}{\varepsilon_2}}E_2^* - \frac{i\omega_2}{2}\sqrt{\frac{\mu_0}{\varepsilon_2}}dE_1E_3^* e^{-i(k_1 - k_3 + k_2)z} \tag{2.16}$$

$$\frac{dE_3}{dz} = -\frac{\sigma_3}{2}\sqrt{\frac{\mu}{\varepsilon_3}}E_3 - \frac{i\omega_3}{2}\sqrt{\frac{\mu_0}{\varepsilon_3}}dE_1E_2 e^{-i(k_1 + k_2 - k_3)z} \tag{2.17}$$

where we have used $k_i = 2\pi/\lambda_i$. These equations are coupled to each other by the nonlinear coefficient d and represent the governing relations for the nonlinear optical interactions that will be considered throughout this thesis.

In the case of SHG, $\omega_1 = \omega_2 = \omega$, where ω represents the fundamental frequency, and $\omega_3 = 2\omega$ is the SHG frequency. Using these expressions and neglecting absorption, so that $\sigma_{1,2,3}=0$, Eqn. 2.17 gives

$$\frac{dE_{2\omega}}{dz} = -i\omega\sqrt{\frac{\mu_0}{\varepsilon_{2\omega}}}d\left(E_\omega(z)\right)^2 e^{i(\Delta k)z} \tag{2.18}$$

where $\Delta k \equiv k_{2\omega} - 2k_\omega$.

As a further simplification to help illustrate conditions which frequently apply in a large number of the SHG approaches discussed in this section, by assuming that the input field at ω is not strongly depleted due to conversion to the 2ω field then it is possible to set $E_\omega(z)$ = constant in (2.18). Now, with the further assumption that $E_{2\omega}(0) = 0$ and integrating (2.18) over the length l of the SHG crystal we obtain:

$$E_{2w} = -i\omega\sqrt{\frac{\mu}{\varepsilon_{2\omega}}}d(E_\omega)^2\frac{e^{i(\Delta k)l}-1}{i\Delta k} \tag{2.19}$$

The output power for an input beam of cross-sectional area A is then given by

$$P_{2\omega} = 2\left(\frac{\mu_0}{\varepsilon_0}\right)^{3/2}\frac{\omega^2 d^2 l^2}{n^3}\frac{\sin^2\left(\Delta kl/2\right)}{\left(\Delta kl/2\right)^2}\frac{P_\omega^{\,2}}{A} \tag{2.20}$$

In bulk nonlinear crystals (2.20) shows that the *phasematching* condition for efficient SHG is

$$k_{2\omega} = 2k_\omega \tag{2.21}$$

such that $\Delta k = 0$. If $\Delta k \neq 0$, then a spatial interference pattern resulting from the term

$$\frac{\sin^2\left(\Delta kl/2\right)}{\left(\Delta kl/2\right)^2} \tag{2.22}$$

will result. In this case, the *coherence length* is a useful measure describing the maximum nonlinear crystal length useful for SHG. The coherence length is given by

$$l_c = \pi/\Delta k \tag{2.23}$$

Phasematching in bulk nonlinear materials takes advantage of these materials' natural birefringence. For SHG, the requirement that $\Delta k = 0$ also requires that $n_{2\omega} = n_\omega$. Since in materials with normal dispersion n increases with ω, it is generally impossible to obtain phasematching using fundamental and SH fields of the same polarization. Type I phasematching refers to the case in which two fundamental photons of the same polarization produce one SHG photon of the orthogonol polarization. Type II phasematching occurs when one extraordinary wave photon and one ordinary wave

photon generate one SHG photon, the polarization of which will depend on dispersion characteristics of the nonlinear material.

2.4.2 Single-pass Frequency Conversion of Diode Laser Output in Bulk Materials

Direct single-pass SHG of diode laser output using bulk nonlinear crystals has been explored by several researchers.[42-46] Single-pass SHG was found to be limited by the relatively low power of the diode lasers employed in these experiments. The phase-matching geometries used in these experiments also required that the less desirable off-diagonal elements of the second-order susceptibility tensor d_{ijk} be employed. The values of the off-diagonal d coefficients are lower by a factor of 3-20 as compared to diagonal d coefficients.

In a direct doubling experiment by Jiang, et. al. using the new organic crystal 3-methoxy-4-hydroxy benzaldehyde (MHBA), 3 μW at 404.5 nm was generated from a fundamental input of 1 W from an AlGaAs diode laser.[45] A 4 mm long MHBA crystal was employed using the d_{31} coefficient for SHG (21 pm/V).

Waarts et al. obtained 1.2 mW in the blue-green at 494 nm from single-pass SHG in $KNbO_3$ using 0.5 W fundamental output from a monolithically integrated flared master oscillator power amplifier (MOPA).[46] In this work, a focused spot size of 20 x 30 μm FWHM in the transverse and lateral axes, respectively, was used to pump a 7 mm long b-cut $KNbO_3$ crystal.

2.4.3 Frequency Conversion of Diode Laser Output in External Resonant Cavities

For most CW lasers, including diode lasers, the single pass conversion efficiency is not sufficient to construct practical devices. To overcome this difficulty, resonant devices have been developed[47-50] in which the nonlinear material, typically $KNbO_3$, is placed in a Fabry-Perot resonator external to the diode laser. The resonator mirrors were dichroic with the input mirror coated to transmit the input fundamental frequency ω of

the diode laser and reflect the second harmonic frequency 2ω and the output mirror of the resonator coated to reflect ω and transmit 2ω. This approach can achieve much improved conversion efficiencies owing to the much larger circulating intracavity intensity in comparison to the input fundamental intensity. It is important to note that low loss nonlinear materials are required to achieve large resonant increases in the circulating intensity.[48]

Using $KNbO_3$ in an external resonator configuration, Koslovsky and co-workers[49] generated 42 mW at 428 nm by pumping with 105 mW from a 856 nm diode laser. This result was achieved using temperature-tuned non-critical phase-matching. Frequency doubling of a 972 nm distributed Bragg reflection (DBR) semiconductor laser optically locked to an external enhancement ring resonator containing $KNbO_3$ was demonstrated by Zimmerman.[48] This device generated a maximum output of 1.2 mW of tunable blue output near 486 nm from a fundamental input power of 25 mW.

2.4.4 Frequency Conversion of Diode-Pumped Solid State Lasers

In 1974, Keyes and Quist reported that they had arranged five GaAs diode lasers to transversely pump a U^{3+}:CaF_2 solid state laser.[51] This device, the first diode-pumped solid state laser (DPSSL), produced quasi-CW laser output at 2.613 μm. Keyes and Quist noted in their report that GaAs diode lasers should be ideal for pumping Nd lasers and had the potential to be more efficient than lamps. In less than twenty years, these observations by the pioneers in DPSSLs have become established fact. In an excellent review, Fan and Byer summarized the development of DPSSLs through 1988.[52] Hughes and Barr described more recent developments in their 1992 review.[53]

Early work in the application of DPSSLs for frequency conversion applications was performed by Fan who demonstrated that 0.3 mW of green light could be generated from a Nd:YLF laser pumped by a 30 mW diode laser.[12] In this device, frequency conversion was accomplished using an intracavity-placed piece of MgO:$LiNbO_3$. Baer used KTP as the intracavity frequency doubler in a diode-pumped Nd:YLF laser and

reported the so-called "green problem", which caused the green output power to fluctuate due to the nonlinear coupling of the longitudinal modes of the solid state laser resonator.[13] These early experiments indicated the limitations of frequency doubling using diode-pumped solid state lasers. These limitations include: inherent spectral non-tunability of the rare earth lasants that can be efficiently pumped by available diode lasers; Stokes emission characteristics of diode-pumped solid state lasers (solid state laser emits at longer wavelength than diode pump wavelength); experimental difficulties arising from the preference to operate solid state laser on single-longitudinal mode; and phase-matching limitations that require use of less efficient off-diagonal nonlinear d coefficients.

Despite these difficulties, the advantage of utilizing a solid state laser to act as a spectral and spatial mode converter of high-power diode lasers[54] has motivated notable advances in the generation of green, blue, and ultraviolet CW laser light from frequency-converted diode-pumped solid state lasers in recent years. The outstanding work to date is the demonstration by researchers at Sony's Kubota Optoelectronics Laboratory of 1 W CW 266 nm output from frequency-quadrupled Nd:YAG.[15] The Sony laser consists of a diode pump module comprising 14 Sony 324ZT diode lasers, each rated for 1.8 W CW output, and temperature-tuned to emit 808 nm output. The diode laser output is fiber-coupled to provide up to 18 W of available pump power to a folded solid state laser resonator containing the Nd:YAG rod and KTP for intracavity doubling to the green. The green output is resonantly doubled in a bow-tie ring cavity containing β-BaB_2O_4 (BBO). This work is illustrative of the advantages and limitations of frequency conversion using diode-pumped solid state lasers. Over 2.5 W of 532 nm CW power and over 1.0 W of 266 nm CW power were generated with a total 808 nm AlGaAs diode laser input power of 14.0 W. Direct conversion of the diode output would have been impractical due to the broad spectral bandwidth and strong axial divergence asymmetry of the diode laser source. The solid state laser resonator efficiently converts the 14.0 W diode laser output into single-longitudinal mode 532 nm TEM_{00} output suitable for input to the external

resonant cavity containing the BBO. Note, however, that the choice of material systems employed in this design (AlGaAs laser diodes, Nd:YAG solid state laser crystal, KTP SHG crystal, BBO FHG crystal) can yield only discrete spectral lines; indeed, the lines selected in this work are the strongest and most maturely developed. Moreover, the large number of elements and considerable complexity inherent in this laser are representative of the difficulty in generating high CW power output levels using conventional phase-matching techniques in bulk nonlinear crystals.

Work towards CW diode-pumped solid state lasers emitting in the blue also continues at a rapid pace. In January 1996, researchers at the University of Southhampton in the United Kingdom reported generating 49 mW of CW 473 nm blue light by frequency doubling a diode-pumped 946 nm Nd:YAG.[55] They accomplished this notable success by quasi-phase-matching in a KTP waveguide. This technique is discussed in detail in the next section. A similar approach using 770 nm fundamental CW output from an AlGaInP diode laser-pumped Cr:LiCAF laser to generate quasi-phase-matched frequency-doubled output at 385 nm from a KTP waveguide had been previously described by Baird and DeFreez.[56]

2.4.5 Frequency Conversion of Diode Laser Output Using Nonlinear Optical Waveguides

In bulk materials, the single-pass efficiency is limited by the competing requirements of tight focusing of the fundamental beam into the nonlinear material to achieve high intensities and the need for a large depth of focus to obtain sufficient interaction lengths. Stegeman and Seaton[57] observed that the efficiency of single-pass frequency conversion could be improved by a factor scaling approximately as L/w in a waveguide device as compared to a bulk device for the same medium, where w is a dimension characteristic of the waveguide spatial mode and L is the interaction length. The resulting enhancement in SHG efficiency makes waveguide SHG devices an attractive alternative to complicated resonant cavity frequency conversion devices.

In 1970, Tien reported SHG in a planar optical waveguide[58] in which the SH field was emitted into the substrate at a significant angle with respect to the waveguide axis. This scheme, known as Cherenkov SHG, was improved upon by Taniuchi to produce about 1 mW at 420 nm from 65 mW fundamental power from a diode laser coupled into a $LiNbO_3$ channel waveguide.[59] As further explored by Jongerius[46] and other workers,[61,62] it has proven difficult to transform the crescent-shaped output beam into a beam which could be subsequently focused to a diffraction-limited spot.

Planar and channel nonlinear optical waveguides for SHG have been fabricated in KTP.[63,64] Bierlein noted that the mode indices of the fundamental and SH fields must be controlled to within 10^{-4} to obtain high conversion efficiency through phasematching.[65] Risk reported obtaining Type II second harmonic generation and sum-frequency mixing in KTP channel waveguides.[64] The fundamental wavelength cut-off for Type II frequency conversion in KTP (y propagation) is reported to be 993 nm.[65] Fluck and co-workers demonstrated blue light generation by frequency doubling diode laser output in $KNbO_3$ channel waveguides.[64]

It is important to recognize that the cut-off wavelengths for SHG in non-quasi-phase-matched $LiTaO_3$, $LiNbO_3$, and $KNbO_3$ planar and channel waveguides is the same as that for bulk conversion. Therefore, this class of nonlinear waveguide devices remain limited by birefringent phase-matching techniques in the range of SHG wavelengths that they can produce.

The problem of achieving phasematching in materials which are not birefringent or at wavelengths for which birefringent materials cannot be efficiently phasematched has received wide attention. This is not surprising given the relatively small number of nonlinear optical materials that exhibit the required combination of optical, thermal, and mechanical properties for harmonic generation.[67] Armstrong, Bloembergen et al. proposed a technique for introducing a periodic reversal of sign of the nonlinear d coefficient in a stack of nonlinear crystals, in which each crystal is one coherence length thick and oriented such that d changed sign in each crystal.[39] This technique has been

termed *quasi-phasematching* (QPM). Rustagi subsequently developed a quantitative theory for QPM in crystal stacks, including consideration of pump depletion and sum and difference frequency generation.[68] Somekh and Yariv examined QPM for the case of obtaining phasematching in a thin film waveguide.[69]

Demonstration of blue SHG output in nonlinear waveguides using QPM was first reported in 1990 by van der Poel using a Ti:Sapphire-pumped periodically segmented KTP waveguide.[56] They reported generating about 0.2 mW at 425 nm with a fundamental input power of 100 mW, yielding a normalized conversion efficiency of 80±15%/W cm^2.

In QPM nonlinear waveguides, a periodically segmented structure, as shown in Figure 2.5, provides the spatial modulation of the d coefficient. This class of nonlinear waveguides have been termed *periodically segmented waveguides* (PSWs). For a PSW, the SHG power generated in a perfectly quasi-phase-matched guide of length l is

$$P_{2\omega} = 2\left(\frac{\mu}{\varepsilon_0}\right)^{3/2} \frac{\omega^2 d^2 l^2}{n^3} \frac{\sin^2\left(Nq/2\right)}{\left(q/2\right)^2} \frac{P_{2\omega}^{\ 2}}{A} \tag{2.24}$$

where

$$q = \Delta k^a l^a + \Delta k^b l^b \tag{2.25}$$

$$\Delta k = k_{2\omega} - 2k_{\omega} \tag{2.26}$$

N is the number of periods, and the superscripts indicate the segment. Note that the sine function in (2.24) will peak if the SHG fields from successive periods contribute in phase. This imposes the quasi-phase-matching condition

$$q = 2\pi m \tag{2.27}$$

where m = ±1,±2,±3, . . . and indicates the *order* of QPM. The QPM order m affects the SHG power as $P_{2\omega} = 1/m^2$. Note that A now represents an effective interaction area.

Since the first report by Bierlein and co-workers of blue SHG from a KTP PSW[56], PSWs in a variety of other material systems, including $LiNbO_3$, $LiTaO_3$, and $KNbO_3$ have been reported.[71,72,76-78,80,81,84-90,94-99]

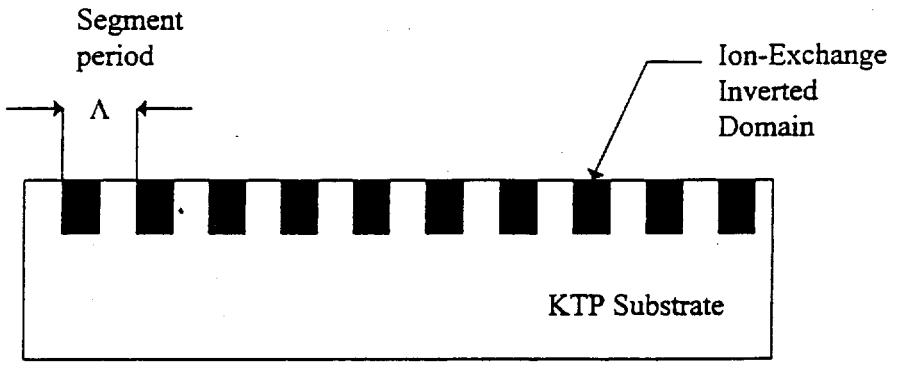

Figure 2.5 Schematic view of KTP PSW

$LiTaO_3$ has attracted wide interest as a PSW material due to its low susceptibility to optical damage[59] and large d_{33} coefficient (26 pm/V).[74] In 1991, Yamamota and Mizuuchi et al. fabricated $LiTaO_3$ PSWs using a proton-exchange method to form the domain-inverted regions and demonstrated blue SHG using Ti:Sapphire pumping.[71] In 1992, they used 77 mW incident fundamental output from an AlGaAs diode laser to obtain 1.1 mW at 436 nm from a $LiTaO_3$ PSW.[72]

Extensive work on $LiNbO_3$ PSWs has been reported. $LiNbO_3$ exhibits a relatively high d_{33} nonlinear coefficient (33 pm/V).[75] Lim et al. at Stanford University first demonstrated violet SHG at 410 nm in a $LiNbO_3$ PSW in 1989.[76] Fejer et al. continued this pioneering work to produce periodically poled crystals displaying ferroelectric domain reversal.[77] This work succeeded in achieving an QPM SHG output of several microwatts at 407 nm with a fundamental input of 87 mW. Yamada and co-workers at Sony developed a method of fabricating periodic domain structures in $LiNbO_3$ by applying an external field.[78] Using devices created with this method, they subsequently created waveguides using proton exchange. They obtained 20.7 mW of 426 nm SHG output from devices with a 3 mm interaction length using 196 mW of input fundamental from a Ti:Sapphire laser. The calculated η_{eff} was estimated to be 600%/W-cm^2, which continues to represent a state-of-the-art level for blue SHG generation in QPM $LiNbO_3$

devices. The measured η_{eff}, for the *normalized conversion efficiency,* is commonly used by workers to express the SH conversion efficiency of nonlinear waveguides. Fujimura et al. successfully obtained ferroelectic domain inversion using electron beam scanning.[79] In a significant demonstration of frequency doubling of AlGaAs diode laser output using QPM $LiNbO_3$ waveguides, Lu and co-workers[80] coupled 250 mW incident fundamental power from a CW multi-longitudinal mode AlGaAs diode laser into a waveguide and obtained 0.35 mW of 405 nm third-order SHG output. The diode laser emission bandwidth was measured to be approximately 1.5 nm. Lu noted that about half of the diode laser emission fell within the waveguide's calculated SHG wavelength acceptance bandwidth.

Fluck et al. reported the generation of 0.5 mW of blue light at 430 nm using a $KNbO_3$ channel waveguide by frequency doubling the CW 150 mW output from an SDL 5422 series AlGaAs diode laser.[81] The waveguide was fabricated using He^+ ion implantation. An external grating was used to provide a frequency feedback signal to the diode laser.

The KTP PSW structure first reported by Bierlein and co-workers consists of a linear periodic array of Rb-exchanged segments alternating with unexchanged KTP segments.[70] The Rb-exchanged segments have a higher refractive index at both the fundamental and second harmonic wavelengths than the unexchanged KTP segments. The Rb-exchanged segments are typically about 4-6 microns wide, with the smaller widths generally used for short wavelength devices, and with segment lengths of about 1.3 - 3 microns long in the propagation direction. For QPM SHG between 0.38 and 0.48 microns the typical duty cycles (defined as the fractional length of the Rb-exchanged segment) are between 60 and 85%, where the actual length of the unexchanged KTP segment is selected to achieve a $-\pi$ phase mismatch between the fundamental and SH waves.[82] Domain inversion in the Rb-exchanged segment produces a π phase shift of the nonlinear susceptiblity which compensates for the $-\pi$ phase mismatch of the waves exiting the unexchanged KTP segment. This scheme is possible due to the polar nature

of KTP. In KTP, the nonlinear d coefficient changes sign during a ferroelectric domain inversion.[83] This sign change is equivalent to a π phase shift. Addition of ~3 mole % $Ba(NO_3)_2$ into the $RbNO_3$ bath used for ion exchange produces the required domain inversion. Photolithographically-produced masks are used to pattern the waveguides prior to immersion in the $RbNO_3$ bath. This production process, therefore, can be used to simultaneously form segmented waveguides and produce domain inversion in the exchanged segments. Its relative simplicity has led to substantial efforts to commercialize it for production applications.[84]

The presence of sharp vertical walls between the Rb-exchanged and unexchanged segments produces distinct refractive index boundaries between segments along the direction of propagation and laterally. One consequence of this sharp refractive index boundary behavior is the presence of reflected waves from these boundaries. These reflections, termed Bragg reflections, have been exploited as feedback signals to lock the emitting wavelength of diode lasers serving as the fundamental source.

In the first report of type I blue SHG from a KTP PSW, Bierlein and co-workers obtained values of $\eta_{eff} \sim 50\text{-}100\%/W\text{-}cm^2$ using a tunable Ti:Sapphire laser for first order QPM at SHG wavelengths near 425 nm.[70] KTP PSWs were fabricated using both flux and hydrothermal KTP. In this report they noted that when pure Rb or mixed Tl/Rb ion-exchange baths were used to fabricate the waveguides, no phase-matched type I SHG could be observed above their detection limit of about $0.004\%/W\text{-}cm^2$. When $Ba(NO_3)_2$, however, was added to the molten salt ion-exchange bath, the η_{eff} values quoted above were observed. This observation led to conducting low-temperature electrostatic toning and surface SHG experiments which indicated that the origin of the high η_{eff} values was ferroelectric domain reversal in the Rb-exchanged segments, as discussed earlier in this section.

Jongerius and co-workers fabricated KTP PSWs using a Rb/Tl/Ba nitrate bath for ion-exchange.[60] They produced 5 mm long guides with a segmentation period of 4 microns and with segment depths of 6 μm and 13 μm. The deep guides clearly displayed

a wider SHG spectral emission range compared to the shallower guide, which displayed a $sinc^2$ type of SHG wavelength spectrum. Moreover, the shallower guide showed a much higher η_{eff}, 150%/W-cm^2 as compared to 28%/W-cm^2 for the deeper guide. Jongerius attributed this result to multiple domain inversion in the diffused segments in the deeper guides.

In an interesting experiment, Laurell, Brown, and Bierlein reported on simultaneous generation of near ultraviolet, blue, and green light from a single 4 micron wide KTP PSW using two infrared fundamental wavelengths from two Ti:Sapphire lasers.[86] A short wavelength Ti:Sapphire laser was tuned to produce 37 μW of SHG at 358.9 nm using the m=2 (second order) QPM. The second Ti:Sapphire laser was tuned to produce 54 μW of sum frequency generation at 420.8 nm using the m=1 QPM and 54 μW of SHG at 508.5 nm using balanced phase matching.

Eger, Oron, and Katz produced KTP PSWs using flux-grown KTP wafers and characterized the optical performance of these devices using a tunable Ti:Sapphire laser.[87] The waveguides were fabricated for first-order QPM SHG in the 400-440 nm range. An important aspect of their report was the measurement of the blue SHG power associated with the three highest order spatial modes of their devices. They reported an approximate 20:1 relationship between the SHG power in the TM_0 spatial mode near 420 nm in comparison to the TM_2 mode near 415 nm. The highest η_{eff} reported was 250%/W-cm^2. The maximum blue output power was about 3.0 mW for 100 mW IR power in the waveguide.

Generation of 425 nm SHG from a KTP PSW optically pumped by an AlGaAs single quantum well (SQW) GRINSCH diode laser using an external diffraction grating to provide optical feedback to frequency-stabilize the diode laser was reported by researchers from IBM.[88] The KTP PSW used in this experiment had a 4 μm width and length of 4.5 mm and was fabricated by DuPont. Both input and output faces of the waveguide were AR-coated with a single λ/4 layer of MgF_2 to yield a reflectivity of about 0.2%. Using a Ti:Sapphire laser to characterized the waveguide, η_{eff} was measured

to be 275%/W-cm^2 for a broad-band ($\Delta\nu$ < 2 GHz) Ti:Sapphire laser but only 100%/W-cm^2 for a single-frequency ($\Delta\nu$ < 500 Khz) Ti:Sapphire laser. This surprising result was attributed to an additional contribution of sum-frequency mixing of axial modes. A 900 line/mm grating blazed for 880 nm was used as the diffraction grating, which could be tilted to tune the frequency of the extended-cavity laser. With this configuration, 1.2 mW of 425 nm SHG was measured exiting the dichroic beamsplitter for a fundamental IR power of 68.3 mW transmitted through the waveguide. This corresponded to a η_{eff} of 127%/W-cm^2.

In a 1994 report, Jongerius, Bolt, and Sweep obtained a peak η_{eff} of approximately 200%/W-cm^2 at 424 nm from a 5 μm wide flux-grown KTP PSW using tunable Ti:Sapphire laser excitation.[90] The SH output exhibited a fundamental mode distribution and the maximum blue power was 0.5 mW for a fundamental power of 35 mW confined inside the waveguide. The SH output power as a function of fundamental wavelength exhibited a strong correlation to a sinc^2 function with a 0.15 nm FWHM, which correlated well to the theoretical value of 0.17 nm. They observed they could obtain a stable output power of about 2 mW in the blue from a confined pump power of about 75 mW which remained stable for at least ten minutes without degradation. They noted that unstable SH power behavior was observed when using a 4 μm guide width on the same sample chip when or the initial blue power level was increased above about 2 mW. The degradation in SH power manifested itself by an attendant decrease in η_{eff} to about 90%/W-cm^2 and a significant broadening of the phase-matching spectrum. In addition, pump beam transmission decreased from 47% to 42%. A slight restoration in efficiency occurred after reducing the power to a low value; however, even after the pump laser input was removed, the sample annealed for several hours at 200 °C, and the sample re-tested several weeks later, the device did not show any further restoration of efficiency.

In the same report, Jongerius and co-workers reported fabricating PSWs using 120 ppm Sc-doped KTP. These devices displayed peak pump to SH conversion efficiencies

of 325%/W-cm^2. A maximum of 3.7 mW near 425 nm was obtained from these devices when the fundamental power in the waveguide was increased to 83 mW. After 6 minutes of maintaining the fundamental power in the guide at 80 mW the blue output decreased to 2.5 mW, corresponding to a decrease in η_{eff} from 300% W/cm^2 to 190% W/cm^2. The pump beam transmission decreased from 59% to 52%. By removing the incident pump beam from the waveguide and then recoupling, the pump beam transmission was found to be restored to 57% and the phase-matching spectrum also recovered its original shape. In higher pump power testing, at 115 mW fundamental power in the waveguide a peak SHG power of 6.3 mW, corresponding to an η_{eff} of 240%/W-cm^2 was obtained for a short period. Noteworthy of these devices was the restoration of the low-power (about 30 mW fundamental in the guide) η_{eff} value near 300%/W-cm^2 after the power was decreased and the device was allowed to recover for several minutes indicating the possibility of stable SH output of about 0.5 mW from these devices near 425 nm.

The authors concluded that an optically induced nonuniformity was responsible for the loss of efficiency in both the undoped and Sc-doped KTP PSWs they studied. An important observation for high-power optical pumping applications was they did not find that the optically induced nonuniformites were exclusively caused by high pump powers within the waveguides; rather, the presence of SHG was found to be required for the nonuinformities to occur and for the optical power losses to be observed. This observation led the authors to conclude that the phenomena causing the power loss in their devices corresponded qualitatively to the characteristics reported for gray-track formation in bulk KTP by variety of workers.[91-93]

For diode-pumped KTP PSWs, control of the diode wavelength is required for efficient SHG operation. Waveguide structures designed to provide a Bragg reflection for diode wavelength stabilization have achieved significant success in meeting this important requirement. Bierlein described two structures, one in which both the SHG and the Bragg reflection were continually generated along the waveguide, and a second in which the SHG occurs in one section of the waveguide and the Bragg reflection occurs in

a second section of the same waveguide.[94] Previously, Bierlein had described how the Bragg and SHG wavelengths could be made to coincide by temperature tuning the KTP substrate through use of a thermal electric cooler (TEC).[85] The device with separate SHG and Bragg sections, was fabricated with an SHG section 4.5 mm in length and the Bragg section about 2 mm in length, and with AR coatings (< 0.5%) centered at 850 nm applied to both input and output faces. Testing this device's η_{eff} using a Ti:Sapphire laser yielded a value of 350%/W-cm^2. An SDL 5422 Fabry-Perot index-guided AlGaAs diode laser with a high quality AR coated output facet was coupled into the KTP PSW with a coupling efficiency of 60%. The emitting wavelength of the diode laser was successfully locked to the Bragg reflection and the temperature of the KTP PSW was set for coincidence of the SHG and Bragg wavelengths. The temperature control to achieve stable blue output was reported to be about ±2.5°C. This configuration produced 1.6 mW near 427 nm using about 100 mW input CW power from the diode laser.

Eger et al. reported very high η_{eff} values in the 700-800%/W-cm^2 range for blue light generation near 425 nm in KTP PSWs.[96] The waveguides were fabricated on the z surface of flux grown KTP by an ion exchange process using a $Rb(Ba)NO_3$ salt bath. The waveguides were 3.8 mm in length with a guide width of 3.6 μm. Output from a Ti:Sapphire laser was end-coupled into the waveguides. An output power of 1.8 mW near 425 nm was reported for the TM_0 mode. The TM_1 appeared at 423 nm and emitted about 0.7 mW. Transmitted infrared light through the waveguides was measured and totaled about 40 mW. In this report, Eger noted a large discrepancy between the measured and calculated η_{eff} values based on using the expression

$$\eta_{eff} = \frac{8\pi^2 d_q^2}{n_\omega^2 n_{2\omega} c \varepsilon_0 \lambda_\omega^2} |J|^2 \tag{2.28}$$

given by Fejer et al., where J represents the overlap integral between the fundamental and SH electric fields.[77] This discrepancy was attributed to either an incomplete theory or an incorrect value for the nonlinear d coefficient. Using the above relationship and a value for d_{eff} = 13.7 pm/V, Eger et al. calculated an η_{eff} value of only 100%/W-cm^2.

In a later report, Eger et al. described simultaneous blue light generation and Bragg reflection locking of the output of an AlGaAs diode laser used as the fundamental source.[96] This was accomplished by performing the SHG in one section of the waveguide while providing the Bragg reflection from a second section in a similar fashion to the previously described work by Bierlein's group. Eger et al. also used an SDL Model 5422 single-mode AlGaAs diode laser, operating near 860 nm, as the fundamental source. The infrared power fed back into the diode laser from the Bragg section of the waveguide was measured to be about 8%. This was comparable to the expected reflected power taking into account the coupling efficiency, DBR reflectivity, and back coupling into the diode laser. A maximum blue SHG output of about 3 mW was reported for a diode power input of 128 mW. For laser diode input powers below about 40 mW, the SHG output power scaled with a quadratic dependence as expected. Above this input power level, however, a significant deviation from the quadratic dependence was noted. For diode input powers in the 40-128 mW range, the SHG output power measured significantly less than the extrapolated quadratic dependence curve. The diode laser wavelength was determined to be stable to within ±0.02 nm for several hours of operation and the short-term (≈ 10 s) fluctuations in the SHG output were about 1%. The stability was reported to depend strongly on the relative intensities of the reflections from the laser facet and the DBR. The diode laser used by Eger in this report had a standard AR coating. Further improvements in laser stability were predicted if the AR coating of the diode laser output facet could be further improved.

The IBM group fabricated distributed Bragg reflectors in ion-exchanged KTP waveguides.[97] Using a grating with one hundred 0.7 μm periods, they measured feedback to the SDL Model 5419 diode laser used as the pump source to be about 12%. This was sufficient to cause the diode laser to oscillate in a single longitudinal mode of an extended cavity consisting of the waveguide and the diode laser. The measured linewidth was 8 MHz, which was instrument-limited.

Risk and Chen continued the work on KTP PSWs at IBM by demonstrating that electric field poling can produce deep inverted domains.[98] Shallow domain inversion, due to reduced transverse index contrast, was shown to produce an enhanced TM_1 mode and a loss of efficiency in the TM_0 mode. To accomplish the electric field poling, a high voltage pulser applied periodic 2 kV pulses across a 7 mm thick KTP substrate. A 4 μm wide waveguide was subsequently formed through ion-exchange in a $3\%Ba(NO_3)_2/97\%RbNO_3$ bath for 30 minutes at 325°C. The waveguide length was 3.6 mm.

These waveguides were optically characterized using a Ti:Sapphire laser as the fundamental source. Using an input cw power of 146 mW at 862 nm, a maximum of 12 mW at 431 nm was produced. By calculating the η_{eff} value using an effective interaction length of 2.8 mm based on an analysis of the phase-matching curve wavelength bandwidth, Risk and Chen claimed an $\eta_{eff} = 720\%/W\text{-}cm^2$ using the fundamental and SHG powers given above. They claimed a significantly larger "highest" $\eta_{eff} \sim 1100\%/W\text{-}cm^2$ when the input power was reduced to 120 mW to yield an SHG power of 9.2 mW at 431 nm. It should be pointed out that had Risk and Chen used the actual guide length of 3.6 mm, as customarily used by workers in the field, the η_{eff} values they reported would have been reduced to $435\%/W\text{-}cm^2$ and $665\%/W\text{-}cm^2$, respectively for the two values given above. Regardless of the method used to calculate the η_{eff} value, their results are among the best reported for KTP PSWs and reflect well upon the potential of electric poling as a technique for producing domain inversion in this material system.

2.5 Discussion

Researchers continue to make progress towards a reliable process technology for the fabrication of blue, violet, and near ultraviolet semiconductor lasers. Someday, most observers agree, this laser technology will dominate the applications requiring a compact ultraviolet laser. Today, wide bandgap semiconductor lasers are a celebrated

achievement for the researchers who have created the very first devices displaying stimulated emission at short visible and near ultraviolet wavelengths. However, practical devices employing these emerging material systems are years away.

Today, as discussed in this chapter, diode-pumped PSW lasers can provide the capable researcher an attractive approach to the generation of modest levels of CW power in the blue and violet. Challenges remain in extending this approach into the near ultraviolet and obtaining useful output power at the several milliwatt level. In advance of the availability of semiconductor lasers operating at these wavelengths, diode-pumped PSW lasers offer promise to deliver comparable wavelength and cw power performance in a compact package.

As summarized in this chapter, KTP PSWs have received substantial attention as the nonlinear substrate material of choice for PSWs operating in the deep blue and violet. Bierlein and co-workers at DuPont have demonstrated that a Ti:Sapphire laser-pumped KTP PSW could emit SHG power in the near ultraviolet. In a subsequent personal communication, Bierlein expressed optimism that with further development work KTP PSWs could be fabricated that would operate efficiently in the 380-400 nm spectral range.[99] Efficient utilization of such devices would require development of spatially coherent, frequency-stabilized diode laser sources; a detailed understanding of the spectral and beam propagation characteristics of KTP PSWs in the near ultraviolet; spatially coherent, frequency-stabilized diode laser sources; and methods for integrating these discrete devices to form a compact, near ultraviolet laser.

The following chapter discusses the design considerations for a diode-pumped KTP PSW laser for operation in the near ultraviolet, and the rationale and requirements for an unstable resonator semiconductor laser for use as the required diode pump source for this application.

CHAPTER 3
DESIGN CONSIDERATIONS FOR URSL-PUMPED KTP WAVEGUIDE LASERS

The first demonstration by van der Poel, Bierlein, and co-workers of blue SHG from a KTP PSW utilized fundamental output from an argon-ion laser-pumped Ti:Sapphire laser.[70] For purposes of optical characterization, an argon-ion laser-pumped Ti:Sapphire laser offers the advantages of: wide spectral tunability, gaussian spatial mode behavior, and ample optical output power. The disadvantages include: a large mechanical footprint, which, when including the required laser optics, can occupy the majority of a standard optical table; typically 400 VAC, 30-50 A electrical requirements; substantial water cooling; and very high capital costs. When unfairly compared to the thumbnail size and approximate cost of one dollar for the typical low power 780 nm diode laser used in current compact disc players, the imperative for a diode-pumped KTP waveguide laser comes into focus. Numerous applications for near ultraviolet diode-pumped KTP waveguide lasers require the successful integration of the appropriate diode laser source with a properly designed KTP waveguide. While substantial progress, most notably the collaborative effort of Pioneer and DuPont[18], has been made towards the development of a blue diode-pumped KTP waveguide lasers operating in the 420-430 nm range, no previous reports exist concerning near ultraviolet diode-pumped KTP waveguide laser development.

A preliminary set of design requirements for a near ultraviolet diode-pumped KTP waveguide laser was developed by considering the specific applications for such a device. A particularly demanding application, as discussed in the preceding chapter, is the need for a near ultraviolet laser for use in photoactivation of pharmaceutical agents.

Development of photoactivated drugs, such as psoralen for the treatment of accelerated atherosclerosis, requires the availability of near ultraviolet laser sources capable of producing CW powers in the 1-100 mW range.[19] Many emerging photodynamic therapies are highly experimental. In these cases, a wavelength-tunable light source or light source which can be constructed to emit at a specific wavelength is often an important advantage. The SHG CW output power, to be useful, needs to be modestly stable to provide reliable and accurate light dosimetry. For most applications, it is preferable for the SHG output to be emitted in the fundamental spatial mode to allow the greatest flexibility in optical coupling.

Based on these considerations, a preliminary set of design requirements for a diode-pumped KTP waveguide laser was constructed. These requirements are shown in Table 3.1

Wavelength Range	380-390 nm
SHG CW Power	1-20 mW
Infrared Pump Power	≥ 250 mW
SHG Spatial Mode	TM_0
SHG CW Power Stability	≤ +/- 5%, min/max
Waveguide Type	Periodically segmented KTP waveguide
Infrared Pump Laser	770 nm, +/- 10 nm AlGaAs diode laser

Table 3.1 Preliminary Design Requirements for Diode-Pumped KTP Waveguide Laser

To translate these preliminary design requirements to a practical experimental design for a diode-pumped KTP waveguide laser, a detailed understanding of the processes controlling SHG process in the near ultraviolet in diode-pumped KTP waveguides must be developed.

3.1 KTP Waveguide Process and Wafer Considerations for NUV Operation

To establish the KTP waveguide process and wafer type, the available reports for both Ti:Sapphire-pumped and diode-pumped KTP waveguide operation were examined. A representative summary of these results is given in Table 3.2. A discussion of these results as they relate to waveguide wafer and process considerations for NUV operation follows.

The loss of efficiency over time caused by optically induced nonuniformities, as reported by Jongerius et al.[90], represents a principal consideration in determining a KTP PSW design. This effect has not been well characterized in the spectral range below 420 nm. As noted by Jongerius et al., the presence of SHG in the waveguide is required for the nonuniformities to occur. They concluded that the phenomena causing the power loss in their devices corresponded qualitatively to the characteristics reported for gray-track formation in bulk KTP. Morris et al.[100] conducted a series of experiments to characterize KTP PSWs at high power densities using 458 nm, 514 nm, and 790 nm pump wavelengths to probe the transmission of KTP PSWs fabricated from flux and hydrothermal KTP substrates. This set of experiments also examined the effect of the Ba concentration used in the ion-exchange bath and the effect of heat sinking the KTP PSW. These experiments did not involve SHG generation in the KTP PSWs. Morris et al. concluded that the effect responsible for decreasing the transmission of KTP PSWs increases with pump intensity over the range from 1 kW/cm^2 to 1 MW/cm^2; increases with decreasing wavelength; is more severe in flux KTP PSWs than in hydrothermal KTP PSWs; increases with Ba concentration in flux KTP PSWs; and is more severe for TM polarization than for TE polarization. A photorefractive-like process caused by the pyroelectric effect with an approximate thermal dependence of $\Delta n/\Delta T \sim 0.0001/°C$ was suggested as the mechanism responsible for the transmission loss. Heat sinking was shown to reduce the observed effect. Based on this interpretation, Morris et al.concluded that the observed transmission loss in KTP PSWs at high power densities was not gray

Reference	SHG Wavelength (nm)	Pump Type	Maximum SHG CW Power (mW)	η_{eff} (%/W-cm^2)	Process
Eger et al.[106]	420	Ti: Sapp	3.0	250	flux KTP $Rb(Ba)NO_3$
Jongerius et al.[107]	433	Ti: Sapp	1.8	150	flux KTP $Rb(Tl/Ba)NO_3$
Laurell et al.[101]	359	Ti: Sapp	0.037	Not reported	flux KTP $Rb(Ba)NO_3$
Risk et al.[124]	425	Diode		275	flux KTP $Rb(Ba)NO_3$
Jongerius et al.[90]	425	Ti: Sapp	3.7	325	flux sc:KTP
Eger et al.[96]	425	Ti: Sapp	1.8	700	flux KTP $Rb(Ba)NO_3$
Eger et al.[95]	429	Diode	3.6	Not reported	flux KTP $Rb(Ba)NO_3$
Bierlein et al.[94]	427	Diode	1.6	~100	flux KTP
Risk et al.[98]	431	Ti: Sapp	12	435	flux KTP $Rb(Ba)NO_3$ electric poling

Table 3.2 KTP Waveguide Performance Summary

track absorption. Photorefractive damage, instead, was suspected by Morris et al. Methods cited to minimize the suspected photorefractive changes in the linear index included use of hydrothermal KTP wafers and heat sinking.

These two reports, considered together, suggest that both photorefractive changes in the linear index due to high density optical pumping and gray tracking during QPM SHG operation may occur in KTP PSWs. Due to these effects, in certain cases, the reports of maximum SHG power reported by various workers in Table 3.2 may overstate the steady-state SHG power produced in their KTP PSWs. Certain reports are specific about the time-dependence of the SHG power output. Jongerius et al. gives the maximum and steady-state values for η_{eff}.[90] Eger noted that fluctuations over about 10 seconds in the SHG output were about 1%.[96] Generally, however, most workers have not reported the temporal stability of the SHG power emitted from their devices under constant pump power conditions. With this uncertainty, a review of Table 3.2 suggests that the η_{eff} values reported by workers using diode laser pump sources fall within the range from ~ 100 -300%/W-cm^2. Note that all of these diode-pumped results used flux grown KTP wafers.

3.2 KTP Waveguide Spectral Characteristics

For SHG at 385 nm, the condition for first-order QPM

$$\Delta k_a l_{a1} + \Delta k_b l_b = 2\pi \tag{3.1}$$

yields $\Lambda = 2.78$ μm for

$$l_a + l_b = \Lambda \tag{3.2}$$

where $\Lambda \equiv$ waveguide period length, and l_a and l_b are the lengths of the diffused and undiffused regions, respectively, and where $\Delta n_{a,b} = (n_{385\ nm} - n_{770\ nm}) = 0.138$ in both the diffused and undiffused segments, and where the KTP refractive indices given by Ghosh[102] were used.

To determine the spectral bandwidth tunability for QPM SHG, Fejer et al.[103] evaluated

$$E_2 \approx ie^{-\Delta kl/2}\Gamma d_q L\,\mathrm{sinc}(\Delta kl/2) \tag{3.3}$$

where $\Gamma \equiv i\omega E_1^2 / n_2 c$ and $d_q=2d_{eff}/m\pi$. Since the SHG power according to (3.3) goes as $\mathrm{sinc}^2(\Delta kl/2)$, they determined that the SHG power falls to one-half its peak value when

$$\Delta kl/2 = 0.4429\pi \tag{3.4}$$

Then by expanding Δk as a Taylor series about λ_0, Fejer obtained

$$\Delta k(\lambda,\lambda_0) = (\lambda-\lambda_0)\frac{\partial \Delta k}{\partial \lambda}+\ldots \tag{3.5}$$

where higher order terms have been neglected since Δk has a first order dependence on λ. Using (3.4) and (3.5), and doubling the result to obtain the FWHM gives

$$\Delta\lambda = \frac{5.57}{L}\left|\frac{\partial \Delta k}{\partial \lambda}\right|^{-1} \tag{3.6}$$

which then yields

$$\Delta\lambda = \frac{0.4429\lambda}{L}\left|\frac{n_2-n_1}{\lambda}+\frac{\partial n_1}{\partial \lambda}-\frac{1}{2}\frac{\partial n_2}{\partial \lambda}\right|^{-1} \tag{3.7}$$

Evaluating this expression numerically for λ=770.0 nm, using n_2=1.983, n_1=1.846, $\partial n_1/\partial\lambda$=-0.09 μm^{-1}, $\partial n_2/\partial\lambda$=-1.313 μm^{-1} and L=7.0 mm gives $\Delta\lambda$ = 0.065 nm for the FWHM wavelength acceptance bandwidth for QPM SHG. Equivalently, the QPM SHG frequency bandwidth is about 33 GHz for the values used in this sample calculation.

This FWHM wavelength acceptance bandwidth imposes severe requirements on the spectral emission characteristics of the diode laser pump source. The longitudinal mode spacing for a diode laser[104] is given by

$$\Delta\nu = c/2n_g L_r \tag{3.8}$$

where

$$n_g = n+\nu\left(\partial n/\partial \nu\right) \tag{3.9}$$

As an estimate of the longitudinal mode spacing, consider an AlGaAs diode laser with length L_r=500 μm. For this material system, n ≈ 3.4 and n_g ≈ 4.0 at 770 nm and (3.8) gives Δν ≈ 75 GHz or $\Delta\lambda = \lambda^2\Delta\nu/c \approx 0.15$ nm. Typical spectral linewidths of AlGaAs diode lasers designed to operate on a single longitudinal mode range from 1-50 MHz. The SDL 5700 Series Distributed Bragg Reflector diode laser is an example of a single longitudinal mode device that has been employed as a fundamental pump source[18,96] for diode-pumped KTP waveguide experiments. The SDL 5700 series diodes display a 3 MHz emission spectral width and produce up to 100 mW CW at 852 nm.[5]

Clearly, the wavelength acceptance bandwidth for NUV SHG in KTP waveguides is of similar order as the longitudinal mode spacing in typical AlGaAs diode lasers. The typical longitudinal mode linewidths encountered in AlGaAs diode lasers are significantly smaller than the QPM wavelength acceptance bandwidth. Therefore, careful consideration must be given to controlling the longitudinal mode behavior of the diode laser used as a fundamental wavelength pump source in a diode-pumped KTP waveguide laser designed for efficient NUV SHG operation.

Since the fundamental wavelength at which quasi-phase-matching will be achieved is subtly governed by processing variables, such as actual period length and diffused region refractive indices at the fundamental and SH wavelengths, a fine means of varying the diode laser wavelength is needed. Varying the temperature of the diode laser active region is a well-known method of achieving wavelength control in diode lasers.[105] In Fabry-Perot AlGaAs diode lasers, the wavelength changes with temperature at an approximate rate $d\lambda/dT \approx 0.3$ nm/°C. This implies a temperature stability requirement substantially less than 0.1 °C to avoid temperature-dependent wavelength drift in a single-longitudinal mode AlGaAs diode laser from contributing significantly to SHG output instability. Use of a closed-loop thermoelectic temperature controller can achieve better than 0.01°C temperature stability for most diode lasers packaged with a TEC. This translates to a temperature-limited wavelength stability of about 0.003 nm, which appears adequate considering a QPM wavelength acceptance bandwidth of 0.065 nm.

Effects of thermal expansion on the segment lengths governing the waveguide period and the temperature-dependence of the refractive indices of the diffused and undiffused segments of the KTP waveguide must also be considered when evaluating the spectral characteristics of a diode-pumped KTP waveguide laser. By controlling the temperature of the waveguide, the quasi-phase-matching wavelength can be tuned to the emission wavelength of the pump diode laser.[100]

3.3 Spatial Mode Considerations

The SHG power produced in a nonlinear waveguide depends intrinsically on the nature of the spatial modes supported by the waveguide. Since the SHG power scales as the square of the fundamental power, obtaining a high degree of spatial overlap between the fundamental and SH guided modes stands out as an obvious requirement for efficient conversion of the fundamental input power into SHG output power. For KTP PSWs, van der Poel et al. reported that the most efficient interaction was type I coupling through the d_{33} nonlinear coefficient ($TM_{\omega} \rightarrow TM_{2\omega}$).[70]

Fejer et al. developed an analytical model to evaluate the effect of the spatial mode overlap on η_{eff} for an ideal waveguide in which the d coefficient is modulated such that it reverses sign each half-period along the length of the waveguide.[77] For this case, Fejer et al. give

$$\eta_{eff} = \frac{8\pi^2 d_Q^2}{n_\omega^2 n_{2\omega} c \varepsilon_0 \lambda_\omega^2} \left| \int_{-\infty}^{\infty} E_{2\omega}^*(y) E_\omega^2(y) dy \right|^2 \tag{3.10}$$

where $d_Q=(2/m\pi)d_{eff}$, where d_{eff} is the effective nonlinear d coefficient for a conventional interaction involving the same optical fields. From (3.10), the dependence of n_{eff} on the modal overlap of the fundamental and SH guided modes in the waveguide is apparent.

In an effort to correlate experimental results indicating a very high η_{eff} to a value expected from theory, Eger et al.[106] used (3.10) with d_{eff}=13.7 pm/V[15] and obtained $\eta_{eff} \approx$ 100%/W-cm^2, which was far below the experimentally determined value of 700-800%/W-cm^2. Even accounting for a maximum factor of 2 increase which can be

obtained using a multimode pump[89], Eger et al. concluded that either the theory used was incomplete or the value of d_{eff} in the waveguide is much different than in bulk KTP. Also, Eger et al. appears to have used experimental measurements to determine the amplitudes of the electric fields used in (3.10) and assumed perfect centration of the maxima for each mode.

The spatial mode characteristics of KTP PSWs have been the subject of several reports.[108-110] Li and Burke[17] modeled a segmented channel waveguide as an equivalent continuous channel waveguide. This equivalent continuous waveguide is obtained by averaging the index along the propagation direction in the segmented waveguide case and using this average index for the channel index for the continuous waveguide.[108] A similar method was independently developed by A. Suna and J. Bierlein.[109] The propagation constants and field distributions of the modes obtained using this model for the equivalent continuous waveguide were found to be almost identical to those determined analytically for the segmented waveguide.[109] Weitzmann and Hardy modeled the spatial modes for KTP PSWs using a beam propagation method (BPM) treatment.[110] They launched a finite plane wave into a KTP PSW and observed that the wave propagating in the waveguide is first diffracted and then corrected, but not fully restored, after propagating through one period of the waveguide. They theorized that the resulting phase ripples are filtered out via radiation, and as a result, the waveguide is inherently leaky. While this contributed an interesting theoretical result, their work did not address the practical and much more interesting case of the propagation behavior arising from launching a gaussian fundamental input field into a KTP PSW.

Significant limitations have been identified in each of these models. For example, the theoretical expression given by (3.10) does not account for the lateral spatial variation of the d coefficient and electric fields. The average index method used by Li and Burke cannot analyze the effect of diffraction arising from index changes on the optical fields propagating along the length of the waveguide. The BPM studies by Weitzmann and Hardy were inconclusive due to the large computational grid sizes used

and very short propagation distances over which the simulated PSW was modeled. Nor do any of these reports present results for fundamental wavelengths below 840 nm. A more complete discussion of these models and their usefulness and limitations is included in Chapter 4.

While it is not possible based on existing reports in the literature to determine a good estimate of η_{eff} for NUV SHG output from a diode-pumped KTP PSW, a reasonable understanding of the number and spectral separation of spatial modes for a given waveguide geometry can be estimated based on consideration of a KTP PSW as an asymmetric slab waveguide and by comparing the results to the careful experimental work on the subject performed by Roelofs et al.[111]

The number ρ of guided spatial modes supported by an asymmetric slab waveguide of dimension d is given by

$$\rho = \left[\left(1/\pi \right) \left\{ V - \tan^{-1} \left[\phi \left(n_2^2 - n_3^2 \right)^{1/2} \Big/ \left(n_1^2 - n_2^2 \right)^{1/2} \right] \right\} \right]_{\text{int}} \tag{3.11}$$

where

$$V = \frac{2\pi d}{\lambda} \left(n_1^2 - n_2^2 \right)^{1/2} \tag{3.12}$$

$$\phi = \frac{n_1^2}{n_3^2}, \text{ TM modes; } \phi = 1, \text{ TE modes} \tag{3.13}$$

and where the notation $[\ ]_{int}$ indicates that the integer whose value is just larger than the value of the number in brackets must be taken and where n_1, n_2, and n_3 are the refractive indices, respectively, of the three layer asymmetric slab waveguide.[112]

Roelofs et al. described a geometrical construction for determining the wavelengths of the guided SH modes and determining the relative spectral spacing between adjacent spatial modes. Curves representing the index of refraction of the substrate and the modes at both the fundamental and SH wavelengths are drawn. At each fundamental wavelength, a vertical line is drawn of length λ/Λ_a. Where these lines exactly join a fundamental mode to an SH mode, that interaction will be quasi-phase-

matched. Applying this technique to the case of a fundamental TM_0 mode exciting the SH TM_0, TM_1, and TM_2 as the wavelength of the fundamental is tuned over the range from 845 nm to 840 nm, Roelofs et al. determined that the spectral spacings are approximately $\Delta\lambda \sim 2.7$ nm between TM_0 and TM_1 and $\Delta\lambda \sim 1.8$ nm between TM_1 and TM_2.

Based on these considerations, it is clear that the spectral separation of the QPM NUV SH spatial modes are significantly larger than the quasi-phase-matching spectral bandwidth. For a fundamental pump source with total spectral linewidth less than the QPM spectral bandwidth, single SH spatial mode operation, therefore, should be expected. Note, however, that if a fundamental source with broad spectral emission is employed, for example, a broad area AlGaAs diode laser, two or even three SH spatial modes could be simultaneously excited. Whether this approach could be useful depends critically on the spatial overlap of the fundamental and SH guided modes in the specific implementation.

3.4 Diode Laser Requirements

The fundamental CW power required from a 770 nm diode laser used to pump a KTP PSW is dependent on η_{eff}, the guide length, and the desired SH output power at 385 nm. As noted in the preceding section, no experimental or theoretical values of η_{eff} have been previously reported for NUV SHG from a diode-pumped KTP PSW. The lack of a clear understanding of the spatial mode properties of KTP PSWs together with the incomplete development of the theoretical treatment of SHG generation in nonlinear waveguides, in general, limits an *a priori* assessment of calculated values for η_{eff}. KTP PSWs with SH interaction lengths between 4.0 mm and 8.0 mm have been experimentally demonstrated to yield η_{eff} values in the range from 100%/W-cm^2 to 800%/W-cm^2 in the blue and violet. This suggests that a conservative estimate for η_{eff} should fall at the low end of this range. Assuming a waveguide SH interaction length of 7.00 mm and an $\eta_{eff} \approx 100\%/\text{W-cm}^2$, to produce 10 mW at 385 nm requires coupling 142 mW of 770 nm optical output power from the diode laser into the fundamental guided

mode of the waveguide, assuming a fundamental $TM_0 \rightarrow$ SH TM_0 interaction. This simple estimate immediately suggests that 100 mW diode lasers will not meet the design requirements given in Table 3.1. This is a discouraging result in the sense that AlGaAs index-guided diode lasers are generally limited to CW output powers less than 200 mW. This power limitation is governed by the optical intensity above which catastrophic optical damage occurs at the facets.[113] To increase the cw power output from a diode laser, employment of broader active regions becomes necessary. But as the active region becomes broader, the ability to laterally tailor the refractive index to achieve desirable lateral waveguiding characteristics is gradually lost. It is this trade-off between increased cw power and spatial coherence that is reflected by the decisions of previous workers to limit their diode laser choices to index-guided AlGaAs devices. To efficiently utilize a high-power broad area semiconductor laser, the optical output must be focused to a nearly diffraction-limited spot size in order to efficiently couple into the fundamental guided spatial mode of the KTP PSW. The waveguide parameters controlling the spatial mode properties of KTP PSWs will be detailed in Chapter 4. To achieve nearly diffraction-limited performance from a high-power broad area semiconductor laser imposes the stringent requirement that it achieve a comparable brightness to a index-guided diode laser in order for the increased optical power to efficiently couple to the guided waveguide spatial mode. The optical brightness of broad area semiconductor lasers has been discussed by Bao.[114] The brightness is given by

$$\textit{Brightness} = P_{op}/AS_a \tag{3.14}$$

where P_{op} is the total output power, A is the light emitting area, and S_a is the solid angle subtended by the output beam. For an astigmatism-corrected laser, A is given by

$$A = h_l h_t \tag{3.15}$$

where h_l and h_t are the respective lateral and transverse source sizes (FWHM). The solid angle S_a can be approximated as

$$S_a = 2\theta_l\theta_t/\pi \tag{3.16}$$

and where θ_l and θ_t, respectively are the FWHM lateral and transverse divergence angles. The brightness value for a 100 mW SDL 5410 series index-guided diode laser using (3.14) and catalog values[11] for h_l, h_t, θ_l, and θ_t is about 150 MW/cm^2-sr. High-power broad area semiconductor lasers produce brightness values typically an order of magnitude smaller than this value. The primary mechanism responsible for reduced brightness in broad area semiconductor laser is the characteristically filamentary structure observed in their optical near-field patterns.[115,116] These filaments arise from a nonlinear interaction between the carriers and the optical field in the active area of the laser. The process of stimulated emission effectively reduces the gain profile within the active area and results in an increase in the refractive index in the portion of the active area contributing most strongly to the optical mode. This region of increased refractive index is bounded by regions of the active area which do not contribute so strongly to the optical mode and are characterized by smaller refractive index values. This lateral variation in refractive index in a local region within the active area of the diode laser forms a local lateral index guide. When the active area is broader than about 5-10 μm, it is possible at, say, 12 μm width, for many such index-guided regions to develop. Stimulated emission within each such lateral index-guided region within the active area occurs in the form of a filament that is only partly spatially coherent, or is spatially incoherent, with respect to neighboring filaments. This filamentation phenomenon is therefore a fundamental source of lateral spatial incoherence in high-power, broad area semiconductor lasers, and consequently places severe limits on the optical brightness obtainable from such devices.

In addition to the brightness limitations of these devices, they also typically display multi-longitudinal mode output. The CW output power of high-power, broad area AlGaAs diode lasers is contained in a multi-longitudinal mode spectrum that typically spans several 2-4 nm. Figure 3.2 shows the measured power spectrum for a 0.5 W Sony 303XT AlGaAs diode laser. The active region width of this device is 100 μm. The power spectrum is composed of five or six predominant modes spaced according to the relationship given by (3.8).

To effectively utilize the high CW output power available from broad area AlGaAs diode lasers for use as a KTP waveguide pump laser, some means of obtaining a spatially coherent and spectrally narrow output must be devised. A method for obtaining high-power, nearly diffraction-limited optical output from high-power, broad area semiconductor lasers using FIBM processing to fabricate URSLs has been demonstrated by laser diode workers at Oregon Graduate Institute, Linfield Research Institute, and at the Semiconductor Laser Branch in Phillips Laboratory at Kirtland Air Force Base.

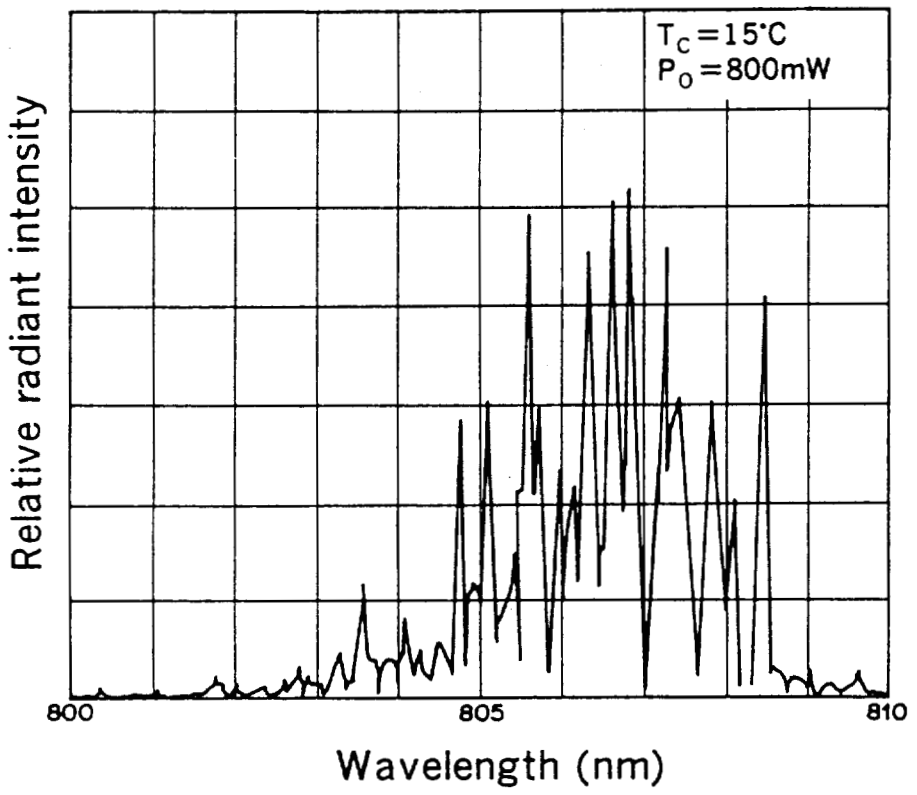

Figure 3.1 Power Spectrum of Sony 303XT AlGaAs 0.5 W broad area diode laser

This research has led to the development of low-magnification half-symmetric URSLs.[114,117-119] The curved mirror facets of these devices were micromachined using a focused ion beam. The high quality of the curved mirrors produced by FIBM is considered to be responsible for the high brightness values reported by Bao for URSLs made with this technique.[114]

Bao reported on fabrication of GRINSCH-SQW URSLs in the GaInP/AlGaInP, GaAs/AlGaAs, and InGaAs/GaAs material systems.[114] Brightness values exceeding 200 MW/cm^2-sr were obtained from devices in each of these material systems. Of particular interest to the present work, Bao obtain a brightness of 431 MW/cm^2-sr from an GaAs/AlGaAs device emitting near 840 nm when operated in pulsed mode. The maximum power reported for this device was 2.0 W. Also, Bao was able to obtain a brightness of 92 MW/cm^2-sr from an InGaAs/GaAs GRINSCH-SQW URSL emitting near 970 nm with a maximum CW power of 1.20 W. These encouraging results indicated the feasibility of developing a 0.5 W GaAs/AlGaAs GRINSCH SQW half-symmetric URSL with high brightness using the FIBM techniques extensively developed at Oregon Graduate Institute, and later at Linfield Research Institute by DeFreez and co-workers.

The devices fabricated by Bao were all multi-longitudinal mode devices and did not contain frequency-selective elements. The severe $\Delta\lambda_{QPM}$ requirements for the a diode pump source force consideration of a frequency-stabilized URSL. In addition, the frequency-stabilized URSL must be capable of being wavelength-tuned to match the QPM wavelength and having its emission wavelength bandwidth narrowed to efficiently match the QPM wavelength acceptance bandwidth.

Figure 3.4 shows several structures that have been used to produce single longitudinal mode output from diode lasers. Several of these structures offer promise for integration with a broad area URSL to form a single-frequency URSL; others, such as the coupled-cavity structures appear to be too complicated, particularly from a processing viewpoint, to be seriously considered.

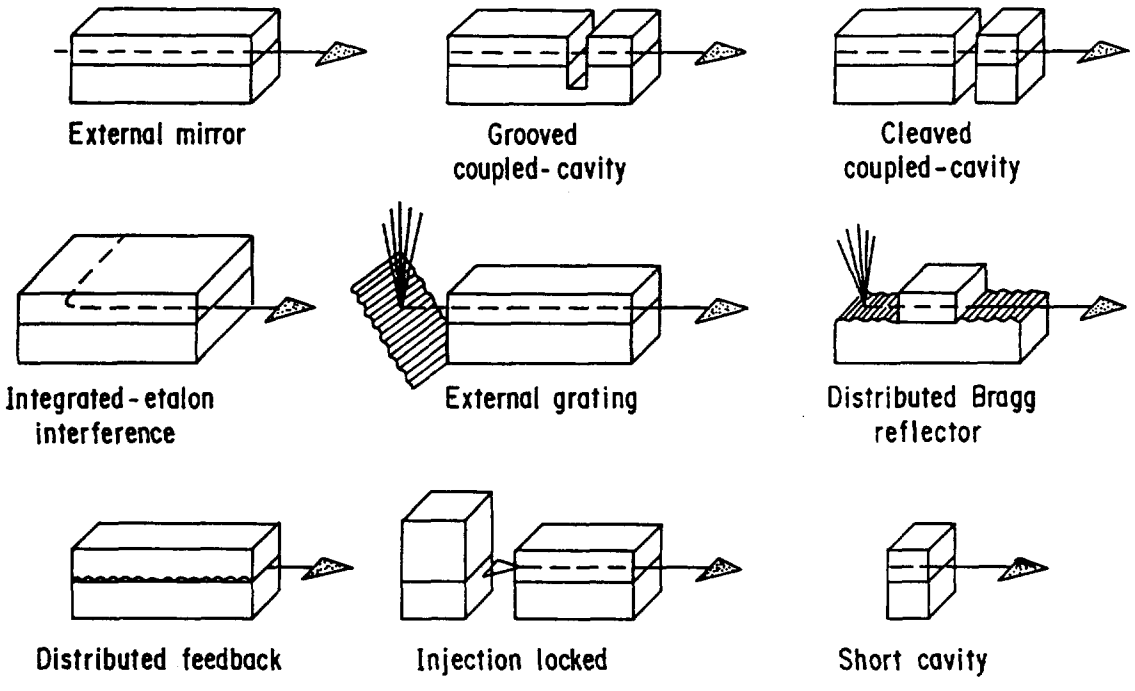

Figure 3.2 Frequency-selective laser diode structures
(After Ikegumi et al., ref. 120)

Inclusion of frequency-selecting elements, whether by an external grating or by a periodic structure in the laser cavity, can provide an effective method for the production of a single-frequency diode laser. To obtain the most compact device, formation of the periodic structure within the laser structure is preferable. The periodic structure can be formed as either a distributed feedback (DFB) laser or a distributed Bragg reflector (DBR) laser. In a DFB laser, the grating is formed in a layer close to the active region of the device and grown with materials of lower refractive index, thus providing a periodic variation in the effective refractive index. To be effective, the emission wavelength of the diode laser must be adjusted to the neighborhood of the roundtrip gain peak by controlling the grating pitch or active layer composition.

Development of high-power, frequency-stabilized, spatially coherent semiconductor sources is currently receiving considerable attention. A monolithic tapered-stripe InGaAs URSL operating at 952 nm produced over 5.0 W under pulsed conditions.[121] In this device, light reflected from a grating section is amplified as it diffracts in a tapered-stripe amplifier section. After reflection from the output facet, a small amount of the amplified beam is recaptured by the waveguide, seeding the oscillation. In this fashion, the device is claimed to be similar to an unstable resonator, in which the on-axis portion of a broadly diverging beam is used to seed the laser oscillation. The Bragg reflector monolithically integrated at the narrow end of the taper provides significant frequency-selectivity. A spectral emission bandwidth of 0.21 nm was reported. Spectra Diode Labs reported on another similar monolithic tapered-stripe InGaAs URSL fabricated with distributed Bragg reflectors which operated in a single longitudinal mode at 941 nm while emitting over 1.0 W CW output power.[122] The measured spectral bandwidth was less than 0.2 nm. At the 1 W CW output power level, ~ 85% of the total output power was contained in the main diffraction-limited lobe, which displayed a FWHM angle of about 0.3° for the far field radiation pattern.

The recognition that the core region of the active area of a half-symmetric URSL controls the evolution of the sub-threshold, near-field spatio-spectral patterns,[123] led DeFreez et al. to suggest that a core grating DFB URSL could provide high-power, frequency-stabilized CW output from an AlGaAs SQW-GRINSCH semiconductor laser.[125] This approach, based upon the demonstrated spatial coherence obtained by Bao[114] for low-magnification SQW-GRINSCH AlGaAs URSLs, and the capability of the material system to support efficient 770 nm operation, led to its selection as the diode laser design for development as a pump laser for a compact ultraviolet laser.

3.5 Discussion

The development of an URSL-pumped KTP waveguide laser can meet the requirements for a compact near ultraviolet laser source capable of emitting 1-20 mW.

The selection of the device technologies that compose this design, a frequency-stabilized SQW-GRINSCH AlGaAs URSL emitting near 770 nm, and hydrothermal KTP waveguides processed for QPM-SHG at 385 nm, are novel. Neither of these devices have been demonstrated previously. The integrated compact near ultraviolet laser, an URSL-pumped KTP waveguide laser, represents a promising new laser technology with potential for wide applications. Accordingly, the successful development of these device technologies and their successful integration to form an URSL-pumped KTP waveguide laser marks an important advancement in photonics technology. The development and testing of these devices is discussed in Chapters 7 and 8.

CHAPTER 4
MODELING OF SPATIAL MODES OF NONLINEAR WAVEGUIDES

4.1 Introduction

A nonlinear waveguide, such as a KTP PSW, acts as a spatial mode converter in addition to its more familiar function as a frequency converting device. As a result of the QPM waveguide fabrication conditions, the index contrast in a KTP PSW for operation in the near ultraviolet is quite small. Typically, the index contrast between the undiffused KTP regions and the exchanged regions measures $\Delta n \approx 0.015$ or less. Clearly, such a small index contrast supports only weakly guided spatial modes in the lateral dimension. The extension of the guided spatial modes at the fundamental and the SH wavelengths into the lateral regions outside the grating channel merits careful examination. Important consequences of such weak lateral waveguiding include effects on the overlap between the fundamental and SH guided modes, and the dependence of the SH optical field on the sign of the d coefficient, which, of course, has a lateral as well as longitudinal variation.

The transverse behavior of the spatial modes can be expected to display strong mode confinement at the waveguide/air interface. However, due to the modest depth over which ion-exchange occurs, the variation in refractive index with depth has been shown by Risk to best fit a complimentary error function (erfc)[124] and by Roelofs to fit an exponential decay.[111] The increase in the refractive index over the undiffused value in both cases decays from a maximum value at the surface. For an SH wavelength of 425 nm, Roelofs found that use of a 1/e depth value of 7.43 μm represented a good fit for the change in refractive index with depth using an exponential fit. This strong variation with depth in the transverse refractive index profile indicates that the transverse spatial modes, and, hence, the overall spatial mode profiles will be non-circular. Qualitatively, the slow

variation in the transverse index profile suggests that the transverse spatial mode profiles can be expected to have a greater extent towards the bottom (substrate) side of the guide in comparison to the top (air) side of the guide.

As introduced in Chapter 3, several efforts have been made to describe the spatial mode characteristics of KTP PSWs. The independent work of Li and Burke[108] and Suna and Bierlein[85] led to a treatment of approximating a KTP PSW as an equivalent continuous waveguide. Li and Burke did not analyze a periodically segmented channel waveguide; rather, they analyzed a periodically segmented slab waveguide, assuming that the refractive index in the diffused regions was constant with depth. The periodically segmented slab waveguide was analyzed as a lamellar (rectangular groove) grating using the modal method.[126] An attractive aspect of this solution method is that it yields the effective index and guided mode power attenuation rate. Using this method, Li and Burke determined numerically that the effective indices obtained using the grating method to model the periodically segmented slab waveguide were identical to those obtained using a conventional non-segmented slab waveguide model provided that the index of the slab was taken to be the weighted (by segmentation duty cycle) average of the diffused and undiffused segments. In their simulations, Li and Burke used a fundamental wavelength of 850 nm and a $\Delta n=0.02$ as the refractive index difference between the diffused and undiffused regions. They considered only propagation of the TM_0 mode at 850 nm. In plots of the electric-field distribution of a 50% duty cycle guide, they observed weak oscillations superimposed on the mode profile in the direction of propagation; but, overall, they noted that the field distribution differs little from that of a uniform slab waveguide whose refractive index is the weight average of that of the diffused and undiffused segments. Li and Burke posed several questions at the conclusion of their report. These questions included:

"Why and how does the segmented structure guide light?", and

"Why is the scattering loss so low?".

To the first question, Li and Burke recalled the reasoning of Bierlein et al.[127] that the high index segments are responsible for waveguiding. They reasoned this was an adequate explanation for reasonable duty cycles, considering that the short length of low index undiffused segments was short in comparison to the defocusing depth of the guided wave; however, they stated that this explanation was tenuous when the duty cycle is reduced to a fraction of a wavelength since in such a case the high index segment would be very thin. In turn, they suggested that their numerical results indicated that the guided mode "feels only the average index of the waveguide and pays little attention to the segmentation of the index distribution." In answer to the second of their questions, which reflected experimentally observed low loss[127], they suggested that for high duty cycle devices, increasing mode confinement explained the low loss observed experimentally and confirmed by their numerical simulations.

The work of Li and Burke[108] helped to establish that a segmented waveguide behaves similarly, in some respects, to an equivalent continuous waveguide. However, since their work approximated away the lateral index variation and index variation with depth characteristic of KTP PSWs, the spatial mode profiles reported in their work are not useful for estimating either the lateral or transverse nature of the fundamental spatial modes. Since the critical parameter to be considered in the operation of any laser-pumped KTP waveguide device is the overlap of the guided modes as these modes propagate along the effective *length* of the waveguide, even an exact calculation of the guided mode spatial distributions at one point along the guide length will not yield an unambiguous value for the average spatial mode overlap everywhere in the waveguide.

Roelofs et al.[111] made an important step towards improving the understanding of the transverse spatial mode profiles of the fundamental and SH electric field amplitudes by solving a scalar wave equation and using an exponential decay function given by

$$\Delta n(y,z) = \Delta n_{surf}\, g(y) e^{(-z/d)} \tag{4.1}$$

where g(y) represents the relative index profile along the y direction (lateral dimension), Δn_{surf} is the increase in refractive index for the equivalent continuous waveguide at the

air/KTP surface interface, d is a fitted depth parameter, and z is the depth dimension variable.[111] Using Δn_{surf}=0.00684 and d=7.43 μm, Roelofs et al. obtained the calculated transverse electric field distributions for the fundamental and SH TM_0 and TM_1 spatial modes shown in Figure 4.1. Note how the fundamental and SH TM_0 mode electric field amplitudes fall to zero at the air/KTP interface (z=0), obtain peak amplitude near the top of the waveguide, and then decay slowly with depth. This behavior, which should be expected based on the qualitative discussion at the beginning of this section, is notably different from the electric field distributions given by Li and Burke for the same wavelength but for Δn_{surf}=0.01 shown in Figure 4.2, which shows the field decaying much more rapidly.

In principal, beam propagation methods (BPM) can accurately model the propagating spatial mode behavior for nonuniform waveguide structures.[128,129] Weissman and Hardy used two BPM methods to study Rb:KTP PSWs.[110] They used a conventional fast Fourier transform FFT-BPM to model 2-D waveguides and a finite-difference (FD) BPM to model 3-D waveguides. For the 2-D cases, they used a computation window of 50 μm, a 128-point grid, and a typical propagation step of 0.5 μm. To avoid reflections from the window boundaries, they added edge absorbers. The BPM analysis was restricted to forward propagation and back reflections were ignored. They argued that since all the BPM points lie outside the (guided) reflection bands that the accuracy of the BPM analysis should not suffer from considering only the forward propagation. Figure 4.3 shows the wavefront evolution calculated by Weissman and Hardy for the fundamental guided mode over a single period of a 8 μm period simulated segmented waveguide with a width of 4 μm. The fundamental wavelength is 850 nm and n_f=1.85 with Δn=0.01. The input field is alternately described as the fundamental TE mode of the segmented waveguide and as being a planar wavefront. Weissman and Hardy use this figure to describe from a "lens-waveguide perspective" that the modes of a PSW are periodically diffracted and phase-corrected as they propagate.

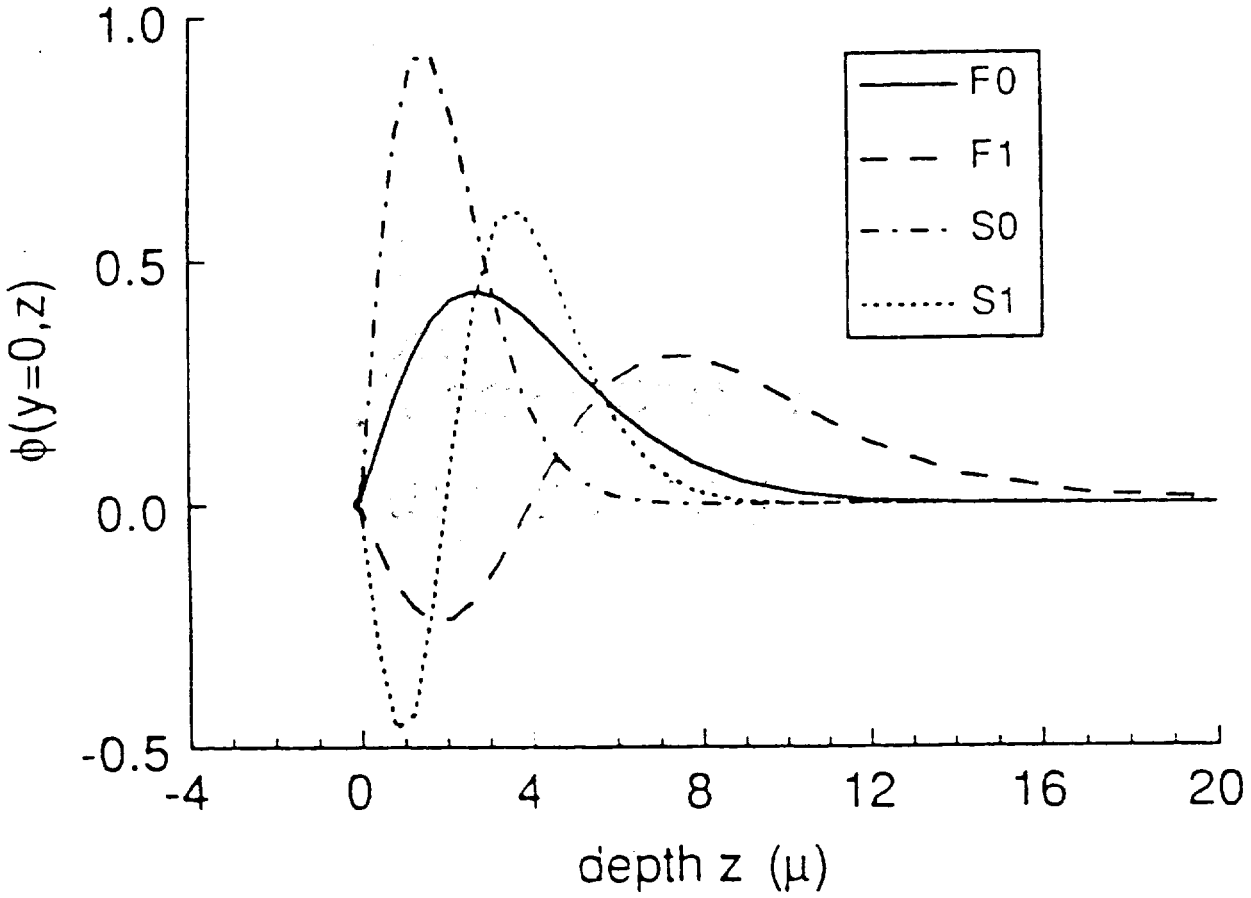

Figure 4.1 Transverse TM_0 and TM_1 spatial mode profiles for fundamental (F) and SH (S) components

(After Roelofs et. al., ref. 111)

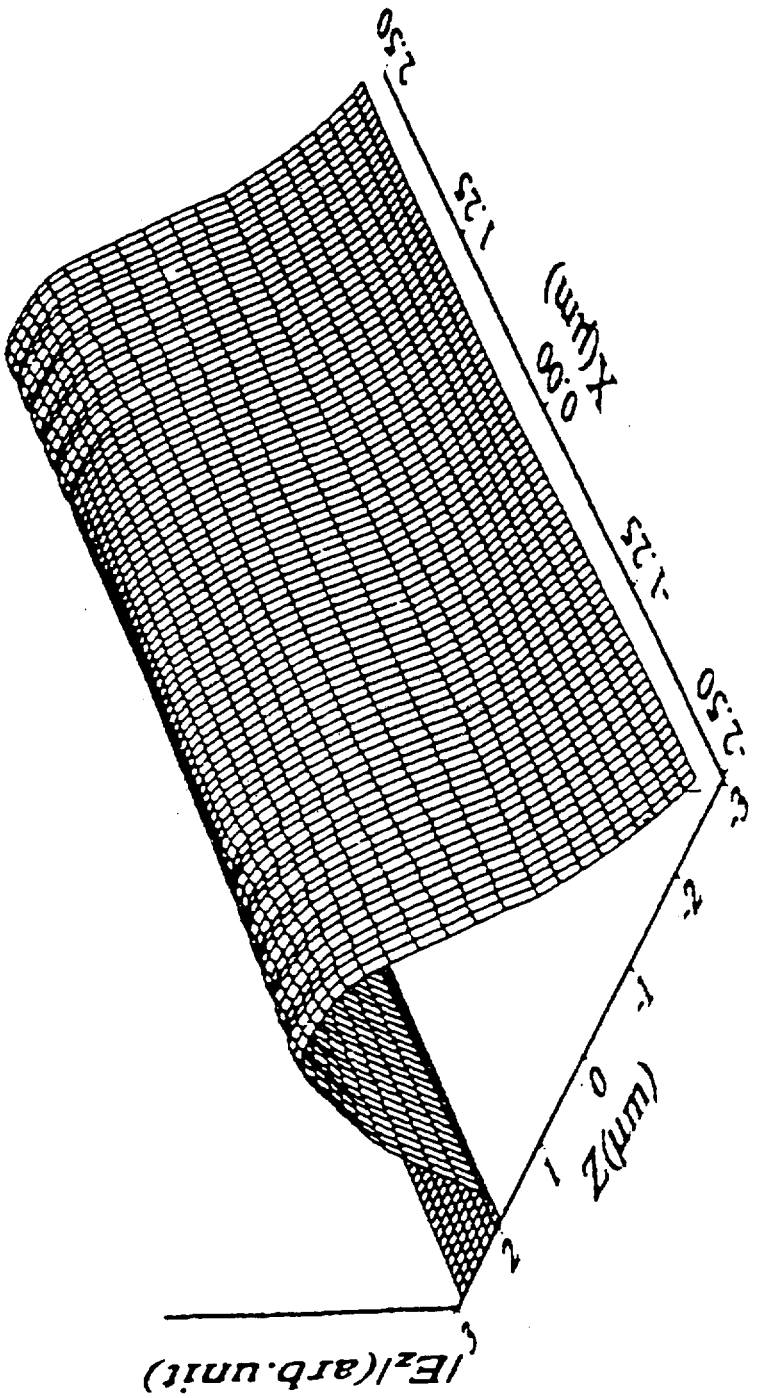

Figure 4.2 Electric field distributions for $\Delta n = 0.010$

(After Li and Burke, ref. 108)

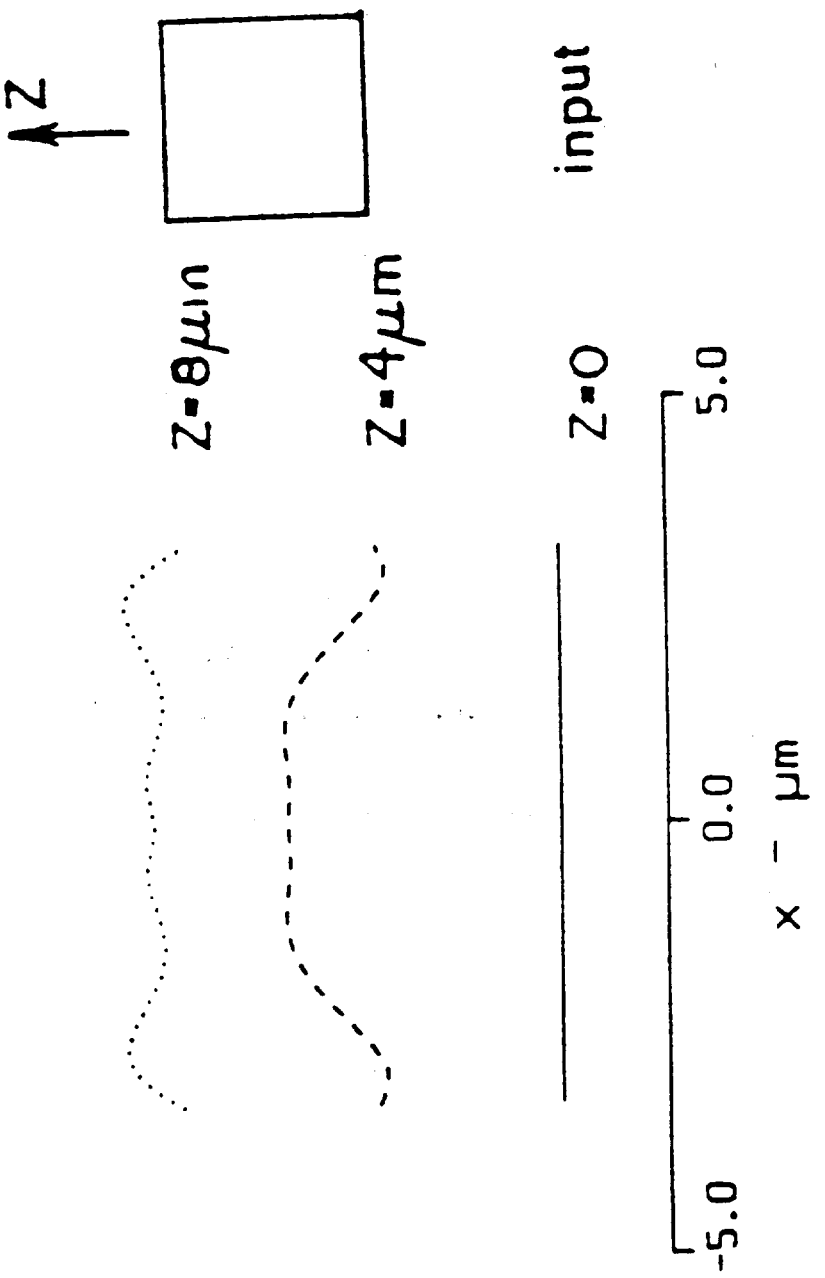

Figure 4.3 Fundamental TE planar wavefront propagated through one waveguide period (After Weissman and Hardy, ref. 110)

They deduced from the results represented by Figure 4.3 that the planar wavefront "is not fully restored" after propagating through one period. The phase ripples apparent in the propagating mode are suggested to be filtered out via radiation, leading Weissman and Hardy to conclude that the waveguide is "inherently leaky".

While the discussion of their results is well-considered, a troubling question arises when considering Figure 4.3. Consideration of the near-field diffraction of a 2-D plane wave by a slit suggests that the wavefront evolution shown in this figure is likely strongly dominated by this phenomenon; therefore, it is unclear what, if any, information this figure conveys concerning the evolution of spatial modes propagating in KTP PSWs. As a secondary remark, the laser pumping beams used to excite KTP PSWs commonly possess a TEM_{00} or TM_0 spatial mode profile rather than a uniform intensity planar wavefront. Particularly over the first few periods, these differences in the input pumping beam spatial characteristics should be expected to contribute significantly to the details of the evolution of the fundamental and SH spatial intensity profiles inside the waveguide. Certainly, when using BPM models, it remains prudent to avoid judgments regarding the propagation behavior of guided modes until these fields have been clearly propagated beyond where near-field diffraction effects can be expected to predominate.

This early work on the spatial modes of KTP PSWs all focused on a fundamental wavelength of 850 nm. Only Roelofs et al. considered the associated SH guided modes at 425 nm and that work was limited to evaluation of the transverse spatial mode profiles.[111] Thus, to evaluate the potential performance of a laser-pumped KTP waveguide laser operating in the near ultraviolet required improved models for calculating the guided spatial mode characteristics of nonlinear waveguides. An effective index method was selected by the author to determine the 2-D spatial mode profile in the plane perpendicular to propagation and to evaluate the overlap between the fundamental and SH TM_0 spatial modes in this plane. To study the effects of diffraction and study the evolution of fundamental and SH guided modes in a KTP PSW, a 2-D FFT-BPM model

was also constructed. The results of these studies and models are discussed later in this chapter.

Before presenting the results of these new models, a new expression for η_{norm} for SHG in a continuous nonlinear waveguide is derived. As will be discussed, previous derivations[69,77] have ignored the variation of the d coefficient and refractive index in the dimension orthogonal to propagation and waveguide depth. Using this new expression, values for η_{norm} were computed and found to agree well with experimental results.

4.2 Derivation of Improved Expression for the Normalized Conversion Efficiency

The relative performance of diode-pumped QPM waveguides are commonly compared by a figure of merit termed the normalized conversion efficiency and defined as

$$\eta_{norm} = \frac{P_{2\omega}}{P_{\omega}^{2} L^{2}} \tag{4.2}$$

where the normalized conversion efficiency is expressed in %/W cm^2. Values for the normalized conversion efficiency for various reports of laser-pumped KTP waveguides are given in Table 3-2 in Chapter 3.

A new expression for η_{norm} for second harmonic generation (SHG) is derived here for the case of a continuous nonlinear waveguide in the limit of $\Delta k \rightarrow 0$ and in which the d coefficient and refractive index vary as a function of the guide lateral and depth variables (x,y). The index contrast in this lateral dimension is significant to the lateral mode profiles in the waveguide and the modal overlap between the fundamental and second harmonic guided waves. This expression is evaluated for the case of a 2-D KTP channel waveguide and the results are compared to those obtained using the expression for η_{norm} derived by Fejer.[69,77] The values for η_{norm} computed using the expression derived here

are much larger than those reported by Eger[106] and compare well to experimental values reported for KTP waveguides by Risk[126], Eger[87], and Bierlein.[85]

Consider phase-matched second harmonic generation from a *continuously* guided lowest order spatial mode at the fundamental frequency. Assume a symmetric guide. Assume all refractive indices are real. For simplicity, assume the guide only supports one even spatial mode at the fundamental frequency and one at the second harmonic frequency.

The total second harmonic power as a function of the propagation distance in the waveguide direction is given by:

$$P_2(z) = \int_{-\infty}^{\infty}\int_{-\infty}^{\infty} I_2(x,y,z)\,dxdy \tag{4.3}$$

which, in turn, following Yariv[41], can be expressed in terms of the second harmonic fields:

$$P_2(z) = \frac{c\varepsilon_o}{2}\int_{-\infty}^{\infty}\int_{-\infty}^{\infty} n_2(x,y)E_2(x,y,z)E_2^*(x,y,z)\,dxdy \tag{4.4}$$

In the limit of $\Delta k \rightarrow 0$, the second harmonic field can be expressed as:

$$E_2(x,y,z) = -i\omega\sqrt{\frac{\mu_o}{\varepsilon_2}}d_{33}(x,y)z\,E_1^2(x,y,z) \tag{4.5}$$

which yields:

$$E_2(x,y,z)E_2^*(x,y,z) = \frac{4\pi^2 d_{33}^2(x,y,z)z^2}{\varepsilon_0^2\lambda_{0,1}^2 n_2^2(x,y)}E_1^2(x,y)E_1^{*2}(x,y,z) \tag{4.6}$$

After substituting for the field product directly above, P_2 becomes:

$$P_2(z) = \frac{2\pi^2 cz^2}{\varepsilon_o\lambda_{0,1}^2}\int_{-\infty}^{\infty}\int_{-\infty}^{\infty}\frac{d_{33}^2(x,y)}{n_2(x,y)}E_1^2(x,y,z)E_1^{*2}(x,y,z)dxdy \tag{4.7}$$

Since E_1 is a guided mode it may be written as the product of a real tangential function and a complex longitudinal function:

$$E_1(x,y,z) = E_{T,1}(x,y)E_{L,1}(z). \tag{4.8}$$

Upon substitution of this expression into the preceding equation, the total second harmonic power generated as a function of position can be written as:

$$P_2(z) = \frac{2\pi^2 cz^2}{\varepsilon_o \lambda_{0,1}^2} E_{L,1}^2(z) E_{L,1}^{*2}(z) \int_{-\infty}^{\infty}\int_{-\infty}^{\infty} \frac{d_{33}^2(x,y)}{n_2(x,y)} E_{T,1}^4(x,y)\, dxdy \tag{4.9}$$

Note that the power of the second harmonic depends only on the square of the *d* coefficient and, so, is not affected by the inversion of the sign of *d* at the edges of the diffused region which forms the lateral waveguide. On the other hand, the sign of the *d* coefficient directly affects the variation of the second harmonic field phase which will, in turn, affect the overlap of the total second harmonic field generated with the second harmonic guided wave, the latter being a guided mode with a uniform phase front across its total lateral extent.

The fundamental guided power is given by:

$$P_1(z) = \frac{c\varepsilon_o n_{1,eff}}{2} \int_{-\infty}^{\infty}\int_{-\infty}^{\infty} E_1(x,y,z) E_1^*(x,y,z)\, dxdy \tag{4.10}$$

$$= \frac{c\varepsilon_o}{2} E_{L,1}(z) E_{L,1}^*(z) n_{1,eff} \int_{-\infty}^{\infty}\int_{-\infty}^{\infty} E_{T,1}^2(x,y)\, dxdy \tag{4.11}$$

Substitution for P_1 and P_2 yields the following expression for the conversion efficiency:

$$\eta_{norm} = \frac{8\pi^2}{\varepsilon_0 c \lambda_{0,1}^2 n_{1,eff}^2} \frac{\int_{-\infty}^{\infty}\int_{-\infty}^{\infty} \frac{d_{33}^2(x,y)}{n_2(x,y)} E_{T,1}^4(x,y)\, dxdy}{\left[\int_{-\infty}^{\infty}\int_{-\infty}^{\infty} E_{T,1}^2(x,y)\, dxdy\right]^2} \tag{4.12}$$

where the permittivity has been included within the nonlinear *d* coefficient.

When considering not the total second harmonic power generated but rather that which is coupled into the guided second harmonic wave, a slightly more complicated situation occurs. In this case, the guided second harmonic power becomes:

$$P_2(z) = \frac{c\varepsilon_o n_{2,eff}}{2} \int_{-\infty}^{\infty}\int_{-\infty}^{\infty} E_{2g}(x,y,z) E_{2g}^*(x,y,z)\, dxdy \tag{4.13}$$

where

$$E_{2g}(x,y,z) = \frac{\int_{-\infty}^{\infty}\int_{-\infty}^{\infty} E_2^*(x',y',z)E_{02g}(x',y')dx'dy'}{\int_{-\infty}^{\infty}\int_{-\infty}^{\infty} E_{02g}^2(x',y')dx'dy'} E_{02g}(x,y) \tag{4.14}$$

and where $E_{02g}(x,y)$ represents the field distribution of the lowest order guided mode supported by the waveguide at the second harmonic wavelength.

The guided second harmonic power then becomes:

$$P_{2g}(z) = \frac{c\varepsilon_o n_{2,eff}}{2}\int_{-\infty}^{\infty}\int_{-\infty}^{\infty}\left[\frac{\int_{-\infty}^{\infty}\int_{-\infty}^{\infty} E_2^*(x',y',z)E_{02g}(x',y')dx'dy'}{\int_{-\infty}^{\infty}\int_{-\infty}^{\infty} E_{02g}^2(x',y')dx'dy'}\right] \times\left[\frac{\int_{-\infty}^{\infty}\int_{-\infty}^{\infty} E_2(x',y',z)E^*{}_{02g}(x',y')dx'dy'}{\int_{-\infty}^{\infty}\int_{-\infty}^{\infty}\left|E_{02g}(x',y')\right|^2 dx'dy'}\right] E_{02g}(x,y)E_{02g}^*(x,y)dxdy \tag{4.15}$$

which can be expanded to the following:

$$P_{2g}(z) = \frac{2\pi^2 cz^2 n_{2,eff}}{\varepsilon_o\lambda_{01}^2\left[\int_{-\infty}^{\infty}\int_{-\infty}^{\infty}\left|E_{02g}(x',y')\right|^2 dx'dy'\right]^2}\int_{-\infty}^{\infty}\int_{-\infty}^{\infty}\left[\int_{-\infty}^{\infty}\int_{-\infty}^{\infty}\frac{d_{33}(x',y')}{n_2(x',y')}E_1^{*2}(x',y',z)E_{02g}(x',y')dx'dy'\right]$$

$$\times\left[\int_{-\infty}^{\infty}\int_{-\infty}^{\infty}\frac{d_{33}(x',y')}{n_2(x',y')}E_1^2(x',y',z)E^*{}_{02g}(x',y')dx'dy'\right]E_{02g}(x,y)E_{02g}^*(x,y)dxdy \tag{4.16}$$

Noting that the product of integrals within square brackets is only a function of z, it can be factored from the integral over x and y, giving the following.

$$P_{2g}(z) = \frac{2\pi^2 cz^2 n_{2,eff}}{\varepsilon_o \lambda_{01}^2 \left[\int_{-\infty}^{\infty}\int_{-\infty}^{\infty} E_{02g}^2(x',y')dx'dy'\right]} \left[\int_{-\infty}^{\infty}\int_{-\infty}^{\infty} \frac{d_{33}(x',y')}{n_2(x',y')} E_1^{*2}(x',y',z) E_{02g}(x',y')dx'dy'\right]$$
$$\times \left[\int_{-\infty}^{\infty}\int_{-\infty}^{\infty} \frac{d_{33}(x',y')}{n_2(x',y')} E_1^{2}(x',y',z) E_{02g}(x',y')dx'dy'\right] \tag{4.17}$$

where the fact that for perfect phase matching with the fundamental mode the lateral second harmonic mode is real has been used.

Writing the fundamental guided wave as the product of a real lateral field and a complex longitudinal field yields:

$$P_{2g}(z) = \frac{2\pi^2 cz^2 n_{2,eff} E_{L,1}^{*2}(z) E_{L,1}^2(z)}{\varepsilon_o \lambda_{01}^2 \left[\int_{-\infty}^{\infty}\int_{-\infty}^{\infty} E_{02g}^2(x',y')dx'dy'\right]} \left[\int_{-\infty}^{\infty}\int_{-\infty}^{\infty} \frac{d_{33}(x',y')}{n_2(x',y')} E_{T,1}^{*2}(x',y') E_{02g}(x',y')dx'dy'\right]$$
$$\times \left[\int_{-\infty}^{\infty}\int_{-\infty}^{\infty} \frac{d_{33}(x',y')}{n_2(x',y')} E_{T,1}^{2}(x',y') E_{02g}(x',y')dx'dy'\right] \tag{4.18}$$

Since the lateral components of the guided fields are real, the following holds:

$$E_{T,1}^2(x,y) = E_{T,1}^{*2}(x,y) \tag{4.19}$$

which allows the following reduction:

$$P_{2g}(z) = \frac{2\pi^2 cz^2 n_{2,eff} E_{L,1}^{*2}(z) E_{L,1}^2(z)}{\varepsilon_o \lambda_{01}^2 \left[\int_{-\infty}^{\infty}\int_{-\infty}^{\infty} E_{02g}^2(x',y')dx'dy'\right]} \left[\int_{-\infty}^{\infty}\int_{-\infty}^{\infty} \frac{d_{33}(x',y')}{n_2(x',y')} E_{T,1}^{2}(x',y') E_{02g}(x',y')dx'dy'\right]^2 \tag{4.20}$$

The normalized conversion efficiency can then be expressed by

$$\eta_{nor} = \frac{8\pi^2 n_{2,eff}}{\varepsilon_o c \lambda_{0,1}^2 n_{1,eff}^2} \frac{\left[\int_{-\infty}^{\infty}\int_{-\infty}^{\infty} \frac{d_{33}(x',y')}{n_2(x',y')} E_{T,1}^2(x',y') E_{02g}(x',y') dx'dy'\right]^2}{\left[\int_{-\infty}^{\infty}\int_{-\infty}^{\infty} E_{T,1}^2(x,y)\, dxdy\right]^2 \left[\int_{-\infty}^{\infty}\int_{-\infty}^{\infty} E_{02g}^2(x',y') dx'dy'\right]} \tag{4.21}$$

which, in the *physically unrealistic case* of d_{33}, n_1, and n_2 being invariant with x and y, reduces to

$$\eta_{nor}^{pu} = \frac{8\pi^2 d_{33}^2}{\varepsilon_o c \lambda_{0,1}^2 n_2 n_1^2} \frac{\left[\int_{-\infty}^{\infty}\int_{-\infty}^{\infty} E_{T,1}^2(x',y') E_{02g}(x',y') dx'dy'\right]^2}{\left[\int_{-\infty}^{\infty}\int_{-\infty}^{\infty} E_{T,1}^2(x,y)\, dxdy\right]^2 \left[\int_{-\infty}^{\infty}\int_{-\infty}^{\infty} E_{02g}^2(x',y') dx'dy'\right]} \tag{4.22}$$

which is equivalent to Eq. (3) in Eger.[106] It should also be noted that the absolute value bars in their Eq. (2) around what is equivalent to the ratio of integrals to (4.22) in this work are unnecessary since all of the enclosed quantities are real since they represent *modal* functions.

4.2.1 Evaluation of η_{norm} for case of 2-D KTP channel waveguide

We have compared the normalized conversion efficiency η_{norm} as calculated from (4.21) and (4.22) for the case of phase-matched second harmonic generation in a 2-D channel waveguide. Figure 4.4 shows the values of the refractive indices chosen for the computations. The value of the substrate refractive index at the fundamental wavelength of 770 nm was chosen to correspond to the value for KTP at this wavelength according to the Sellmeier coefficients of Ghosh.[102] The value of the refractive index at the SHG wavelength was selected such that the effective indices at the fundamental and SHG wavelengths, the guided modes n_{1eff}=n_{2eff}=1.85458 for the layer refractive indices shown in Figure 4.4.

Two cases were considered. In the first case, a 1-D slab waveguide program, Waveg.345 was used to find the best fit gaussian approximation to the TM_0 fundamental and SHG guided modes. Equations (4.21) and (4.22) were then numerically evaluated using these values for ω_{01} and ω_{02}. In the second case, the exact 1-D waveguide solutions derived by Waveg.345 were used explicitly to evaluate the overlap integrals in (4.21) and (4.22). For all cases considered, d33a=-13.7 pm/V and d33b=13.7 pm/V. The results from the computations for both cases are shown in Table 4.1.

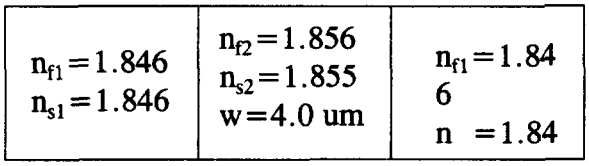

Figure 4.4 Channel Waveguide Structure

Case	*Gaussian Approximation (%/W cm^2)*	*Exact 1-D waveguide Solution (% /W cm^2)*
Eq. (4.21)	*828*	*1054*
Eq. (4.22)	*965*	*1100*

Table 4.1 Computed Values of η_{norm}

4.2.2 Discussion of Results

The results shown in Table 4.1 indicate that the lateral spatial variation of the d coefficient and the refractive index incorporated in (4.21) results in a 14% reduction in the calculated η_{norm} in comparison to the less exact formulation of (4.22). This reduction can be explained by observing that, for the weakly guiding case considered, a significant fraction of the fundamental and SH modes extend into the lateral substrate region where the substrate retains its non-inverted d coefficient value. It should be noted that actual

device designs may incorporate smaller index steps than that used for the calculations presented. The smaller lateral index contrast in such cases would result in weaker waveguiding by the structure. This demonstrates the importance of carefully considering the lateral spatial variation of the d coefficient and the refractive index in deriving (4.21). As discussed earlier, the sign of the d coefficient directly affects the variation of the second harmonic phase and thereby the overlap of the fundamental and SH guided waves. Since the analysis leading to (4.22) assumes a constant value of d in the plane transverse to propagation, it is expected that the value of η_{norm} computed using it should be greater than for the value computed using (4.21).

While the cases for which η_{norm} was calculated here do not represent SHG in quasi-phase-matched nonlinear waveguides, the results from the present work can be viewed as suggesting the order of η_{norm} for QPM KTP waveguides assuming a single-frequency, single spatial mode fundamental pump source and considering an approximate reduction of $(2/\pi)^2$ in the effective d coefficient for first-order QPM. The reduction is actually less than $(2/\pi)^2$ since in the region laterally adjoining an undiffused segment the guided modes see the same d coefficient as in the undiffused segment. This approximation would suggest a value of $\eta_{norm} \sim 430$ %/W cm^2. The present numerical computations, however, assumed a 1-D solution for the waveguide modes by considering the solutions in the guide axis with lateral index symmetry; the actual case is considerably more complicated with a solution by the effective index method indicating that the transverse (depth) profile displays significantly stronger modal confinement near the air/substrate interface.[130] The stronger modal confinement is predicted to result in higher values of η_{norm} than computed for the values shown in Table 4.1.

4.3 Effective Index Method Modeling Methods and Results

A useful technique for solving the paraxial wave equation for optical waveguides was introduced by Buus.[131] This technique, known as the *effective index method* (EIM), is applicable in problems in which the refractive index varies slowly in one dimension,

allowing the dimensionality of the problem to be reduced by one. This technique is applicable to modeling the spatial modes of KTP PSWs by considering that the transverse variation of the refractive index is slow in comparison to the lateral index variation. In practice, the EIM solution to the paraxial wave equation for a KTP PSW is used to obtain the effective index for successive steps in depth.

The KTP PSW geometry used for the EIM modeling is depicted in Figure 4.5. The depth dependence of the refractive index is given by[111]

$$n(z) = \Delta n_{surf}\, erfc(z / d) \tag{4.24}$$

where Δn_{surf} is the increase in the refractive index above the substrate value at the air/KTP interface. A FORTRAN code, KTPSELL (see Appendix A), was developed to compute the value of the refractive index of KTP using Sellmeier coefficients reported by Ghosh.[102] Figure 4.6 displays the value of the refractive index as a function of the wavelength for fundamental and SH wavelengths of interest.

The equivalent waveguide theory[85,108] was used to establish the value of Δn_{surf} to be used. For the fundamental wavelength case, λ_f=770.0 nm and n_f=1.8460. Using Δn_f=0.015 as the refractive index difference between the diffused region and the undiffused KTP at the surface and taking the segmentation duty cycle as 50% yields Δn_{surf}=0.0075 according to the equivalent waveguide theory. Following Roelofs et al., the same value of Δn_{surf} is used for both the fundamental and SH wavelengths.[111] For the SH wavelength case, λ_s=385.0 nm and n_s=1.9832.

To initiate the EIM modeling of the spatial modes for the KTP PSW structure shown in Figure 4.5, the lateral mode profile and effective index was obtained for successive layers using the MODEIG code.[132] MODEIG is a FORTRAN modeling

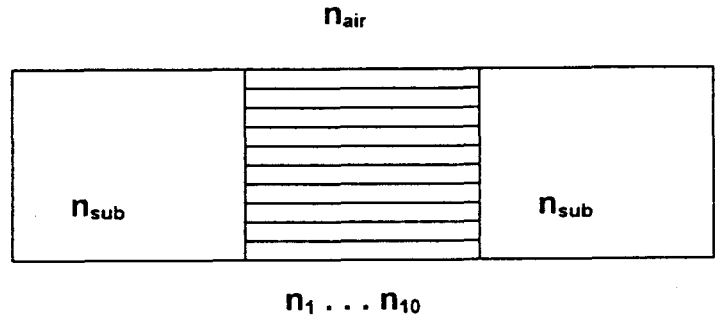

Figure 4.5 KTP PSW structure employed for EIM modeling

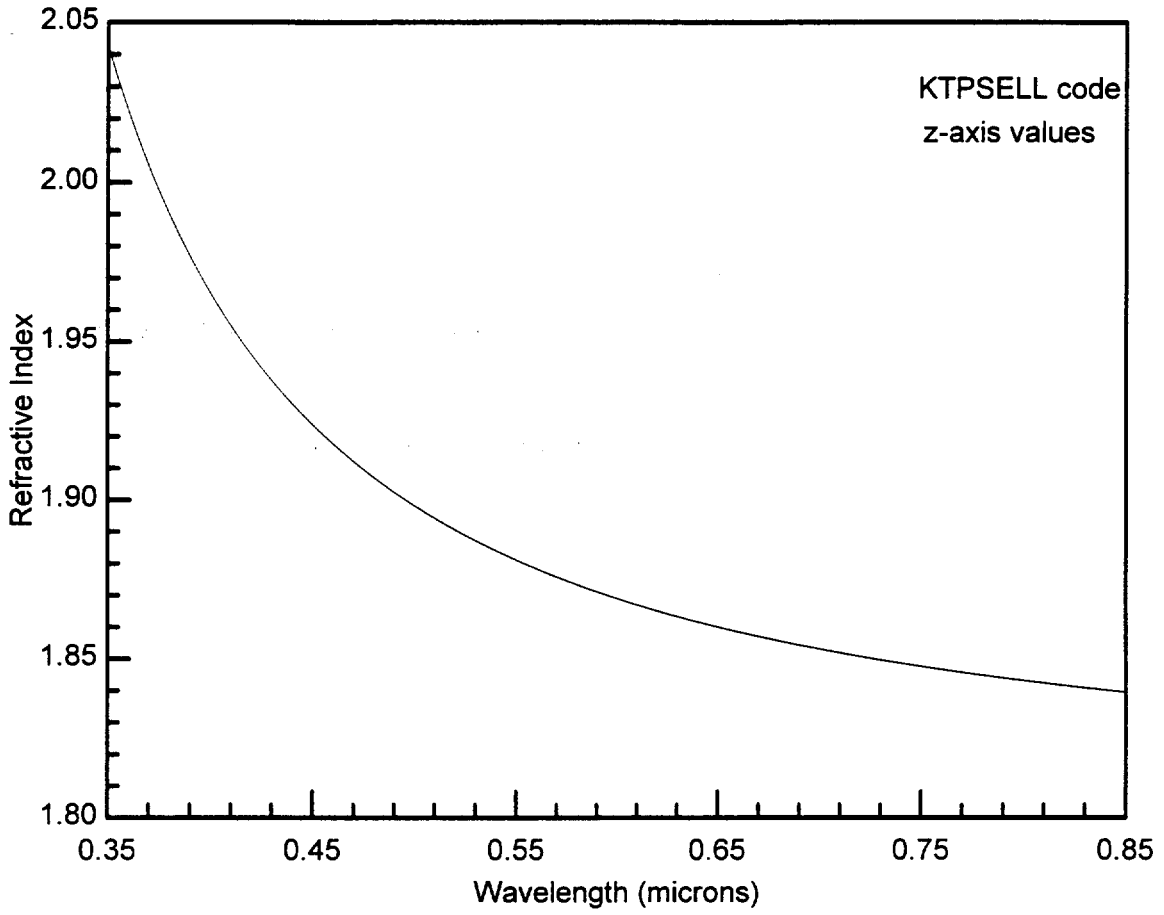

Figure 4.6 KTP refractive index vs. wavelength

program capable of determining the propagation constants, and near and far field intensity profiles for multiple-layer waveguides. Tables 4.2 and 4.3 list the lateral index profiles, depth, and value of the effective index for that profile returned by MODEIG for the fundamental and SH wavelengths, respectively.

The effective indices for each successive layer in depth were input into MODEIG to obtain the transverse spatial mode profiles at both the fundamental and SH wavelengths. Figure 4.7 shows the transverse TM_0 spatial mode profiles supported by the waveguide construction depicted in Figure 4.5. Figure 4.8 displays the fundamental lateral TM_0 spatial mode profiles. It is interesting to compare the transverse profiles to those obtained by Roelofs shown in Figure 4.1. The qualitative features are quite similar. In both cases, the SH TM_0 spatial mode has a significantly larger peak intensity, by approximately a factor of 2, than the fundamental TM_0 spatial mode amplitude; the spatial modes do not extend significantly above the air/KTP interface; and the SH modes exhibit much tighter confinement nearer to the air/KTP interface than the fundamental modes, as expected due to the increased index contrast seen at the SH wavelengths. The lateral spatial mode profiles reveal the lateral broadening of the spatial mode profile as a function of depth caused by the reduction in index contrast with depth that is characteristic of KTP PSWs.

Importantly, the spatial modes at 770 nm and 385 nm calculated by MODEIG have a significantly smaller extension into the substrate than the spatial modes at 850 nm and 425 nm calculated by Roelofs et al. For example, the SH TM_0 mode at 385 nm calculated using MODEIG approaches zero amplitude at a depth of 4.2 μm, whereas the SH TM_0 mode at 425 nm calculated by Roelofs approaches zero amplitude near a depth of 6.0 μm. Similar behavior is exhibited by the fundamental TM_0 modes. Note, however, that the relative overlap of the fundamental and SH TM_0 modes are quite comparable in the two cases; it is difficult to judge accurately which is larger purely on

the basis of Figures 4.1 and 4.7, and Roelofs et al. do not give a computed overlap value for the distributions shown in Figure 4.1.

Layer #	z (μm)	n_s	n_g	n_s	n_{eff}
0	---	1.0000	1.0000	1.0000	---
1	0.00	1.8460	1.8535	1.8460	1.8522
2	0.70	1.8460	1.8527	1.8460	1.8514
3	1.40	1.8460	1.8518	1.8460	1.8510
4	2.10	1.8460	1.8510	1.8460	1.8499
5	2.80	1.8460	1.8503	1.8460	1.8492
6	3.50	1.8460	1.8496	1.8460	1.8486
7	4.20	1.8460	1.84897	1.8460	1.8480
8	4.90	1.8460	1.8484	1.8460	1.8475
9	5.60	1.8460	1.8479	1.8460	1.8471
10	6.30	1.8460	1.8475	1.8460	1.8468
11	7.00	1.8460	1.8472	1.8460	1.8466

n_s≡substrate refractive index; n_g≡diffused region refractive index; n_{eff}≡effective index

Table 4.2 770 nm Refractive Index Construction and Effective Index Data

Layer #	z (μm)	n_s	n_g	n_s	n_{eff}
0	---	1.0000	1.0000	1.0000	---
1	0.00	1.9832	1.9907	1.9832	1.9903
2	0.70	1.9832	1.9899	1.9832	1.9894
3	1.40	1.9832	1.9890	1.9832	1.9886
4	2.10	1.9832	1.9882	1.9832	1.9878
5	2.80	1.9832	1.9875	1.9832	1.9871
6	3.50	1.9832	1.9868	1.9832	1.9864
7	4.20	1.9832	1.9862	1.9832	1.9858
8	4.90	1.9832	1.9856	1.9832	1.9853
9	5.60	1.9832	1.9851	1.9832	1.9848
10	6.30	1.9832	1.9847	1.9832	1.9844
11	7.00	1.9832	1.9844	1.9832	1.9841

n_s≡substrate refractive index; n_g≡diffused region refractive index; n_{eff}≡effective index

Table 4.3 385 nm Refractive Index Construction and Effective Index Data

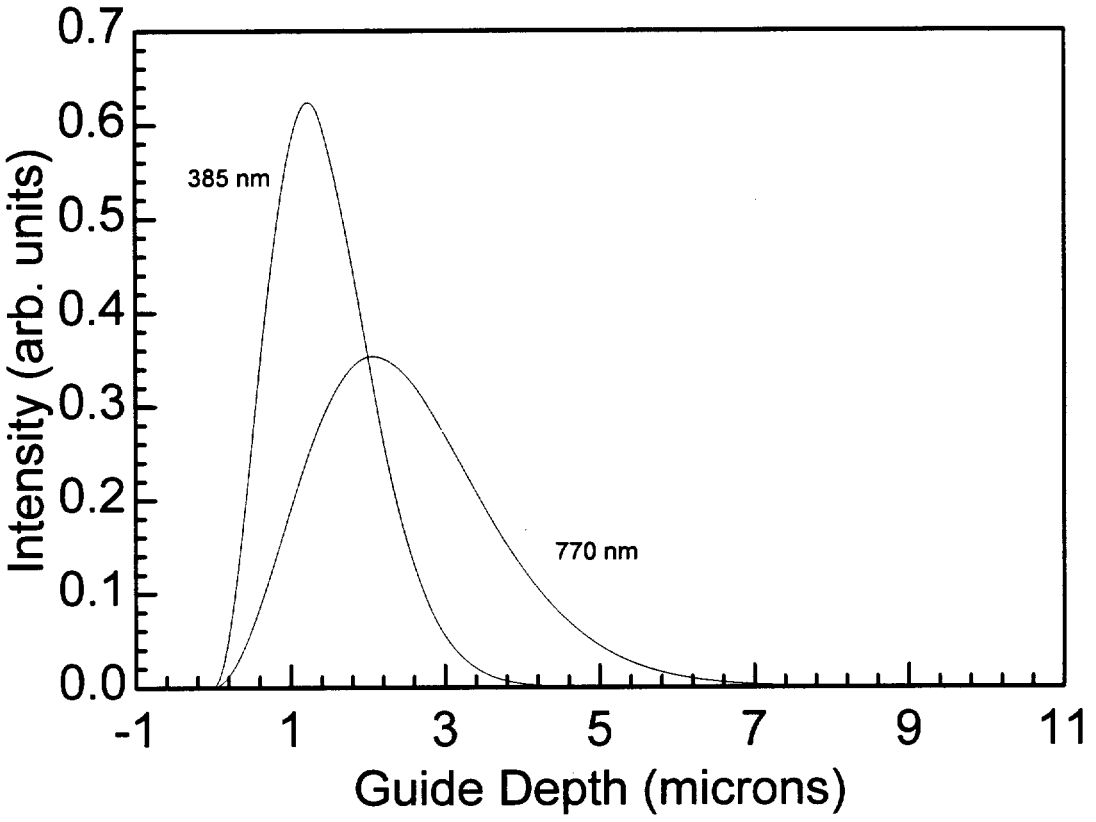

Figure 4.7 Transverse TM_0 spatial mode profiles for KTP PSW

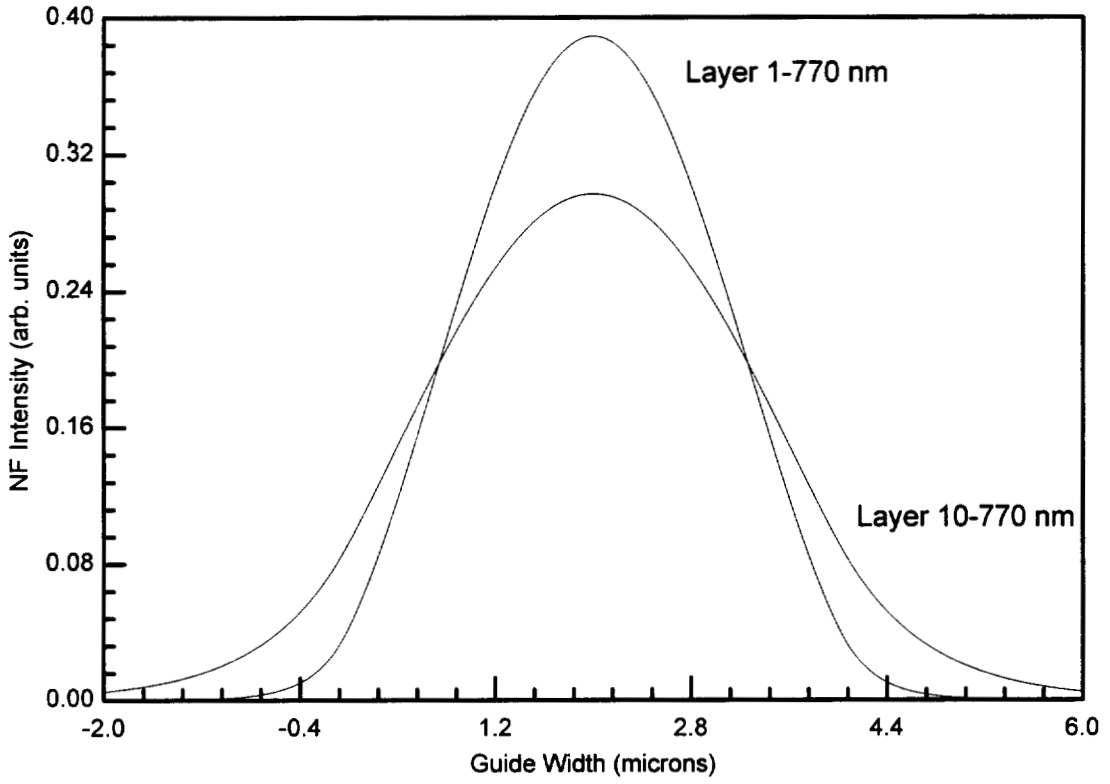

Figure 4.8 Fundamental lateral TM_0 spatial mode profiles at 770 nm for KTP PSW

The consistency of the qualitative features of these results computed using independent methods strongly indicate that the transverse profiles of the TM_0 spatial modes of KTP exhibit transverse modal asymmetry as a consequence of the refractive index asymmetry introduced in the depth dimension during the ion-exchange process.

While no attempt was made to replicate the results obtained by Roelofs et al. by using the EIM method outlined above, it is reasonable to expect tighter confinement of the 770 nm and 385 nm TM_0 transverse spatial mode profiles strictly based on the higher refractive index at these wavelengths in comparison to the refractive index values at 850 nm and 425 nm. Possible secondary considerations in explaining the increased extent observed in the transverse spatial mode profiles calculated by Roelofs et al. include his use of an exponential decay profile, rather than the complimentary error function decay profile used in this work, to describe the change with depth in the refractive index above the undiffused KTP substrate value; and his use of Δn_f=0.01368, which is slightly smaller than the value of Δn_f=0.015 used in this work, and which would have the effect of slightly reducing the index contrast seen by both the fundamental and SH modes in Roelofs et al. calculations.

To determine the full TM_0 spatial mode profiles in the plane orthogonal to propagation, the values of the transverse spatial mode intensity at each successive layer was used to normalized the lateral mode profiles for the each respective layer. Using this process, the normalized full TM_0 spatial modes profiles were obtained for the first time for KTP PSWs. Figure 4.9 displays the full TM_0 spatial mode profile at the fundamental wavelength of 770.0 nm and Figure 4.10 shows the profile for the SH wavelength of 385.0 nm. One striking feature of these profiles is the pronounced non-circular aspect of the modes at each wavelength. The FWHM diameters of the TM_0 spatial modes in the lateral and transverse dimensions are: 1.8 μm and 2.0 μm, respectively for the SH mode; and 2.0 μm and 2.4 μm, respectively for the fundamental mode. It is also apparent that both modes lie quite close to the air/KTP surface interface. The modal overlap calculated for the full normalized spatial mode intensities is 0.62.

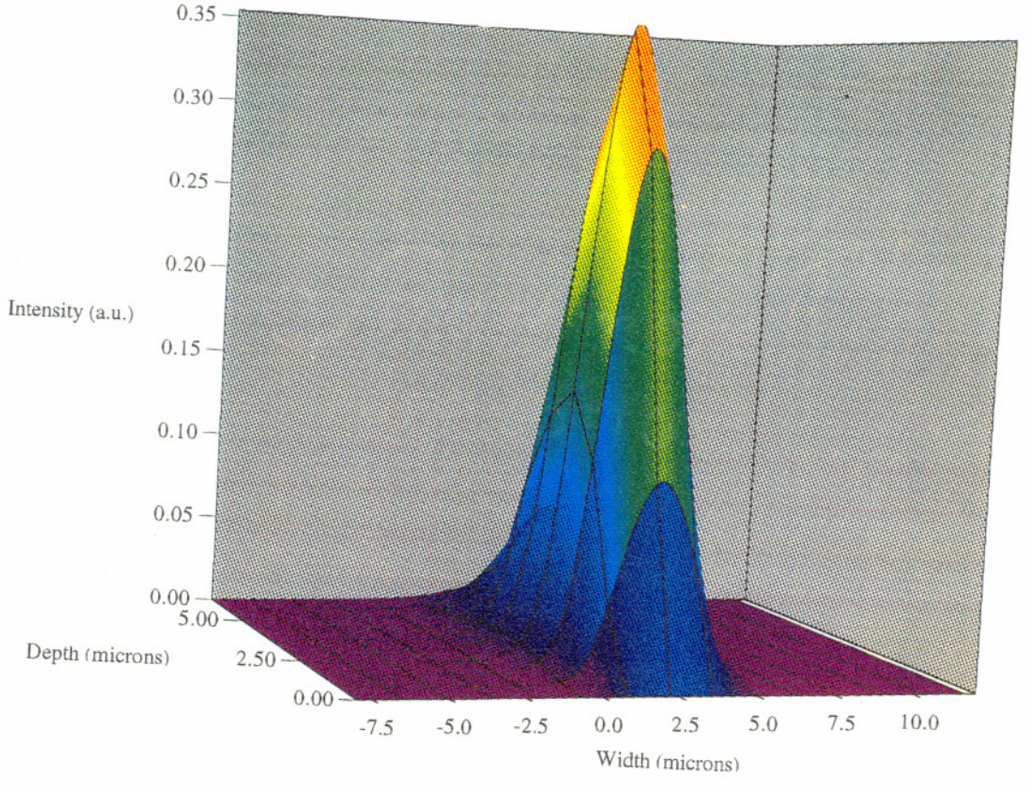

Figure 4.9 TM_0 spatial mode profile at 770 nm

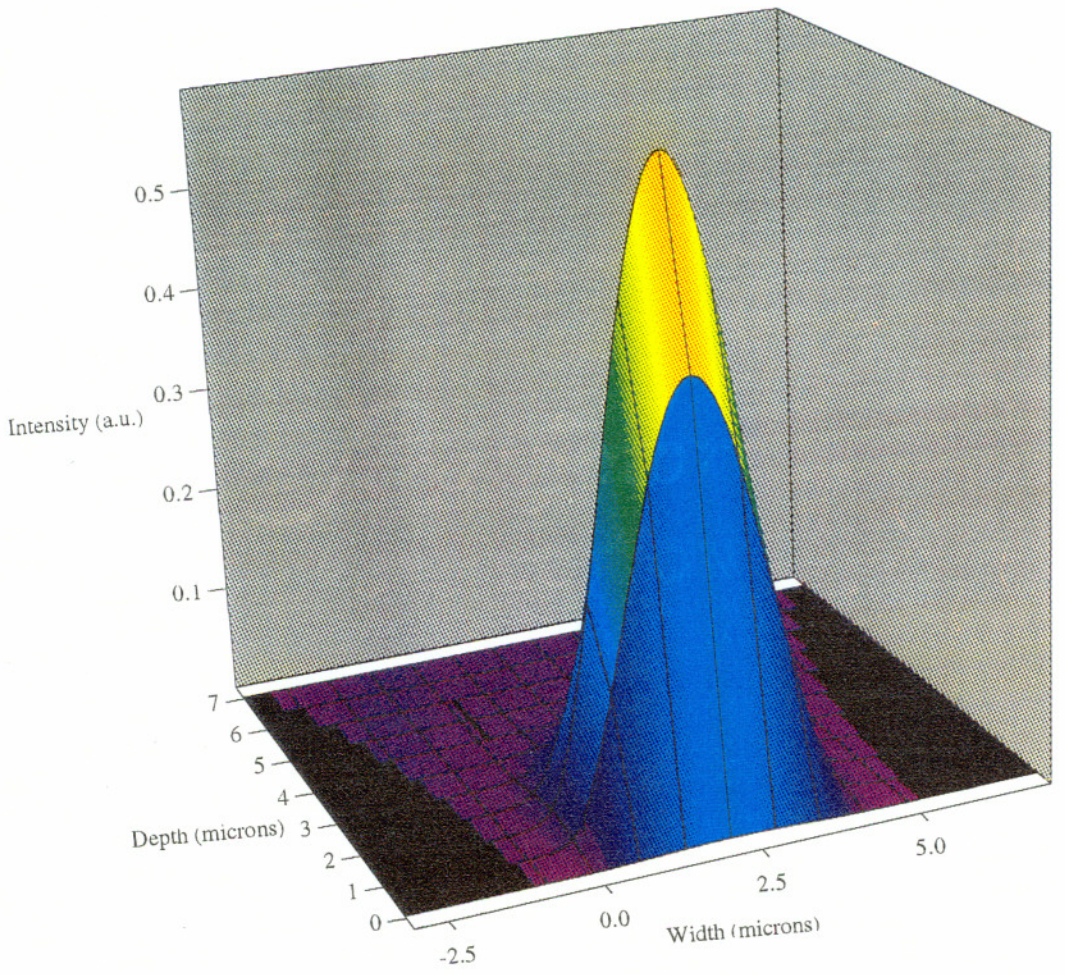

Figure 4.10 TM_0 spatial mode profile at 385 nm

Evidently, the TM_0 spatial mode at the fundamental and SH wavelengths laterally occupies the full width of the diffused region. But in the transverse plane, the spatial modes only partially overlap, which is principally responsible for the reduction from unity in the overlap value. A practical consequence of the partial overlap of the fundamental and SH modes is that when optical pumping a KTP PSW, steering the pumping beam away from the top of the waveguide is likely to result in a significant loss in SH TM_0 guided mode power, while simultaneously increasing the fundamental TM_0 guided mode power transmitted by the waveguide. If the pumping beam was not initially wavelength-tuned for QPM, it would be possible to adjust the pumping beam alignment for maximum fundamental TM_0 mode power transmission, then, after adjusting the pumping beam wavelength to obtain QPM, discover that a further adjustment to the pumping beam alignment would be necessary to obtain maximum SH TM_0 mode power transmission. This behavior, as will be described in Chapter 6, is quite common when aligning laser-pumped KTP PSW devices.

4.4 Beam Propagation Method Model and Results

To study the evolution of the spatial mode development in a KTP PSW designed to generate NUV, use of the Beam Propagation Method (BPM) affords powerful insight into the propagation of electromagnetic fields in optical waveguides. It is particularly well-suited to the analyses of modal evolution in optical waveguides excited by external fields.

BPM is an established technique for simulation of the propagation of optical fields in a wide range of optical media. BPM was first developed by Feit and Fleck to model the light propagation in graded-index optical fibers.[133] The method is based on accurate numerical solutions to the paraxial wave equation for the complex field amplitude E(x,y,z). Feit and Fleck used a Fourier transform approach to approximating the solutions to the wave equation, using the Fast Fourier Transformation (FFT) to

efficiently calculate the discrete summations. They applied their method to a Corning 1151 fiber with a 125 μm outer diameter and 62.5 μm core diameter. The input field was coherent, uniform illumination with a wavelength of 1 μm. The upper right quadrant of the fiber was represented by a 64 x 64 computational grid with $\Delta x=\Delta y=0.98$ μm. This created a maximum possible spatial bandwidth of $\Delta k_{max} = 2\pi/\Delta x = 6.41 \times 10^4$ cm^{-1}. The longitudinal step size used was 10 μm. To prevent reflections from the outer fiber boundary, a strong absorber was placed on the outer circumference of the fiber. With this computational model, Feit and Fleck were able to obtain the on-axis intensity as a function of propagation distance along the fiber. Feit and Fleck later extended the FFT-BPM to allow calculation of pulse dispersion in graded-index multimode fibers[134] and to compute the mode-related properties such as propagation constants and group delays in optical waveguides for use in analysis of optical fiber dispersion.[135]

Since this pioneering work, several workers have discussed modifications and improvements to beam propagation method analysis for specific problems. Yevick introduced use of a finite-difference (FD) BPM to solve the scalar paraxial wave equation and demonstrated its applications to the analysis of rib waveguides.[136,137] Vectorial BPM (VBPM) schemes have recently been developed for treatment of difficult optical waveguide problems, where the polarization dependence and mode coupling due to geometric effects cannot be ignored, such as in cases where material anisotropy contributes to coupling between orthogonal polarization modes.[138-142] These VBPM methods all use either the discrete FFT or an FD scheme in order to implement the propagation of the initial field within the device under study. A full VBPM for modeling 3-D optical waveguides has recently been reported by Huang and Xu in which the coupled equations for the transverse field were solved by an implicit FD scheme for E or H formulations.[140] Liu and Li have developed a full VBPM using an iterative Lanczos reduction and applied it to vector mode analysis of rib waveguides.[141] Xu and Huang recently reported extension of their full VBPM technique to propagation in anisotropic media.[142]

In 1995, results of benchmark tests for different numerical BPM algorithms were reported by Nolting and Marz.[143] For the BPM benchmark test of propagating the fundamental mode along a non-tilted waveguide, all BPM algorithms tested, including FFT-BPM and FD-BPM algorithms using various means for controlling edge reflections, were judged effective. Discrepancies began to become significant when very high order modes (e.g. 10th order) were propagated with substantial waveguide tilt angle.

The BPM benchmark test results indicate that either a scalar FFT-BPM or FD-BPM will provide satisfactory results for analysis of the weak waveguiding characteristics of KTP PSWs, which, as discussed earlier, support few spatial modes. With respect to computational effort, the FFT-BPM, somewhat surprisingly, was judged by Nolting and Marz during benchmarking of algorithm efficiencies and mean CPU time to compare equally with the fastest FD-BPM algorithms tested.

Tilton et al. outlined a solution technique for BPM modeling of the optical fields within a diode laser using the Fourier transform approach to approximating solutions to the paraxial wave equation and described the criterion for selection of the lateral and longitudinal computational step sizes.[117] The clarity of the description and excellent results describing the spatial modes of URSLs obtained by Tilton et al. using this technique suggested extending this approach to the development of a FFT-BPM model for the spatial modes of nonlinear optical waveguides. The derivation below follows that by Tilton et al..

Consider the 2-D paraxial wave equation

$$\left(\frac{1}{2ik}\frac{\partial^2}{\partial x^2}+\frac{\partial}{\partial z}\right)\vec{E} = ikn(x,z)\vec{E} \tag{4.25}$$

where the electric field is assumed to behave as a traveling wave propagating in the longitudinal z-direction as $\vec{E}(x,z)\exp(ikz-iwt)$. We begin by assuming that $\vec{E}(x,z)$ is periodic and imbedded in a periodic domain such that

$$\vec{E}(x,z) = \vec{E}(x+a_x,z) \tag{4.26}$$

where a_x is a periodic window that is selected to be greater than or equal to the problem domain. Now, using a Fourier expansion to represent $\vec{E}(x,z)$ as

$$\vec{E}(x,z) = \sum_{n=0}^{N_x - 1} \vec{\phi}_n(z) e^{i\left(\frac{2\pi x}{a_x}\right)n} \tag{4.27}$$

the problem can be discretized in x by defining

$$x_m = m(a_x/N_x) \tag{4.28}$$

This yields the discrete function

$$\vec{E}(x_m,z) = \sum_{n=0}^{N_x-1} \vec{\phi}_n(z) \exp\left(\frac{i2\pi nm}{N_x}\right) \tag{4.29}$$

The above summation can be efficiently performed using a Fast Fourier Transform algorithm. Now by iteratively applying the Fourier transform to the initial field distribution $\vec{E}(x,z)$, obtaining the Fourier expansion coefficients $\vec{\phi}_n(z)$, and then propagating a distance Δz by applying the free-space propagation law, the final field at z + Δz, $\vec{E}(x,z+\Delta z)$, can be obtained as

$$\vec{E}(x,z+\Delta z) = \sum_{n=0}^{N_x-1} \vec{\phi}_n(z+\Delta z) \exp\left(\frac{i2\pi nm}{N_x}\right) \exp\left(\Delta z g(x,z)\right) \tag{4.30}$$

where

$$\vec{\phi}_n(z+\Delta z) = \vec{\phi}_n(z) \exp\left(\frac{-i\pi\lambda n^2 \Delta z}{a_x^2}\right) \tag{4.31}$$

Using this solution technique, Tilton et al. reported that energy was conserved to one part in 10^6 for various test cases. That report represents additional support for the conclusion from the benchmark tests by Nolting and Marz that FFT-BPM is a suitable method for simulating beam propagation in optical waveguides. Tilton et. al. explained that the stability condition that governs the point resolution required for the propagation steps demands that the grid Fresnel number F_n obeys

$$F_n \equiv \Delta x^2/\lambda\Delta z < 1 \tag{4.32}$$

This condition is generally less stringent than the stability condition governing stable implementation of FD-BPM algorithms, according to Tilton et al.

A 2-D FFT-BPM program, named BPMG7, based on the solution formalism given by Tilton et al. was coded, debugged, tested, and used to evaluate the evolution of the spatial modes supported by a simulated 2-D KTP PSW at 770 nm and 385 nm. The program code is listed in Appendix A along with a sample input data file.

BPMG7 was written in Microsoft FORTRAN 5.1 for operation on a PC. The program was later adapted for operation using Sun FORTRAN and run successfully on a Sun Sparcstation. The program is constructed in modular fashion. A main program opens an input data file containing the wavelength, lateral computational window size, PSW geometry, real and imaginary refractive index profile, grating period and number, lateral and longitudinal propagation step sizes, edge absorber width, input Gaussian field radius and amplitude, and output file control parameters. The main program then sets the simulated problem geometry, creates the requested output files, sets the initial field conditions and then controls the looped propagation calls to subroutine PROP and subroutine FFTC. Intensity and field are written to separate output files. The intensity may be written at each longitudinal propagation step or once per period dependent on parameter flags set in the input data file. Similarly, a parameter in the input data file allows the user to select the minimum and maximum lateral step size within which data is written to the output files. This active selection of the output file domain size was required to allow for substantial propagation distances over which the intensity data may be written to the output file once per propagation step, allowing for fidelity in observing the modal evolution. For example, use of a 0.1 μm lateral step size by 0.05 μm longitudinal step size and writing to the intensity output file each step results in an output file size over 3 MB after 100 μm propagation when writing just 6.1μm in width. This tailoring of the output domain size allowed BPMG7 to be run on a 486/50 MHz PC with 8 MB RAM and yield very large output files (up to 6 MB) suitable for import into the Spyglass Transform surface plotting software utility.

The subroutine PROP propagates the field through one period of the waveguide. For each longitudinal step, it sets the complex refractive index for each lateral step, including the absorbing boundary layer and the domain edge. The value of the imaginary index of the absorbing boundary was carefully analyzed to eliminate reflections from the domain boundary, while minimizing power loss in the propagating mode. The value of the imaginary index for the absorber region selected from this analysis was 0.005 for an absorber width of 40 μm when the total domain size was selected to be 204.8 μm. PROP calls subroutine FFTC to Fourier transform the field prior to propagation through the longitudinal step and then calls FFTC a second time to inverse Fourier transform the field after propagation through the longitudinal step. The propagated field then is attenuated by the edge absorber prior to the next propagation step. PROP is exited after each propagation step to allow for the main program to write to the output files and check for the end of the propagation domain loop.

The subroutine FFTC was adapted from a standard FFT algorithm.[144] It uses a Cooley-Tukey FFT algorithm for computation. To employ this robust algorithm, the lateral domain must be of size 2^n. As noted above, the typical total lateral domain size was selected to be 204.8 μm with a lateral step size of 0.1 μm, yielding a total number of 2048 discrete lateral steps (i.e. 2^{11}). To obtain stable results, care is given to assure that problem features, such as waveguide segment boundaries, do not cross lateral or longitudinal steps.

The running time of BPMG7 on a 486/50 MHz PC for propagation through one 2.81 μm period clocked out at about 1.2 minutes when using a 0.1 μm lateral step size by 0.05 μm longitudinal step size computational grid with 2048 discrete lateral steps.

To study the evolution of a Gaussian input beam in a simulated 2-D KTP PSW, the parameters given in Table 4.4 were used. The modal evolution in a continuous guide was studied by setting the diffused segment length equal to the period length and setting the index of refraction in the undiffused segment equal to that of the diffused segments for this special case.

λ_f (μm)	λ_s (μm)	n_{fu}	n_{su}	Guide width (μm)	Period (μm)	Absorber width (μm)	k_{abs}
0.770	0.385	1.846	1. 983	4.0	2.81	50	.005

Table 4.4 Principal data parameters for BPMG7 analysis

BPMG7 was used to analyze evolution of the fundamental spatial mode at 0.770 μm and 0.385 μm using the values for the refractive indices and guide geometry given in Table 4.4. Both continuous and segmented guides were examined. In each case, the input optical field was a best fit gaussian determined through consideration of the equivalent three-layer slab waveguide problem using Waveg.345 code. Figures 4.11 and 4.12 show 2-D surface intensity plots where the refractive index was varied longitudinally to simulate a PSW with a 2.81 μm period with equal length of the diffused and undiffused segments (50% duty cycle). This simulated PSW was excited by the best fit gaussian input fields at 0.770 μm and 0.385 μm, respectively, with $\Delta n_f=\Delta n_s=0.01$ in both cases (e.g. $n_{fd}=1.856$ and $n_{sd}=1.993$). The input gaussian intensity profile was modeled to have zero phase front curvature. Figures 4.13 and 4.14 show 1-D plots of the intensity versus propagation dimension along the waveguide longitudinal axis. In these plots, the periodic segmentation of the waveguide is clearly observed to modulate longer period modulation of the modal intensity induced by mode beating occurring between the symmetric spatial modes. Note that the TM_1 mode was not excited since the input field was symmetric. It is interesting to observe that the long period mode beating results in significantly larger amplitude fluctuations in the on-axis intensity for the 0.385 μm case in comparison to the 0.770 μm case. The stronger modal confinement at the shorter wavelength is responsible for this effect. Figures 4.13 and 4.14 indicate that strong modulation at both the waveguide period and beat period are prevalent during propagation through the first twenty periods. This demonstrates that results drawn from

analyses over short propagation lengths, such as reported by Weissman and Hardy,[110] are unreliable due to the powerful near-field diffraction effects predominating in this region. While not obvious in these figures due to the narrow plotted width, minor radiation lobes are present in the intensity profiles. These radiation lobes represent field strength being diffracted by the simulated slit waveguide aperture into the corresponding Fraunhofer diffraction orders.

Figures 4.15 and Figure 4.16 show 2-D surface intensity plots of the fundamental spatial mode evolution for the special cases of continuous channel guides, under excitation by the best fit gaussian input field at 0.770 μm and 0.385 μm, respectively, with $\Delta n_f = \Delta n_s = 0.01$ in both cases (e.g. $n_{fd}=1.856$ and $n_{sd}=1.993$). Note how the mode is well confined within the guide width and the region of prominent intensity decrease near 15 microns, indicating power coupling into the TM_2 mode is significant in this region.

The index contrast was increased to $\Delta n_f = \Delta n_s = 0.015$ in the computations of the intensity profiles shown in Figures 4.17 - 4.20. Most striking is the observance of powerful mode beating effects in the 2-D surface intensity plot shown in Figure 4-18. The increased index contrast results in significant intensity modulation along the full 0.1 mm length shown in this plot. Particularly interesting is the localized on-axis increases in the intensity to values over 30% higher than the on-axis value of input best fit gaussian mode.

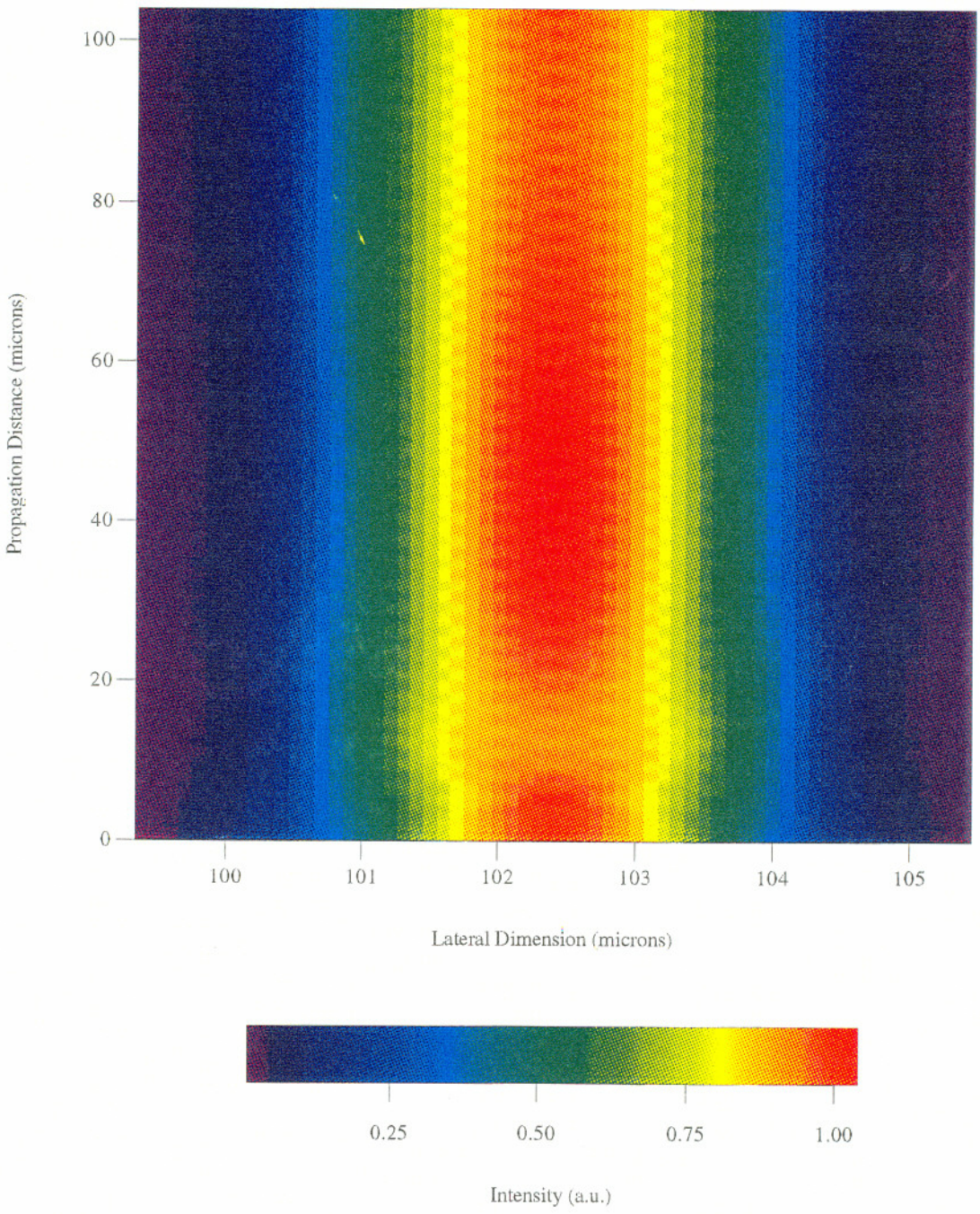

Figure 4.11 2-D surface plot of fundamental intensity for PSW waveguide for $\Delta n=0.010$

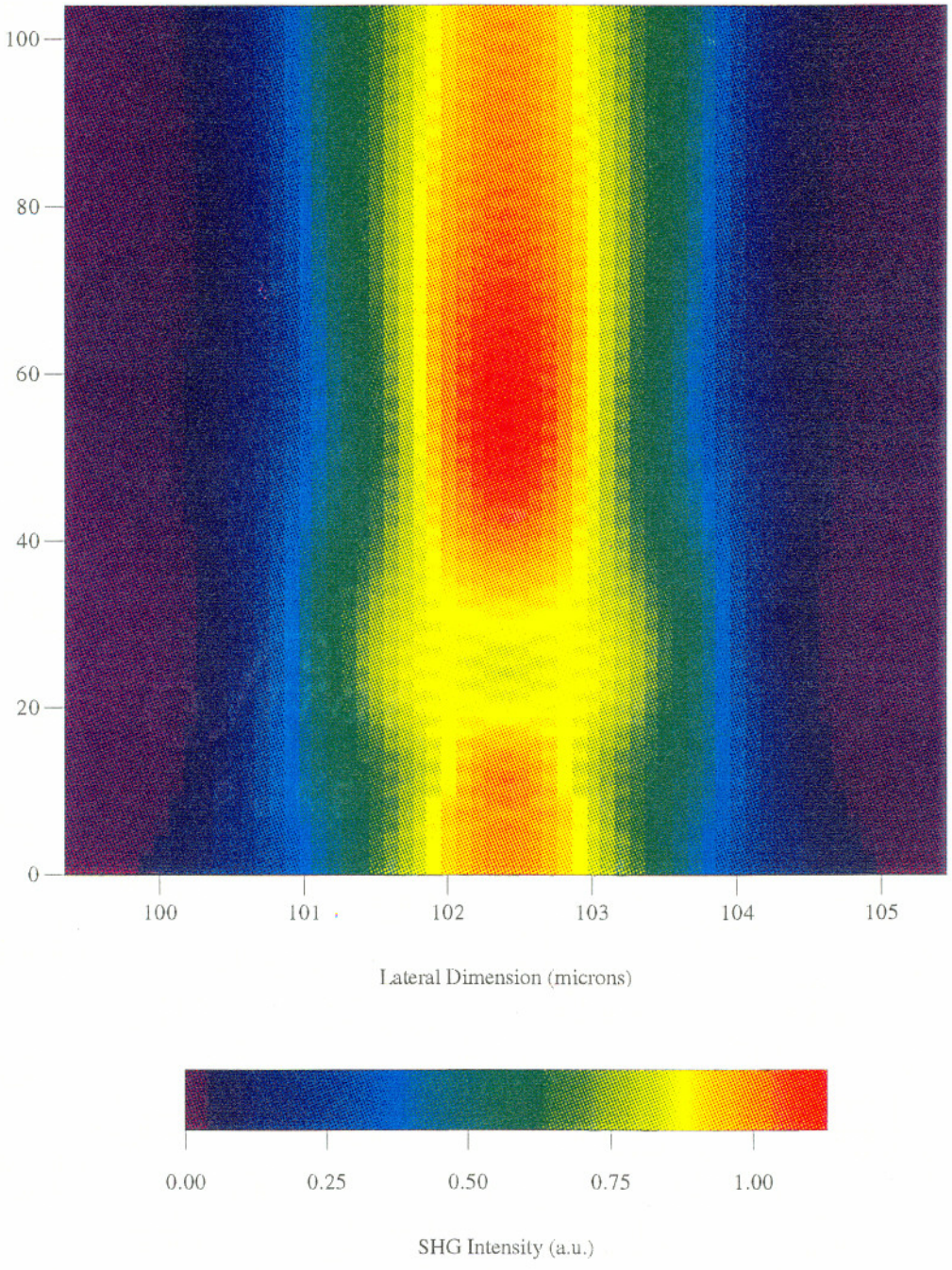

Figure 4.12 2-D surface plot of SH intensity for PSW waveguide for Δn=0.010

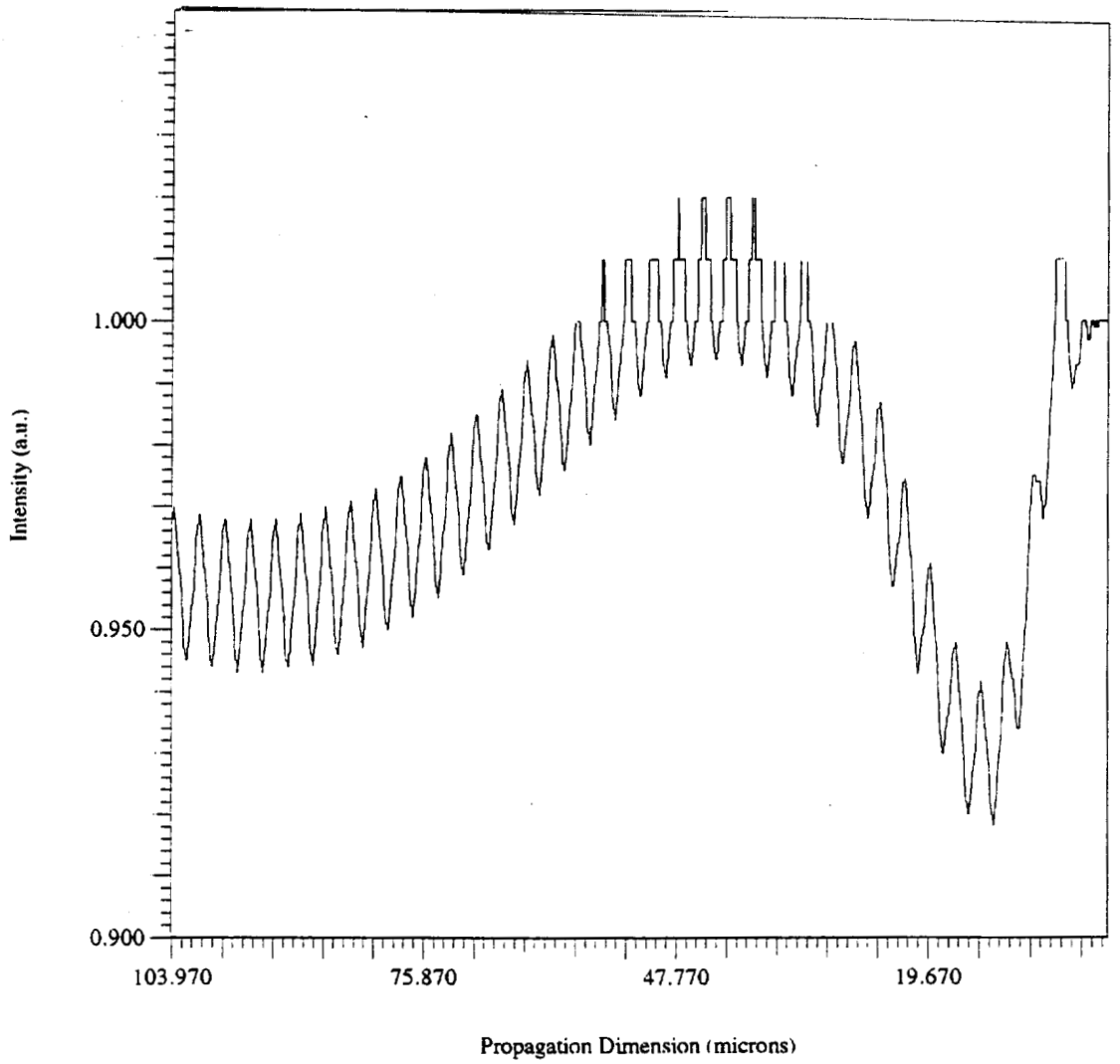

Figure 4.13 On-axis fundamental intensity vs. propagation distance for $\Delta n=0.010$

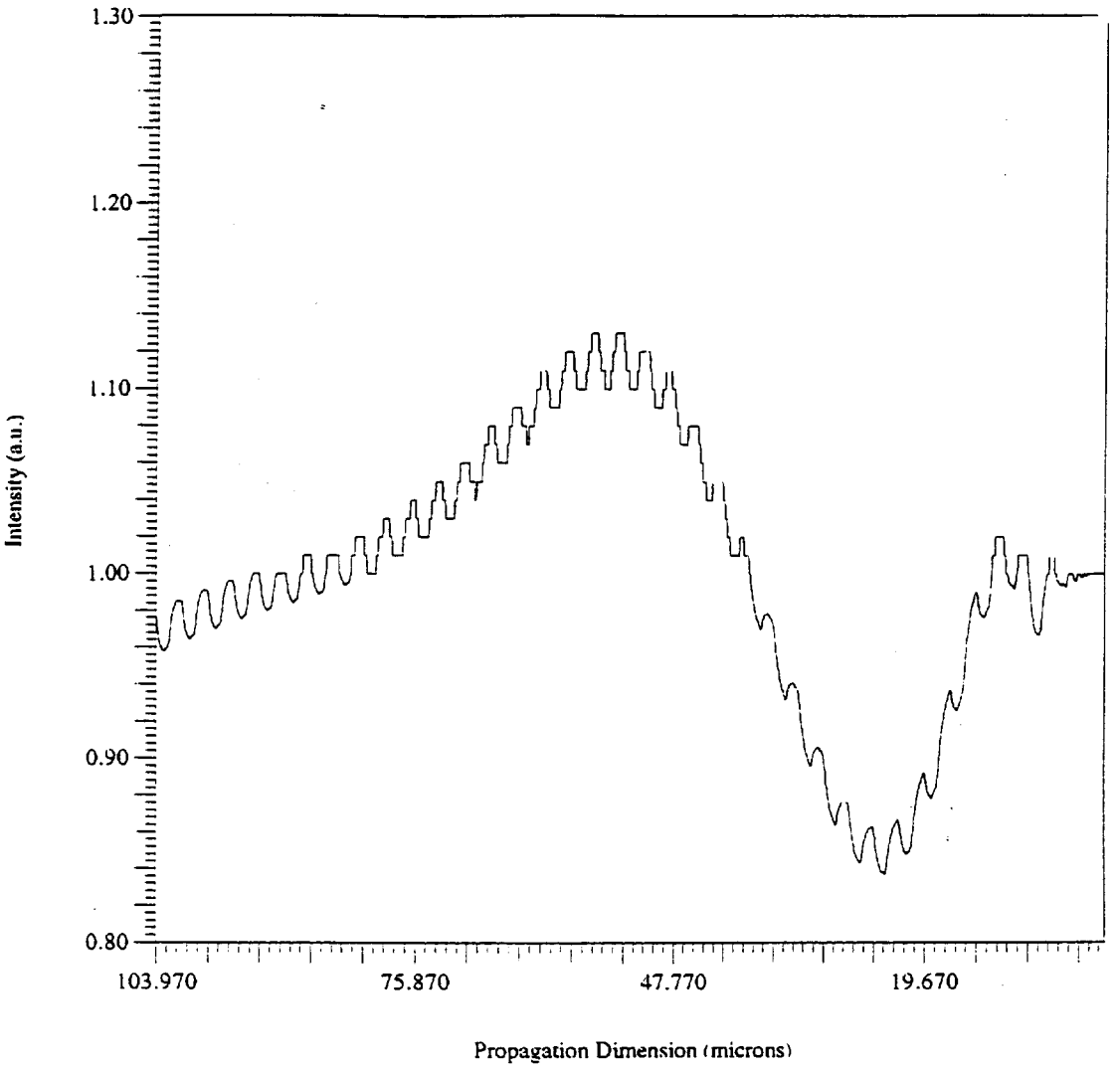

Figure 4.14 On-axis SH intensity vs. propagation distance for Δn=0.010

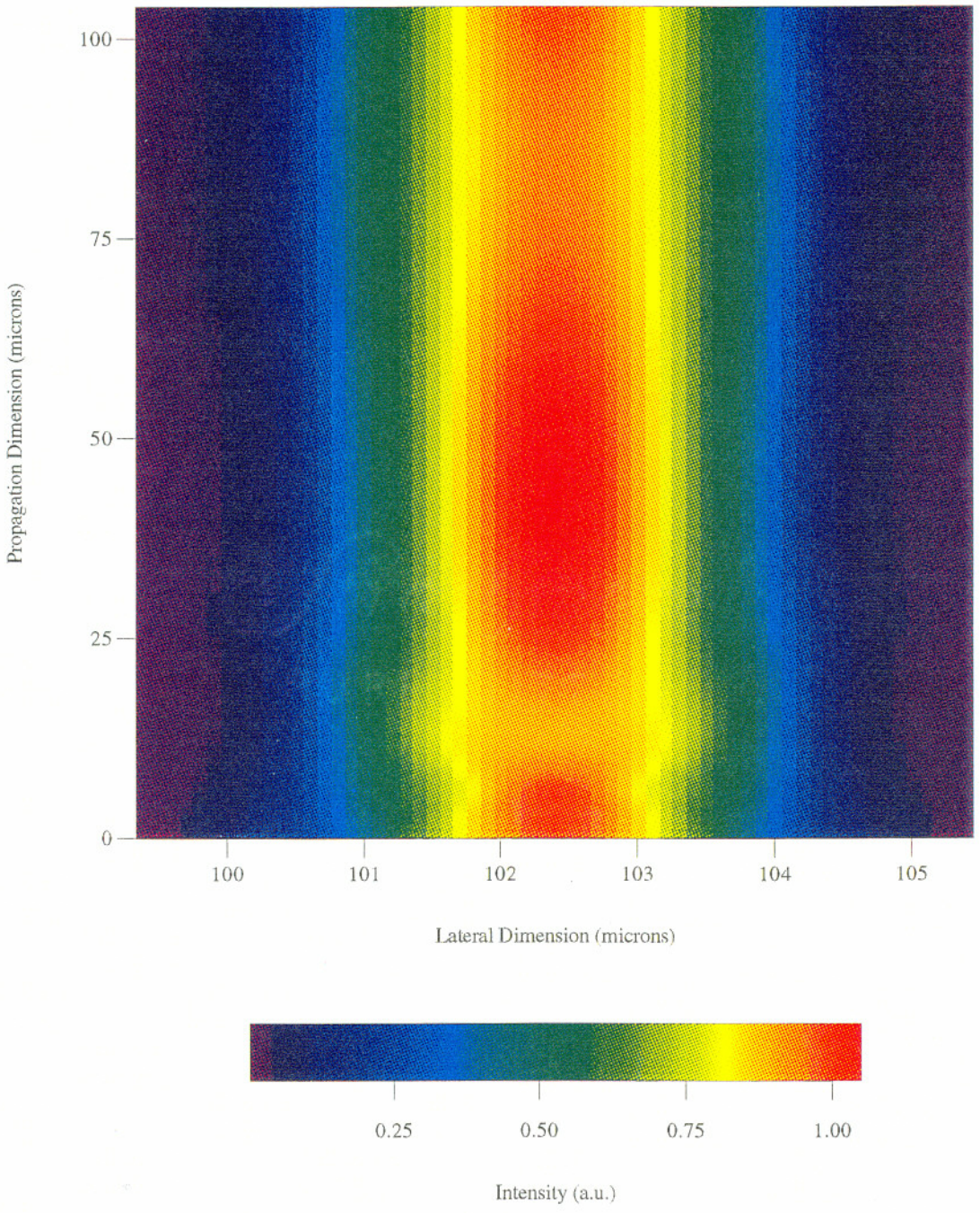

Figure 4.15 2-D Surface plot of fundamental intensity for channel waveguide

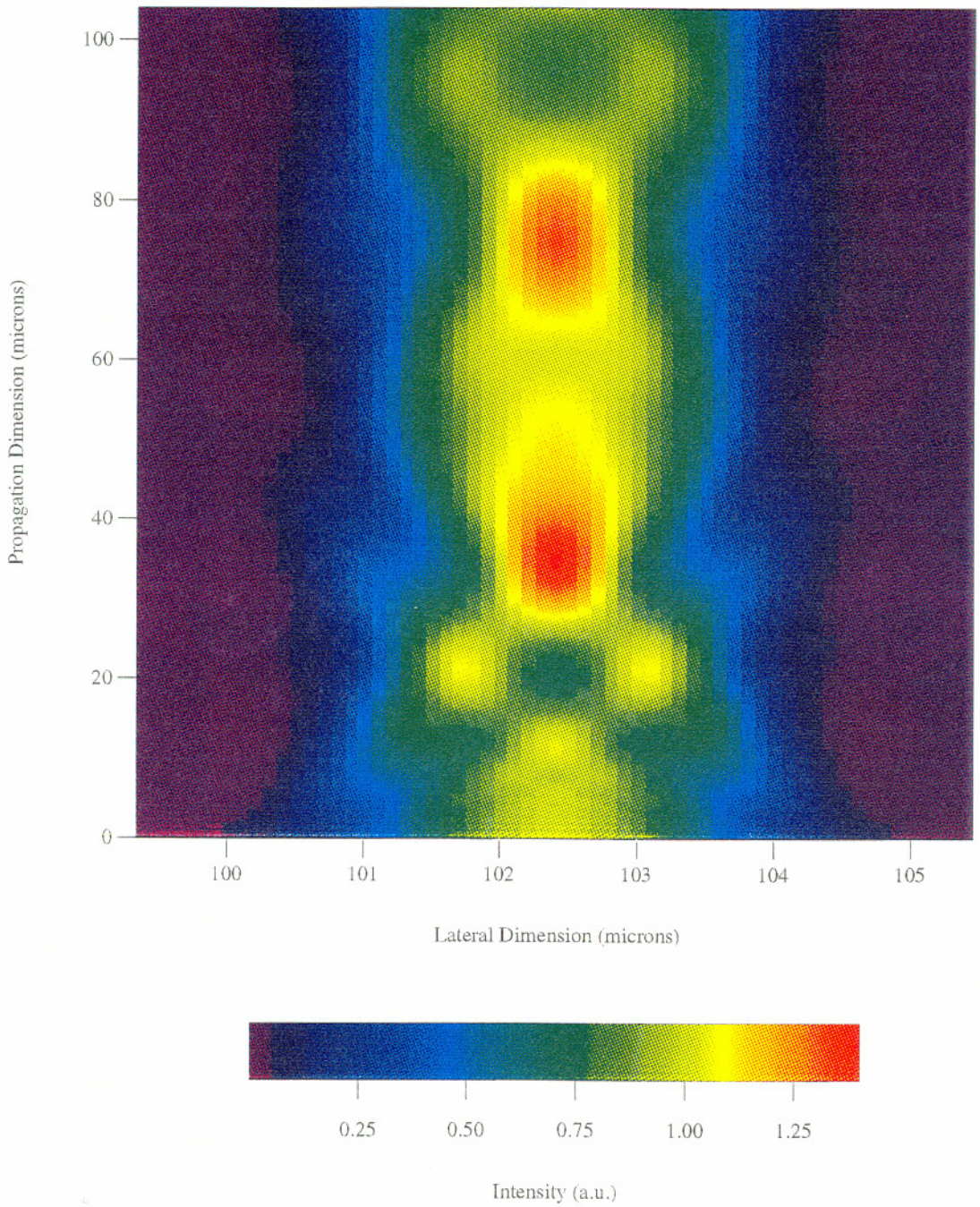

Figure 4.16 2-D Surface plot of SH intensity for channel waveguide

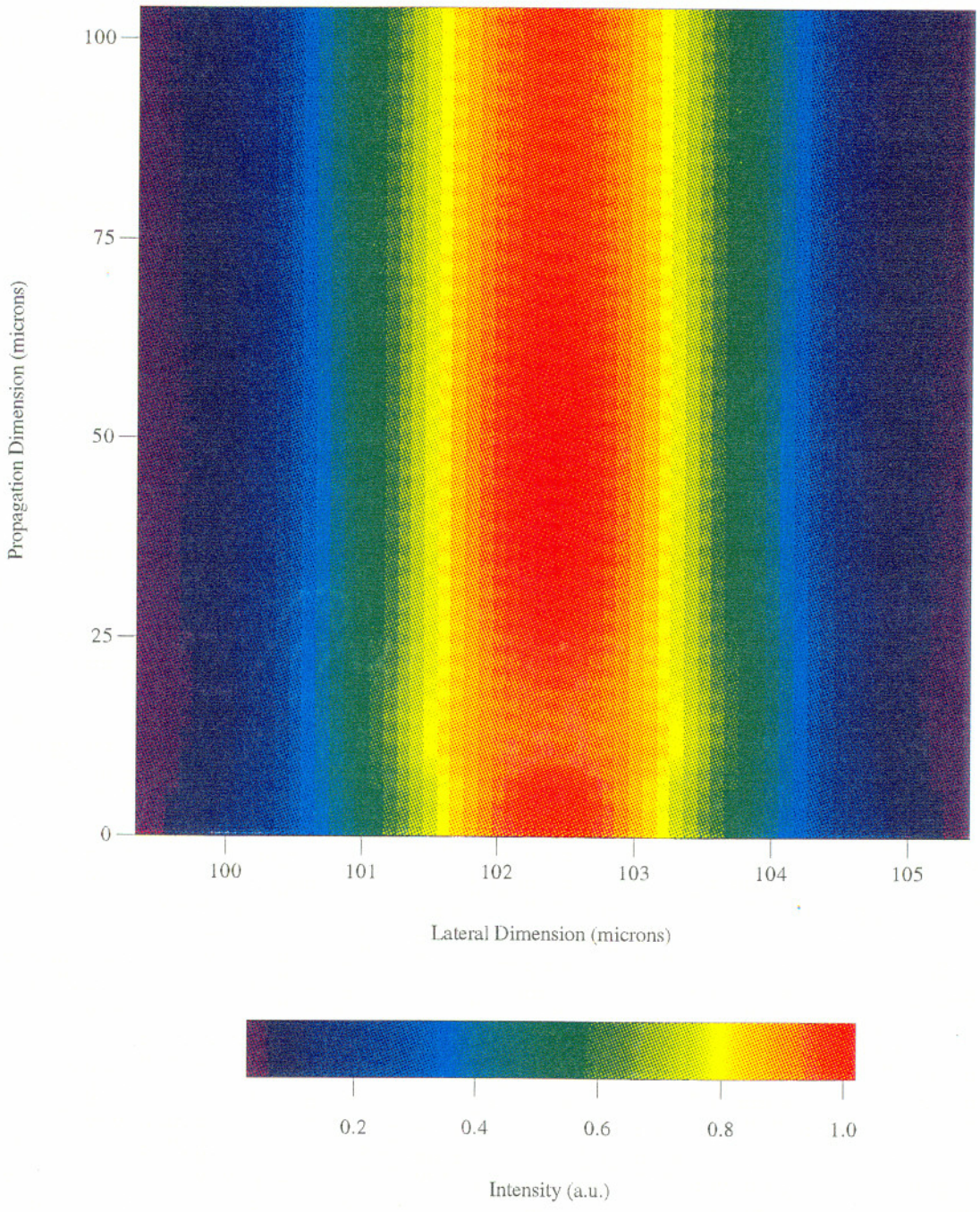

Figure 4.17 2-D surface plot of fundamental intensity for PSW waveguide for $\Delta n=0.015$

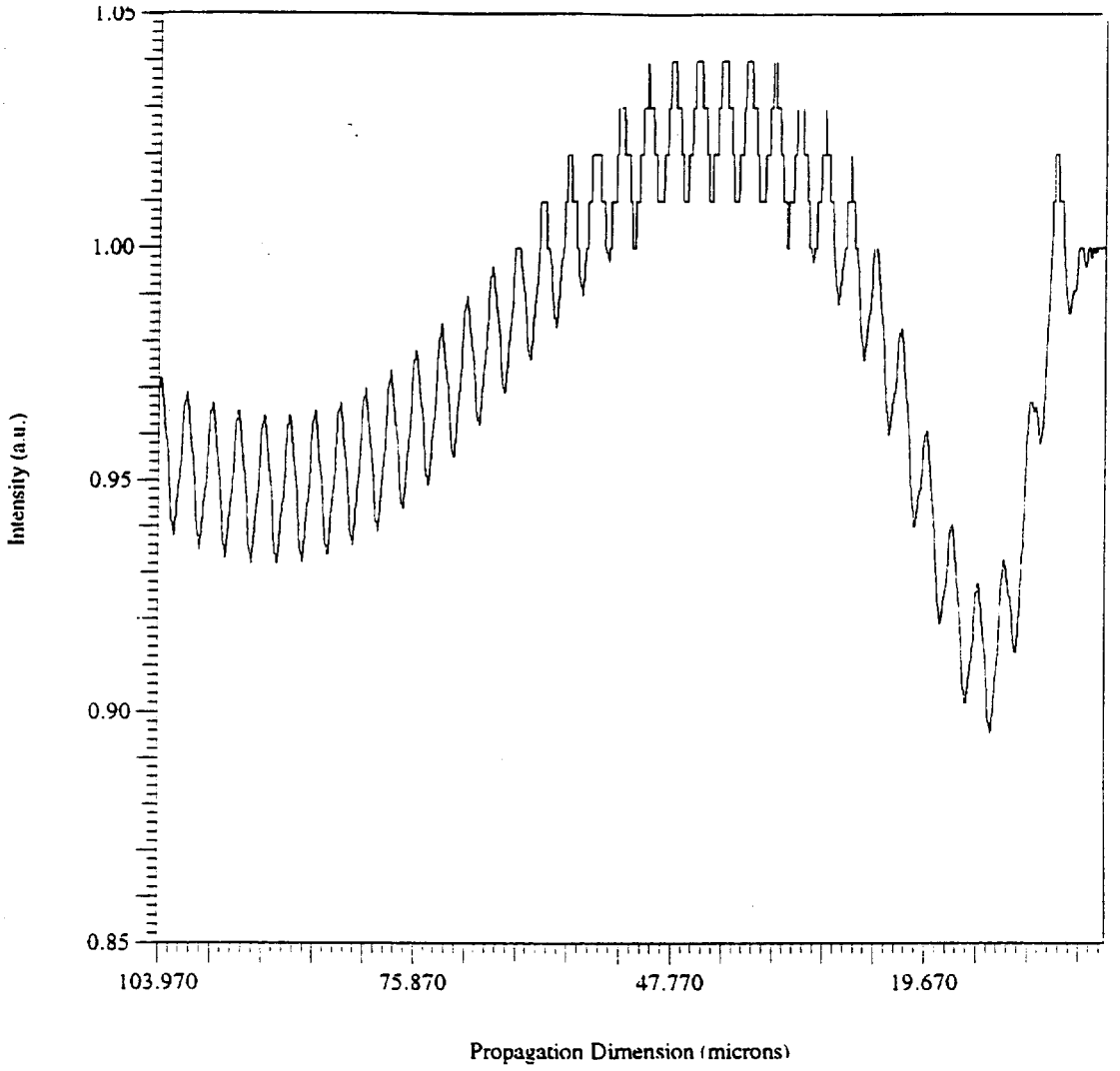

Figure 4.18 On-axis fundamental intensity vs. propagation distance for Δn=0.015

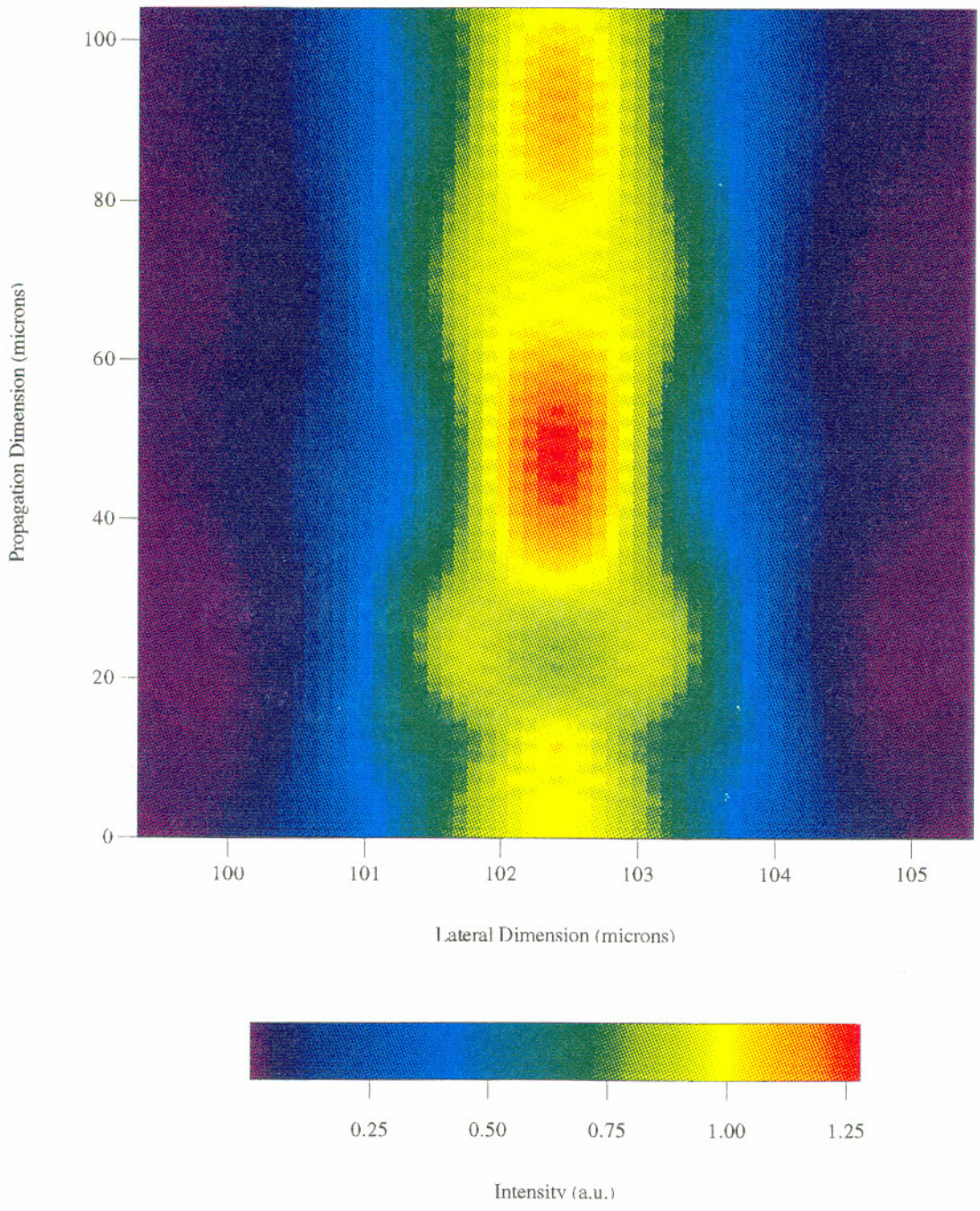

Figure 4.19 2-D surface plot of SH intensity for PSW waveguide for $\Delta n=0.015$

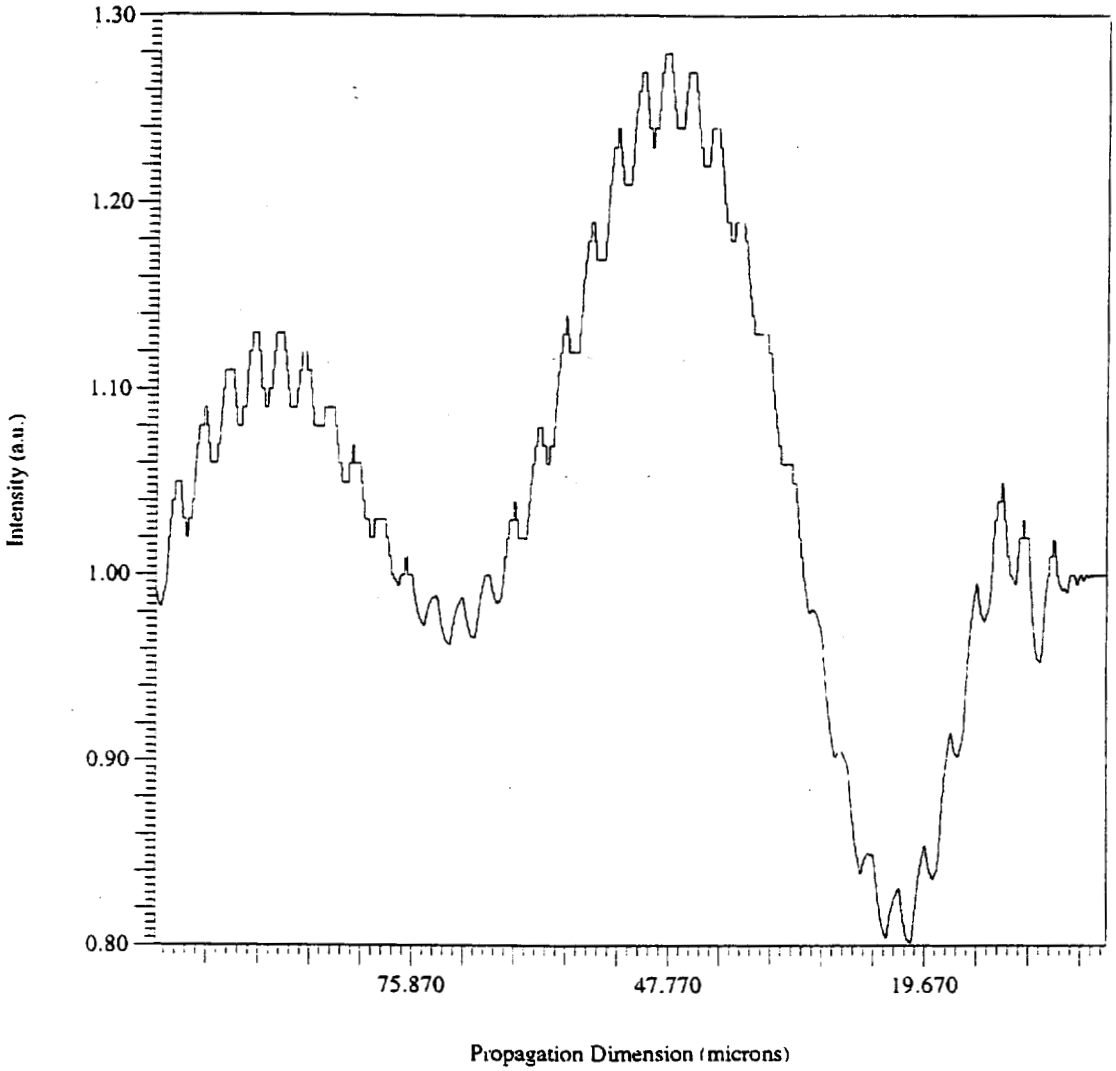

Figure 4.20 On-axis SH intensity vs. propagation distance for $\Delta n=0.015$

4.5 Discussion

In summary, an expression for η_{norm} was derived which accounts for the dependence of the overlap of the generated SHG field and the guided SHG mode on the lateral variation of the nonlinear coefficient, d, and refractive index, n. This expression was evaluated for the case of phase-matched SHG in a uniform 2-D KTP channel waveguide and was compared to the value obtained using a previous expression which assumed uniform values of d and n in the plane transverse to light propagation. The calculated values indicate that for weakly guiding structures, such as QPM waveguides, the derived expression results in a smaller value of η_{norm} than the previous expression.

The EIM modeling presented in this chapter for the first time theoretically established that the fundamental and SH TM_0 guided spatial modes of KTP PSWs are, in general, asymmetric due to the reduction in refractive index with depth characteristic of these devices. The FWHM spatial mode intensity profiles were shown to be smaller than the diffused dimension of the modeled waveguides, indicating that fundamental pump beams need to be focused to near diffraction-limited spot sizes for efficient optical coupling into the waveguide guided mode. This work identified that the most powerful modal confinement and largest overlap of the fundamental and SH TM_0 spatial modes occurs near the air/waveguide interface. These key results will be shown to be experimentally confirmed in Chapter 6.

An FFT-BPM model was developed to study the beam propagation behavior in KTP PSWs. Results from this model showed that the waveguide spatial mode intensity profiles are dominated by near field diffraction during propagating through the first ten to twenty PSW periods. Since the waveguide supports two symmetric TM modes, the simulation results indicate powerful spatial mode beating effects predominating for the SH beam propagation for twenty to thirty waveguide periods. Development of the linear FFT-BPM model set the stage for development of a beam propagation method model explicitly incorporating second harmonic generation for simulation of periodically segmented nonlinear waveguides. This model and its results are discussed in Chapter 5.

CHAPTER 5
BEAM PROPAGATION METHOD MODELING OF SECOND HARMONIC GENERATION IN NONLINEAR WAVEGUIDES

5.1 Introduction

The development of efficient device technologies is required for a clear understanding of the interdependence of the guided spatial mode properties at the fundamental and second harmonic (SH) wavelengths. The 2-D FFT BPM model discussed in Chapter 4 was shown to effectively describe the propagation of the lowest order symmetric spatial modes supported by both continuous and segmented KTP waveguides in the infrared and near ultraviolet. As these results indicated, substantial spatial mode beating effects couple with the refractive index periodicity to modulate the intensity of the propagating modes. Since the generated and guided SH fields can be expected to be responsive to the local intensity variations in the fundamental fields, it is reasonable to anticipate that η_{eff} for a KTP PSW will experience a similar modulation. Additionally, an important unanswered question in the study of optical fields propagating in QPM waveguides is the degree of homogeneity of the propagating fundamental and SH optical fields. Since BPM has been shown to be particularly useful in analyzing the diffraction effects associated with optical propagation in a weakly guiding structure containing a longitudinally varying index grating, a 2-D FFT BPM which integrates the governing equations for SH generation and depletion might be expected to help resolve these issues.

Few reports exist of extending BPM models to study SHG processes in optical waveguides. In 1984, Hermansson and co-workers first reported an extension of the 2-D FFT BPM to study SHG in channel $LiNbO_3$ waveguides using a 1.07 μm fundamental

wavelength.[145] In order to avoid the prohibitive computational time required for a full 3-D model, they used the effective index approximation to reduce the number of dimensions involved in the computation by one. Of note, they used a 128-point, 70-80 μm wide lateral grid, yielding a lateral step size ranging between 0.547 μm and 0.625 μm, and a longitudinal step size of 1.0 μm. While use of these lateral and longitudinal step sizes obey the stability criteria given by equation (4.32), the lateral step sizes are on the order of the SH wavelength and the longitudinal step size exceeds it by a factor of 2. Despite this relatively coarse grid, Hermansson reported obtaining results for phase-matched SH generation displaying the expected quadratic power dependence with propagation length, while also observing that for non-phase-matched condition, the SH guide mode power oscillated with propagation length. More recently, Weitzman and Osterberg reported using a modified BPM to model SHG in optical fibers.[146] Masoudi and Arnold used a full 3-D FD-BPM to study SHG in a nearly perfect phase-matched rib waveguide.[147] They also applied their model to study of QPM in the same rib waveguide structure by introducing a longitudinal rectangular index grating and where the nonlinear d coefficient is given its effective full value or zero in alternating half-periods of the rectangular grating. Further, Masoudi and Arnold reduced the value of the effective d coefficient by $1/\pi$ from its bulk value. Using this model, they obtained results for the normalized depletion of the fundamental intensity and the nonlinear phase shift $\theta_{NL,}$ both as a function of Δkl. The Masoudi and Arnold model extension to QPM interactions, however, does not apply to SHG in PSWs. The modeled structure, in the case reported, is a rib waveguide in which the d coefficient is modulated from $1/\pi$ of its bulk value to zero in alternating half-periods. The refractive indices used for the rib waveguide assume a substrate index of 3.4 and fundamental wavelength of 1.55 μm. While Masoudi and Arnold do not indicate what specific problem their model is intended for, it appears they may have a semiconductor optoelectronics application in mind, as indicated by the wavelength, structure geometry, and refractive indices used.

5.2 Development of BPMSHG

To extend the 2-D BPM model discussed in Chapter 4 to model nonlinear SHG in nonlinear waveguides, the coupled field equations[148] for generation and depletion of the SH and fundamental fields were added to the model. The new code, which incorporates solution of the coupled field equations during each propagation step, also using the same Cooley-Tukey FFT algorithm used in BPMG7, was termed BPMSHG.

The coupled field equations derived directly from Maxwell's equations are given by

$$\frac{dE_f}{dz} = \frac{-ik_f}{2n_f\varepsilon_0} d_{NL} E_s E_f^* \exp(-i\Delta kz) \tag{5.1}$$

$$\frac{dE_s}{dz} = \frac{-ik_s}{2n_s\varepsilon_0} d_{NL} E_f^2 \exp(-i\Delta kz) \tag{5.2}$$

where, for notational clarity, the notation d_{NL} has been used to represent the nonlinear d coefficient and where $\Delta k = k_s - 2k_f$. These equations, representing differential variation in the fundamental and SH fields with propagation distance are ideally suited for computation using BPM.

BPMG7 was used as the starting point for extension of the 2-D FFT BPM model of PSWs to allow calculation of the nonlinear process in optical waveguides. The resulting program, named BPMSHG, is shown in Appendix A. BPMSHG incorporated a second propagation subroutine, named PROP2, allowing both the fundamental and SH fields to be propagated during each loop through the main program. The main program of BPMG7 was modified to include algorithms to set the refractive index and d coefficient value for each grid point. After each longitudinal propagation step, the fundamental and SH fields returned by the PROP and PROP2 subroutines, respectively, are used by the main program to compute the new fundamental and SH fields using equations (5.1) and (5.2). The main program also includes conversion factors for calculating the fundamental and SH power.

BPMSHG operates using an input data file, named inputshg.dat, similar in construction to the input file used by BPMG7. A sample inputshg.dat file is shown in Appendix A. The BPMSHG input file lists the refractive index data for the modeled waveguide at both the fundamental and SH wavelengths; best fit gaussian beam waist radii for each wavelength; values for the d coefficient; and the power (in watts) of the input fundamental field.

Figures 5.1 and 5.2 display 2-D surface intensity plots for the case where n_f = 1.856/1.846, n_s = 1.990/1.980, Λ= 2.80 μm, and where the fundamental was selected to be 0.7512 μm. Note that the QPM condition given by

$$\Lambda = \frac{\lambda_f}{2\Delta n} \quad \text{for m=1} \tag{5.3}$$

yields Λ=2.803 μm for these input values, and would yield 2.800 μm exactly using a fundamental wavelength of 0.7504 μm. Note that a relatively long propagation corresponding to > 250 μm is required to recognize that the actual QPM condition has not been met. Further, as will be discussed in the next section, for the above parameter set, BPMSHG finds QPM at a longer wavelength (at 0.75447 μm) than predicted by (Eqn 5.3). These results indicate how a well-tested tool, such as BPMSHG, can offer insight into nonlinear optical waveguide problems that defy analytical solution.

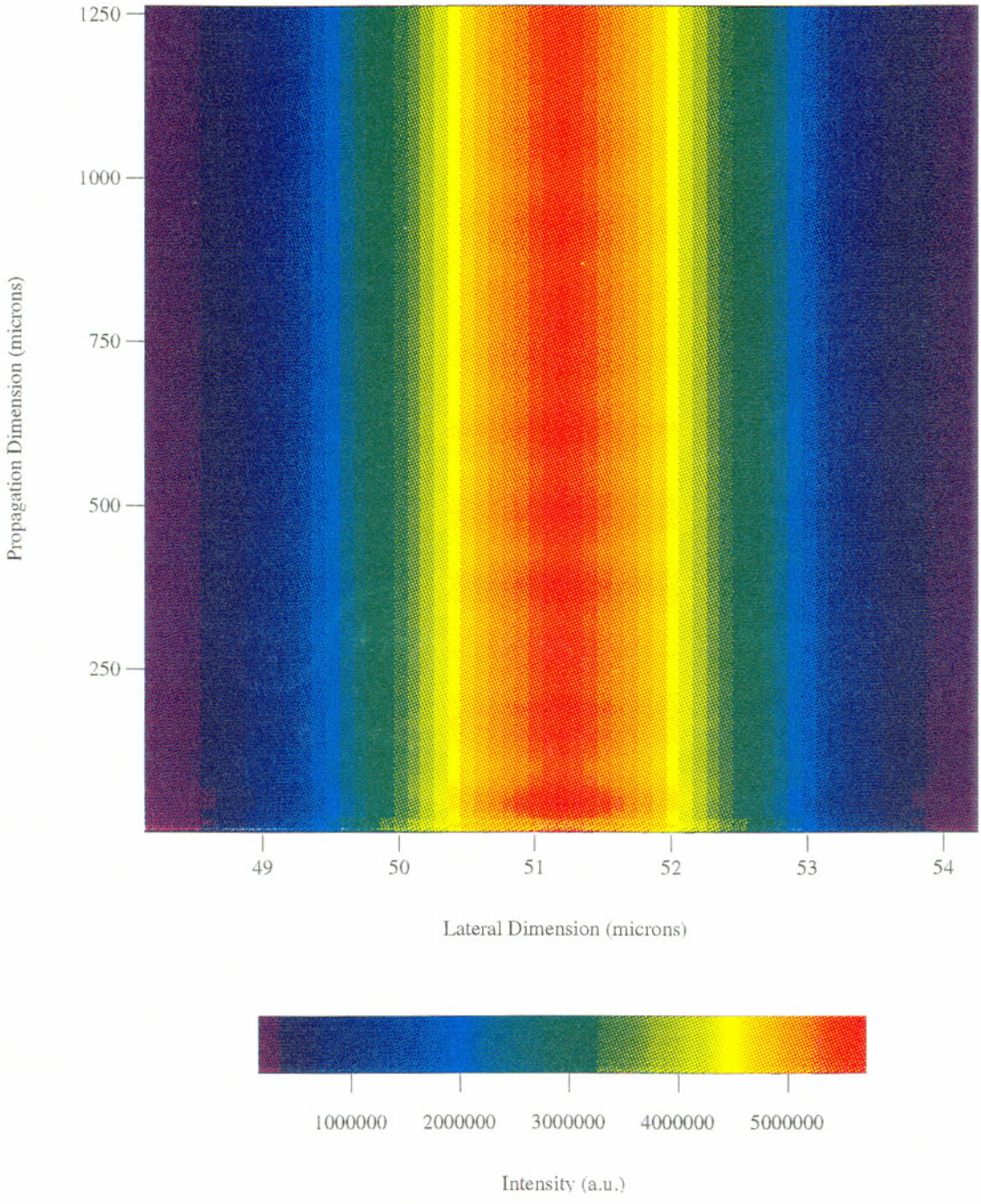

Figure 5.1 2-D Surface Intensity Plot for λ=0.7512 μm

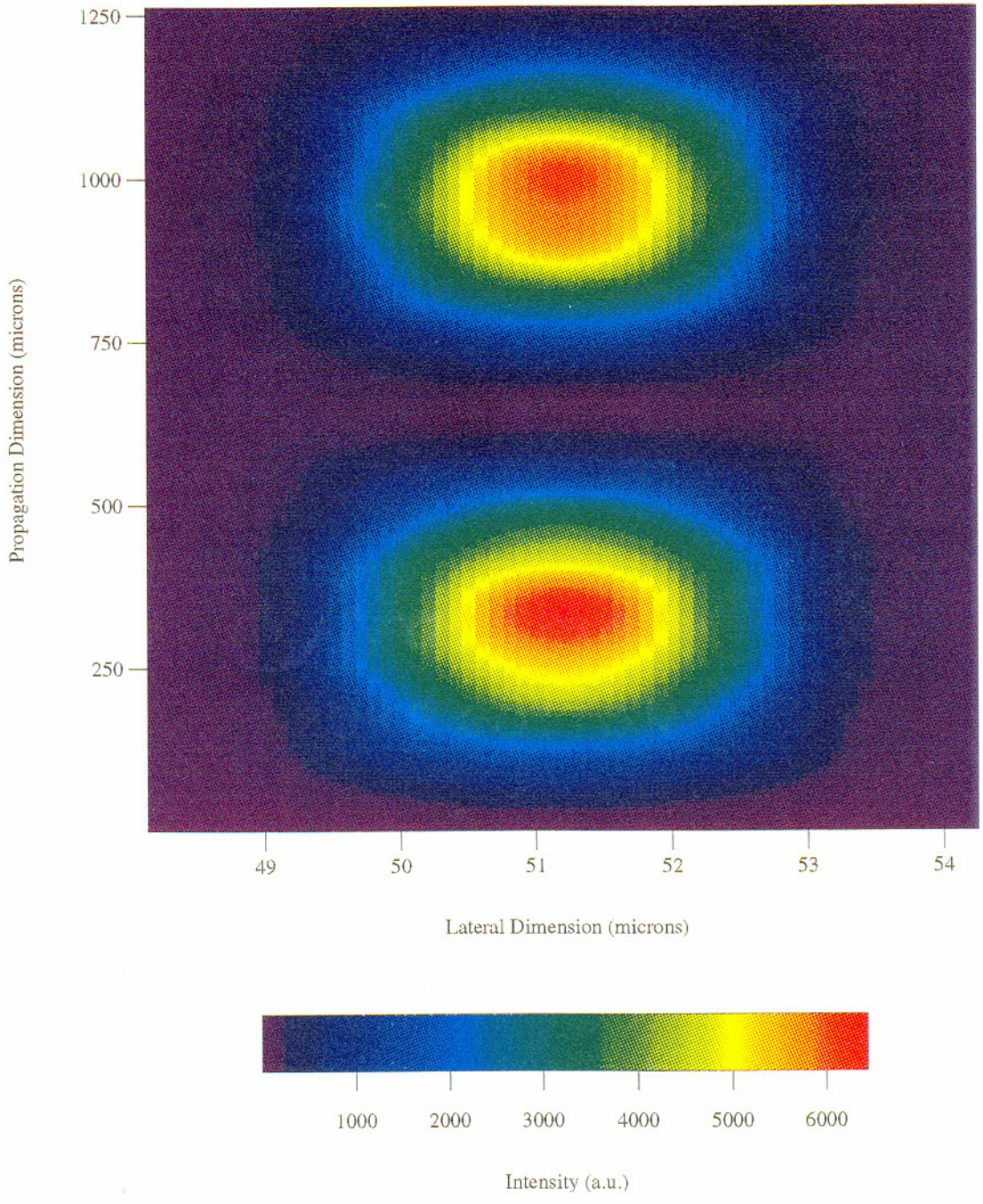

Figure 5.2 2-D Surface Intensity Plot for λ=0.3756 μm

5.3 BPMSHG Results for KTP Periodically Segmented Waveguides

Similarly to BPMG7, BPMSHG utilizes a large computational window (typically > 100 microns). Absorbing lateral boundary conditions are implemented to avoid spurious field reflections from the domain boundaries. Computational meshes of 0.05 micron (longitudinal) x 0.05 micron (lateral) are typical. Feature boundaries lie along computational mesh lines.

The model was used to analyze optical propagation and SHG in a 4.0 μm wide periodically segmented waveguide with refractive indices of n=1.856 in the diffused regions and 1.846 in the undiffused regions with Λ=2.80 μm. The chosen duty cycle was 50%. Refractive indices of n=1.990 in the diffused regions and 1.980 in the undiffused regions at the SHG wavelength were selected. A d_{33} coefficient of 13.7 pm/V was used for the simulation. A 2.15 μm radius fundamental Gaussian field was chosen as the input field. This value was chosen through consideration of the spatial mode solutions to the equivalent 3-layer slab waveguide problem using WAVEGUIDE345.

As noted at the conclusion of the preceding section, the fundamental wavelength corresponding for QPM for this structure does not occur at λ_f=0.7504 μm as predicted using (Eq. 5.3). Rather, BPMSHG finds the condition for QPM met for this simulated KTP PSW for λ_f=0.75447 μm. This suggests that BPMSHG observes an increase in the propagation constant corresponding to the SH guided mode relative to the propagation constant for the fundamental guided mode, resulting in an increase in the effective index difference seen by the guided modes. This causes an increase in the effective Δn by 0.00073. The increased modal confinement of the SH TM_0 spatial mode relative to the fundamental TM_0 mode is likely responsible for the small increase in the effective Δn. This very small increase in the effective Δn is responsible for the red shift in the value for λ_f for QPM seen by BPMSHG. The red shift in λ_f for this case corresponds to 4.0 nm. For an AlGaAs diode laser whose wavelength is being adjusted by temperature control, this red shift would correspond to a temperature change of approximately 13 °C.

For the simulated KTP PSW described above, Figure 5.3 shows a detail of the results for the SHG power variation with propagation length for a fundamental input power of 100 mW. The figure shows the SHG power over a propagation range of four periods, following propagation through the first 100 waveguide periods. This choice results in a view of the SHG power sufficiently removed from the region near the input where strong near field diffraction effects, as discussed in the previous chapter, predominate. The results clearly display the periodic power dependence on period length characteristic of QPM SHG and predicted by Eqn. (2.24). The effectiveness of the switching the sign of the d coefficient can be clearly observed, showing the essential property of a properly quasi-phase-matched KTP PSW. This represents the first demonstration of the effectiveness of BPM to simulate this characteristic behavior of QPM waveguides.

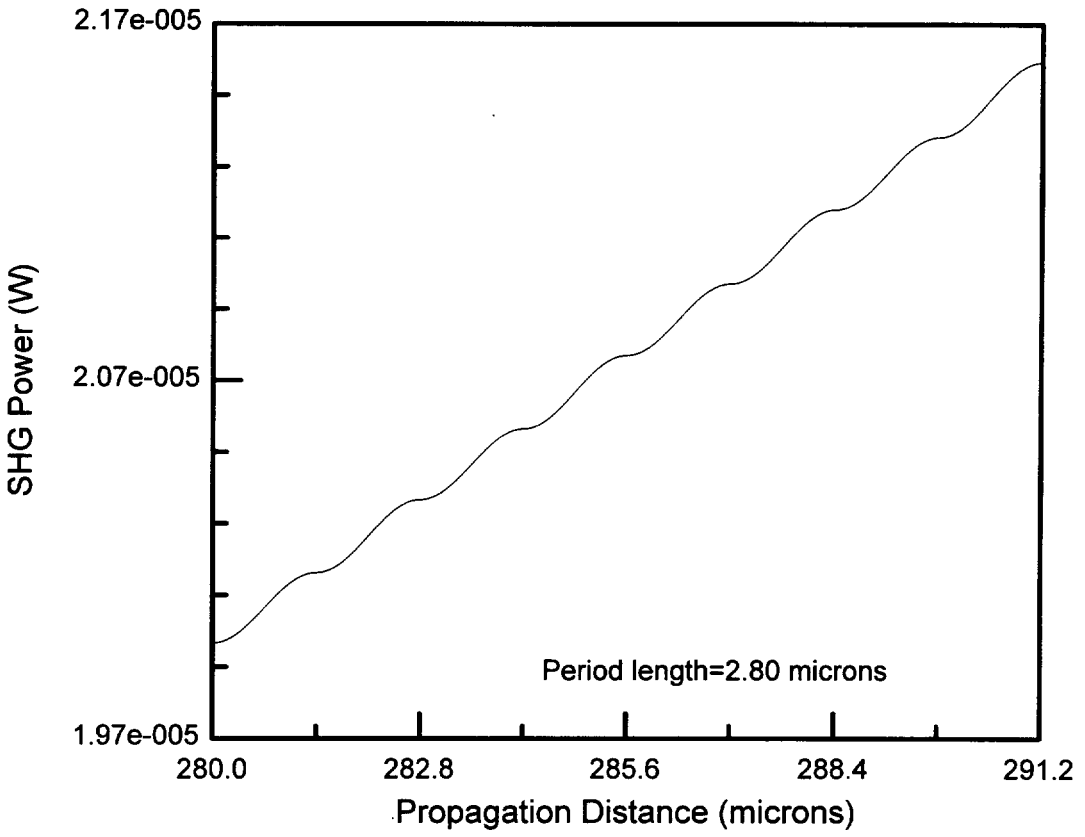

Figure 5.3 SHG power vs. propagation distance

A 2-D surface intensity plot of the fundamental spatial mode at 0.75447 μm over 9 mm of propagation length is shown in Figure 5.4. The depletion of the guided mode is clearly evident. This is believed to be the first 2-D BPM simulation of fundamental depletion obtained for SHG in a nonlinear optical waveguide and the first BPM simulation of this phenomenon in PSWs.

Figure 5.5 displays the computed fundamental intensity as a function of propagation length along the longitudinal axis of the waveguide. This figure is noteworthy in illustrating three distinct regimes, in which different processes are dominant in shaping the intensity profile. In the first regime, closest to the input face of the waveguide, near field diffraction effects predominate. After the first several hundred microns, this strong intensity modulation subsides to be replaced with a damped oscillation which finally decays about 5.0 mm deep into the guide. Beyond this depth, the on-axis fundamental intensity decays parabolically. Note the large fluctuation in the on-axis fundamental intensity caused by near-field diffraction near the input. Unlike the strong mode beating effects seen in Figures 4.14 and 4.20 showing the on-axis SH intensity fluctuating by +/- 15-30% during the first ten periods of propagation *under the condition of excitement by the fundamental best-fit gaussian at 385 nm*, in the BPMSHG case of NUV SHG under excitement by the best-fit fundamental gaussian these mode beating effects are not distinguishable. This observation is consistent with the SH TM_0 and TM_2 spatial modes having different wavelengths for QPM SHG under fundamental TM_0 excitation as predicted by Roelofs et al.[111]

The SHG power after a propagation distance of 9.0 mm was 16.67 mW corresponding to a normalized conversion efficiency of 206%/W-cm^2. This compares to a value of 252%/W-cm^2 found at 1.0 mm, indicating that the effects of pump depletion become significant at these propagation lengths and power levels. While these values reflect a simulated 2-D KTP PSW, these values for η_{eff} fall well within the range of values reported in Table 3.2.

Figure 5.6 displays the corresponding surface intensity profile for the SH field generated in the waveguide. Note the clear confinement of the spatial mode within the waveguide. The SH spatial mode shows no signs of spatial mode beating, indicating that only the TM_0 spatial mode is quasi-phase-matched. Figure 5.7 shows the intensity parabolically increasing with propagation length until depletion of the fundamental becomes significant. The smoothness of increase indicates that the diffraction effects seen strongly modulating the on-axis fundamental intensity for the first 2000 μm of propagation in Figure 5.5 do not result in a corresponding modulation of the SH intensity over the same propagation range.

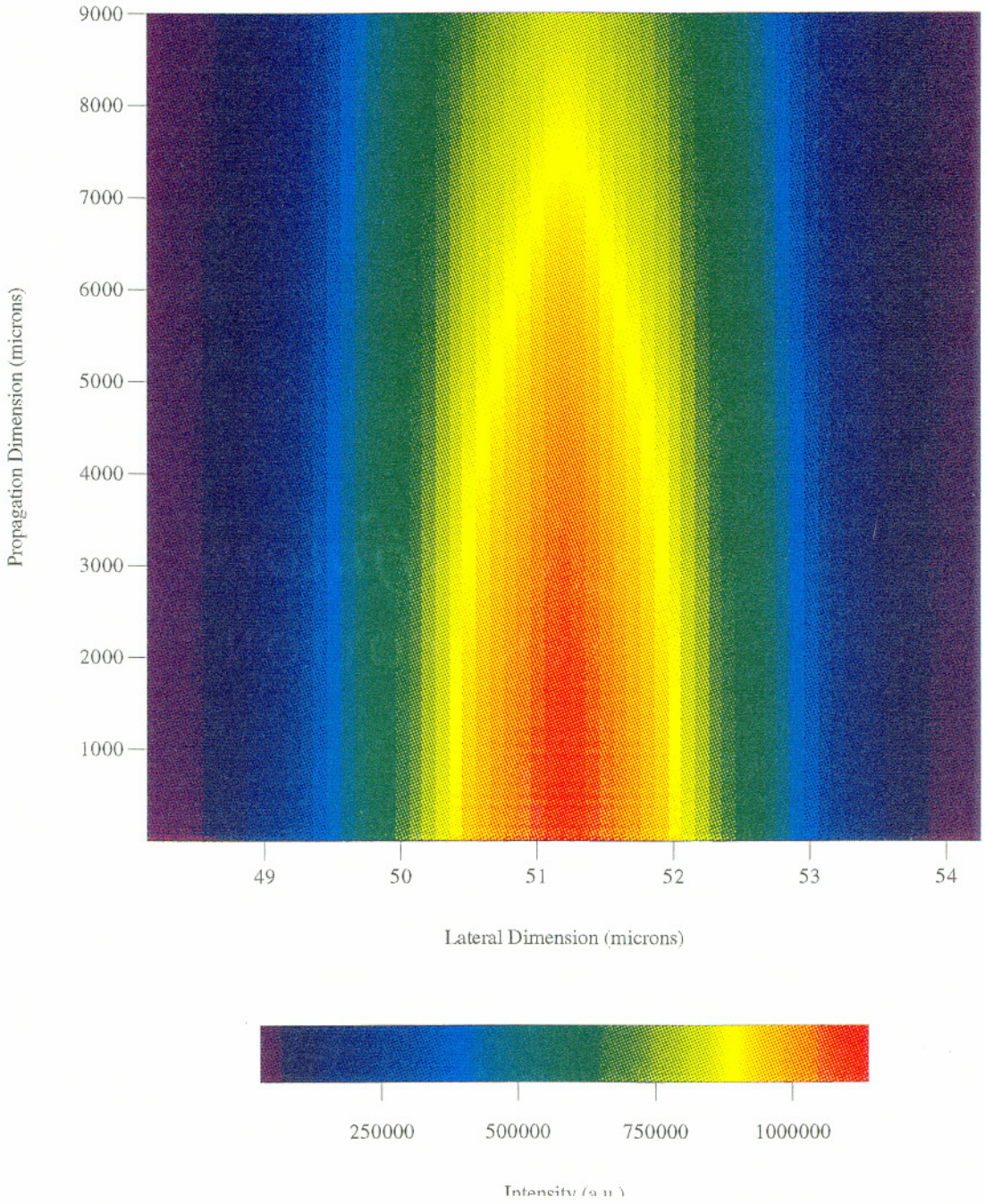

Figure 5.4 2-D Surface Intensity Plot at λ_f=0.75447 μm

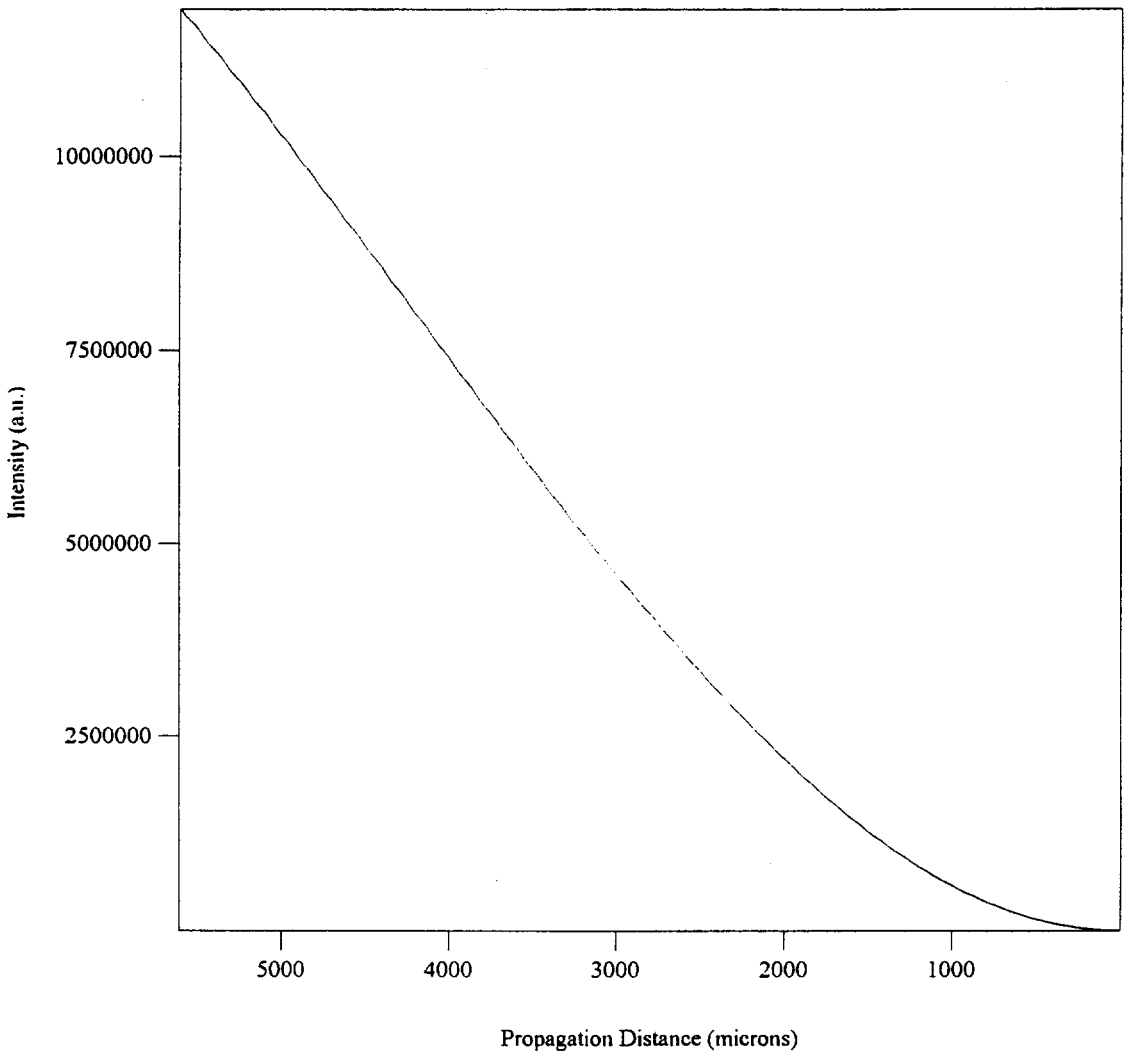

Figure 5.5 On-axis Intensity vs. Propagation Distance Plot at λ_f=0.75447 μm

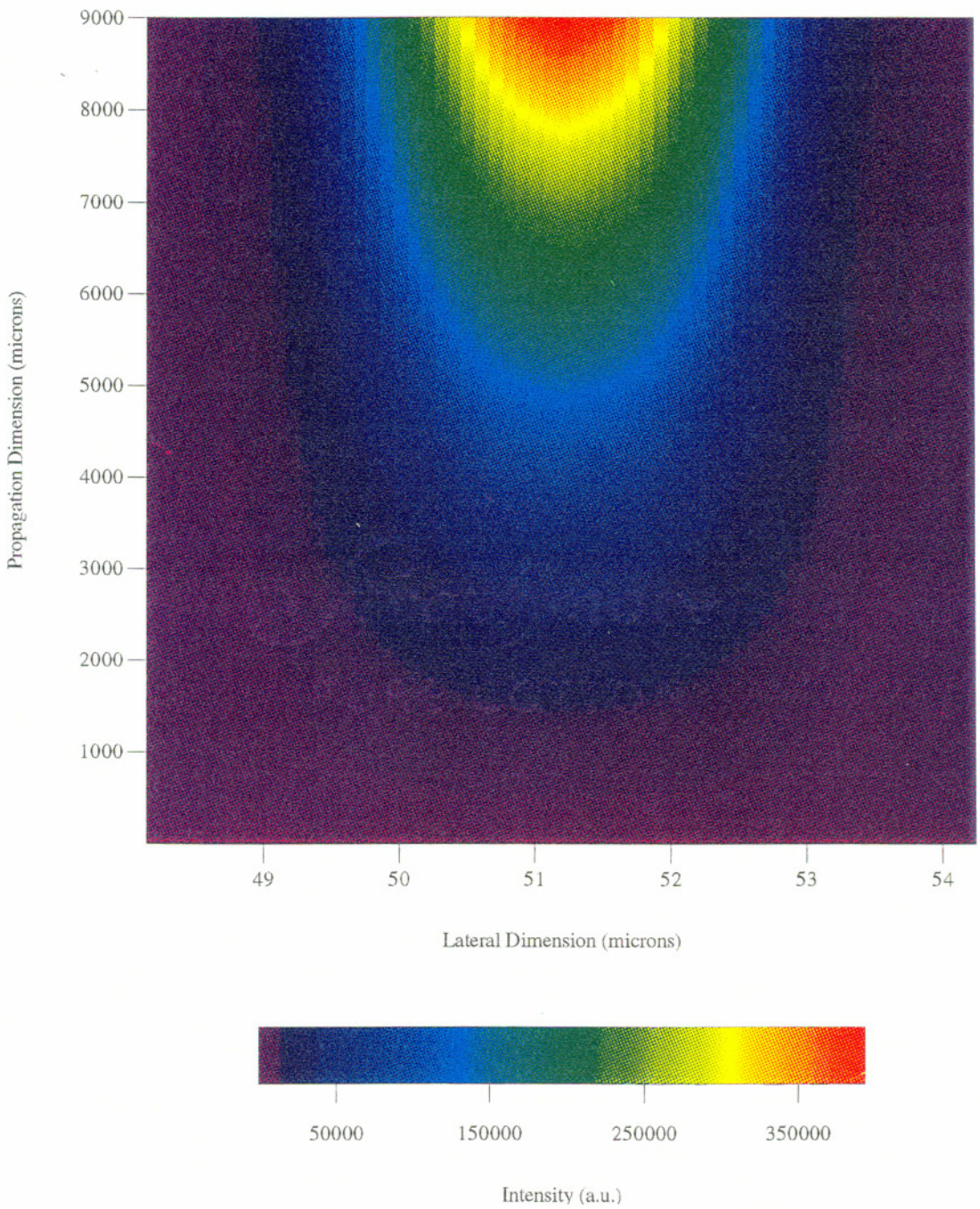

Figure 5.6 2-D Surface Intensity Plot at λ_{SH}=0.37723 μm

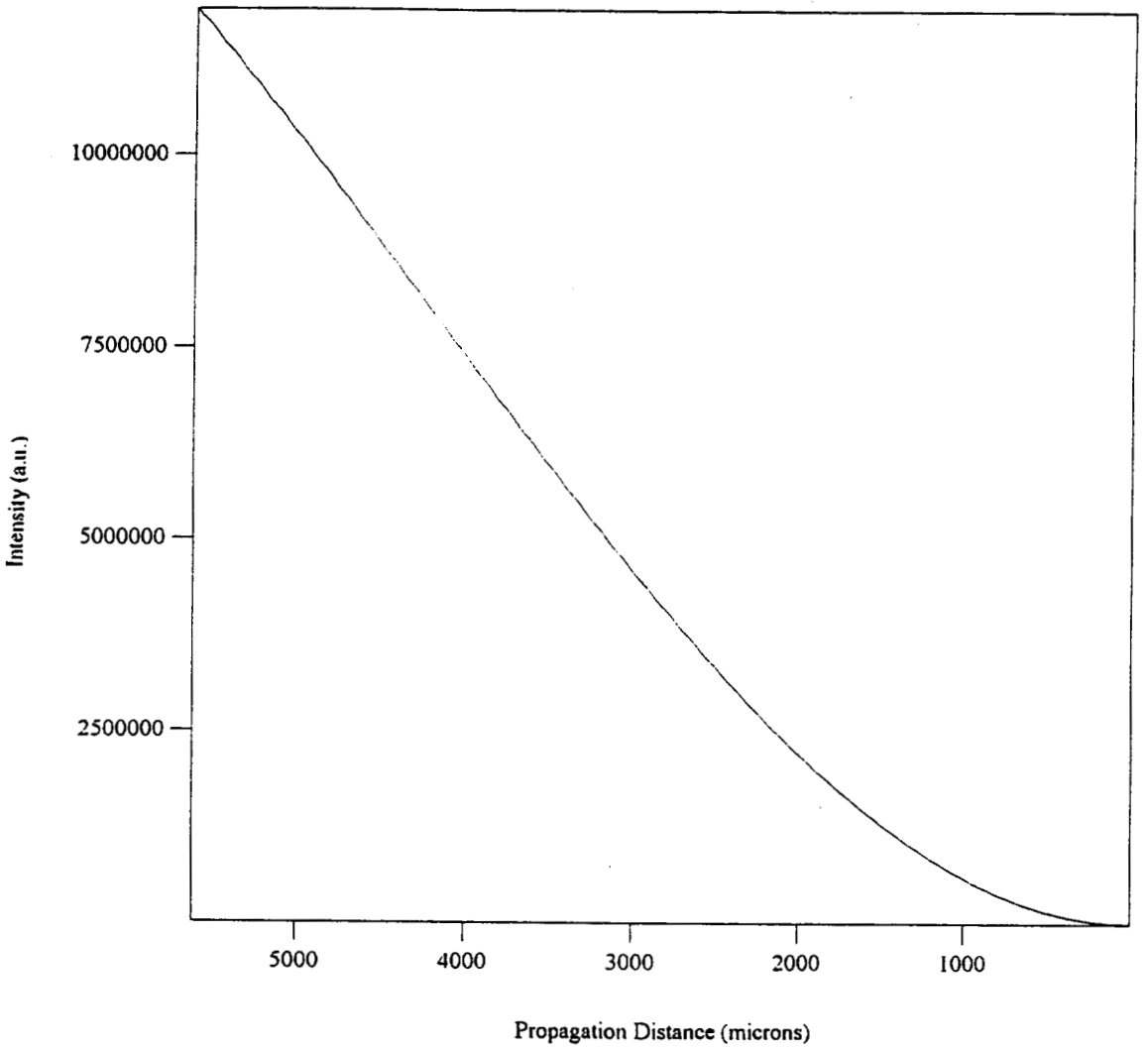

Figure 5.7 On-axis Intensity vs. Propagation Distance Plot at λ_{SH}=0.37723 μm

5.4 Discussion

The 2-D FFT-BPM SHG code, termed BPMSHG, has produced the first numerical BPM model results for SHG in PSWs. The development of BPMSHG represents an important contribution to the development of numerical methods for modeling nonlinear waveguides, in general, and provided important details on how the cooperative effects of diffraction, QPM, and spatial mode beating affect the overall SHG process in KTP PSWs. Diffraction effects appear to strongly modulate the fundamental spatial mode intensity. This modulation does not appear in the SH intensity.

The SHG power after a propagation distance of 9.0 mm was 16.67 mW. The normalized conversion efficiency of 252%/W-cm^2 at 1.0 mm, decreasing to a value of 206%/W-cm^2 found at 9.0 mm, indicates that the effects of pump depletion become significant at these propagation lengths and power levels. While these values reflect a simulated 2-D KTP PSW, these values for η_{eff} fall well within the range of values reported in Table 3.2 and will be seen to be comparable to the values obtained for NUV SHG from Ti:Sapphire-pumped KTP PSWs discussed in Chapter 6.

While BPMSHG was used to simulate a KTP PSW for QPM SHG in the NUV, the code is widely applicable to second harmonic generation in bulk and waveguide nonlinear materials. Extension of this model to 3-D appears straightforward, although probably requiring supercomputer-level computational resources.

CHAPTER 6
EXPERIMENTAL CHARACTERIZATION OF KTP NONLINEAR WAVEGUIDES

6. Experimental Overview

The development of an URSL-pumped KTP waveguide laser requires detailed characterization of the SH performance of KTP waveguides in the near ultraviolet. Very limited characterization of the performance of KTP waveguides at wavelengths below 400 nm has been reported.[86,149] These reports both addressed waveguides produced on flux-grown KTP.

As discussed in Chapter 3, research conducted by Du Pont had led John Bierlein and Mark Roelofs to suggest that hydrothermal KTP processed in an exchange bath containing a high Ba concentration offered good prospects for yielding KTP waveguides capable of producing modest SH NUV output.[150] This processing technique was selected to produce the waveguides used in this work.

6.1 Argon-ion pumped-Ti:Sapphire laser Characterization

For purposes of characterizing the spatial mode, SH conversion efficiency, and power handling capability of KTP waveguides in the NUV, an argon-ion laser-pumped Ti:sapphire laser was used as the near infrared pump source. A Coherent Innova 200 argon-ion laser capable of producing over 10 W of multiline CW output was coupled to a Coherent 899 Ti:sapphire ring laser. The Coherent 899 Ti:sapphire laser was equipped with "short wave" optics to allow the wavelength of its output to be tuned using a micrometer-driven three-plate birefrigent filter. Using this optics set, the wavelength of the Coherent 899 Ti:sapphire laser could be tuned from 730 nm to 830 nm, with peak CW output near 780 nm.

The output power from the Coherent 899 Ti:sapphire laser was spectrally analyzed by coupling several milliwatts into a Polytech optical fiber whose ends had been AR-coated for 800 nm and which had been fitted with FC connectors. This allowed direct coupling of the fiber output into the input port of an Advantest TQ8345 optical spectrum analyzer. The Advantest TQ8345 is a Michelson interferometer-type spectrum analyzer with a specified resolution of 0.01 nm over the 400-1100 nm spectral range. The accuracy of its wavelength output calibration was verified through measurement of the wavelength of a HeNe laser. To further establish the resolution limit of the Advantest TQ8345 near the wavelength range of interest, the CW power output from a Sony 304 XT GRINSCH AlGaAs diode laser was fiber-coupled into the optical spectrum analyzer. Figure 6.1 shows a plot of the measured spectrum for this device when operated to produce 800 mW. As indicated in the figure, the individual longitudinal modes can be resolved with a spectral linewidth of <0.01 nm.

To calibrate the birefringent filter micrometer position to the actual wavelength, the output wavelength of the Ti:Sapphire laser was scanned while observing the measured wavelength reported by the Advantest TQ8345. Figure 6.2 displays a plot of this wavelength calibration of the birefringent filter micrometer position. Note that the spectral output of the Ti:Sapphire laser was observed to always consist of a single dominant longitudinal mode. The measured linewidth of the Ti:Sapphire laser was an instrument-limited 0.01 nm.

As seen in Figure 6.2, the output power in the wavelength range 720-830 nm could be obtained with the birefringent filter changing order above 790 nm. Since the center wavelength of interest for the optical characterization studies was 770 nm, this observed shift in order was conveniently located a comfortable 20 nm above the wavelength at which the etalon changes order. This allowed continuous tuning through a single order, as shown in Figure 6.3, to be used to access the wavelength range of interest.

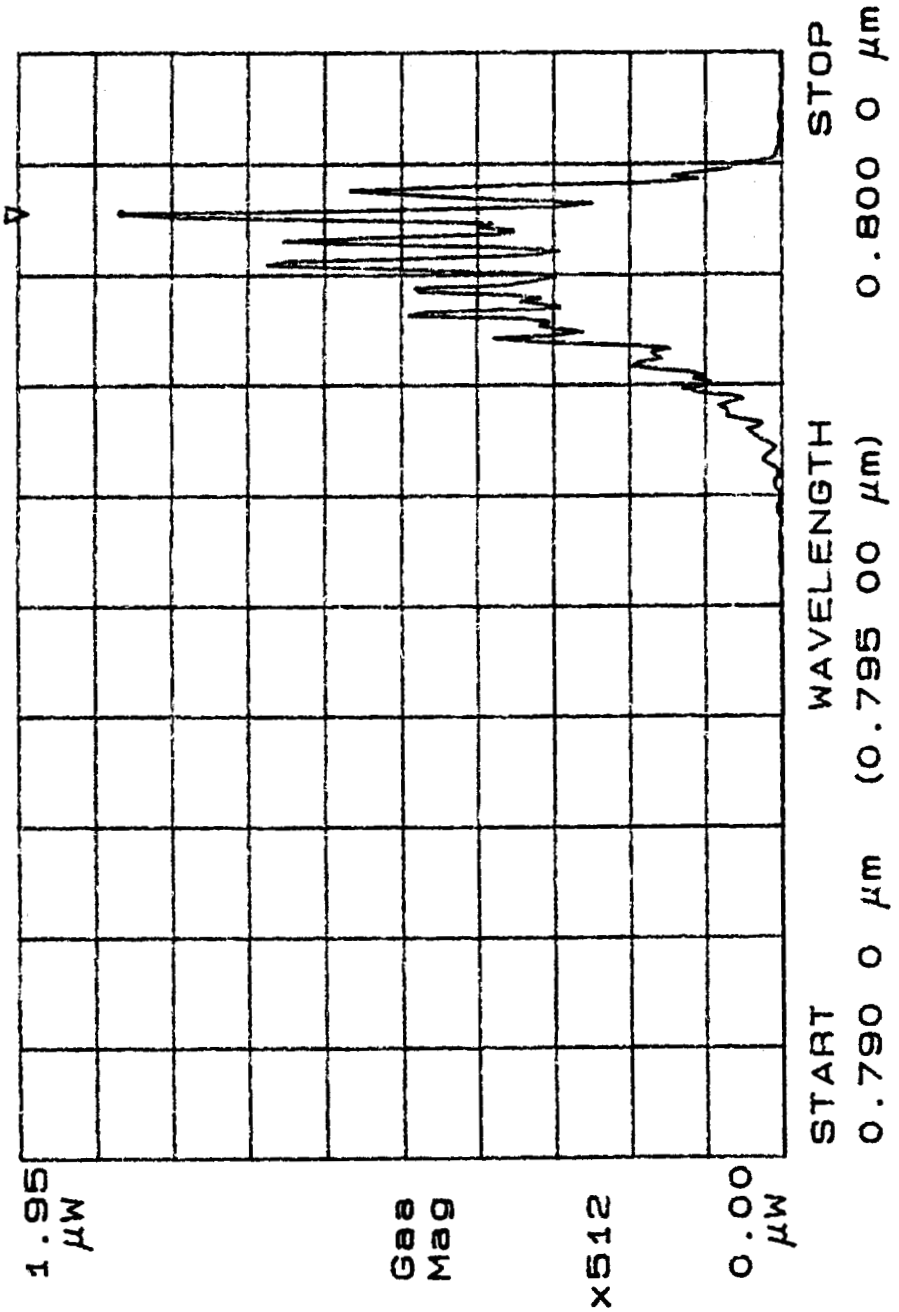

Figure 6.1 Power Spectrum of Sony 304XT AlGaAs laser diode

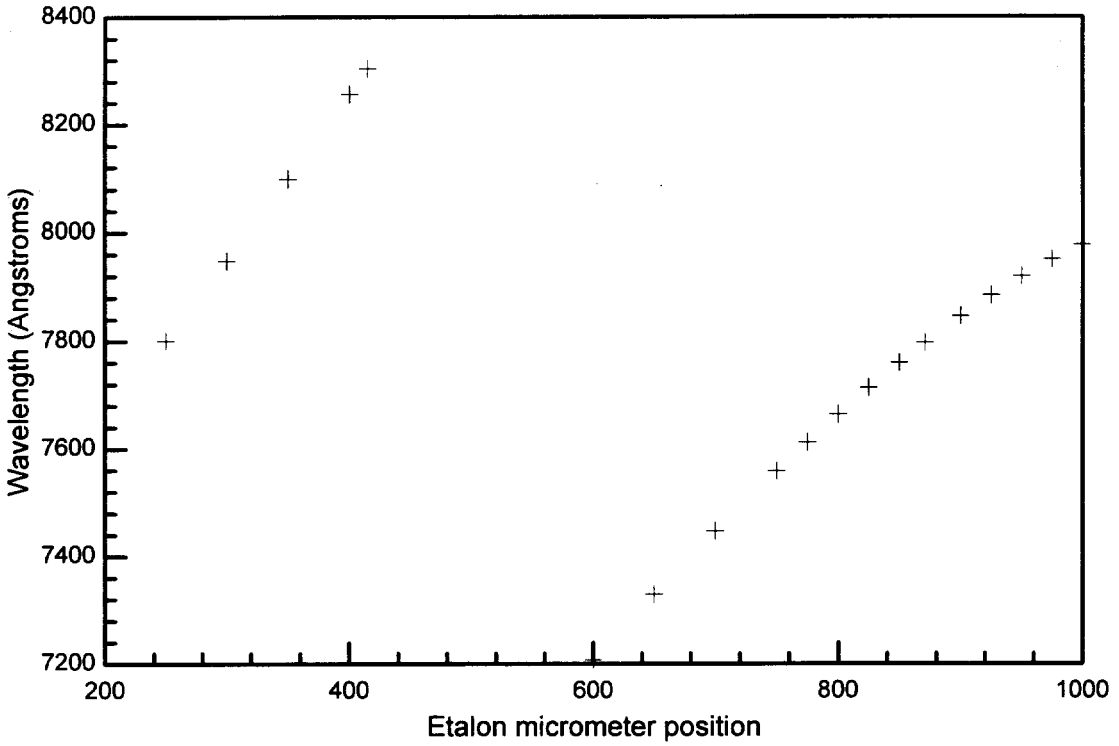

Figure 6.2 Ti:Sapphire wavelength vs. etalon micrometer position

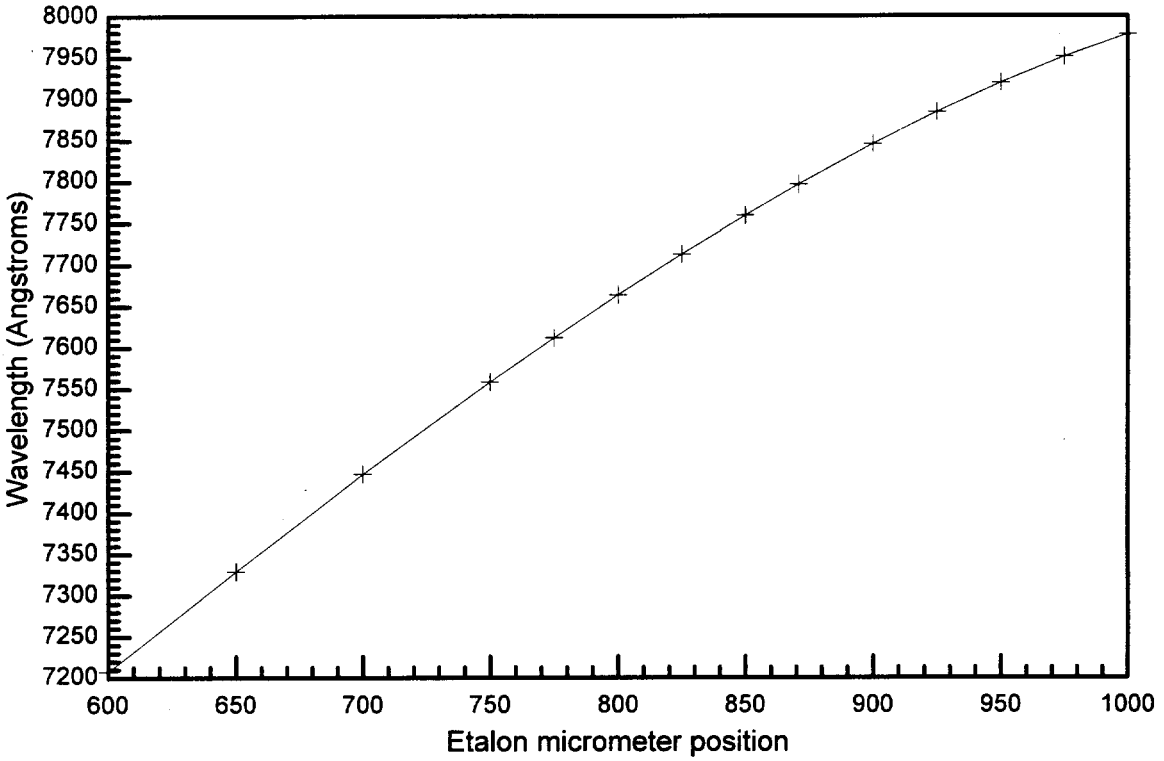

Figure 6.3 Ti:Sapphire wavelength vs. etalon micrometer position fit

The beam propagation behavior of the Ti:Sapphire laser output was evaluated to determine the requirements for the beam expander and objective lens required to focus the fundamental output into the KTP waveguides. To evaluate the beam propagation characteristics, two independent sets of the measurements were made. The first measurement set was obtained using a Coherent ModeMaster beam propagation analyzer. The Coherent ModeMaster uses a scanning lens to focus the sampled beam on slits on a rotating drum to obtain a measurement of the beam size in two orthogonal axes as a function of focus position.[151] This information is then processed to determine the actual beam waist location relative to the instrument and to compute the mode quality parameter M^2 which indicates the spatial mode quality of the sampled beam. Accurate measurement of M^2 is particularly important when attempting to obtain small focus spot sizes.[152] A second independent measurement of the output beam was made using a Beamscan Model

2180-XYLA beam profiler. This instrument uses a scanning drum fitted with slits, similar to the Coherent ModeMaster, but does not incorporate a stage-driven objective lens. The instrument was moved along the propagation axis of the Ti:Sapphire laser to obtain beam diameter data as a function of propagation distance.

The ModeMaster beam waist diameter data was input into Gaussian propagation code, GAUSS, and used to generate a computed beam waist diamenter as a function of propagation distance. The source code for GAUSS is given in Appendix A. Note that the ModeMaster observed that the x axis beam waist position was offset 18 mm further inside the resonator (with respect to the output coupler) compared to the y axis beam waist position. The Beamscan data, adjusted for the astigmatic offset in the beam waist positions measured by the Coherent ModeMaster, was then plotted, as shown in Figure 6.4, with respect to the GAUSS code data using the ModeMaster beam diameter and beam waist position input. As evident in Figure 6.4, the plotted beam propagation profiles obtained from these independent measurements are nearly coincident. In addition, the plotted data displays the astigmatic and elliptical character of the Ti:Sapphire output beam propagation.

The ModeMaster beam waist diameter data was input into gaussian propagation code, GAUSS, and used to generate a computed beam waist diamenter as a function of propagation distance. The source code for GAUSS is given in Appendix A. Note that the ModeMaster observed that the x axis beam waist position was offset 18 mm further inside the resonator (with respect to the output coupler) compared to the y axis beam waist position.

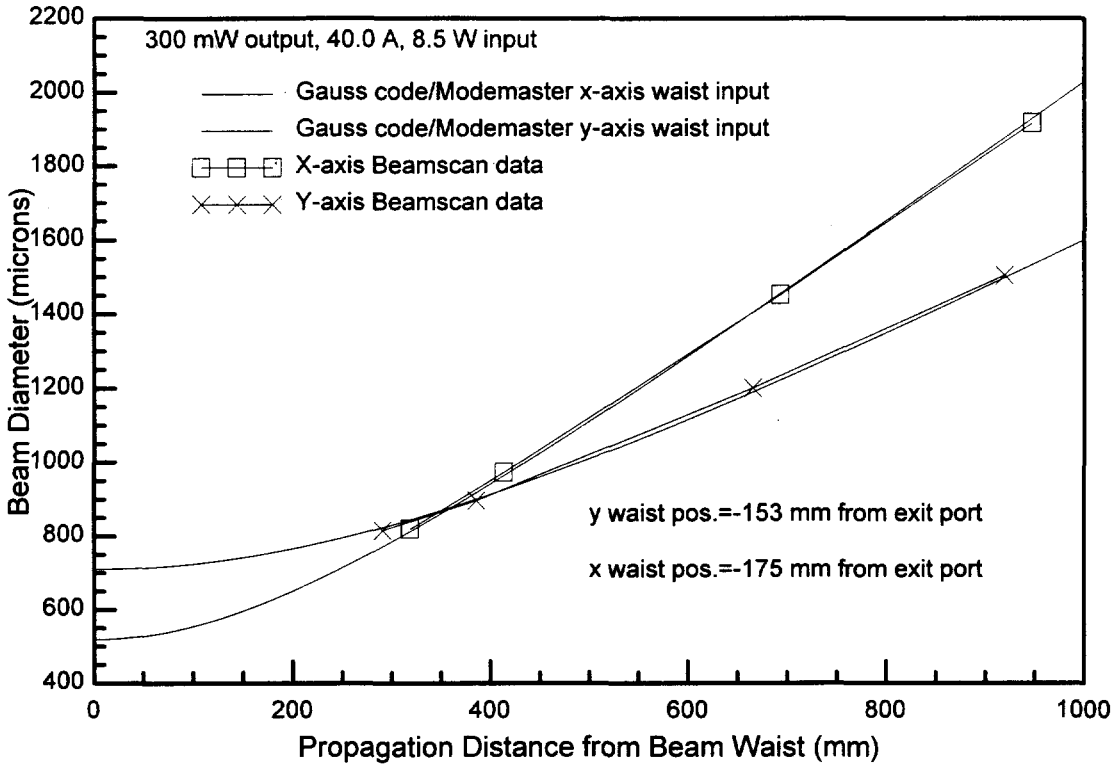

Figure 6.4 Ti:Sapphire beam diameter vs. propagation distance

The Beamscan data, adjusted for the astigmatic offset in the beam waist positions measured by the Coherent ModeMaster, was then plotted, as shown in Figure 6.4, with respect to the GAUSS code data using the ModeMaster beam diameter and beam waist position input. As evident in Figure 6.4, the plotted beam propagation profiles obtained from these independent measurements are nearly coincident. In addition, the plotted data displays the astigmatic and elliptical character of the Ti:Sapphire output beam propagation.

A variable beam expander was used to increase the Ti:Sapphire laser output beam diameter. Figure 6.5 shows a plot of the expanded Ti:Sapphire beam diameter versus propagation distance where the measured data was again obtained using the Coherent ModeMaster and Beamscan Model 2180-XYLA. Note that the x and y beam waist positions shown in this figure are the new beam waist positions as transformed by the

variable beam expander and located by the Coherent ModeMaster. For comparison purposes, the unexpanded beam diameters plotted with respect to the transformed beam waist locations are also shown. As indicated by the figure, the plotted data from the two independent measurements is nearly coincident. This expanded beam propagation data was used for determination of the focusing objective requirements for the fundamental input beam.

Additional Beamscan measurements were obtained in the beam diameter range anticipated as the input beam diameter for the focusing objective. These measurements are shown in Figure 6.6. This shows that the two independent measurements agree to within 3% in the y-axis and within 7% in the x-axis when analyzed for a nominal beam diameter of 3.2 mm.

An F1.67 mm objective lens with a 10 mm focal length was employed as the focusing objective lens. This lens is used as the objective lens on the Electro Scientific Industries Model 9000 Series of Laser Memory Repair Systems for dynamic random access memory (DRAM) repair. This lens is designed to be aberration-corrected at 1047 nm and 880 nm and is typically employed to produce $1/e^2$ 3.5 μm spot sizes at 1047 nm using an input beam diameter of 5.5 mm. The availability of this objective lens and the author's experience in its use led to its selection for these characterization experiments. The measured data taken using the Beamscan 2180-XYLA was best-fit to a calculated spot size using the GAUSS code. The best-fit $1/e^2$ spot size to the measured data was 4.3 μm. This is a good match to the 3.6 μm x 4.0 μm (lateral and transverse, respectively) FWHM at the 770 nm fundamental TM_0 mode diameters calculated using the EIM model for a 4.0 μm wide KTP PSW in Chapter 4.

At this point, it is helpful to point out that previous workers[70,87,96,111] have not reported either measured or calculated fundamental wavelength spot sizes used in reports of characterization of KTP PSWs. Therefore, comparisons of device efficiencies must include measurement of the power carried by the transmitted fundamental and SH guided modes.

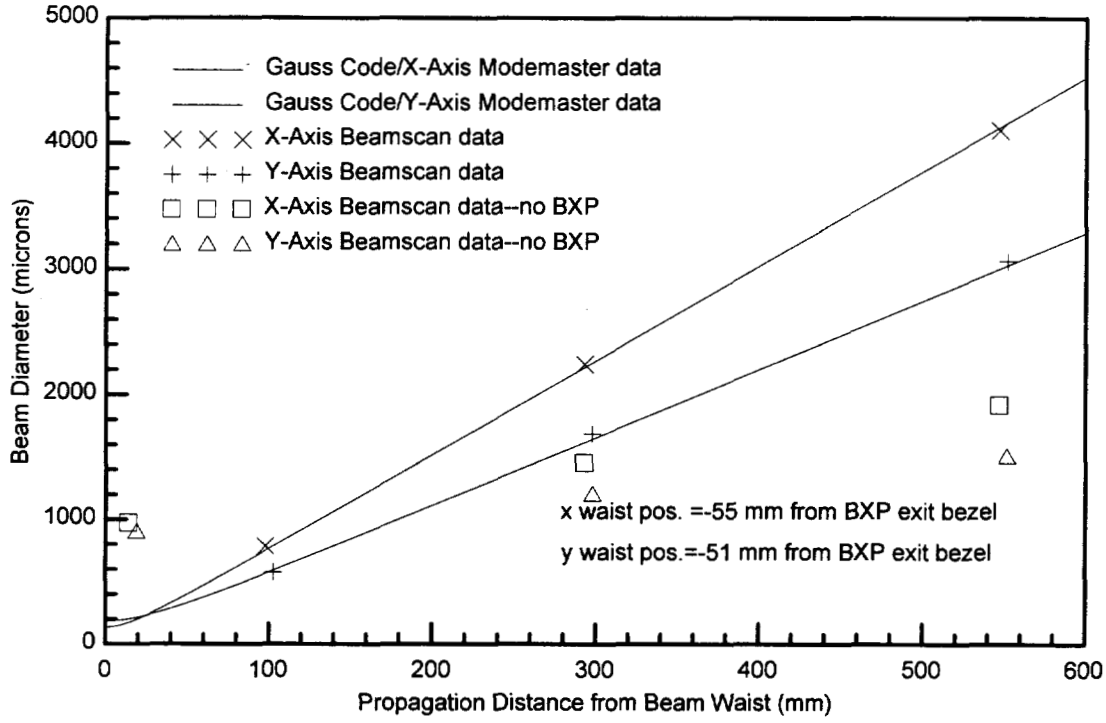

Figure 6.5 Near-field expanded Ti:Sapphire bam diameter vs. propagation distance

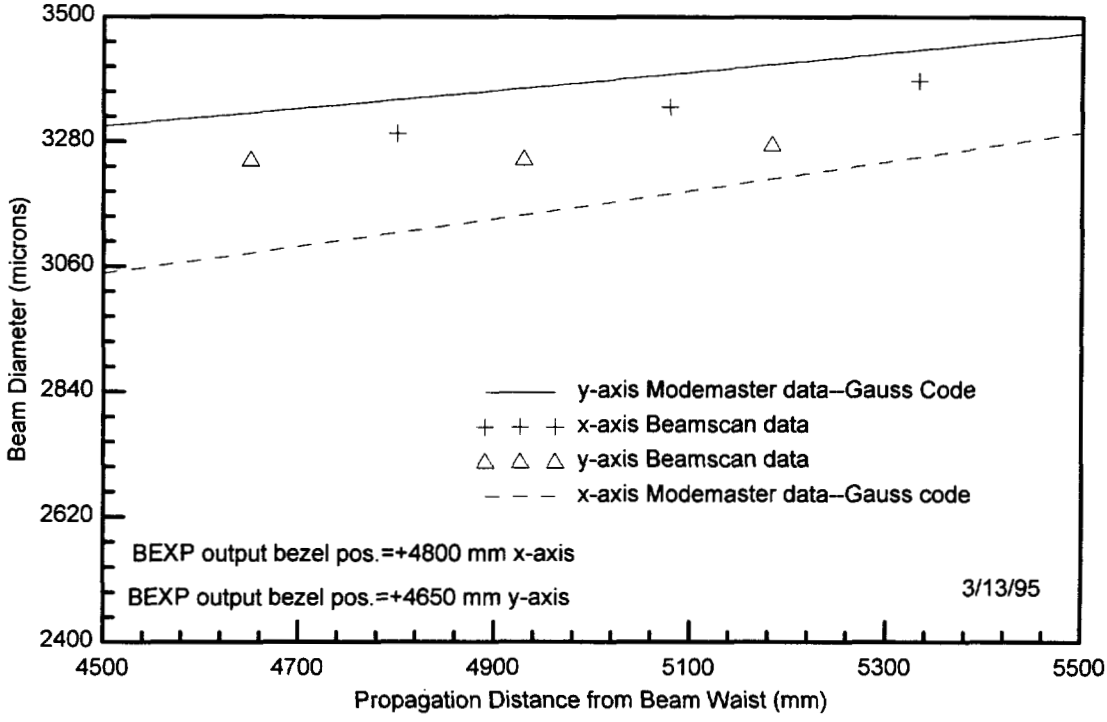

Figure 6.6 Far-field expanded Ti:Sapphire beam diameter vs. propagation distance

6.2 Near Ultraviolet Spectral Characterization of Hydrothermal KTP Waveguides

KTP PSWs fabricated on hydrothermal KTP substrates grown by Litton Airtron were prepared by Du Pont. A mask for photolithographically defining the waveguides for NUV SH operation was designed by Mark Roelofs of DuPont. These waveguides were prepared specifically to meet the preliminary design requirements for a diode-pumped KTP waveguide laser listed in Table 3.1. This mask contained fourteen different waveguide patterns with twelve of the waveguides having design fundamental wavelengths in the range from 768.5 nm to 776.1 nm; one waveguide was designed to operate at 759.4 nm and one at 799.7 nm. Substantial delays following mask design were encountered due to problems for Du Pont in obtaining single domain hydrothermal wafers from Litton Airtron. Photolithography using the NUV mask was performed by Len Pearson of Du Pont using the nanolithography facility at Cornell University. Upon initial evaluation, Du Pont determined that waveguides fabricated on hydrothermal wafers grown by Litton Airtron's low-temperature growth process yielded significantly better performance at short wavelengths compared to waveguides fabricated using wafers grown with a higher-temperature growth process.[153]

Table 6.1 lists the waveguide characteristics for the hydrothermal KTP PSWs fabricated by Du Pont and experimentally characterized in this work. After lithography, chips containing 43 patterned waveguides each were ion-exchanged in molten $Rb(Ba)NO_3$ at 320 °C. The Ba concentration was varied between 8% and 13% in the baths used to process different chips.

All waveguides were fabricated with a 4 μm width. The total length of each waveguide was 12 mm. As indicated in Table 6.1, the mask contained six devices with Bragg branches following the SHG branch. For these Bragg devices, the SHG branch length was 9 mm; the Bragg branch length was 3 mm. For the non-Bragg devices, the Bragg branch segment period was selected to be the same as the SH branch segment

period (e.g. guides 6-13 in Table 6.1). Each guide, except guide 13, was processed to include 0.3 μm rhomboids so as to insert a small wedge angle to misdirect any uncontrolled Bragg reflections that otherwise might result in an unintended frequency feedback signal to the fundamental pump source. Both uncoated and AR-coated chips were produced by Du Pont.

For devices containing Bragg branches, temperature tuning of the Bragg reflection wavelength has previously been demonstrated to yield an effective method for providing a feedback signal at the fundamental wavelength.[85,154]

Roelofs and co-workers[11] determined that in Rb/Ba-diffused KTP PSWs temperature tuning provides a mechanism to shift the relative positions of λ_{Bragg} and λ_{QPM} by 0.035 nm/°C for $\lambda_f \sim 850$ nm. In a similar experiment, also for $\lambda_f \sim 850$ nm, Risk determined for hydrothermal KTP PSWs that the temperature tuning rate for λ_{QPM} was 0.068 nm/°C and 0.016 nm/°C for λ_{Bragg}.[154] Figure 6.7 shows the experimental set-up for the SHG characterization of the hydrothermal KTP PSWs reported on here. A tilt plate arrangement was introduced between the Ti:Sapphire laser and variable beam expander to act as a beam pick-off. The tilt plate pick-off directed 4% of the incident Ti:Sapphire output to a collection point where a Coherent 212 silicon diode detector was located to monitor the incident power used in the experiment. Alternatively, a fiber optic coupling module was located at this point to couple the pick-off output into an optical fiber connected to the Advantest TQ8345 for spectral measurements of the Ti:Sapphire laser output during experiments. As discussed in the previous section, a variable beam expander collimates and expands the Ti:Sapphire laser output and presents it to an F1.67, 10 mm fl objective lens with 9.5 mm working distance which focuses the output to a 4.3 μm $1/e^2$ spot size on the input face of the KTP PSW under test. The KTP PSW was mounted atop a Melcor Frigichip TEC, which is temperature controlled by a Light Control Model 325 Temperature Controller. The output from the KTP PSW was collected by a Bausch and Lomb 50X, 0.45 NA lens with a 12.5 mm working distance.

Guide #	Type	Nominal Fund. λ (nm)	Nominal Bragg λ (nm)	SH Λ (μm)	Bragg Λ (μm)
1	Bragg w/ 0.3 μm rhomboids	759.42	760.73	2.580	2.875
2	Bragg w/ 0.3 μm rhomboids	768.56	770.92	2.715	2.915
3	Bragg w/ 0.3 μm rhomboids	769.59	770.92	2.730	2.915
4	Bragg w/ 0.3 μm rhomboids	770.31	770.92	2.740	2.915
5	Bragg w/ 0.3 μm rhomboids	770.98	770.92	2.750	2.915
6	Non-Bragg w/ 0.3 μm rhomboids	768.56	773.17	2.715	2.715
7	Non-Bragg w/ 0.3 μm rhomboids	769.59	777.28	2.730	2.730
8	Non-Bragg w/ 0.3 μm rhomboids	770.31	780.03	2.740	2.740
9	Non-Bragg w/ 0.3 μm rhomboids	770.98	782.76	2.750	2.750
10	Non-Bragg w/ 0.3 μm rhomboids	773.73	765.39	2.790	2.790
11	Non-Bragg w/ 0.3 μm rhomboids	774.44	768.05	2.800	2.800
12	Non-Bragg w/ 0.3 μm rhomboids	775.46	775.46	2.815	2.815
13	Non-Bragg No rhomboids	776.16	776.16	2.825	2.825
14	Bragg w/ 0.3 μm rhomboids	799.66	801.07	3.180	3.250

Table 6.1 Hydrothermal KTP PSW Characteristics

It was found that use of the comparatively long working distances of both the ESI F1.67 objective lens and the Bausch and Lomb 50X lens, used here as the collimating lens, provided helpful flexibility during positioning to obtain maximum guided mode throughput. An Oriel Band Pass Colored Glass filter (Oriel PN 51720) was used to block both the transmitted scattered and guided mode fundamental power during measurements of the transmitted SH guide mode power. Figure 6.8 shows the relative position on each chip of the waveguides listed in Table 6.1.

Initial coupling into the waveguide was typically performed with about 100 mW fundamental output CW power incident on the waveguide. For consistency, the TEC temperature was set to 20.0 °C. The waveguide under test would be positioned to obtain until a clearly defined guided mode as observed in the collimated output. At this point, the waveguide would be finely positioned to obtain a maximum in the transmitted fundamental power observed in the guided mode as measured using a Coherent 212 silicon detector. Once maximum power had been obtained in the fundamental guided mode, the Oriel filter was inserted and the birefringent filter of the Ti:Sapphire laser tuned until SH output could be observed.

Figure 6.9 displays the SHG power vs wavelength for the TM_0 spatial mode observed from chip A-1/Guide C-5, where in this and all other cases discussed the second mode subscript 0 to denote the lowest order lateral mode has been dropped. To obtain the data displayed in this figure, the Ti:Sapphire laser wavelength was stepped while recording the transmitted NUV power using a calibrated Coherent 212 silicon detector. Not represented in the figure, NUV temporal power fluctuations of 10-30% were typically encountered. The values shown in the figure represent the average CW power observed by the Coherent 212 detector. The FWHM $\Delta\lambda_{SH}$ is 0.6, +/- 0.1 Angstroms. The transmitted guided fundamental power was 113 mW, yielding a η_{eff} = 69 %/W-cm^2, +/- 14 %/W-cm^2, where the experimental error is dominated by the observed SH CW power fluctuations.

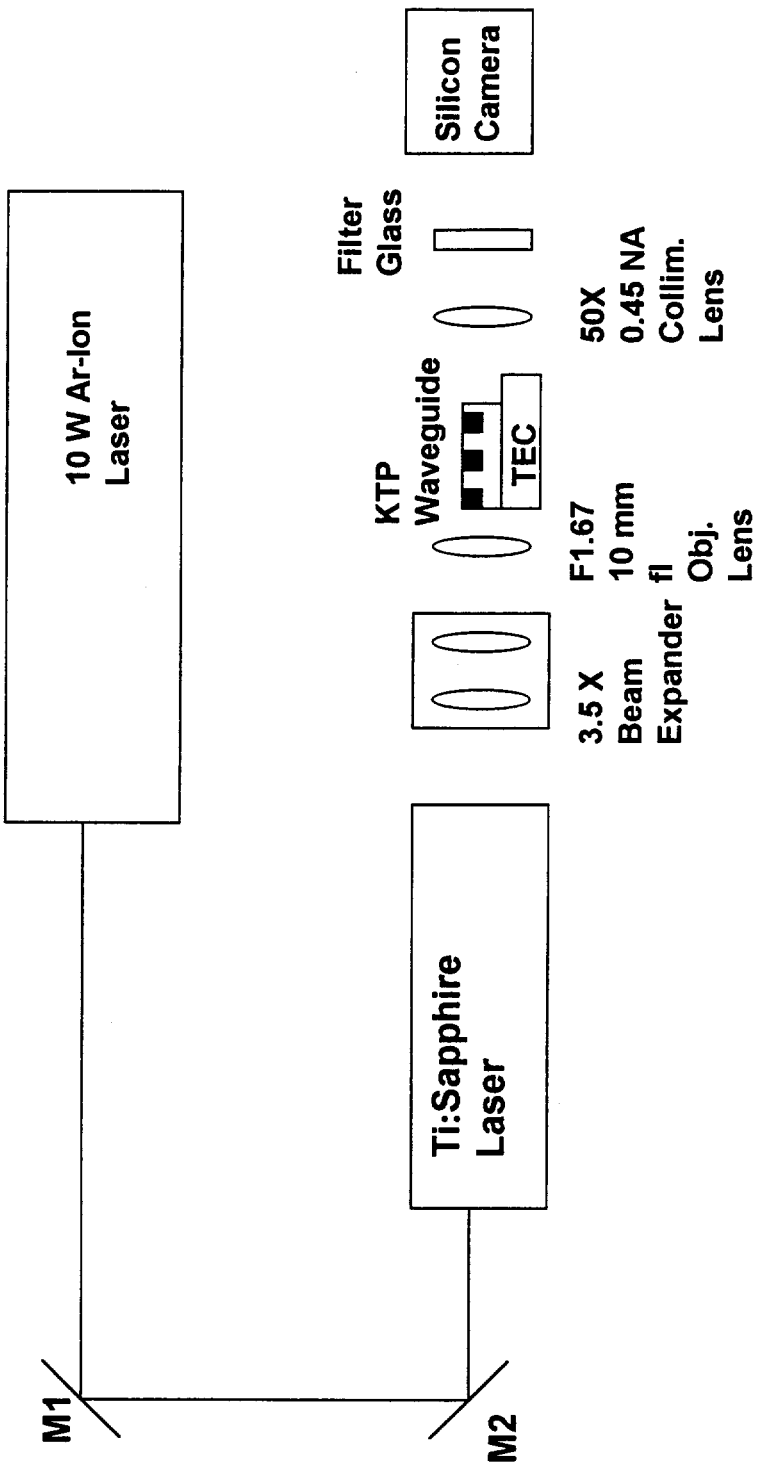

Figure 6.7 Experimental set-up for SHG characterization of KTP PSWs

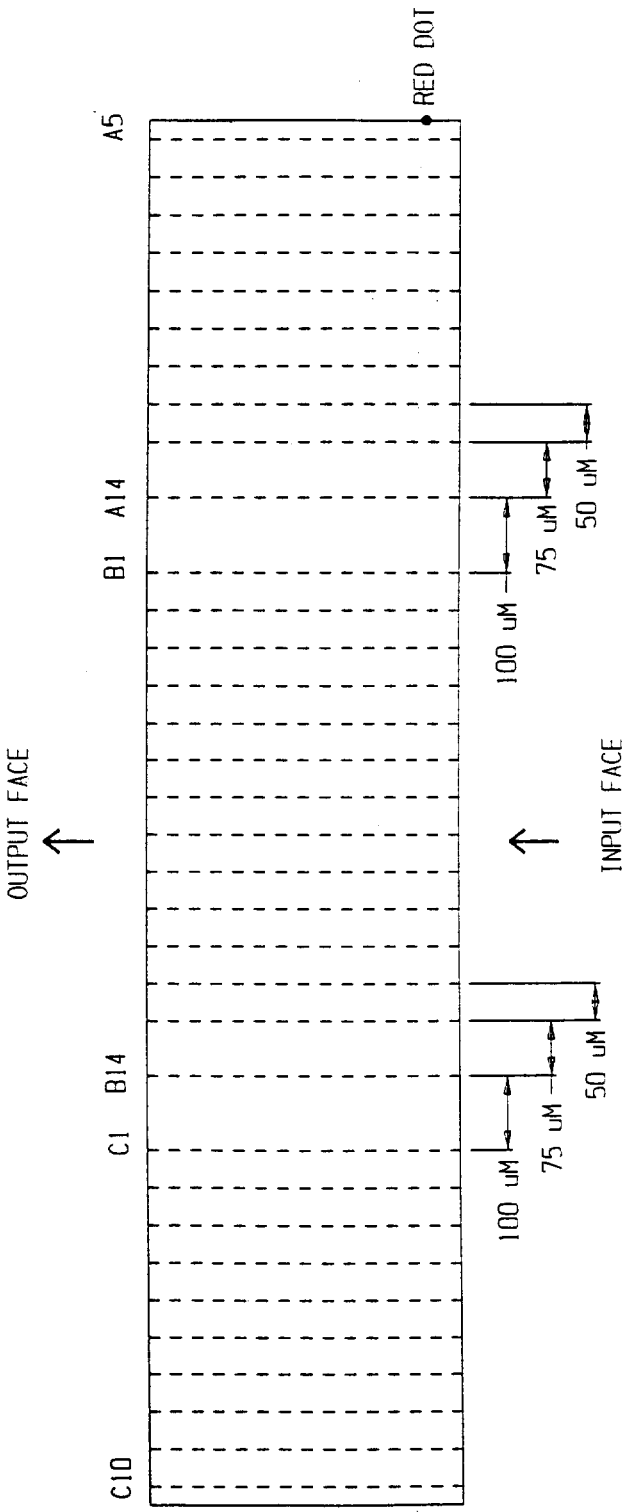

Figure 6.8 Layout of waveguide positions

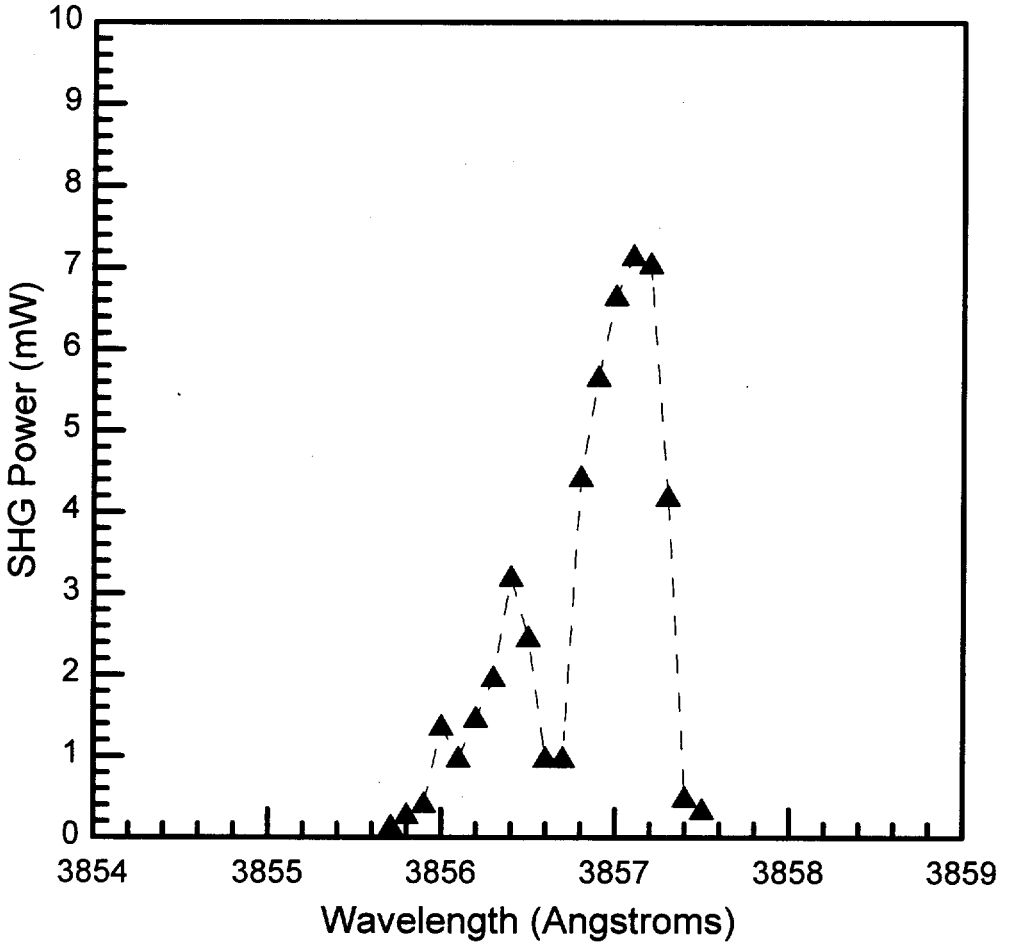

Figure 6.9 SHG Power vs. wavelength: TM_0 (Chip A-1/Guide C-5)

A maximum NUV power of 16.3 mW was produced from the adjacent waveguide C-6 using an input IR power of 580 mW. *This represents the highest NUV output power recorded from a KTP PSW.* The transmitted IR guide mode power was 118 mW. After less than 2 minutes, the NUV power decreased to 5.2 mW. This behavior is consistent with the report by Jongerius et al., discussed in Chapter 3, of optically induced nonuniformities resulting in loss of device efficiency.[90]

The spectral characteristics of the TM_1 spatial mode for the same waveguide are shown in Figure 6.10. The figure indicates the expected blue shift of the higher order

spatial modes with respect to the SH TM_0 spatial mode. The significant reduction in SH power resulting from the significant decrease in the spatial mode overlap between the fundamental TM_0 and SH TM_1 spatial modes. Less well understood is the mechanism or mechanisms responsible for the multiple spectral peaks observed in the SH power spectrum for the TM_1 mode. The FWHM $\Delta\lambda_{SH}$ of the central spectral peak is 0.5, +/- 0.1 Angstroms. The η_{eff} for the TM_1 spatial mode was calculated to be 7.1 %/W-cm^2, +/- 1.4%/W-cm^2.

By continuing to wavelength tune the Ti:Sapphire laser output to shorter wavelengths, the SH TM_2 spatial mode is readily observed. Figure 6.11 displays the SHG power versus wavelength plot for this mode for chip A1/Guide C5. The maximum SH cw power obtained was 0.59 mW at 3843.6 Angstroms. The η_{eff} for the TM_2 spatial mode was calculated to be 5.7%/W-cm^2, +/- 1.1%/W-cm^2.

Interpretation of the power spectrum for the TM_2 spatial mode is difficult, as in the case of the TM_1 spatial mode. Note that the $\Delta\lambda$ between the two peaks in the TM_2 power spectrum is about 0.9 Angstroms. A plausible explanation for the deviation of the observed power spectrum from a sinc^2 functional form is the presence of refractive index inhomogenities resulting from the waveguide processing.[107]

An alternate explanation, which appears more useful in the present case, is the presence of one or more position-dependent steps in the mask period. A single step resulting in a waveguide containing two sections with a relative segmentation shift $\Delta\Lambda$ = .00037 μm could explain the presence of two QPM SH emission peaks separated by 1 Angstrom, assuming a constant Δn=0.134 at λ_f = 770 nm. The relative efficiency of the two peaks, of course, would depend on the length of the section characterized by a given segmentation period. By an extension of this argument, the presence of three distinct peaks, as observed for the TM_1 spatial mode for chip A1/guide C5 could be explained by the presence of three distinct segmentation periods, resulting in a waveguide containing three "guidelets", each with a characteristic segmentation period and QPM relationship. As indicated in Figures 6.10 and 6.11, the higher-order spatial mode power spectrum

display multiple distinct peaks. The higher-order spatial modes occupy larger mode volumes than the TM_0 mode and therefore would be more likely to encounter sections of the waveguide containing additional distinct "guidelets".

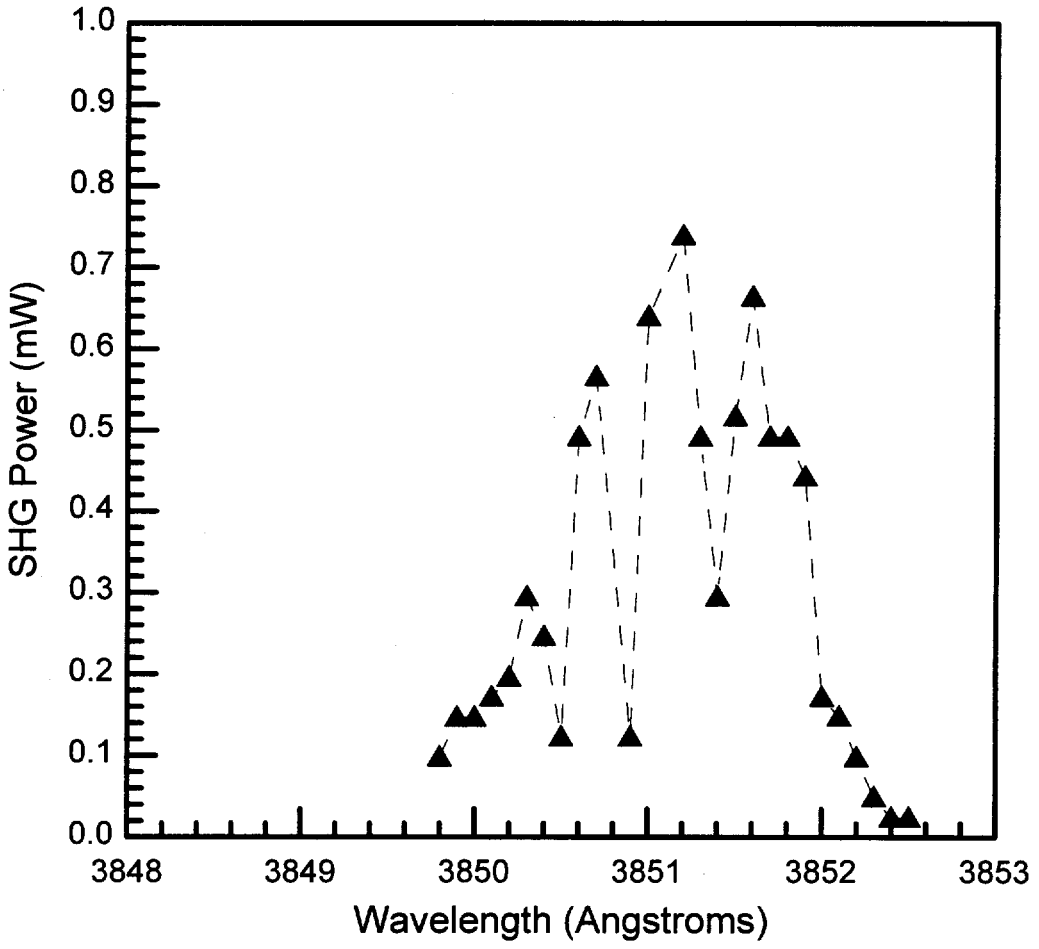

Figure 6.10 SHG power vs. wavelength: TM_1 (Chip A-1/Guide C-5)

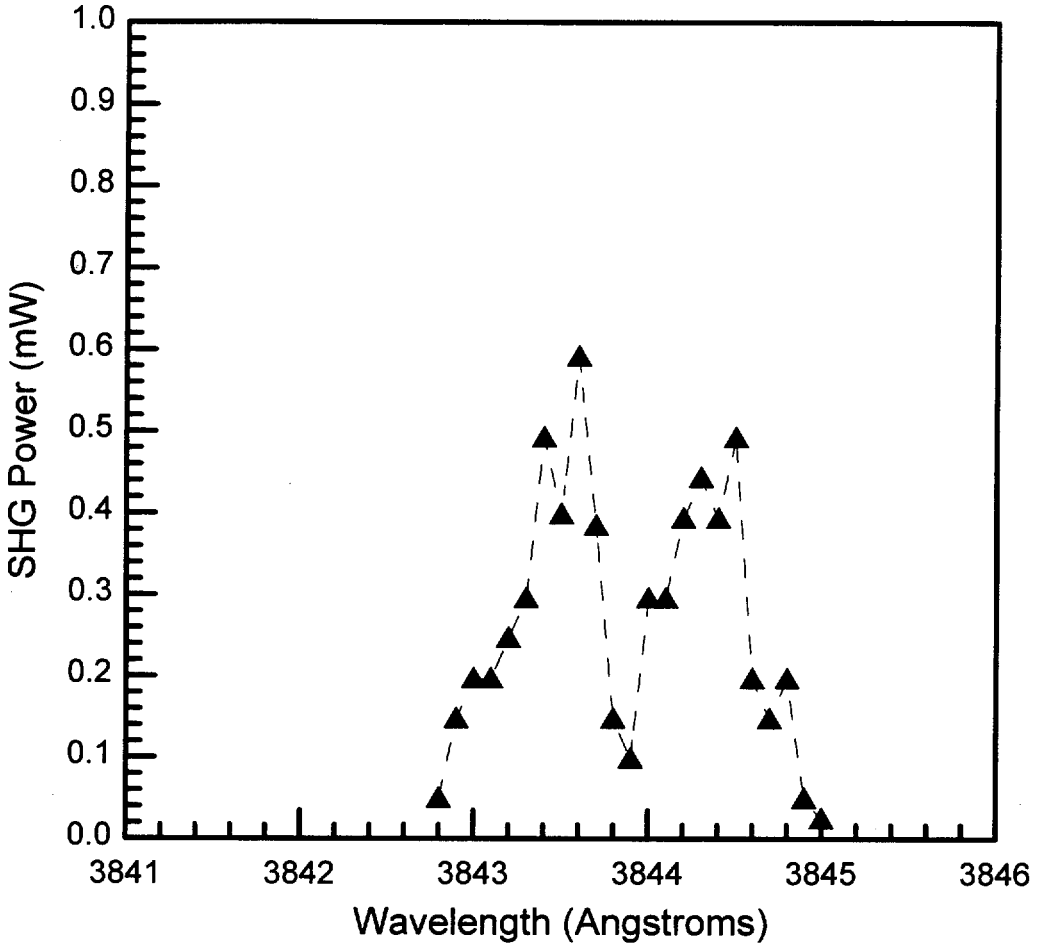

Figure 6.11 SHG power vs. wavelength: TM_2 (Chip A-1/Guide C-5)

While considering that mask process errors resulting in a waveguide being composed of "guidelets" offers a possible explanation for the presence of the multiple SH peaks seen for each spatial mode, other explanations exist and cannot be ruled out. Power dependent photorefractive effects have been observed in other nonlinear waveguide devices.[100] The possibility that a time-dependent photorefractive effect[91] or other optically-induced nonuniformities, such as reported by Jongerius et al.[90], may be involved cannot be eliminated.

The modal SH power spectra from chip A1/guide C5 are summarized in Figure 6.12. This figure clearly shows the blue-shift of the higher order spatial modes with respect to the TM_0 mode characteristic of NUV SH operation in KTP PSWs.

The comparative similarity in the peak SH CW power output of the TM_1 and TM_2 spatial modes can be attributed to the constant Ti:Sapphire laser pump conditions used in the experimental measurement of the power spectra. Note that the Ti:Sapphire laser pump conditions were set-up to obtain maximum output from the TM_0 spatial mode.

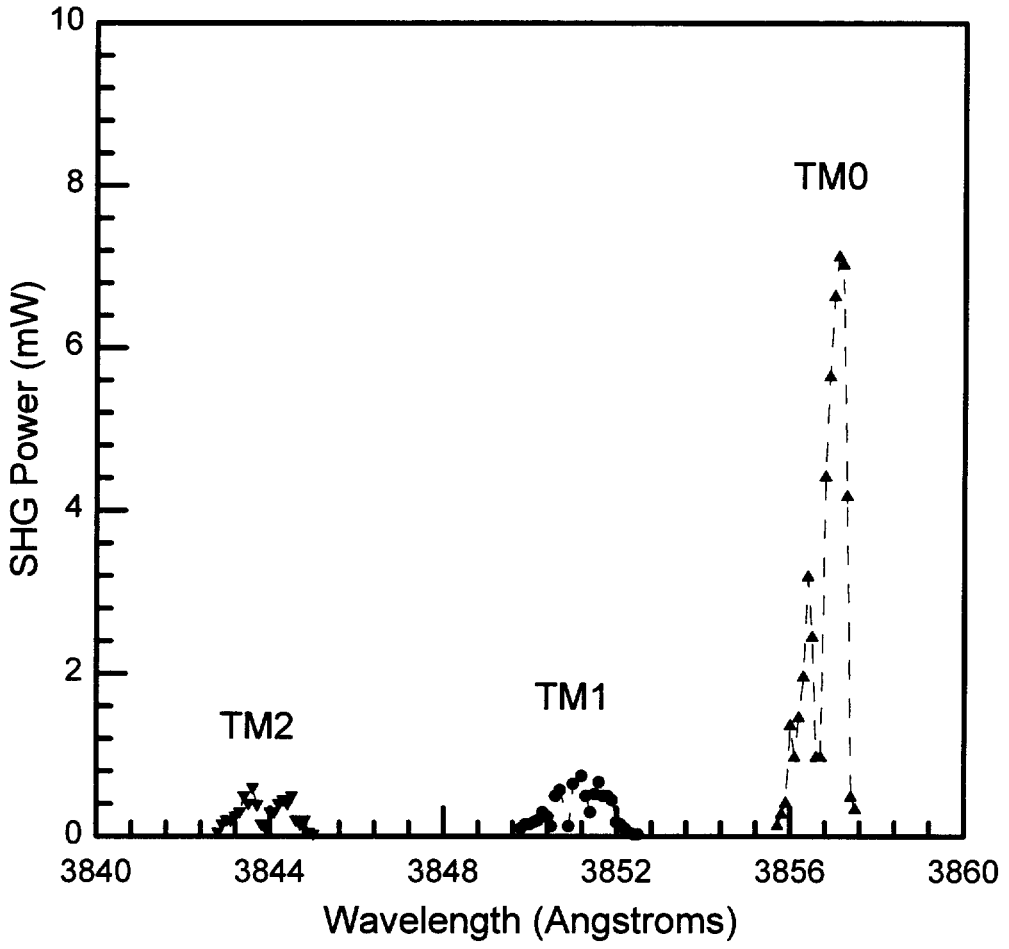

Figure 6.12 Modal SHG power vs. wavelength (Chip A-1/Guide C-5)

Subsequently, the wavelength was tuned to obtain SH output from the higher order spatial modes. Typically, this was obtained when the focused spot from the Ti:Sapphire laser was incident on the uppermost spatial lobe (lobe lying closest to the waveguide/air interface) of the TM_1 and TM_2 modes. As previously discussed in Chapter 4, all guided modes experience their tightest transverse modal confinement nearest to the waveguide/air interface since this is where the transverse index contrast is largest.

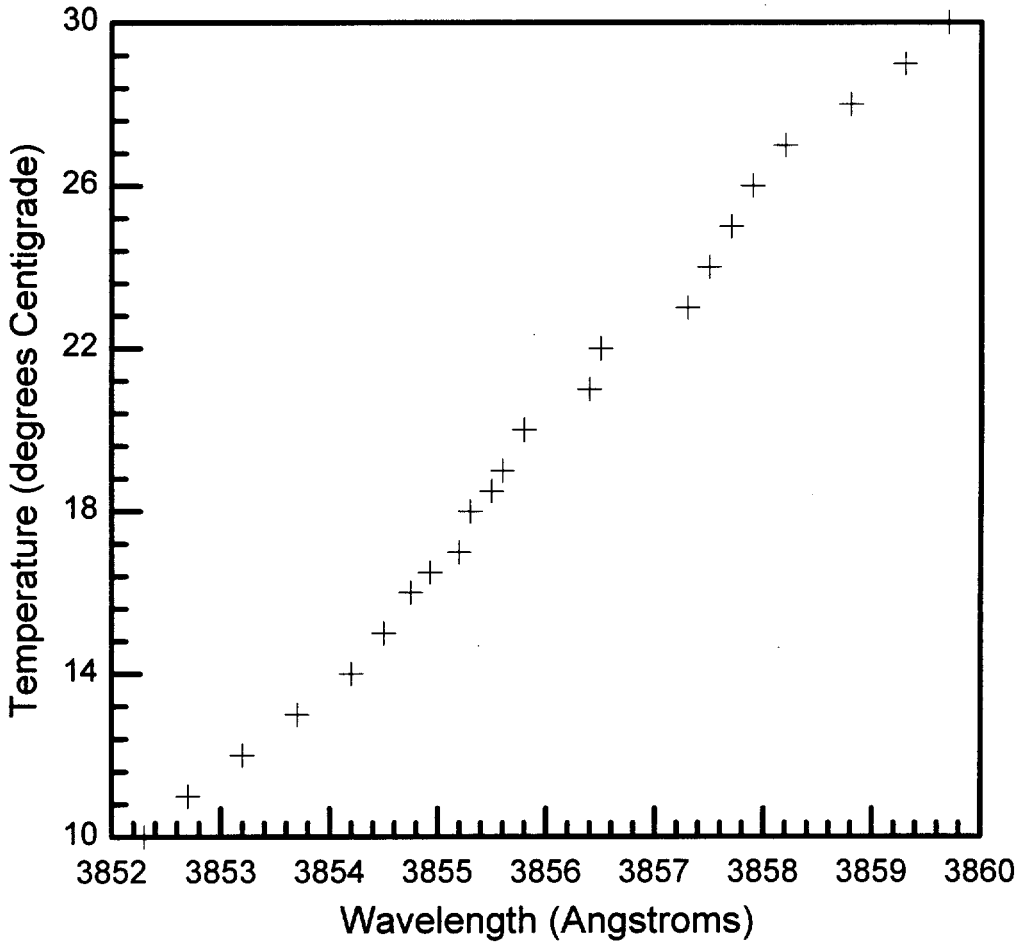

Figure 6.13 SHG wavelength vs. temperature

In anticipation of diode-pumped KTP PSW experiments, the temperature tuning coefficient of peak SH wavelength for the TM_0 spatial mode was measured. The

temperature set point of the Melcor TEC was varied by the Light Control Model 325 Temperature Controller and allowed to stabilize. Once the new temperature had stabilized, the new λ_{QPM} was found by adjusting the birefringent filter position until the SH power was maximized. Figure 6.13 displays the plot of peak SH wavelength vs. temperature for the TM_0 spatial mode. The data gives an average temperature tuning rate of 0.037 nm/°C for the peak SH wavelength. This value is near the 0.044 nm/°C tuning rate reported by Roelofs et al. for flux KTP PSWs for SH wavelengths near 425 nm.[85]

6.3 NUV Spatial Mode Characterization of Hydrothermal KTP Waveguides

In order to further characterize the spatial mode characteristics of hydrothermal KTP PSWs, the SH CW output from various waveguides on chip A1 were imaged using a Sensor Physics Model LS200 Laserscan silicon camera system. A variable ND filter attachment was installed on the camera to allow attenuation of the SH output from the waveguide in order to not saturate the camera.

These are the first experimental images known to the author obtained for the NUV spatial modes from a KTP PSW. The images reveal significant detail concerning the transverse and lateral spatial mode properties and help explain several questions concerning the behavior of the SH output from the higher order spatial modes.

The images shown in Figures 6.14-6.16 display the SH TM_0 spatial mode profiles for guides C9, C12, and C11, respectively. The experimentally observed SH TM_0 spatial modes are distinctive for their strong lateral symmetry and marked transverse asymmetry. In the figures, the waveguide depth axis is displayed in the horizontal axis of the Sensor Physics image. The top of the waveguide is on the image left.

The transverse modal asymmetry is consistent with the results of the effective index method modeling using MODEIG described in Chapter 3. The experimental results clearly display the predicted tight transverse confinement near the air/waveguide interface and display decreasing transverse modal confinement with depth. Also, as predicted, the lateral mode profile is highly symmetric. As seen in Figure 6.14, the lateral

mode profile fits a Gaussian profile to within less than 1%. The experimental measurements shown in this figures clearly confirm the theoretical prediction of non-circular SH TM_0 spatial mode profiles made in Chapter 3.

Figures 6.17 and 6.18 display typical measurements of the higher order SH spatial mode intensity profiles. These measurements revealed that peak CW power is obtained for the higher order SH spatial modes when the pump beam is positioned to overlap the highest lying modal lobe. This observation is readily understood by recognizing that the higher order spatial modes, like the TM_0 mode, also exhibit strongest transverse modal confinement near the air/waveguide interface. By attempting to couple more strongly into the lower lobes by translating the pump beam resulted in significant decreases in the SH CW power. Due to experimental difficulty, it was not possible to obtain intensity profiles resulting from such attempts.

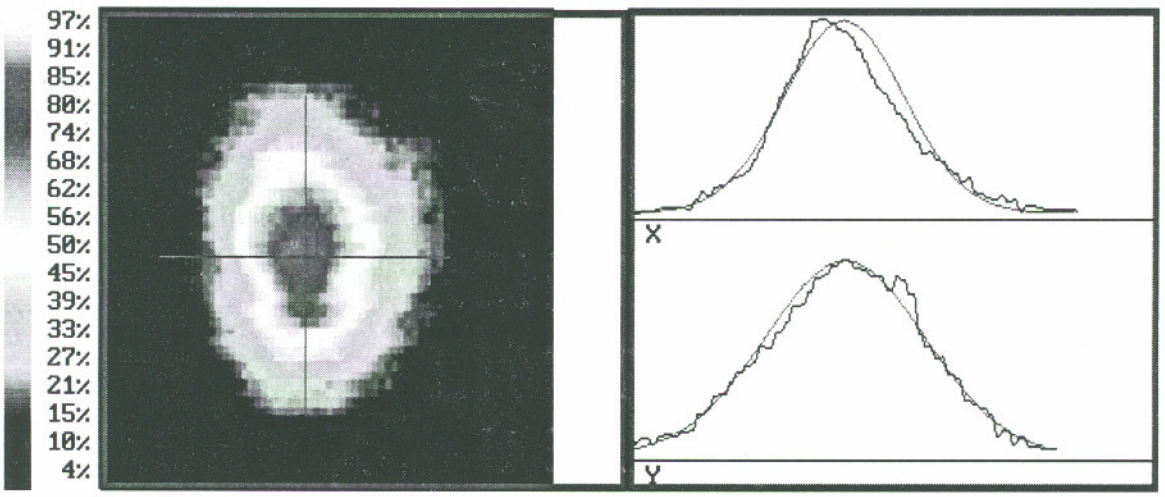

Figure 6.14 SH TM_0 spatial mode profile for Guide C9

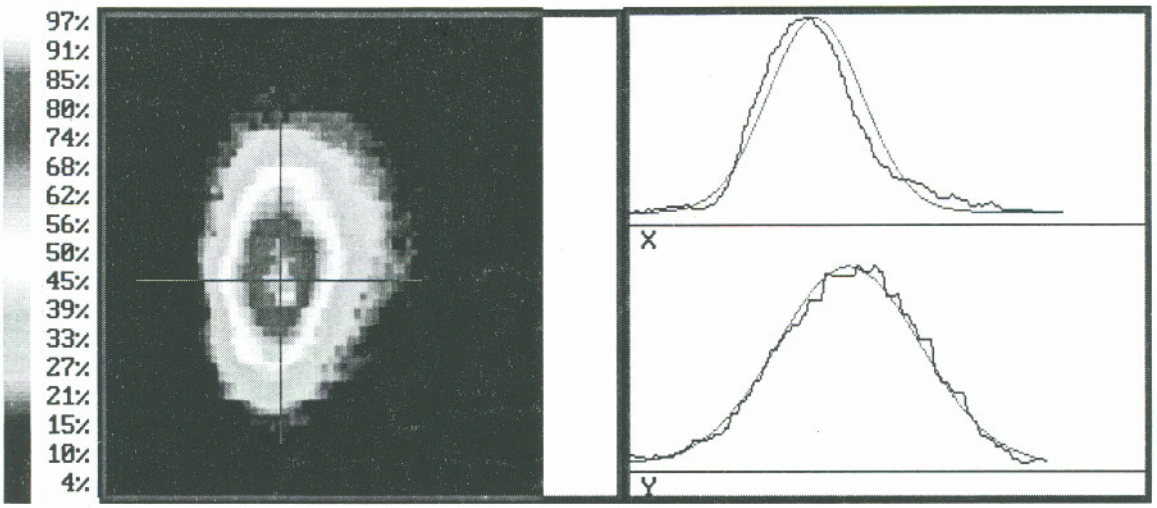

Guide C-12/A1
3876 Angstroms

Figure 6.15 SH TM_0 spatial mode profile for Guide C12

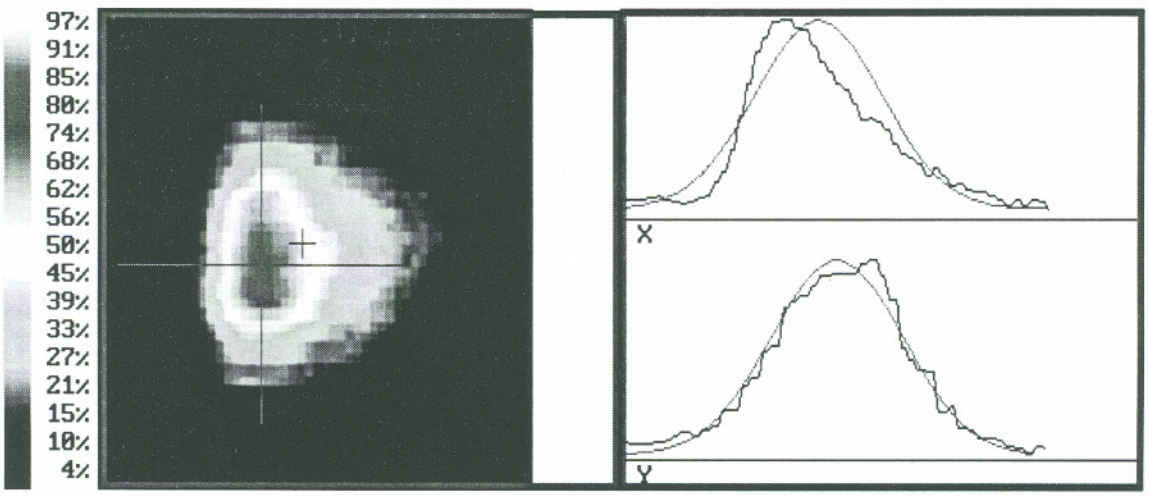

Guide C-11/A1
3871 Angstroms

Figure 6.16 SH TM_0 spatial mode profile for Guide C11

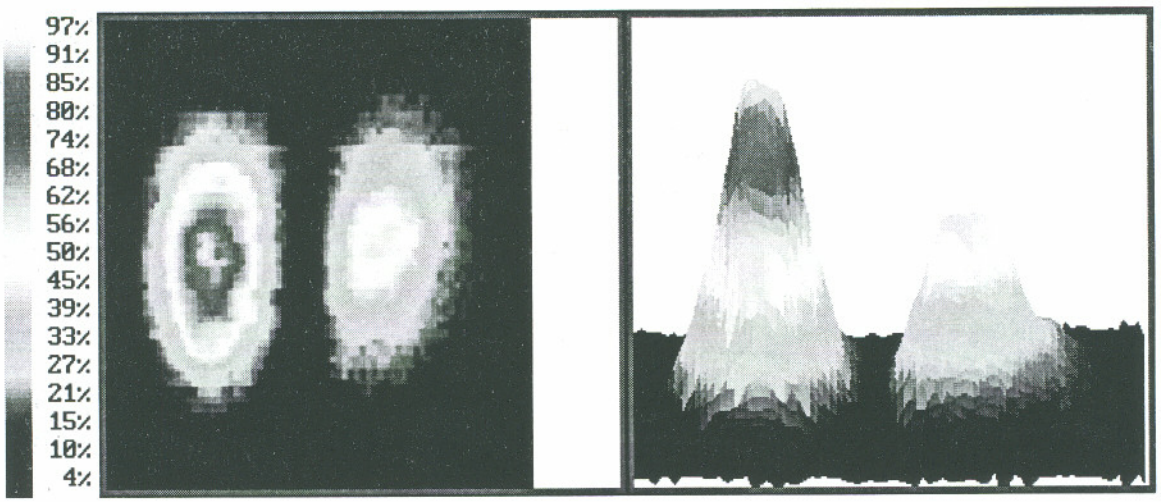

Guide C-10/A1
3870 Angstroms

Figure 6.17 SH TM_1 spatial mode profile for Guide C10

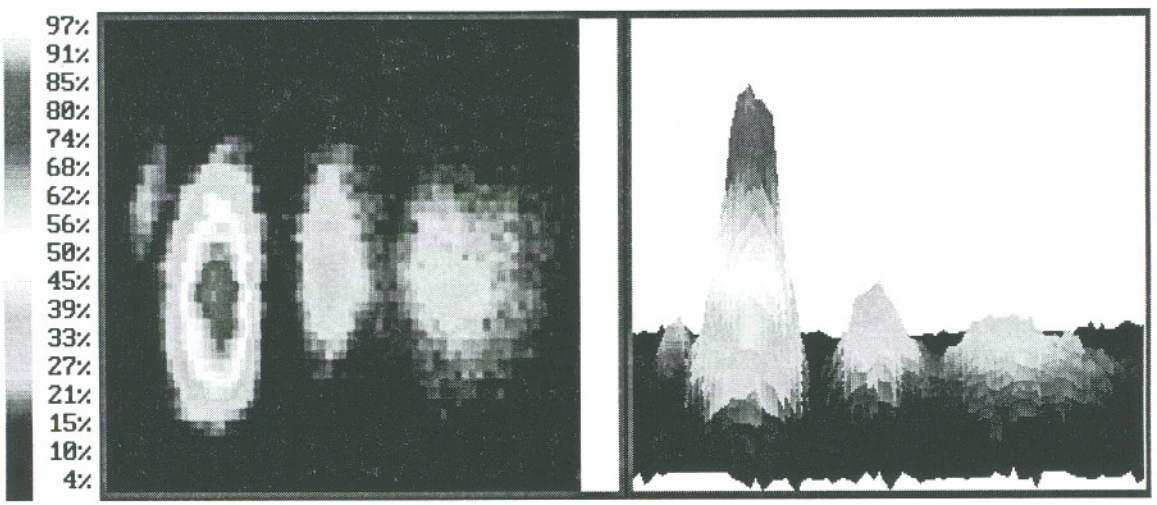

Guide C-11/A1
3842 Angstroms

Figure 6.18 SH TM_2 spatial mode profile for Guide C11

While the experimental set-up was not intended to most efficiently probe the higher order SH spatial modes, it was sufficient to indicate that the limited spatial mode overlap between the fundamental TM_0 and the SH TM_1 and TM_2 modes strongly favors strongest SH emission from the upper lobe.

6.4 Discussion

Under high-power Ti:Sapphire laser pumping, multi-milliwatts of TM_0 NUV SHG was obtained from hydrothermal KTP waveguides. The highest NUV output power was 16.3 mW at 384 nm from chip A-1/Guide C-5. To achieve high NUV output powers, the Gaussian fundamental input was focused to a 4.3 μm, $1/e^2$ spot size at the input face of the KTP PSW. Using this focused spot size, the η_{eff} values for SHG NUV from the TM_0 spatial mode was determined to be 69%/W-cm^2 NUV output power of 7.1 mW, where the fundamental infrared power in the TM_0 guided mode was 106 mW.

The first spatial mode profiles of the NUV TM_0, TM_1, and TM_2 spatial modes of a KTP PSW were obtained. The TM_0 spatial mode profiles are qualitatively in good agreement with the predictions of the EIM model results presented in Chapter 4, which predicted a strongly asymmetric TM_0 spatial mode in the transverse dimension due to the large refractive index contrast seen at the air/waveguide interface. Experimentally, the highest NUV output powers were obtained from all three spatial modes when the fundamental pump beam was focused into the waveguide near the air/waveguide interface. For the TM_1 and TM_2 spatial modes, this resulted in focusing the pump beam into the highest lying (in depth) spatial lobe. In preparation for integration of the URSL-pumped KTP waveguide laser, the Ti:Sapphire laser-pumping experiments established the average temperature tuning dependence of the SHG wavelength as 0.037 nm/°C.

These experiments proved that multi-milliwatt NUV SHG can be obtained from KTP PSWs optically pumped by a single-frequency, high-power fundamental gaussian beam focused to a spot size comparable to the waveguide width. To match or improve upon these results using a high-power semiconductor laser requires it to produce a single-

frequency, spatially coherent output. This was the challenge of the fabrication and testing of the URSLs described in Chapter 7.

CHAPTER 7
FABRICATION AND TESTING OF UNSTABLE RESONATOR SEMICONDUCTOR LASERS

7.1 Introduction

The collaborative research of workers at Oregon Graduate Institute and at the Semiconductor Laser Branch in Phillips Laboratory at Kirtland Air Force Base led to the development of low-magnification half-symmetric URSLs.[114,117-119] The curved mirror facets of these devices were micromachined using a focused ion beam. This micromachining technique was shown through interferometric testing to produce exceptionally smooth mirrors.[119] The high quality of the curved mirrors produced by FIBM are considered to be responsible for the very high brightness values reported by Bao for URSLs made with this technique.[114]

Bao reported on fabrication of GRINSCH SQW URSLs in the GaInP/AlGaInP, GaAs/AlGaAs, and InGaAs/GaAs material systems.[114] Brightness values exceeding 200 MW/cm^2-sr were obtained from devices in each of these material systems. Of particular interest to the present work, Bao obtained a brightness of 431 MW/cm^2-sr from an GaAs/AlGaAs GRINSCH triple QW stack emitting near 840 nm when operated in pulsed mode. The maximum power reported for this device was 2.0 W. Also, Bao was able to obtain a brightness of 92 MW/cm^2-sr from an InGaAs/GaAs GRINSCH-SQW URSL emitting near 970 nm with a maximum CW power of 1.20 W. These encouraging results indicated the feasibility of development of a 0.5 W GaAs/AlGaAs GRINSCH SQW half-symmetric URSL with high brightness using the FIBM techniques extensively developed at Oregon Graduate Institute, and later at Linfield Research Institute, to form the curved mirrors.

Significantly, the coupled CW power and emission wavelength requirements for an URSL-pumped KTP waveguide laser approaches the material limits for the diode lasers fabricated using the GaAs/AlGaAs alloy material system. Kressel and Hawrylo found that the room temperature threshold current density for DH GaAlAs diode lasers begins to rise significantly for Al fractions > 0.17, corresponding to emission wavelengths shorter than 770 nm.[155] Interestingly, a survey of high-power broad area AlGaAs diode lasers available from Sony and Spectra Diode Labs found that the shortest wavelength available was 780 nm for a 0.5 W CW output power-rated device.[5,105]

The lack of extensive growth experience with AlGaAs for high-power CW operation near 770 nm represented a major challenge for the development of a compact ultraviolet laser. Equally as challenging, tested device designs for a single-longitudinal frequency, high-power URSL were not available.

To meet these challenges, a design for a single-frequency SQW-GRINSCH AlGaAs/GaAs URSL capable of producing 0.5 W CW output at 770 nm suitable as a diode pump source for KTP waveguides was prepared by a research team led by Professor Gary Evans of Southern Methodist University and Professor Richard DeFreez of Oregon Graduate Institute. The resulting epitaxial design was provided to Epitaxial Products and Spire Corporation. Each company, over the course of several months, delivered multiple wafers using the design epitaxy specifications. These wafers were subsequently processed by Mr. Jay Kirk of Southern Methodist University using four mask levels to complete the wafer-level URSL fabrication tasks. During the course of the wafer-level URSL fabrication tasks, samples of processed wafer sections were evaluated by Prof. DeFreez to determine J_{th}, T_0, and lasing wavelength. These design, fabrication, and evaluation efforts succeeded in the production of processed wafer sections with the correct wavelength, J_{th}, and T_o characteristics. These processed wafer sections were then sliced into bar form and prepared for FIBM. All FIBM work was conducted by the author. Following fabrication of the curved mirrors by FIBM, the best material was selected for mirror coating. The mirror coating work was performed by Laser Diode Inc.

The coated bars were subsequently evaluated by the author and the best coated devices identified for packaging, also by Laser Diode Inc., for CW operation. The selected package type is a TO-3 package with integral TEC. Four packaged URSLs were optically characterized in preparation for integration with a KTP PSW to form an URSL-pumped KTP waveguide laser.

7.2 Wafer Structure, Processing, and Evaluation

Wafers fabricated with the laser structure for the 770 nm URSL were obtained from Spire and Epitaxial Products. Devices from the first wafer obtained from Spire were found to exhibit a moderately high J_{th} value (760 A/cm^2) and a low T_0 (38-78 °K).[156] Devices from the first wafer received from Epitaxial Products displayed a very high J_{th} value (2600 A/cm^2) and a high T_0 (162-245 °K).[156] It was determined that the higher than expected values for J_{th} characteristic of devices from both wafers was due to a more highly absorbing GaAs etch stop layer. This etch stop layer had been introduced into the structure as a processing aid when opening the grating channels using an etching step. In addition, this etch stop layer in the Epitaxial Products wafers was positioned more closely to the quantum well layer than in the Spire wafer, resulting in the even higher observed J_{th} value.

Because of the initial poor results, two new wafers were obtained from Spire which did not have etch-stop layers. Devices from these wafers evaluated by Professor DeFreez showed lower J_{th} values (450-600 A/cm^2); but T_0 remained low. T_0 describes the rate of change of lasing threshold of the material with changing device temperature. For AlGaAs material, typical values for T_0 for good material exceed 200 °K for device operation near room temperature. The research team intensively studied the problem of the low T_0 problem observed in the Spire material and concluded that an increase in confinement of electrons in the QW and GRIN regions was required. The SMU members of the team determined that the original 30%-60% AlAs content in the graded region should have been adequate for 770 nm operation for quantum wells 100 Angstroms or

thicker. However, they found that for thin quantum wells (~50 Angstroms or less) or for structures with high losses, such as in the original structure design with an absorbing etch stop layer overlying the top p-clad layer, leakage currents could become significant.[156] In addition, the Spire wafers contained a strained InGaAlAs QW which was considered to be a likely contributing factor to the low T_0 values observed for devices from these wafers.

Based on these evaluations, the research team revised the laser structure by increasing the AlAs content in the graded GRIN region from 30%-60% to 40%-80% and using a transparent etch stop layer. This revised basic epitaxial laser structure for the 770 nm URSL for use as the KTP PSW pump diode is given in Table 7.1. Since Epitaxial Products routinely grows cladding layers with up to 80% AlAs, whereas Spire does not, a wafer with the revised 80-40 GRINSCH structure was obtained from Epitaxial Products. To meet the CW emission wavelength requirement of 770 nm, the quantum well photoluminescence for the 80-40 GRINSCH structure was specified to be between 755 nm and 760 nm. This requirement was derived from experimental data from Epitaxial wafer E9402395-1 which displayed a photoluminescence peak at 777 nm and a laser emission wavelength at 789 nm under pulsed operation.

A schematic illustration of the original wafer pattern and the geometrical structure of a FIBM half-symmetric URSL are shown in Figure 7.1. The 80-40 GRINSCH wafer was fabricated using the metalization patterns shown in Figure 7.2. In addition to the patterns shown, a non-channel tapered pattern was also employed. The dimensions of the fabricated devices are 500 μm x 500 μm. The metalization-defined active region width for the broad area devices is 200 μm. The active area width of the tapered devices varies from 112 μm to 200 μm. The tapered URSL designs are based on suggestions by Bao.[114] DeFreez et al. has shown theoretically that a tapered URSL has higher lateral mode selectivity and that the metalization for an URSL can be patterned such that the electrical pumping of the active region matches the resonator optical spatial mode, thereby reducing J_{th} and increasing total device efficiency.[125] This design does not utilize the

adiabatic modal diffraction technique employed for flared-amplifier master oscillator optical amplifiers (FA-MOPAs).[121,122,157] The small uncoated back facet in the FA-MOPA is near the focal point of the lasing mode, thereby having the undesirable feature of allowing the optical power density to near the catastrophic optical damage limit at this point.

Layer	Material	Mole Fraction (x)	Thicknes s (μm)	$\lvert N_d-N_a \rvert$ (cm^3)	Type	Dopant
Cap	GaAs		0.12	$>1x10^{19}$	p^+	Zn
12	Al(x)Ga(1-x)As	0.1 - 0.8	0.1	$1x10^{18}$	p^+	Zn
11	Al(x)Ga(1-x)As	0.8	1.25	$1.5x10^{18}$	p	Zn
10	Al(x)Ga(1-x)As	0.2 - 0.8	0.008	$1.5x10^{18}$	p	Zn
9	Al(x)Ga(1-x)As	0.2	0.01	$1x10^{18}$	p	Zn
8	Al(x)Ga(1-x)As	0.2 - 0.8	0.008	10^{18}	p	Zn
7	Al(x)Ga(1-x)As	0.8	0.2	$\sim10^{18}$	p	Zn
6-GRIN	Al(x)Ga(1-x)As	0.4 - 0.8	0.12	---	undoped	---
5-QW	GaAlAs	QW	.009-.0011	---	undoped	---
4-GRIN	Al(x)Ga(1-x)As	0.4 - 0.8	0.12	---	undoped	---
3	Al(x)Ga(1-x)As	0.8	1.25	$5x10^{17}$	n	Si
2	Al(x)Ga(1-x)As	0.1 - 0.8	0.1	$3x10^{18}$	n^+	Si
1-Buffer	Al(x)Ga(1-x)As		0.5	$>1x10^{18}$	n^+	Si
Substrat e	GaAs			$\sim5x10^{18}$		

** Indicates SQW layer where composition is adjusted to give required photoluminescence wavelength.

Table 7.1 Epitaxial Laser Structure Specifications for 770 nm URSL

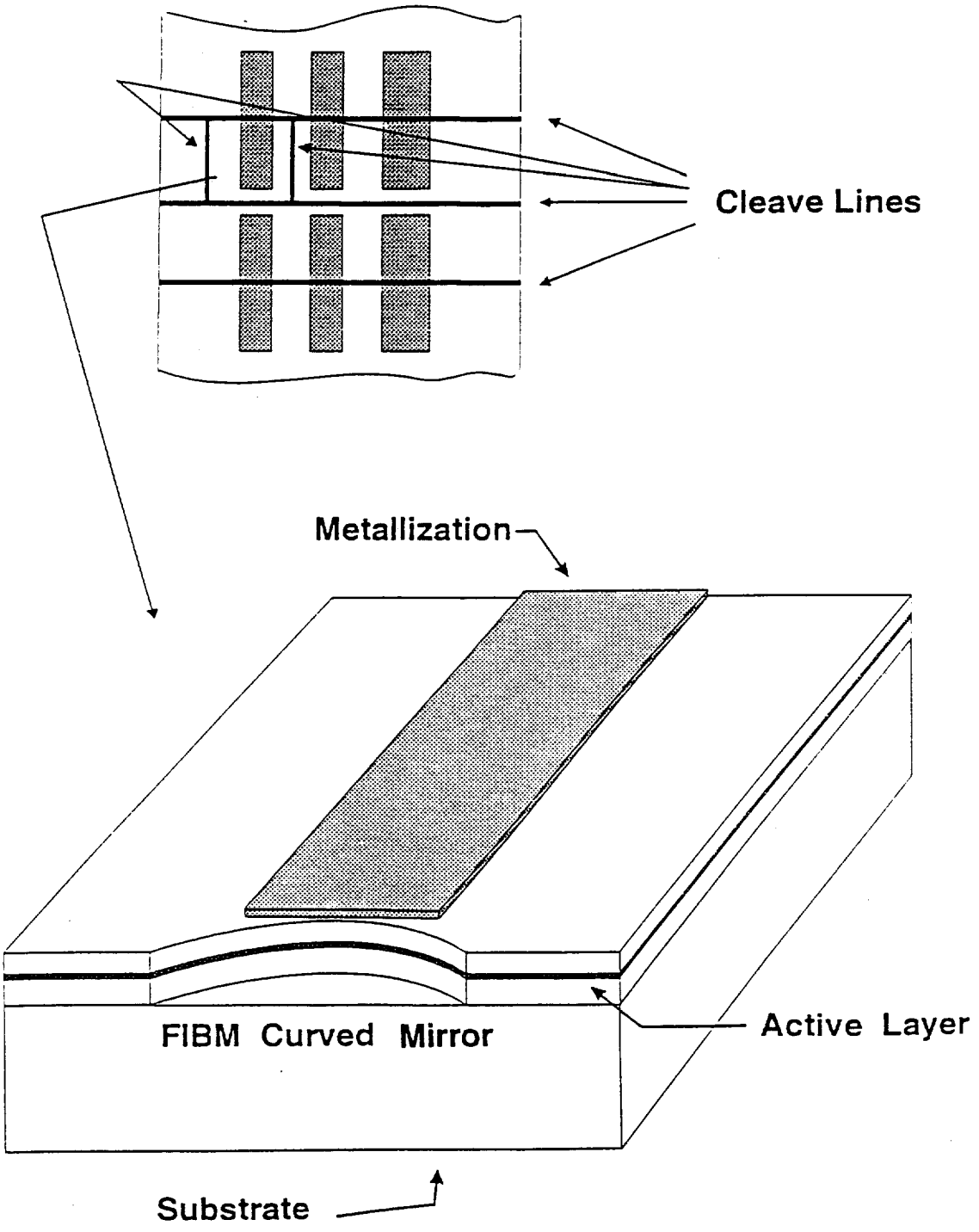

Figure 7.1 Schematic illustration of the original wafer pattern and geometrical structure of a FIBM half-symmetric URSL

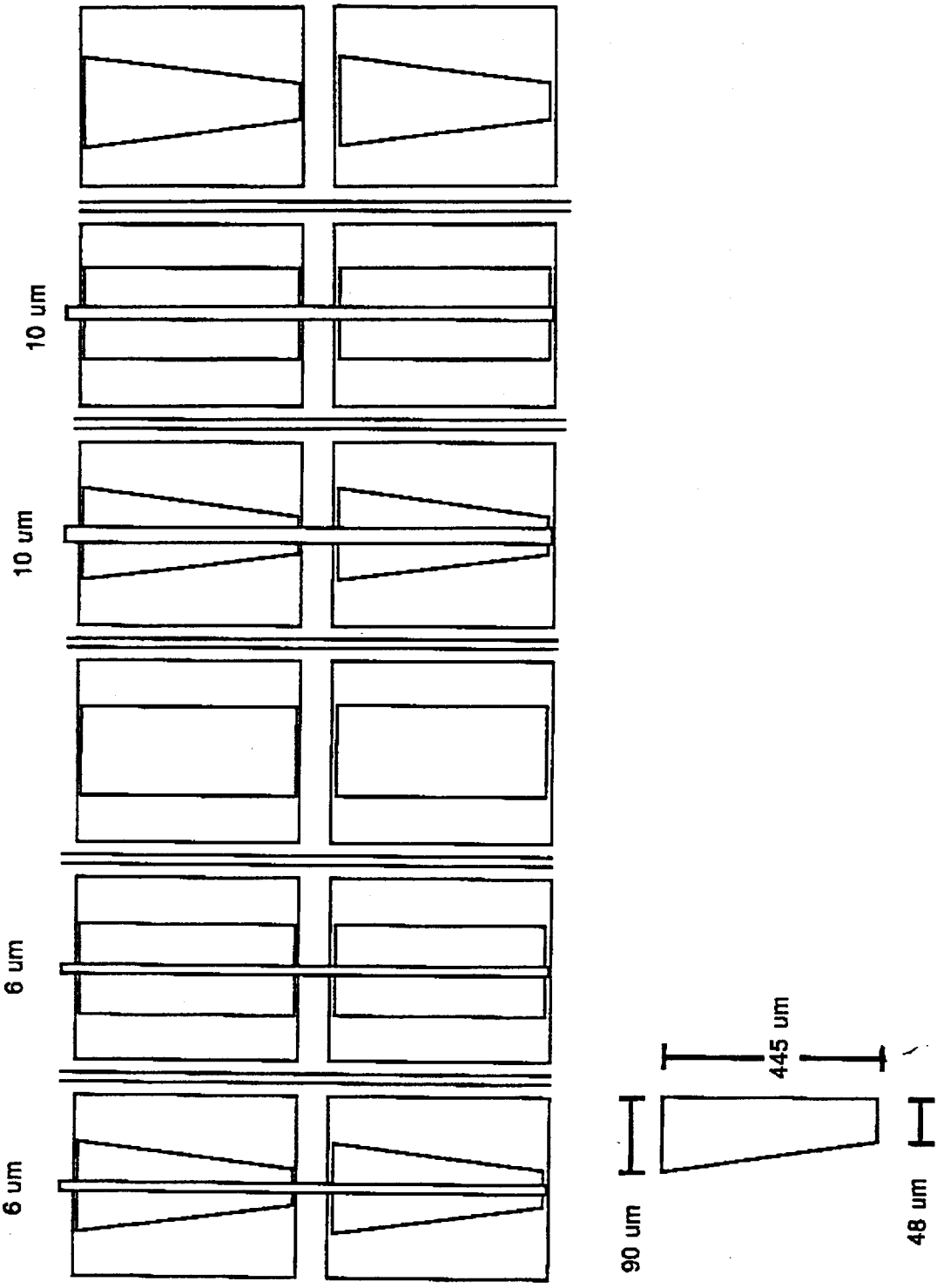

Figure 7.2 Metalization patterns for 770 nm tapered and untapered URSLs

The channels observed in Figure 7.2 for the tapered and broad area metalization patterns are openings in the metalization to allow for deposition of a core grating using a holographic exposure technique. The observation by Bao, DeFreez, and co-workers that the wavelength of the core region of the URSL controls the emission wavelength led to the incorporation of a core grating as the fundamental frequency-selecting element in the present design.[125]

Evaluation of the 80-40 GRINSCH devices under pulsed operation showed good J_{th} values and an acceptable T_0 value of 204 °K. The measured J_{th} was 333 A/cm^2 for a tapered device. A broad area device gave a slightly lower J_{th} value of 320 A/cm^2. The double mirror pulsed output power as a function of pulsed drive current for these two devices are shown in Figures 7.3 and 7.4, respectively. Figure 7.5 shows a plot of $\ln(I_{th})$ vs. temperature for a broad area device. This device had a measured emission wavelength of 764.2 nm at 20 °C and 770.5 nm at 44 °C, yielding a pulsed temperature wavelength tuning rate of 0.26 nm/°C. These spectral measurements indicated that the CW emission wavelength should be within the capability of the TEC to temperature tune the wavelength of a packaged device to 770 nm.

These results indicated that the research team had successfully produced laser structures with the required characteristics for further FIBM processing to fabricate URSLs capable of producing 0.5 W CW output power at 770 nm.

7.3 FIBM Processing of 770 nm URSLs

Fabrication by FIBM of curved mirrors on semiconductor lasers was pioneered by several workers at Oregon Graduate Institute.[114,119,158-164] Development of the techniques used by the author to fabricate curved mirrors on the 80-40 GRINSCH material are based on the methods extensively described by Bao.[114] For a detailed description of these methods, the interested reader is referred to Chapter 4 of the above reference. The discussion that follows is limited to the particular process parameters employed in the FIBM processing of 770 nm URSLs.

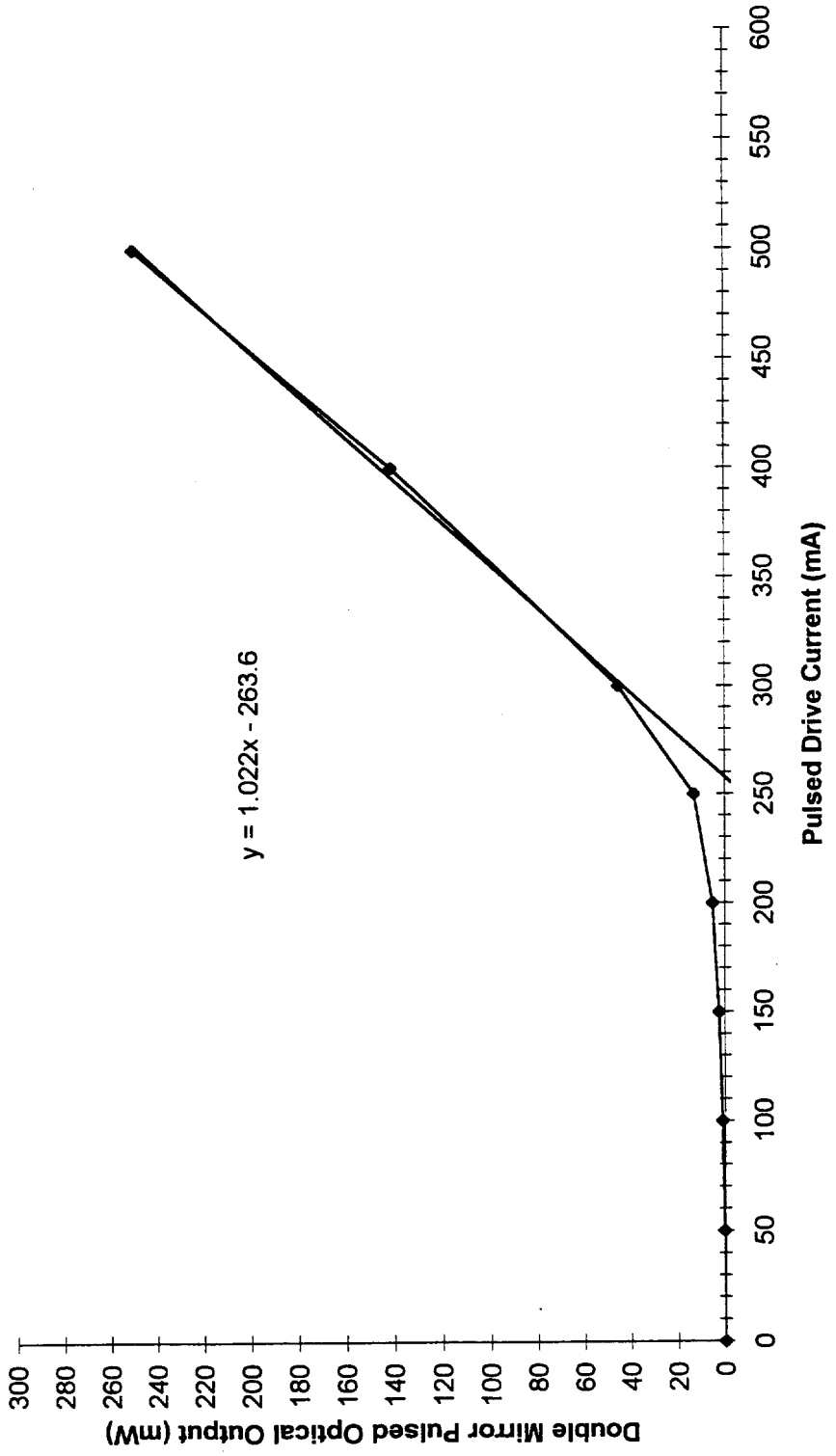

Figure 7.3 Double mirror pulsed output power for tapered device

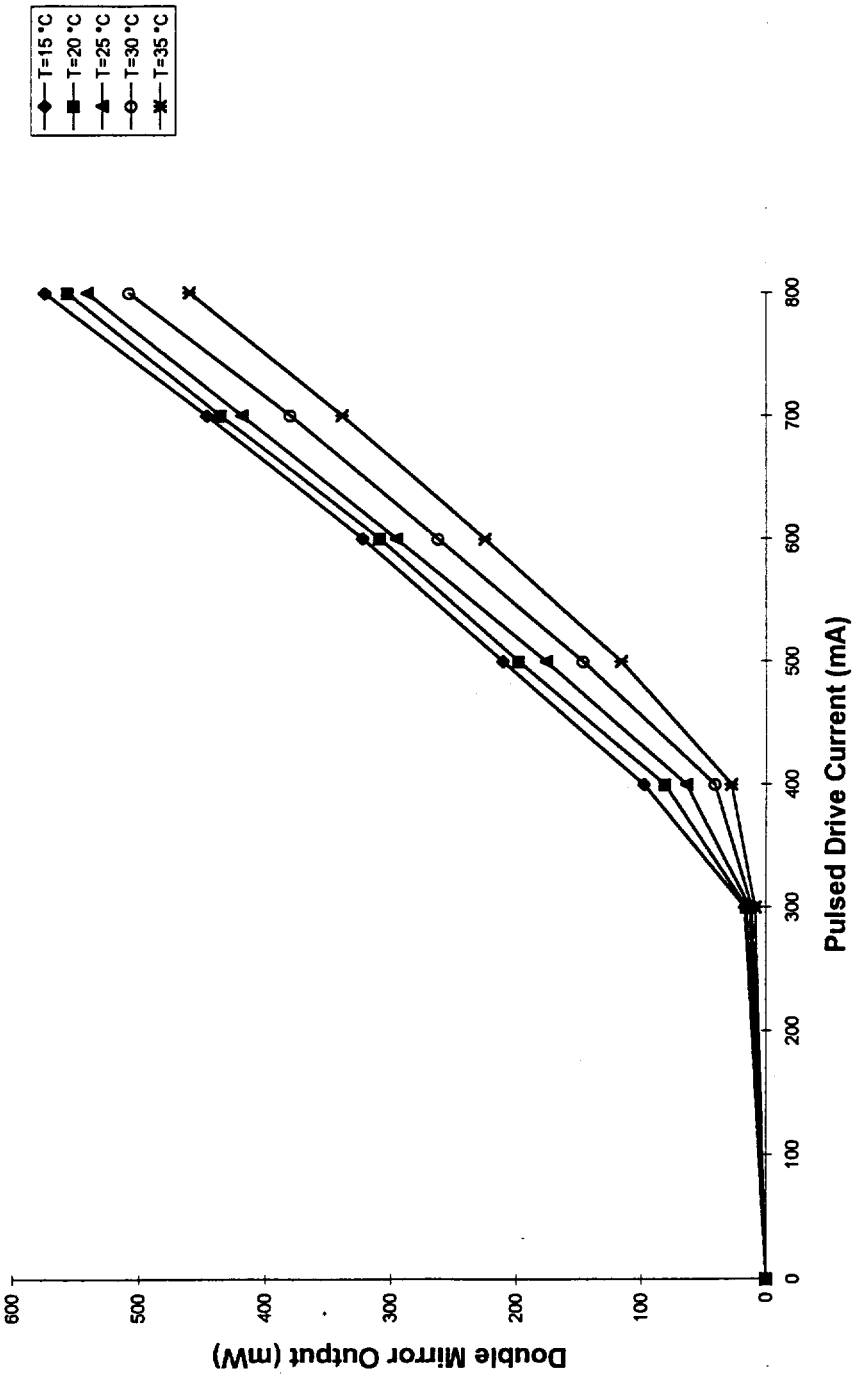

Figure 7.4 Double mirror pulsed output power for non-tapered device

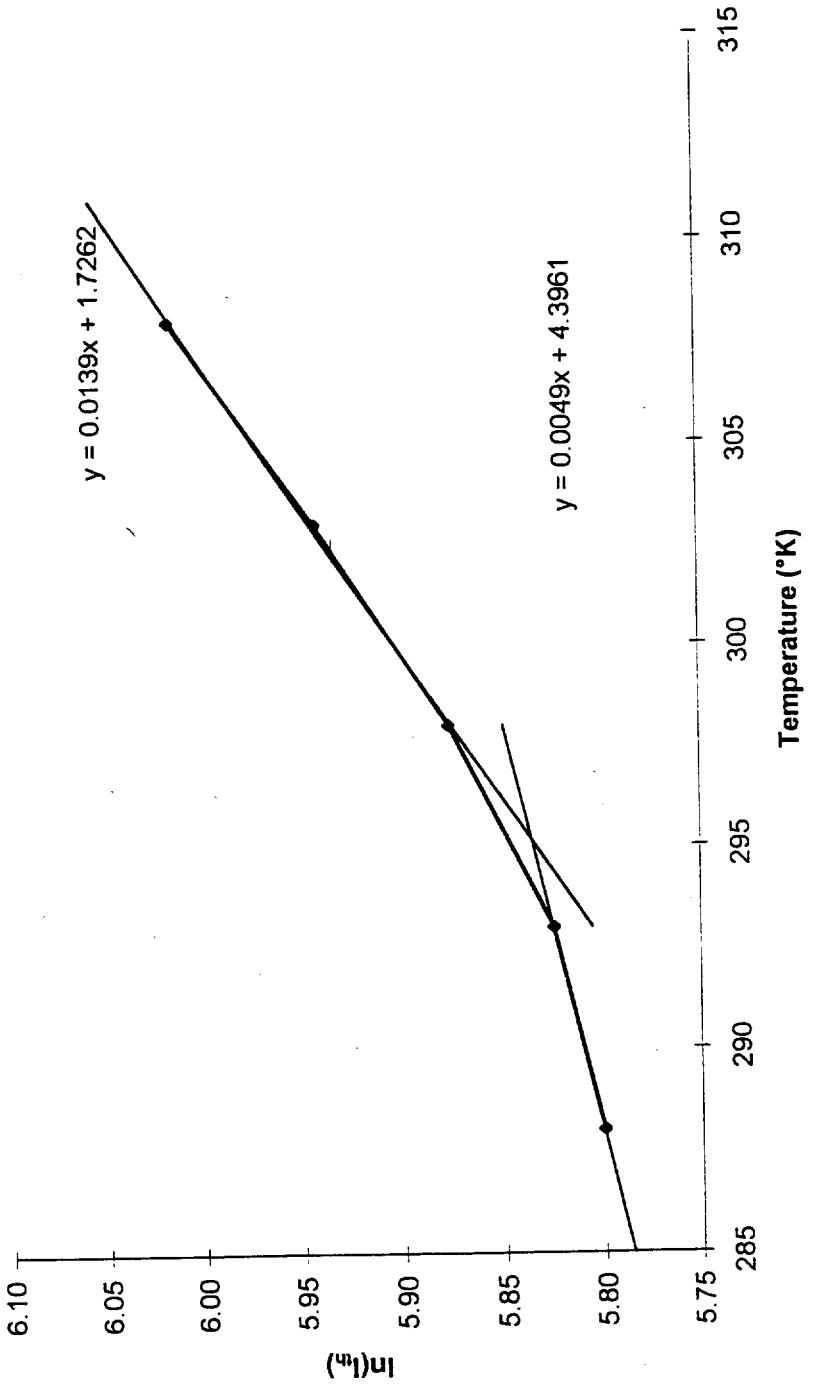

Figure 7.5 $\ln(I_{th})$ vs. temperature for non-tapered device

Bars containing three to ten devices were cleaved from wafer sections of the 80-40 GRINSCH material and mounted using paraffin onto a sample holder. The sample holder was then installed in the sample chamber of the FIBM workstation, which consists of an Amray Model 1830 SEM fitted with an FEI twin-lens FIB gun, ion beam circuitry, and control computer. Detailed information and description of this FIBM workstation can be found in numerous publications[159-165] and dissertation/theses.[158,166-168]

More than fifty devices were micromachined. Devices were micromachined using wafer material which had been processed with and without core gratings. All devices were processed using the FIBM workstation process parameters listed in Table 7.2. The number of processing passes was varied on individual devices between six and fourteen passes. An optimum number of ten to twelve passes for the 80-40 GRINSCH material was subsequently determined through microscopic examination of the quality of the micromachined mirrors.

A microphotograph of a FIBM URSL device fabricated from the 80-40 GRINSCH material is shown in Figure 7.6. The micromachined mirror is clearly visible and symmetric about the channel containing the core grating. An FIBM alignment cross used to determine proper focus for the ion beam is seen to the right of the device.

Ten bars containing a total of thirty micromachined URSLs, representative of wafer material with and without gratings, were selected for coating. These bars were coated by Laser Diode Inc. A standard high reflectivity coating was applied to the curved mirror surface. The non-curved mirror surface received a low reflection coating specified as $R < 3\%$, which was dictated by coating equipment limitations.

Magnification was experimentally determined through SEM measurements of device sag and radius of curvature for four representative devices. These experimental measurements were then numerically fitted using expressions for URSL magnification given by Bao.[114] The measured astigmatism for device I-4 of 310 μm matches to within 1% the calculated astigmatism expected for a device with a magnification of 2.9. The Matchcad file containing these calculations is included in Appendix A.

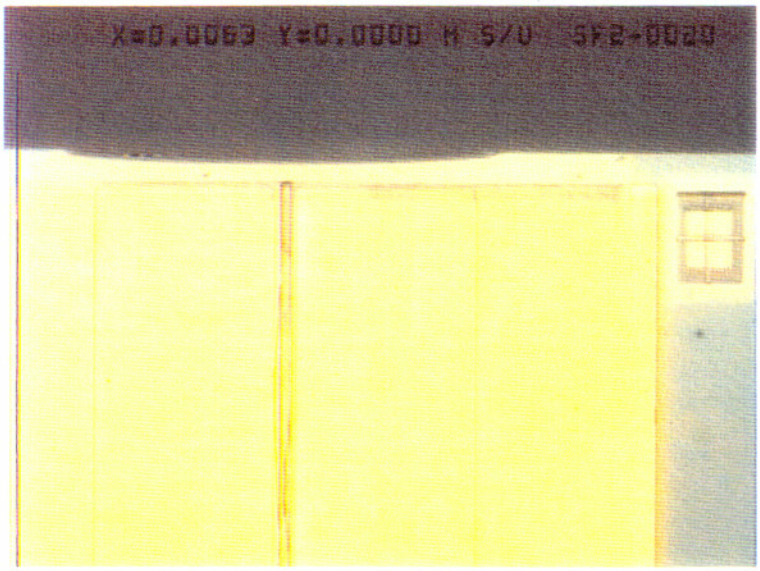

Figure 7.6 Microphotograph of FIBM 80-40 GRINSCH URSL with core grating

Parameter	Value
Magnification	2.9
Radius	1607 μm
Depth	~ 70 μm
Ion beam voltage	25 KeV
Ion beam current	~4000 pA typical
Scan type	Vector
Lines	2000
Off lines	500
Tilt Angle	2°

Table 7.2 FIBM Processing Parameters for 770 nm URSLs

Device	Type
I-2	Tapered URSL without grating
I-3	Tapered URSL with 6 μm grating
I-4	Non-tapered URSL with 6 μm grating
I-5	Non-tapered URSL without grating
I-6	Tapered Fabry-Perot with 10 μm grating

Table 7.3 Summary of packaged device characteristics

During coating, a large number of devices were ruined due to equipment problems. Of the surviving devices, five were assembled into TO-3 packages. Table 7.3 lists the device characteristics of the packaged devices.

7.4 Performance Testing of URSLS

Initial testing of the laser output characteristics of these devices revealed that device I-3 failed to lase and device I-5 was unable to maintain a constant temperature during CW power operation. The L-I curve for one of the remaining two URSLs, I-4, is shown in Figure 7.7.

CW power output from each device was coupled into an Advantest Model TQ8345 optical spectrum analyzer (OSA) to obtain wavelength spectrum measurements. The resolution of the OSA was 0.1 nm. As shown in Figure 7.8, the wavelength spectrum for device I-2 was multi-longitudinal mode. This behavior was evident for all drive current levels above threshold. Since device I-2 did not contain a core grating, its multi-longitudinal mode behavior was anticipated as typical of a broad area AlGaAs diode laser.

The wavelength spectrum for device I-4 at 1.45 A drive current and 250 mW output power is shown in Figure 7.9. The device temperature was tuned to 37.2 ° C to produce an output wavelength of 770 nm. The wavelength spectrum indicates single longitudinal mode operation. Single longitudinal mode operation was observed for all drive current levels ranging from 0.8 A to 1.6 A and for all diode operating temperatures between 12.0 °C and 37.2 °C. At 12.0 °C and 1.6 A drive current, over 400 mW of single-frequency CW output power at 765 nm were produced. These results represent the first demonstration of high power CW output in a single longitudinal mode from a core grating URSL. Importantly for this work, device I-4 produced over 300 mW of CW output power in a single longitudinal mode at 770 nm.

Measurements of the virtual source profiles were performed using the experimental method described by Bao.[114] The apparent virtual source for device I-4 was

measured to be 310 μm behind the output facet. Figure 7.10 displays the lateral spatial intensity profile for I-4 at 1.5 A. These profiles suggest that a reflectivity gradient may exist in the AR coating on the output facet of this device and that this gradient was responsible for the asymmetric lateral intensity profile.

Further measurements of the spatial mode characteristics of device I-4, including measurement of the FWHM virtual source width and calculation of the brightness of this device are presented in the next chapter.

7.5 Discussion

The design, fabrication, and experimental work in this chapter describe the successful first demonstration of single-frequency core grating URSL with high CW output power. This device displayed the critical combination of single-frequency emission and high CW output power required for integration of an URSL with a KTP PSW to form an URSL-pumped KTP waveguide laser.

The 80-40 GRINSCH wafer design demonstrated a J_{th} = 320 A/cm^2 and T_0 > 200 °K. Using this material, in excess of 400 mW single-frequency CW power output at 765 nm was obtained from a core grating non-tapered URSL with a magnification of 2.9. This work demonstrates that low-magnification, single-frequency URSLs can be fabricated at very short wavelengths in the AlGaAs material system and that high CW output power levels can be achieved from these devices.

This work established important empirical relationships between the photoluminescence wavelength and CW laser wavelength for use in future short wavelength AlGaAs SQW GRINSCH device designs. And while results were limited due to the very limited yield of functioning packaged devices, these results were sufficient to validate that a core grating URSL with narrow grating widths (≤ 10 μm) produced by holographic methods are sufficient to produce single-frequency operation in 200 μm wide broad area low-magnification AlGaAs URSLs.

These results indicate significant promise for future development and application of single-frequency, high brightness URSLs and their use in many important applications, including communications, nonlinear waveguide pumping, and spectroscopy.

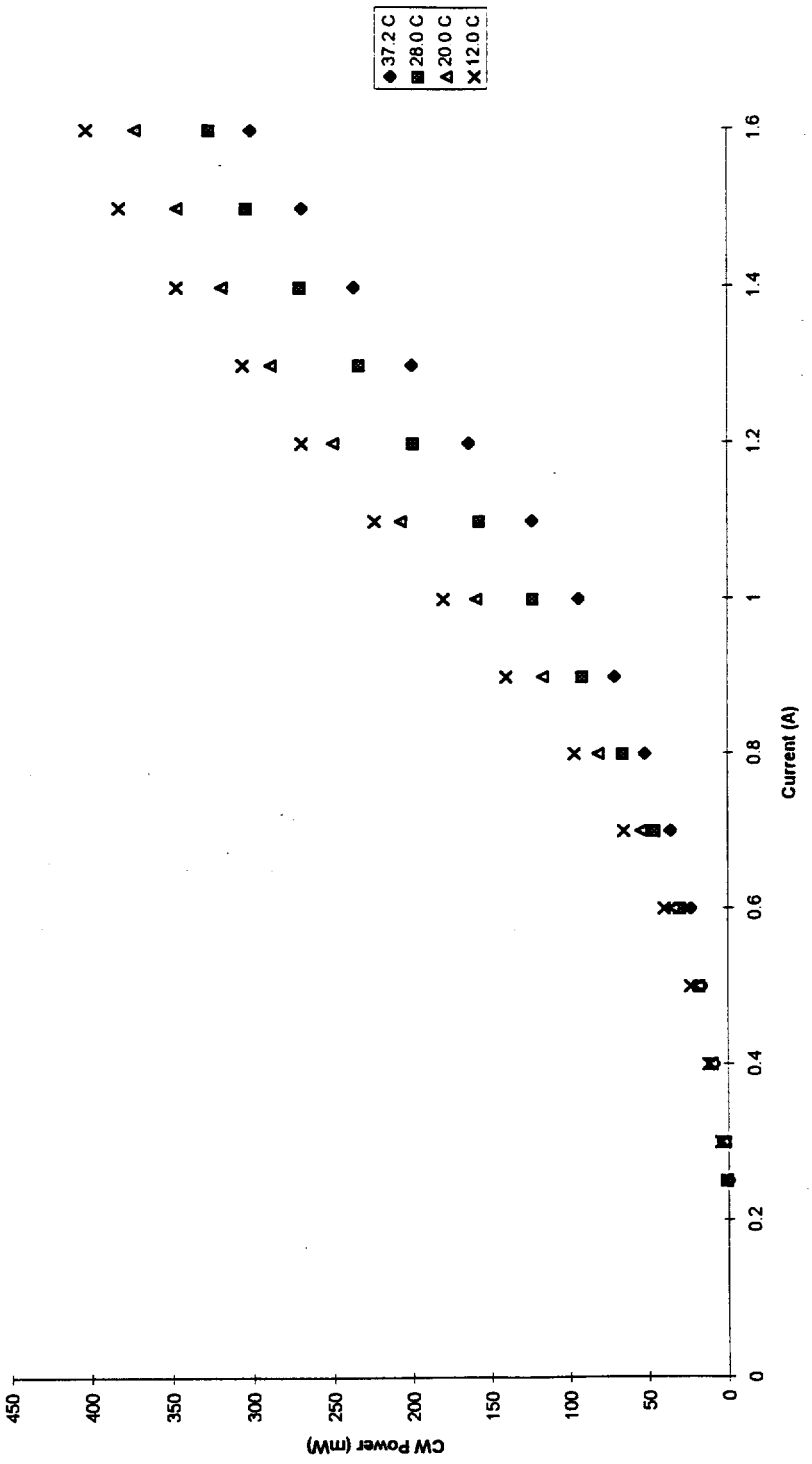

Figure 7.7 L-I curves of URSL device I-4

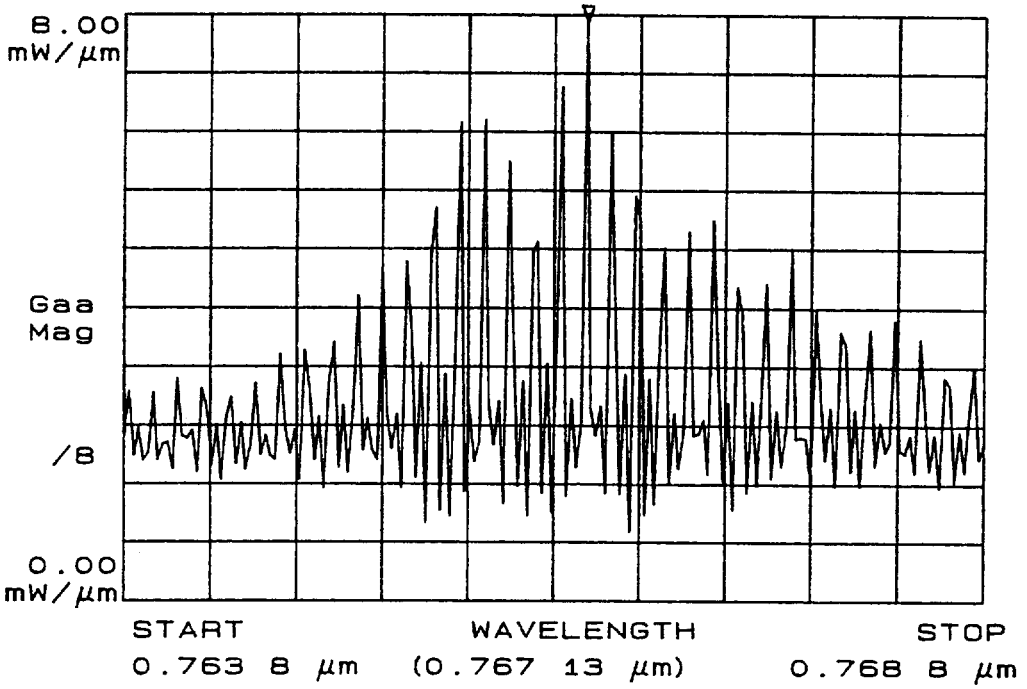

Figure 7.8 Wavelength spectrum for tapered URSL

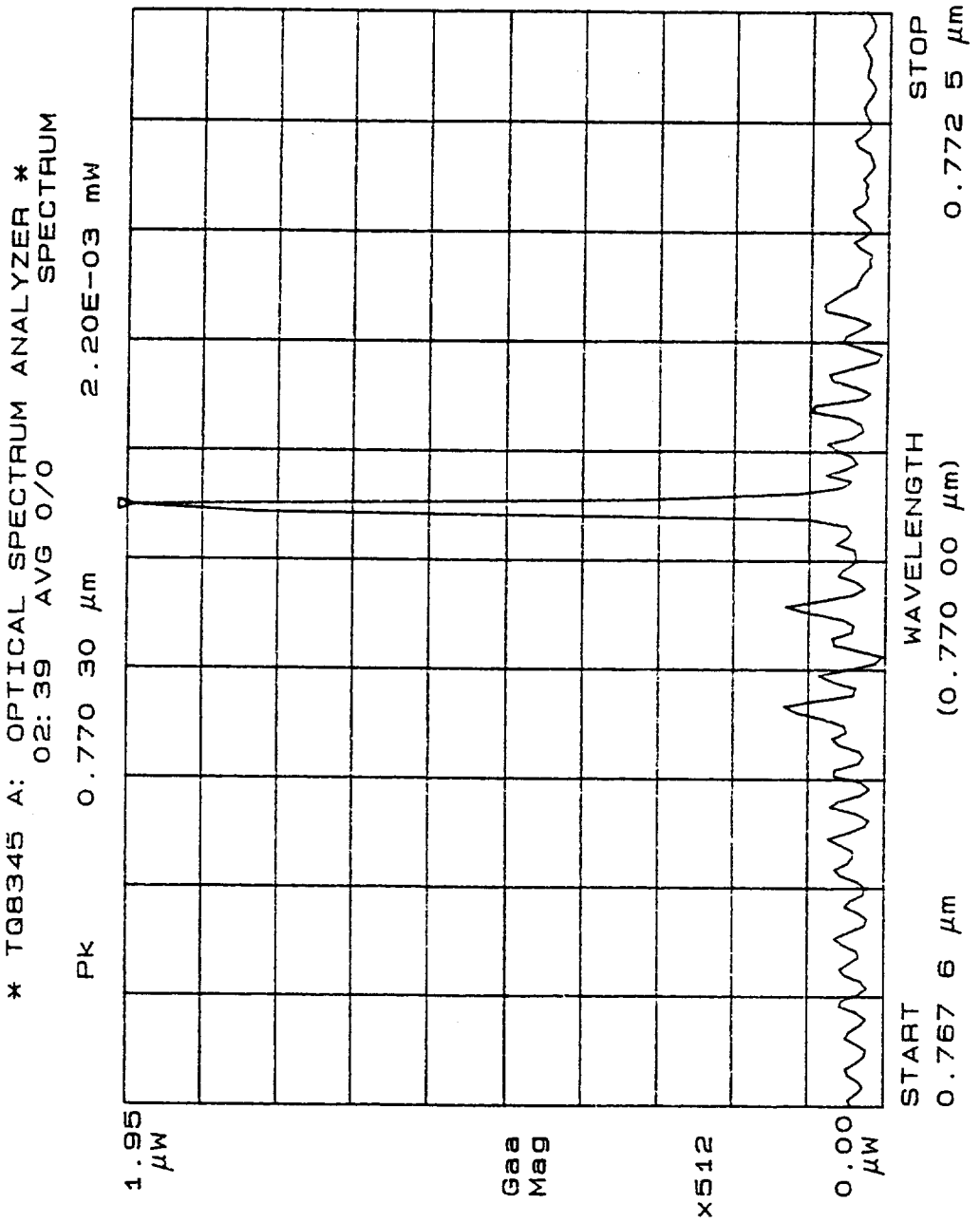

Figure 7.9 Wavelength spectrum for non-tapered core-grating URSL

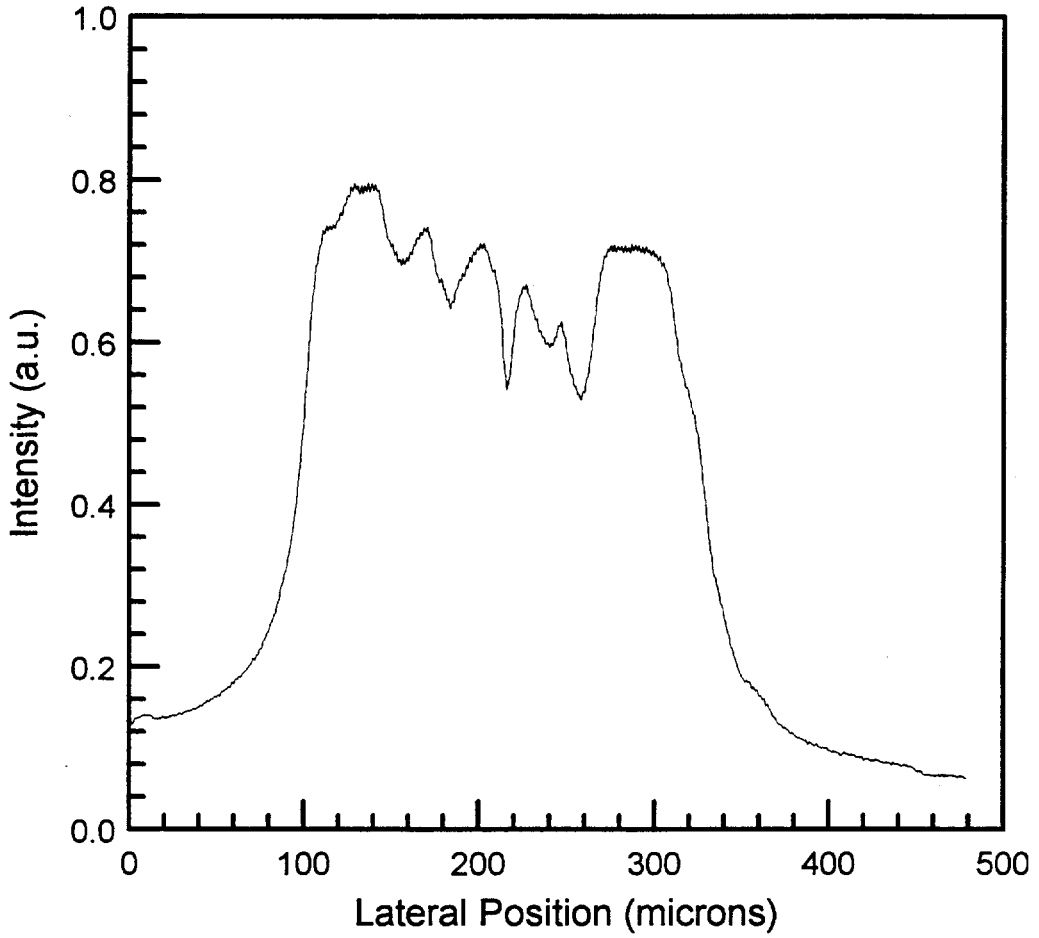

Figure 7.10 Lateral near-field intensity profile for non-tapered core-grating URSL

CHAPTER 8

INTEGRATION AND TESTING OF UNSTABLE RESONATOR SEMICONDUCTOR LASER-PUMPED KTP WAVEGUIDE LASER

8.1 Introduction

The experimental results presented in Chapter 7 for the non-tapered core grating URSL device I-4 demonstrated it produced the required combination of high CW output power from a single longitudinal mode and 770 nm wavelength for pumping KTP PSWs for the purpose of generating NUV SHG. Since previous efforts to produce QPM SHG from diode-pumped KTP waveguides has been limited to the wavelengths greater than 425 nm[18,47], the integration of an URSL-pumped KTP waveguide laser with SHG near 385 nm represents an effort to increase the spectral range of diode-pumped KTP waveguide lasers by 40 nm in addition to the first demonstration of NUV SHG output below 400 nm from a diode-pumped KTP waveguide laser.

As discussed in Chapter 2, most previous efforts at obtaining SHG output from diode-pumped nonlinear waveguide lasers have been limited to using index-guided AlGaAs diode lasers.[18,47,73,80,81,96] These lasers typically exhibit single longitudinal mode and single spatial mode characteristics but are limited to CW output powers of about 200 mW. Optical coupling efficiencies further reduce the available CW power from these lasers to pump nonlinear waveguides.

The narrow QPM spectral bandwidth for NUV SHG measured for hydrothermal KTP waveguides places a severe test on the single longitudinal mode behavior of a core grating URSL. As reported in Chapter 6, the measured QPM spectral bandwidth for 385 nm SHG output is 0.06 nm. Results from MODEIG modeling given in Chapter 4 gave FWHM mode sizes for the respective lateral and transverse dimensions of the

fundamental TM_0 spatial mode of 2.0 μm and 2.4 μm, and 1.8 μm and 2.0 μm for the SH TM_0 spatial mode. The URSL must produce and maintain highly spatially coherent output in order for the diode optics to produce a focused pump beam capable of efficiently coupling the diode output into the guided IR spatial mode. These severe requirements make NUV SHG output from an URSL-pumped KTP waveguide laser a powerful test of the spectral and spatial coherence properties of an URSL.

8.2 URSL-Pumped Waveguide Laser Integration and Testing

To obtain high optical efficiency, the coupling optics employed a 6.5 mm fl, 0.615 NA diode laser collimation lens to collect the output from the URSL. The measured transmission of this first stage in the coupling optics was 68%. This coupling efficiency was largely governed by reflection losses from the eight single-layer MgF_2 coated surfaces of the lens. At normal incidence, at the coating design wavelength of 830 nm, the transmission is specified to exceed 85%. Considering that the incident wavefront from the URSL was non-planar and the emission wavelength was 770 nm, it is expected that the transmission will be reduced from the normal incidence, design wavelength value.

The astigmatism between the lateral virtual and transverse real sources required correction prior to collimation and subsequent focusing of the URSL output into a KTP PSW. The depth of the lateral virtual source behind the transverse real source was determined by imaging the source intensity profiles with a Cohu video camera while translating the URSL. As reported in Chapter 7, the measured astigmatism for device I-4 was 310 μm.

A 150 mm fl cylinder lens was placed 8 mm from the exit surface bezel of the 0.615 NA collection lens to correct for the astigmatism. This position is consistent with correction of astigmatism of approximately 300 μm. The collection lens and cylinder lens were placed on individual five-axis stages for independent positioning. Both of these lens stages were mounted on a stage which allowed the lens pair to be translated as

a unit for collimation purposes once the relative positions had been established to correct for astigmatism.

To establish the correct separation between the collection lens and cylinder lens, the cylinder lens was translated while observing the transverse and lateral intensity profiles using a Beamscan Model 2180-XYLA beam profiler. This instrument utilizes a scanning drum with 25 μm slits and a silicon detector. It provides simultaneous measurement of two orthogonal measurement axes. These instrument measurement axes were aligned to the lateral and transverse output from the URSL. Figure 8.1 displays the simultaneously measured Beamscan lateral and transverse source intensity profiles for device I-4 operating at 37.2 °C and 1.6 A after the cylinder lens had been positioned for best correction of the astigmatism. The figure shows a 4:1 relationship between the FWHM diameters of the lateral and transverse sources. The calculated brightness using Eqn. (3.14) was 78 MW/cm^2-sr, using measured values of θ_t= 21°, θ_l=18° and P_{op}=406 mW at the URSL output facet, and using h_t=1 μm and h_l=4 μm.

Figure 8.2 shows the experimental set-up for testing of the integrated URSL-pumped KTP waveguide laser. An 8.0 mm fl, 0.5 NA diode laser objective lens was used to focus the collimated URSL output into the KTP PSW. This lens is specified to produce a 1.51 μm spot size from a Gaussian input beam filling its aperture at the lens design wavelength of 830 nm. Identical to the set-up used for Ti:Sapphire laser pumping, the KTP PSW was mounted atop a Melcor Frigichip TEC, which was temperature controlled by a Light Control Model 325 Temperature Controller. The output from the KTP PSW was collected by a Bausch and Lomb 50X, 0.45 NA lens with a 12.5 mm working distance. An Oriel Band Pass Colored Glass filter (Oriel PN 51720) blocked both the transmitted scattered and guided fundamental IR power during measurements of the transmitted SH guided mode power. To measure the URSL power spectrum, the transmitted IR power was optically coupled into a 125 μm core fiber for input into the Advantest TQ8345 OSA.

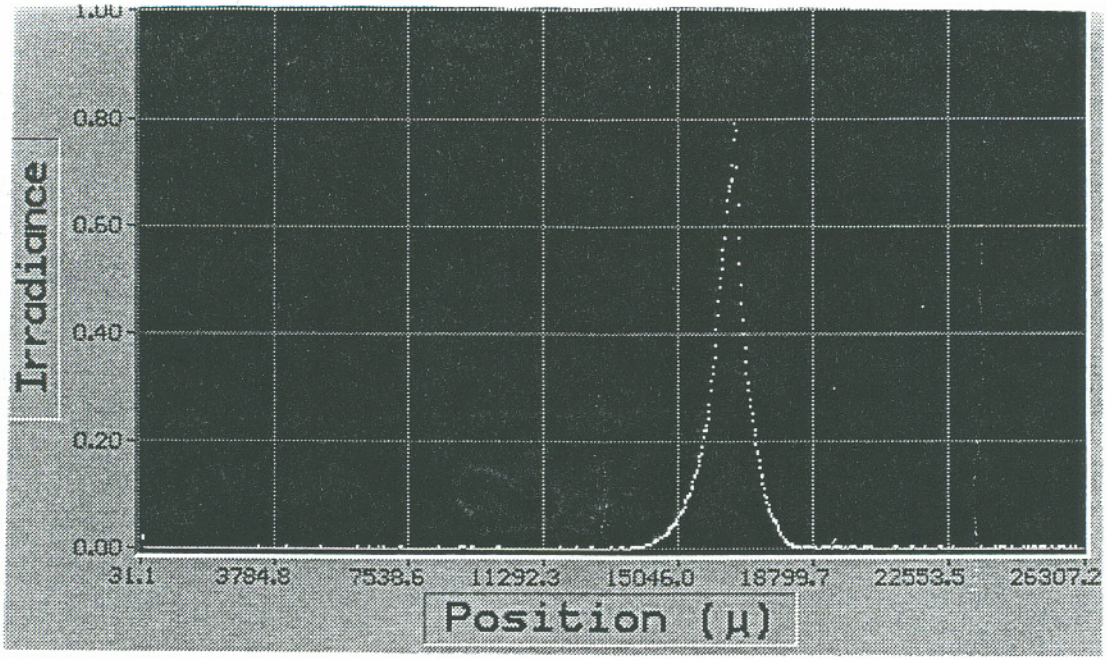

Figure 8.1a Transverse intensity profile of astigmatism corrected URSL

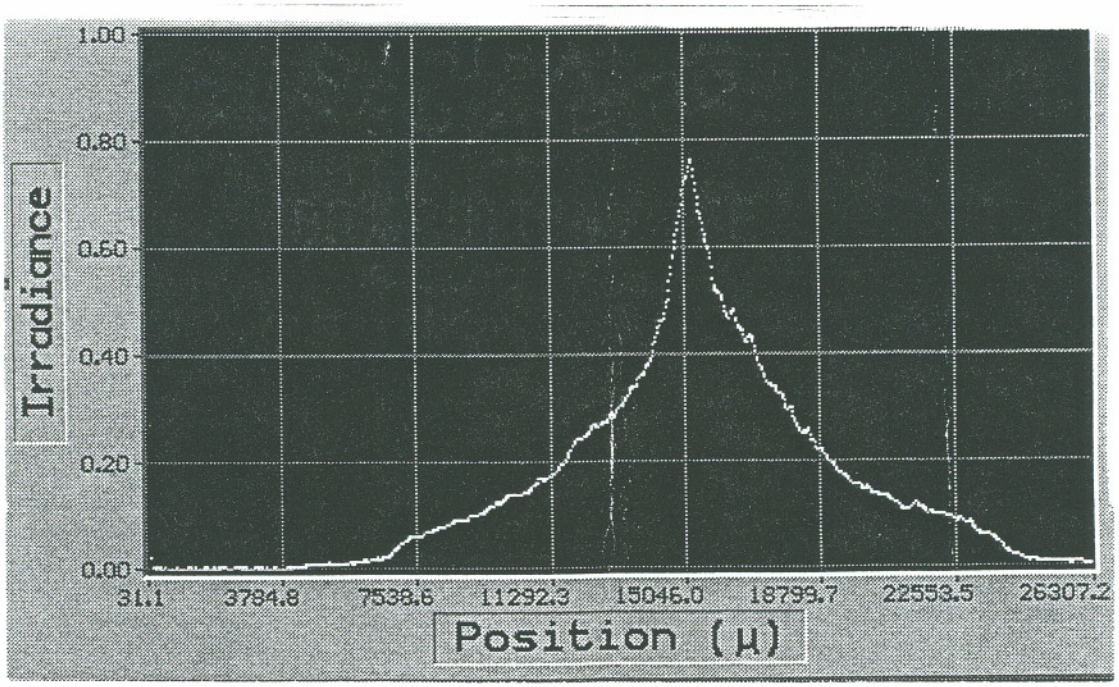

Figure 8.1b Lateral intensity profiles of astigmatism corrected URSL

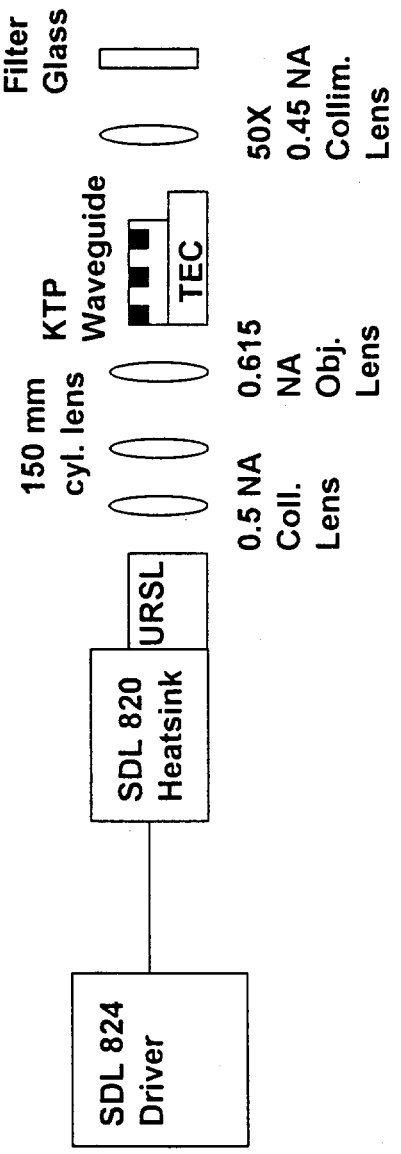

Figure 8.2 Experimental set-up for URSL-pumped KTP waveguide laser

At 1.60 A drive current and 37.2°C diode temperature, the measured CW power transmitted by the 0.50 NA focusing objective was 160 mW. This translates to an optical coupling efficiency of 52% for the lens train shown in Figure 8.2. Waveguide chip 788-A1 was installed on the Melcor TEC and the URSL pump beam was adjusted for best transmitted IR guided mode throughput. Once the URSL pump beam had been properly aligned, it was possible to translate the waveguide horizontally to identify guide number using the layout of waveguide positions shown in Figure 6.8. This was critical to identifying the waveguides listed in Table 6.1 that offered the best spectral characteristics for obtaining QPM output from the URSL.

QPM SHG output was observed from guides C3, C4, and C5 with the strongest SHG output observed from guide C5. Each of these waveguides contain a Bragg reflection branch with a nominal Bragg reflection wavelength of 770.92 nm. The Bragg reflection was measured by Brian Brown of DuPont to be 29.7% at 770.4 nm on guide B5 using Ti:Sapphire laser pumping.[169] Direct measurements of the Bragg reflected IR power were not performed during testing of the URSL-pumped KTP waveguide laser. Figure 8.3 shows a wavelength spectrum measurement of the transmitted fundamental output from the URSL when coupled into guide C5. The transmitted guided IR mode power for this measurement was 16 mW with 160 mW incident on the waveguide input face.

The highest SHG output power was obtained from guide C-5 when URSL I-4 was operated at 1.60 A, 37.2 °C. This corresponds to an incident power on the waveguide endface of 160 mW. At this incident power and following pump depletion by the SH guided mode and reflections from the Bragg section, 17.7 mW of IR power were measured in the transmitted fundamental guided mode. 86.3 μW of SHG output at 385.2 nm were measured in the TM_0 NUV guided mode. The waveguide temperature was set to 29.1 °C. This represents a normalized conversion efficiency of 43%/W-cm^2. This value represents the only NUV CW power output reported from any diode-pumped nonlinear waveguide laser.

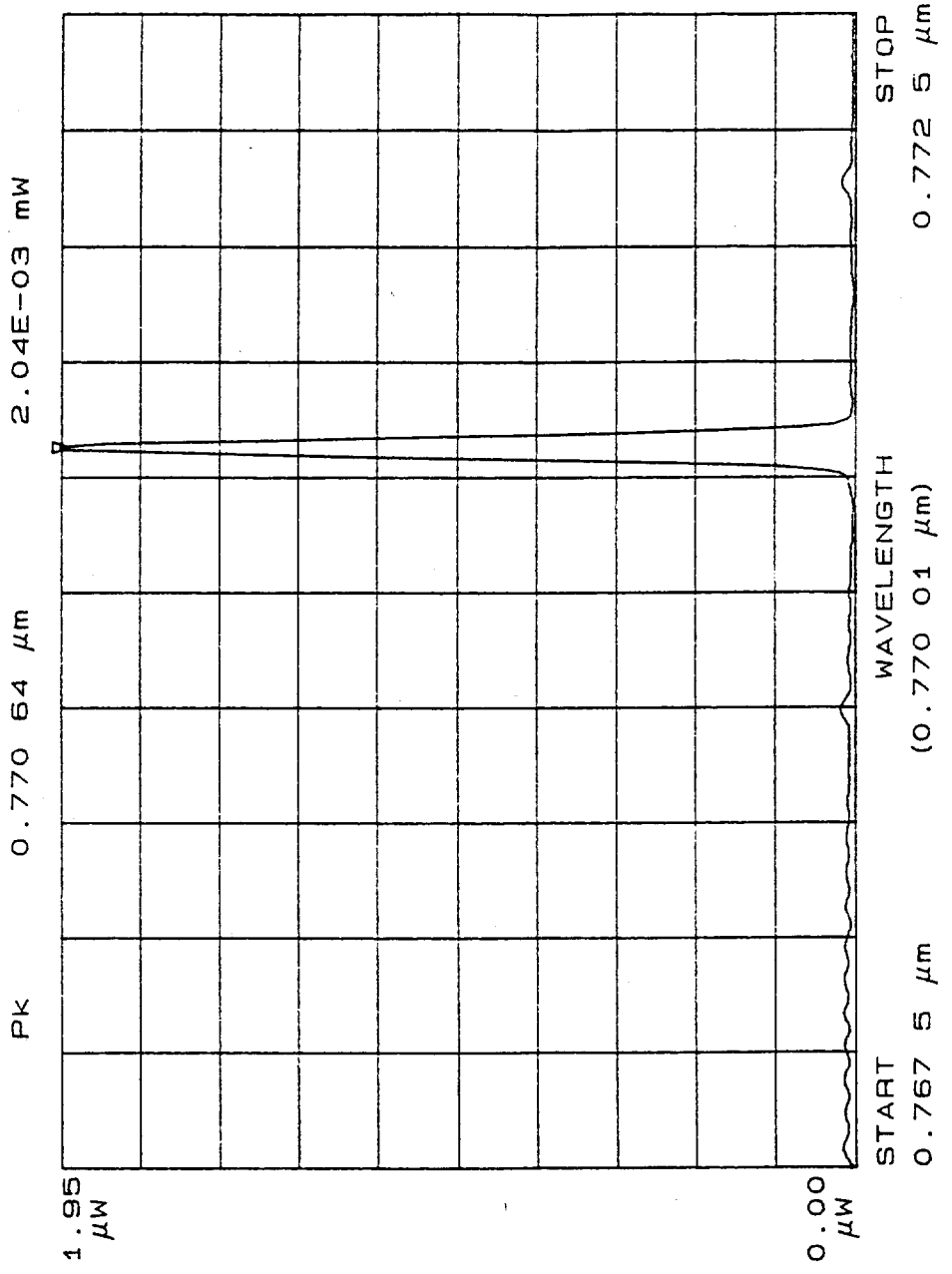

Figure 8.3 Power spectrum of URSL with Bragg feedback from KTP PSW

During efforts to improve on the above transmitted guided fundamental and SH mode powers, the coating on the exit face of the 0.5 NA focusing objective was damaged. Following receipt of a replacement, further efforts to improve the transmitted guided mode powers were unsuccessful. Examination of the L-I curve of the URSL revealed that device I-4 displayed a 25% reduction in output CW power. In addition, the power spectrum of the device displayed multi-longitudinal mode behavior and Beamscan profiles showed that the lateral virtual source no longer exhibited a central intensity maxima. These characteristics were consistent with a conclusion that URSL I-4 had suffered damage. Based on this judgment and the lack of additional URSL sources, experimental testing of the URSL-pumped KTP waveguide laser was concluded.

8.3 Discussion

In this chapter, results from the first integration and testing of an URSL-pumped KTP waveguide laser have been presented. The 86.3 μW of 385.2 nm SHG output obtained from the experimental UPWL represent the first results for NUV output power reported from any diode-pumped nonlinear waveguide laser.

This work demonstrated that the improved spatial coherence and higher brightness obtained from a low-magnification URSL contributed, as expected, to improved optical coupling into KTP PSWs in comparison to Fabry-Perot broad area diode lasers. The results from this experiment, indicated an approximate six-fold increase in the transmitted IR guided mode power after the astigmatism was corrected.

The experimental UPWL displayed the highest NUV SHG output when coupling the URSL fundamental input into a guide containing a Bragg reflection segment. The Bragg reflection succeeded in improving the spectral stability of the URSL by increasing suppression of the adjacent longitudinal modes to -20dB with respect to longitudinal mode selected by the Bragg reflection. The wavelength spectrum was observed to be stable for more than one hour and limited only by the need to make experimental adjustments to the UPWL. This behavior compares well to that reported by Eger et al. for

Bragg reflection locking of an SDL Model 5422 index-guided GaAlAs diode laser by a KTP PSW with Bragg reflection segment.[5]

The 11% coupling of the incident fundamental into the IR TM_0 guided mode transmitted by the KTP PSW indicated that lateral spatial profile of the URSL pump beam could not be well-matched to the KTP PSW IR guided mode. This experimental difficulty was hinted at by the lateral spatial intensity profile shown in Figure 8.1. Although the FWHM lateral and transverse beam diameters showed a 4:1 aspect ratio, the lateral virtual source intensity profile displays a much wider spatial distribution than this ratio when evaluated below the FWHM point. A graphical analysis gave an overlap of 19%, +/- 1.5% for the full intensity profiles.

Despite a number of reports on QPM SHG from diode-pumped KTP PSWs, these reports do not indicate the measured coupling efficiency between the IR power incident on the waveguide endface and the transmitted IR guided mode power.[18,47,73,169] This information would be useful in establishing an empirical value for the input fundamental to transmitted guided mode coupling efficiency for diode-pumped KTP PSWs employing index-guided diode lasers. Based on an understanding of the typical L-I characteristics of the index-guided diode laser used by Risk, et. al. and the report that 37.5 mW of 850 nm transmitted IR power was produced at a drive current of 150 mA, the author estimates that the incident-transmitted coupling efficiency was in the 35%-40% range.[47] In the report by Yamamoto and Mizuuchi of blue QPM SHG from a diode-pumped $LiTaO_3$ device, a coupling efficiency of 60% between the fundamental incident on the waveguide and the transmitted IR guided mode power was given.[73]

While an exact calculation cannot be made due to lack of experimental data on the URSL focused spot profile, it appears reasonable to estimate that the measured 17.7 mW of transmitted IR guide mode power is within a factor of 2 of an upper limit of the transmitted guided mode power based on consideration of the overlap of the lateral and transverse spatial modes and assuming unity overlap of the transverse pump beam with the IR guided mode. If the conversion efficiency reported by Yamamoto and Mizuuchi is

applied together with the graphical overlap value given above, a conversion value of 0.11 is obtained, which is in agreement with the obtained value of 0.11 (160 mW incident, 17.7 mW transmitted). If in addition, an approximate 30% loss to the transmitted fundamental guided mode due to Bragg reflection from the Bragg section is assumed, the *internal* fundamental guided mode power becomes 25.3 mW and the *internal* conversion efficiency of the incident pump power to the *internal* fundamental guided mode is 0.16.

The normalized conversion efficiency value of 43%/W-cm^2 falls within the typical range of values from < 10%/W-cm^2 to slightly greater than 100%/W-cm^2 reported by Du Pont[169] and in Chapter 6 of this work for NUV QPM SHG in hydrothermal KTP PSWs pumped by Ti:Sapphire lasers.

It is anticipated based on these experimental results that an UPWL using a core grating URSL with a reduced lateral virtual source profile, and comparable output power to that displayed by I-4, could produce several milliwatts of NUV QPM SHG.

CHAPTER 9
CONCLUSIONS AND SUGGESTIONS FOR FUTURE WORK

9.1 Summary and Conclusions

Emerging applications, such as optical recording, photodynamic therapy, and atomic absorption monitors, require a compact ultraviolet laser. The development of quasi-phase-matched nonlinear waveguides offered an opportunity and a challenge to integrate these devices with a high-power, spatially coherent AlGaAs diode laser to form a compact laser source emitting in the near ultraviolet. That opportunity and challenge led to the theoretical and experimental work presented in this dissertation and the demonstration of the first unstable resonator semiconductor laser-pumped KTP periodically segmented waveguide laser.

This dissertation presents a comprehensive survey of existing short wavelength laser technologies suitable for development of compact ultraviolet lasers. This survey established the suitability of a diode-pumped KTP PSW laser as an attractive approach for development of a compact ultraviolet laser. The requirements for an efficient diode-pumped KTP PSW laser were formulated, leading to the selection of frequency-stabilized URSLs and hydrothermal KTP PSWs as the component technologies to be developed and integrated.

To better assess the critical spatial mode properties of KTP PSWs operating in the near ultraviolet, extensive analyses and modeling of the spatial mode properties of these devices was presented. An effective index method (EIM) model based on MODEIG was employed to determine the normalized TM_0 spatial mode profiles for the fundamental and SH guided modes. This work correctly anticipated the transverse modal asymmetry later observed experimentally. The transverse modal asymmetry was shown to be a direct

consequence of the refractive index asymmetry introduced in the depth dimension during the ion-exchange process used to fabricate KTP PSWs. To study the evolution of the propagating spatial modes, a two-dimensional fast Fourier transform beam propagation method (2-D FFT-BPM) model was developed. Results using the BPM model illustrated the important influence of diffraction on the spatial mode propagation of the fundamental and SH guided modes. The BPM model showed that the periodic segmentation of a KTP PSW results in modulation of longer period spatial mode intensity fluctuations induced by mode beating between the symmetric spatial modes. The larger on-axis amplitude fluctuations observed for the SH guide modes, as compared to that observed for the fundamental guided modes, were determined to be related to the stronger spatial mode confinement experienced by the SH guided modes. By increasing the index contrast from $\Delta n_f = \Delta n_s = 0.010$ to 0.015 in the simulations, powerful mode beating effects were observed in the surface intensity plots. These effects were most pronounced for the guided SH mode, which exhibited localized on-axis intensity increases to values over 30% higher than the on-axis value of the input best fit gaussian mode.

A new expression for the normalized conversion efficiency η_{norm} was derived which accounts for the dependence of the overlap of the generated SH field and guided SH mode on the lateral variation of the nonlinear d coefficient and the refractive index n. This expression was evaluated for the case of phase-matched SHG in a 2-D KTP channel waveguide and was compared to the value obtained using a previous expression which assumed uniform values of d and n in the plane transverse to light propagation. This new expression gave a reduction of 14% compared to the previous expression in the value of η_{norm} for the case of phase-matched SHG in a 2-D channel KTP waveguide using a best fit gaussian approximation to the fundamental and SH TM_0 guided modes. This reduction demonstrated the importance of careful consideration of the extension of the weakly guided spatial modes of nonlinear waveguides, including KTP PSWs, into the lateral substrate region where the substrate retains its non-inverted d coefficient value.

To assess the theoretical performance of an URSL-pumped KTP PSW, the BPM model was extended to incorporate second harmonic generation. The 2-D FFT-BPM SHG code, termed BPMSHG, gave the first numerical BPM model results for SHG in PSWs. This model represents an important contribution to the development of numerical methods for modeling nonlinear waveguides, in general, and provided important information on the cooperative effects of diffraction and spatial mode beating on the SHG output from KTP PSWs. Results from BPMSHG indicated that the SH guided mode propagation constant increases relative to the propagation constant for the fundamental mode, resulting in an increase in the effective index seen by the guided modes. In the first regime, near field diffraction effects predominate. After several hundred microns, this strong intensity modulation subsides and is replaced with a damped oscillation associated with spatial mode beating between the propagating symmetric modes, which finally decays about 5.0 mm deep into the guide. Beyond this depth, the on-axis fundamental intensity decays parabolically. For 2-D propagation of 100 mW of fundamental input through a 9.0 mm KTP PSW, BPMSHG predicted production of 16.7 mW of SH output corresponding to a normalized conversion efficiency of 206%/W-cm^2. This compares to a computed normalized conversion efficiency of 252%/W-cm^2 after 1.0 mm of propagation. These results showed the importance of fundamental pump depletion at guide lengths and fundamental input powers expected from an URSL-pumped KTP waveguide laser.

The performance of hydrothermal KTP PSWs in the near ultraviolet were characterized under high-power Ti:Sapphire laser pumping. This work included spectral and spatial mode characterization and determination of the temperature dependence of the QPM wavelength in the near ultraviolet. The KTP PSWs used in these experiments were fabricated on hydrothermal KTP substrates grown by Litton Airtron and processed by Du Pont using the nanolithography facility at Cornell University using a mask containing fourteen different waveguide patterns. The mask contained six devices with Bragg

reflection branches and eight non-Bragg devices. After lithography, chips containing patterned waveguides were ion-exchanged in molten $Rb(Ba)NO_3$.

The Ti:Sapphire laser-pumped KTP waveguide power spectra yielded a QPM wavelength acceptance bandwidth $\Delta\lambda_{SH}$ of 0.06, +/- 0.1 nm for the TM_0 spatial mode. For 113 mW transmitted fundamental power and 7.1 mW NUV SHG power, an η_{eff} = 69%/W-cm^2 was measured for the NUV TM_0 spatial mode. Values of 7.1 %/W-cm^2 and 5.7%/W-cm^2 for η_{eff} were obtained for the TM_1 and TM_2 spatial modes, respectively. The significantly lower values for η_{eff} for the higher-order spatial modes resulted from the significant decrease in the spatial mode overlap between the fundamental TM_0 spatial mode and the SH TM_1 and TM_2 spatial modes. The modal SH power spectra displayed a blue-shift of the higher-order spatial modes with respect to the SH TM_0 spatial mode. This behavior was consistent with the blue-shift of the higher-order SH spatial modes reported by Roelofs[111] and Eger[87] for KTP waveguides with SH output near 420 nm. The spectral separation between the SH TM_0 and TM_1 spatial modes was measured to be 0.6 nm, and 1.3 nm between the SH TM_0 and TM_2 spatial modes, where the SH TM_0 spatial mode wavelength was 385.7 nm. The temperature tuning coefficient of the SH TM_0 wavelength near 385 nm was measured to be 0.037 nm/°C. This value is close to the 0.044 nm/°C value reported by Roelofs for Flux KTP PSWs for SH wavelengths near 425 nm.[85]

Experimental images of the SH spatial mode profiles of KTP PSWs in the NUV were obtained for the first time. Images of the SH TM_0 spatial mode were distinctive for their strong lateral symmetry and marked transverse asymmetry. These experimental results clearly displayed the tight transverse confinement near the air/waveguide interface and the decrease of transverse modal confinement with increasing depth predicted by MODEIG EIM modeling. Also as predicted by the MODEIG EIM modeling, the images demonstrated that the lateral spatial mode profile is highly symmetric. Images of the SH TM_1 and TM_2 spatial modes made after the fundamental pump beam had been adjusted to obtain maximum SH power showed that the pump beam had been positioned to

overlap the highest lying transverse modal lobe. This observation emphasized that the higher-order SH spatial modes, like the SH TM_0 mode, exhibit strongest transverse modal confinement and overlap with the fundamental TM_0 spatial mode near the air/waveguide interface.

To meet the challenge for a semiconductor laser suitable for high-power pumping of KTP PSWs, a single-frequency, SQW-GRINSCH AlGaAs/GaAs core grating URSL capable of producing 0.5 W CW output at 770 nm was designed by a research team led by Professor Gary Evans of Southern Methodist University and Professor Richard DeFreez of Oregon Graduate Institute. The metalization pattern design included both tapered and non-tapered devices, each with and without channels for grating deposition. The metalization-defined active region width for the non-tapered devices was 200 μm. The active region of the tapered devices was varied from 112 μm to 200 μm. Following wafer growth and mask fabrication, wafer processing was performed by Mr. Jay Kirk of Southern Methodist University. Samples of the processed wafer sections were subsequently evaluated by Professor DeFreez for verification of J_{th}, T_0, and laser emission wavelength. Wafer sections from material containing a 40%-80% AlAs content in the graded GRIN region and a transparent etch stop layer for use in grating fabrication demonstrated a measured J_{th} of 320 A/cm^2 and an acceptable T_0 value of 204 °K. The pulsed Fabry-Perot laser emission wavelength was measured to be 764.2 nm at 20.0°C. Following these test results, Mr. Kirk deposited core gratings on a section of this wafer material using a holographic exposure technique.

Fabrication of curved mirrors by FIBM yielded devices with a magnification of 2.9 using the FIBM workstation at Linfield Research Institute. More than fifty devices were micromachined. Ten bars containing a total of thirty micromachined URSLs were coated. A standard high reflectivity mirror was applied to the curved mirror surface and a low reflection coating specified as $R < 3\%$ was applied to the non-curved mirror surface. Equipment problems during device coating resulted in the loss of most devices. Five surviving devices were assembled into TO-3 packages.

Of fundamental importance to the advance of high-power, spatially coherent, single-frequency semiconductor lasers, the non-tapered core-grating URSL demonstrated over 400 mW of single-frequency CW output power at 765 nm at 12.0 °C. This device exhibited single-frequency performance over a 500 mA drive current range and for device temperatures ranging from 12.0 °C to 38.0 °C. At 37.2 °C, 1.60 A drive current, this device produced over 300 mW of single-frequency CW output power at 770 nm. The output of the URSL was collected by a two-lens combination, which corrected the beam astigmatism. The ratio of the FWHM transverse to lateral source sizes was measured by a beam profiler to be 1:4, indicating an emitted beam brightness in excess of 50 $MW/cm^2/sr$. These exciting results demonstrate that core grating URSLs can produce high brightness, high-power CW output in a single longitudinal mode.

This non-tapered core grating URSL was integrated with a hydrothermal KTP waveguide to form the first URSL-pumped KTP waveguide laser. The UPWL produced 86.3 μW of SHG output at 385.2 nm in the TM_0 NUV guided mode. This value represents the highest NUV CW power output reported from any diode-pumped nonlinear waveguide laser. The incident fundamental power on the waveguide was 160 mW and 17.7 mW was measured in the fundamental guided mode transmitted by the waveguide. This represents an η_{eff} of 43%/W-cm^2, which is comparable to the value 69%/W-cm^2 obtained using Ti:Sapphire laser pumping, but substantially lower than theoretical calculations indicated could be achieved.

In conclusion, this work represents an early effort to take advantage of the higher CW powers available from high brightness unstable resonator semiconductor lasers in an effort to increase the SH output powers obtainable from diode-pumped nonlinear waveguide lasers and to extend the useful spectral range from these sources into the near ultraviolet. In this effort, an improved understanding of the spatial mode properties of KTP waveguides was gained through development and use of effective index method and beam propagation method models. The extension of the beam propagation method model to explicitly incorporate the effects of second harmonic generation represents an

important contribution to the development of numerical methods for modeling nonlinear waveguides, in general, and provided important information on the cooperative effects of diffraction and spatial mode beating on the SHG output from KTP PSWs. The development and characterization of hydrothermal KTP waveguides reported in this dissertation proved that these devices can produce multi-milliwatt levels in the near ultraviolet. A single-frequency, high brightness unstable resonator semiconductor laser emitting near 770 nm was successfully designed, fabricated, and demonstrated. This URSL was integrated with a hydrothermal KTP waveguide to form the a compact ultraviolet laser, the first unstable resonator semiconductor laser-pumped KTP waveguide laser. This work ushers in a new regime of high brightness diode laser-pumped nonlinear waveguide lasers capable of emission in the visible and ultraviolet.

9.2 Suggestions for Future Work

The experimental work presented in this dissertation demonstrated for the first time that an URSL-pumped KTP waveguide laser can produce significant SH output in the near ultraviolet. Clearly, further increases in the NUV output power would be required for UPWLs employed in applications such as optical recording and photodynamic therapy.

Increasing the spatial coherence of the pump URSL is a key to increasing the NUV output from an UPWL. This work demonstrated an 11% coupling efficiency of the URSL fundamental output incident on the waveguide into the transmitted IR guided mode. Bao has reported producing a high-power GaAs/AlGaAs SQW GRINSCH URSL with 2.5 magnification with 1:1 FWHM aspect ratios between the transverse and lateral sources at threshold and 1:1.5 aspect ratio at many times threshold.[114] To compete with the incident-transmitted guided mode IR powers obtained from index-guided devices,[94,96] an UPWL needs to produce greater than 30 mW of transmitted fundamental guided mode power. This performance can certainly be achieved by an URSL with an improved source size aspect ratio and an improved slope efficiency and improved coupling optics.

The hydrothermal KTP waveguides used in this work demonstrated η_{eff} values of less than 200%/W-cm^2 for NUV operation. For SHG near 385 nm, η_{eff} values ranging from 50%/W-cm^2 to 100%/W-cm^2 were typical. The multiple peaks in the SH power spectrum suggest that process-induced fluctuations are present in these devices. Further improvements in the photolithography and ion exchange processes used in the waveguide fabrication are likely to afford increases in the NUV η_{eff} values for future devices.

Further advances in numerical models would assist in the development of diode-pumped nonlinear waveguide lasers. Extension of BPMSHG to a full 3-D FFT model would enable a more thorough theoretical understanding of the effects of the transverse index variations on device performance. Looking further, development of a reliable and efficient full vectorial 3-D beam propagation model incorporating second harmonic generation represents a major unconquered challenge in the field of theoretical optical physics.

REFERENCES

1. A. Einstein, "Zur Quantentheorie der Strahlung," *Phys. Z.*, vol. 18, pp.121-128, March, 1917.

2. J. P. Gordon, H. J. Zeiger, and C. H. Townes, "Molecular microwave oscillator and new hyperfine structure in the microwave spectrum of NH_3" *Phys. Rev.*, vol. 95, p. 282-284, 1954.

3. A. L. Schawlow, and C. H. Townes, "Infrared and optical masers," *Phys. Rev.*, vol. 112, p. 1940, 1958.

4. T. H. Maiman, "Optical and microwave-optical experiments in ruby," *Phys. Rev. Lett.*, vol. 4, p. 564, 1960.

5. SDL, Inc. *1996 Laser Diode Product Catalog*, San Jose, 1996.

6. R. K. DeFreez, Z. Bao, P. D. Carlson, M. K. Felisky, and C. Largent, "High-brightness unstable resonator semiconductor lasers," *Proc. SPIE, Laser Diode Technol. V*, vol. 1850, pp. 75-83, 1993.

7. Z. Bao, "Focused-ion-beam Micromachined Unstable Resonator Semiconductor Lasers," *Ph.D Dissertation*, Oregon Graduate Institute of Science and Technology, Beaverton, Oregon, 1995.

8. H. Kogelnik and T. Li, " Laser beams and resonators," *Appl. Optics*, vol. 5, pp. 1150-1167, October, 1966.

9. W. Koechner, *Solid State Laser Engineering*, Springer-Verlag, 2nd Ed., p. 87, New York, 1992.

10. A. Yariv, *Introduction to Optical Electronics,* Holt, Rinehart, and Winston, 2nd Ed., p. 179, New York, 1976.

11. D. L. Sipes, "Highly efficient neodymium: yttrium aluminum garnet laser end pumped by a semiconductor laser array," *Appl. Phys. Lett.*, vol. 47 (2), pp. 74-76, 15 July 1985.

12. T. Y. Fan, G. J. Dixon, and R. L. Byer, " Efficient GaAlAs diode-laser-pumped operation of Nd:YLF at 1.047 μm with intracavity doubling to 523.6 nm," *Opt. Lett.*, vol. 11 (4), pp. 204-206, April, 1986.

13. T. Baer, "Large-amplitude fluctuations due to longitudinal mode coupling in diode-pumped intracavity-doubled Nd:YAG lasers," *J. Opt. Soc. Am. B*, vol. 3 (9), pp. 1175-1179, September, 1986.

14. R. Scheps, "Cr:$LiCaAlF_6$ laser pumped by visible laser diodes," *IEEE J. Quantum Electron.*, vol. 27, pp. 1968-1970, 1991.

15. M. Oka, L.Y. Liu, W. Wiechmann, N. Eguchi, and S. Kubota, "1 W Continuous-Wave 266 nm Radiation from an All Solid-State Frequency Quadrupled Nd:YAG Laser," *Proceedings on Advanced Solid State Lasers*, Optical Society of America, pp. 374-376, Salt Lake City, Utah, February 7-10, 1994.

16. W. L. Nighan, S. B. Hutchison, D. Dudley, and M. Keirstead, "Highly efficient Q-switched Nd:YAG laser with 11 W TEM_{00} output," *Technical Digest of Conference on Lasers and Electro-Optics*, Optical Society of America, Paper CWN2, Anaheim, California, June 3-7, 1996.

17. C. D. Orth, S. A. Payne, and W. F. Krupke, "Diode-pumped Solid State Laser Driver for Inertial Fusion Energy Power Plants," *Proceedings on Advanced Solid State Lasers*, Optical Society of America, pp. 280-282, Salt Lake City, Utah, February 7-10, 1994.

18. T. Tohma and J. D. Bierlein, "KTP Blue Laser for Optical Storage," *Technical Digest of the Topical Meeting on Nonlinear Guide Waves and Their Applications*, Paper NFC1-1, Optical Society of America, Dana Point, California, February 23-25, 1995.

19. K. L. March, B. L. Patton, R. L. Wilensky, and D. R. Hathaway, "8-Methoxypsoralen and Longwave Ultraviolet Irradiation Are a Novel Antiproliferative Combination for Vascular Smooth Muscle," *Circulation*, vol. 87 (1), pp. 184-191, January, 1993.

20. W. Wang, M. L. Bortz, M. M. Fejer, R. H. Hammond, C. H. Ahn, and M. R. Beasley, "Atomic Absorption Monitor for Physical Vapor Deposition Process Control Using a Frequency-Doubled Diode Laser," *Annual Report of the Center for Nonlinear Optical Materials*, pp. 38-40, Stanford University, Stanford, California, 1995.

21. S. Prahl, Private Communication, Oregon Medical Laser Center, Portland, Oregon, 1994.

22. S. Prahl, Private Communication, Oregon Medical Laser Center, Portland, Oregon, 1994.

23. H. Jeon, J. Ding, A. V. Nurmikko, H. Luo, N. Samarth, J. K. Furdyna, W. A. Bonner, and R. E. Nahory, "Room-temperature blue lasing action in (Zn,Cd)Se/Znse optically pumped multiple quantum well structures on lattice-matched (Ga,In)As substrates," *Appl. Phys. Lett.*, vol. 57 (23), pp. 2413-2415, December, 1990.

24. H. Amano, M. Kito, K. Hiramatsu, and I. Akasaki, "Stimulated emission near ultraviolet at room temperature from a GaN film grown on sapphire by MOVPE using an AlN buffer layer," *Jpn. J. Appl. Phys.*, vol. 29, p. L205, 1990.

25. H. Amano, I. Akasaki, K. Hiramatsu, N. Koide, and N. Sawaki, "Effects of the buffer layer in metalorganic vapour phase epitaxy of GaN on sapphire substrates,"*Thin Solid Films*, vol. 163, p. 415, 1988

26. K. Itoh, T. Kawamoto, H. Amano, K. Hiramatsu, and I. Akasaki, "Cathodoluminescence properties of undoped and Zn-doped $Al_xGa_{1-x}N$ grown by metalorganic vapor phase epitaxy," *Jpn. J. Appl. Phys.*, vol. 30, p. 1604, August,1991.

27. H. Amano, I. Akasaki, K. Itoh, and H. Murakami, "Perspective of GaN/GaAlN based ultra-violet/blue lasers," *Technical Digest of the Topical Meeting on Compact Blue-Green Lasers*, Paper ThC4, Optical Society of America, Santa Fe, New Mexico, February 20-21, 1992.

28. J. M. Depuydt, M. A. Haase, J. Qiu, and H. Cheng, "II-VI Blue-Green Lasers," *Technical Digest of the Topical Meeting on Compact Blue-Green Lasers*, Paper ThC1, Optical Society of America, Santa Fe, New Mexico, February 20-21, 1992.

29. M. A. Haase, J. Qiu, J. M. Depuydt, and H. Cheng, "Blue-green laser diodes," *Appl. Phys. Lett.*, vol. 59, p. 1272, 1991.

30. H. Jeon, J. Ding, W. Patterson, A. V. Nurmikko, W. Xie, D. C. Grillo, M. Kobayashi, and R. L. Gunshor, "Blue-green injection laser diodes in (ZnCd)Se/ZnSe quantum wells," *Appl. Phys. Lett.*, vol. 59, p. 3619, 1991.

31. C. T. Walker, J. M. Depuydt, M. A. Haase, J. Qiu, and H. Cheng, "Advances in II-VI Blue-Green Lasers," *Technical Digest of the Topical Meeting on Compact Blue-Green Lasers*, Paper CTuC2, Optical Society of America, New Orleans, Louisiana, February 1-4, 1993.

32. K. Akimoto, H. Okuyama, T. Miyajima, Y. Morinaga, F. Hei, and M. Ozawa, "Growth of ZnMgSSe and Fabrication of Blue Laser Diodes," *Technical Digest of the Topical Meeting on Compact Blue-Green Lasers*, Paper CTuC1, Optical Society of America, New Orleans, Louisiana, February 1-4, 1993.

33. S. Taniguchi, T. Hino, S. Itoh, K. Nakano, N. Nakayama, A. Ishibashi, and M. Ikeda, "100h II-VI blue-green laser diode," *Electron. Lett.*, vol. 32, no. 6, March, 1996.

34. P. Zory, Private Communication, University of Florida, Gainsville, Florida, 1996.

35. D. Welch, Private Communication, SDL, Inc., San Jose, California, 1994.

36. P. Zory, Private Communication, University of Florida, Gainsville, Florida, 1996.

37. S. Nakamura, M. Senoh, S. Nagahama, N. Iwasa, T. Yamada, T. Matsushita, H. Kiyoku, and Y. Sugimoto, "InGaN-based multi-quantum-well structure laser diodes," *Jpn. J. Appl. Phys. Part 2*, vol. 35, no. 1B, p. L74, January, 1996.

38. M. Suzuki and T. Uenoyama, "Biaxial strain effect on wurtzite GaN/AlGaN quantum well lasers," *Jpn. J. Appl. Phys. Part 2*, vol. 35, no. 1B, p. L72, January, 1996.

39. J. A. Armstrong, N. Bloembergen, J. Ducing, and P. S. Pershan, "Interactions between light waves in a nonlinear dielectric," *Phys. Rev.*, vol. 127, pp. 1918-1939, 1962.

40. P. A. Franken and J. F. Ward, "Optical harmonics and nonlinear phenomena," *Rev. Mod. Phys.*, vol. 35, pp.23-39, 1963.

41. A. Yariv, *Optical Electronics,* Holt, Rinehart, and Winston, 3rd Ed., p. 234, New York, 1985.

42. W. J. Kozlovsky, "Frequency-doubled Diode Lasers," *Technical Digest of the Topical Meeting on Compact Blue-Green Lasers*, Paper FA2, Optical Society of America, Santa Fe, New Mexico, February 20-21, 1992.

43. L. Goldberg and M. Chun, "Efficient generation of 421 nm by resonantly enhanced doubling of GaAlAs laser diode array emission," *Appl. Phys. Lett.*, vol. 55, pp. 218-220, 1989.

44. D. Fluck, T. Pliska, P. Gunter, "A 10 mW frequency-doubled diode laser at 491 nm," *Technical Digest of the Topical Meeting on Advanced Solid State Lasers*, Paper WF10, Optical Society of America, San Francisco, California, January 31-February 2, 1996.

45. M. H. Jiang, D. R. Yuan, N. Zhang, X. T. Tao, and D. Xu, "Generation of violet- blue light by SHG of infrared laser diode in new organic crystal--MHBA," *Technical Digest of the Topical Meeting on Blue-Green Lasers*, PostDeadline Paper PD2, Optical Society of America, Salt Lake City, Utah, February 10-11, 1994.

46. R. Waarts, R. Parke, D. Nam, D. Welch, D. Mehuys, A. Hardy, R. Lang, S. O'Brien, and D. Scifres, "Second Harmonic Generation of a High Power Coherent Laser Diode," *Technical Digest of the Topical Meeting on Blue-Green Lasers*, Paper JWD3, Optical Society of America, Salt Lake City, Utah, February 10-11, 1994.

47. W. J. Koslovsky, W. P. Risk, W. Lenth, B. G. Kim, G. L. Bona, H. Jaeckel, and D. J. Webb, "Blue light generation by resonator-enhanced frequency doubling of an extended-cavity diode laser," *Appl. Phys. Lett.*, vol. 65, p. 525, 1994.

48. C. Zimmerman, V. Vuletic, A. Hemmerich, T. W. Hansch, "All solid state laser source for tunable blue and ultraviolet radiation,"*Appl. Phys. Lett.*, vol. 66, p. 2318, 1995.

49. W. J. Kozlovsky, W. Lenth, E. E. Latta, A. Moser, and G. L. Bona, "Generation of 41 mW of blue radiation by frequency doubling of a GaAlAs diode laser," *Appl. Phys. Lett.*, vol. 56, pp. 2291-2292, 1990.

50. G. J. Dixon, C. E. Tannr, and C. E. Wieman, "432-nm source based on efficient second-harmonic generation of GaAlAs-diode laser radiation in a self-locking external resonant cavity," *Opt. Lett.*, vol. 14, pp. 731-733, 1989.

51. R. J. Keyes and T. M. Quist, " Injection luminescent pumping of CaF_2U^{3+} with GaAs diode lasers," *Appl. Phys. Lett.*, vol. 4, p. 50-52, 1974.

52. T. Y. Fan and R. L. Byer, "Diode Laser-Pumped Solid State Lasers," *IEEE J. Quantum Electron.*, vol. QE-24 (6), pp. 895-912, 1988.

53. D. W. Hughes and J. R. M. Barr, "Laser diode pumped solid state lasers," *J. Phys. D,* vol. 25, pp. 563-586, 14 April 1994.

54. B. W. Baird and R. K. DeFreez, "Method and Apparatus for Efficient Operation of a Solid-State Laser Optically Pumped by an Unstable Resonator Semiconductor Laser," *U.S. Patent No. 5,260,963*, November 9, 1993.

55. V. Pruneri, R. Koch, P. G. Kazansky, W. A. Clarkson, P. St. J. Russell, and D. C. Hanna, "Highly-efficient cw blue light generation via first-order quasi-phase-matched frequency doubling of a diode-pumped 946 nm Nd:YAG laser," *OSA Trends in Optics and Photonics, Advanced Solid State Lasers, Vol. 1,* pp. 42-45, 1996.

56. B. W. Baird and R. K. DeFreez, "High-Power, Compact, Diode-Pumped, Tunable Laser," *U.S. Patent No. 5,317,447*, May 31, 1994.

57. G. I. Stegeman and C. T. Seaton, "Nonlinear integrated optics,"*J. Appl. Phys.*, vol. 58, pp. R57-R78, 1985.

58. P. K. Tien, R. Ulrich, and R. J. Martin, "Second harmonic generation in form of coherent Cherenkov radiation from a thin-film waveguide,"*Appl. Phys. Lett.*, vol. 17, 447-450, 1970.

59. T. Taniuchi and K. Yammato, "Second harmonic generation in proton exchanged guides," *SPIE Proceedings, Advanced Optoelectronic Technology, Vol. 864*, pp. 36-41, 1991.

60. M. J. Jongerius, R. R. Drenten, and R. B. J. Droste, "Blue Second-Harmonic Generation in KTP, $LiNbO_3$, and $LiTaO_3$ Waveguides," *Philips J. Res.*, vol. 46, pp. 231-265, 1992.

61. G, Tohman, J. Ohya, K. Yamamoto, and T. Taniuchi, "Generation of ultraviolet picosecond pulses by frequency-doubling of laser diode in proton-exchanged MgO:$LiNbO_3$ waveguide," *IEEE Photonics Technol. Lett.*, vol. 2 (9), pp. 629-631, September, 1990.

62. T. Kinoshita, K. Sasaki, Y. Yokoh, H. Ashitaka, and N. Ogata, "Cerenkov-type second harmonic generation in lossy slab waveguides," *Technical Digest of the Topical Meeting on Compact Blue-Green Lasers*, Paper CThC1, Optical Society of America, New Orleans, Louisiana, February 1-4, 1993.

63. L. K. Cheng, J. D. Bierlein, A. A. Ballman, "$KTiOP_xAs_{1-x}O_4$ optical waveguides grown by liquid phase epitaxy," *Appl. Phys. Lett.*, vol. 58 (18), pp. 1937-1939, 1991.

64. W. Risk, S. Lau, R. Fontana, L. Lane, and C. Nadler, "Type-II seond-harmonic generation and sum-frequency mixing in uniform $KTiOPO_4$," *Appl. Phys. Lett.*, vol. 63, no. 10, pp. 1301-1303, 1993.

65. L. K. Cheng and J. D. Bierlein, "KTP and Isomorphs--Recent Progress in Device and Material Development," *Ferroelectrics*, vol. 142, pp. 209-228, 1993.

66. D. Fluck, P. Gunter, M. Fleuster, and Ch. Buchal, "Phase-matched and Cerenkov-type second harmonic blue light generation ion-implanted $KNbO_3$ waveguides," *Technical Digest of the Topical Meeting on Compact Blue-Green Lasers*, Paper CThA3, Optical Society of America, New Orleans, Louisiana, February 1-4, 1993.

67. P. F. Bordui and M. M. Fejer, "Inorganic Crystals for Nonlinear Optical Frequency Conversion," *Annu. Rev. Mater. Sci.*, vol. 23, pp. 321-379, 1993.

68. K. C. Rustagi, S. C. Mehendale, and S. Meenakshi, "Optical Frequency Conversion in Quasi-Phase-Matched Stacks of Nonlinear Crystals," *IEEE J. Quantum Electon.*, vol. QE-18 (6), pp. 1029-1034, June, 1982.

69. S. Somekh and A. Yariv, "Phase matching by periodic modulation of the nonlinear optical properties," *Opt. Comm.*, vol. 6 (3), pp. 301-304, November, 1972.

70. C. J. van der Poel, J. D. Bierlein, J. B. Brown, and S. Colak, "Efficient type I blue second-harmonic generation in periodically segmented $KTiOPO_4$ waveguides," *Appl. Phys. Lett.*, vol. 57 (20), pp. 2074-2076, November, 1990.

71. K. Mizuuchi, K. Yamamoto, and T. Taniuchi, "Second harmonic generation of blue light in a $LiTaO_3$ waveguide," *Appl. Phys. Lett.*, vol. 58, pp. 2732-2734, June, 1991.

72. K. Yamamoto and K. Mizuuchi, "Blue-light generation by frequency doubling of a laser diode in a periodically domain-inverted $LiTaO_3$ waveguide," *IEEE Photonics Technol. Lett.*, vol. 4 (5), pp. 435-437, May, 1992.

73. K. Yamamoto, K. Mizuuchi, K. Takeshiga, Y. Sasai, and T. Taniuchi, "Characteristics of periodically domain-inverted $LiNbO_3$ and $LiTaO_3$ waveguides for second harmonic generation," *J. Appl. Phys.*, vol. 70, pp. 1947- 1951, August, 1991.

74. R. C. Miller and A. Savage, "Temperature dependence of the optical properties of ferroelectric $LiNbO_3$ and $LiTaO_3$," *Appl. Phys. Lett.*, vol. 9, pp. 169-171, August, 1966.

75. S. K. Kurtz, J. Jerphagnon, and M. M. Choy, "Nonlinear Dielectric Susceptibilities," in *Landolt-Bornstein, New Series*, edited by K.-H. Hellwege, vol. 11, p. 682, Springer-Verlag, Berlin, 1979.

76. E. J. Lim, M. M. Fejer, and R. L. Byer, "Blue Light Generation by Frequency Doubling in Periodically Poled Lithium Niobate Channel waveguide," *Electron. Lett.*, vol. 25, pp. 731-732, 1989.

77. M. M. Fejer, G. A. Magel, and E. J. Lim, "Quasi-phase-matched interactions in lithium niobate," *SPIE, Nonlinear Optical Properties of Materials,* vol. 1148, 1989.

78. M. Yamada, N. Nada, M. Saitoh, and K. Watanabe, "First-order quasi-phase matched $LiNbO_3$ waveguide periodically poled by applying an external field for efficient blue second-harmonic generation," *Appl. Phys. Lett.* vol. 62 (5), pp. 435-436, February, 1993.

79. M. Fujimura, K. Kintaka, T. Suhara, H. Nishihara, "$LiNbO_3$ wavguide quasi-phase-matching second harmonic generation devices with ferroelectric-domain-inverted gratings formed by electron-beam scanning," *J. of Lightwave Technol.*, vol. 11 (8), pp. 1360-1367, August, 1993.

80. Y. Lu, L. Mao, and N. Ming, "Blue-light generation by frequency doubling of an 810 nm cw GaAlAs diode laser in a quasi-phase-matched $LiNbO_3$ crystal," *Opt. Lett.*, vol. 19 (14), pp. 1037-1038, July, 1994.

81. D. Fluck, T. Pliska, P. Gunter, M. Fleuster, C. Buchal, and D, Rytz, "Blue light generation by frequency doubling cw diode laser radiation in ion-implnated $KNbO_3$ waveguides," *Electron. Lett.*, vol. 30, pp. 1937-1938, 1994.

82. M. Roelofs, Private Communication, Du Pont, Wilmington, Delaware, 1994.

83. J. D. Bierlein, J. B. Brown, C. J. van der Poel, "Comment on "Mechanism for efficient blue second-harmonic generation in periodically segmented waveguides," *Appl. Phys. Lett.*, vol. 58 (22), pp. 2567, June, 1991.

84. Du Pont, "Blue Laser Diodes with Du Pont KTP-Waveguides," Brochure, Wilmington, Delaware, 1991.

85. M. G. Roelofs, W. Bindloss, A. Suna, J. D. Lee, and J. D. Bierlein, "KTP segmented waveguides as concurrent Bragg reflectors and second harmonic generators," *Technical Digest of the Topical Meeting on Compact Blue-Green Lasers*, Paper CThB2, Optical Society of America, New Orleans, Louisiana, February 1-4, 1993.

86. F. Laurell, J. B. Brown, and J. D. Bierlein, "Simultaneous generation of UV and visible light in segmented KTP waveguides," *Appl. Phys. Lett.*, vol. 62 (16), pp. 1872-1874, April, 1993.

87. D. Eger, M. Oron, and M. Katz, "Optical characterization of $KTiOPO_4$ periodically segmented waveguides for second-harmonic generation of blue light," *J. Appl. Phys.*, vol. 74 (7), pp. 4298-4302, October, 1993.

88. W. P. Risk, W. J. Koslovsky, S. D. Lau, G. L. Bona, H. Jaeckel, and D. J. Webb, "Generation of 425-nm light by waveguide frequency doubling of a GaAlAs laser diode in an extended-cavity configuration," *Appl. Phys. Lett.*, vol. 63 (23), pp. 3134-3136, December, 1993.

89. S. Helmfrid and G. Arvidsson, "Second-harmonic generation in quasi-phase-matching waveguides with a multimode pump," *J. Opt. Soc. Am. B*, vol. 8 (11), pp. 2326-2330.

90. M. J. Jongerius, R. J. Bolt, and N.A. Sweep, "Blue second-harmonic generation in waveguides fabricated in undoped and scandium-doped $KTiOPO_4$," *J. Appl. Phys.*, vol. 75 (7), pp. 3316-3325, April, 1994.

91. B. Boulanger, M. M. Fejer, R. Blachman, and P. F. Bordui, "Study of $KTiOPO_4$," *Appl. Phys. Lett.*, vol. 65 (19), pp. 2401-2403, November, 1994.

92. M. P. Scripsick, D. N. Loiacono, J. Rottenberg, L. E. Halliburton, and F. K. Hopkins, "Grey Track Resistant Flux Grown KTP," *Technical Digest of the Topical Meeting on Advanced Solid State Lasers*, Postdeadline Paper PD17, Optical Society of America, Memphis, Tennessee, January 30-February 2, 1995.

93. T. A. Driscoll, H. J. Hoffman, R. E. Stone, and P.E. Perkins, "Efficient second-harmonic generation in KTP crystals," *J. Opt. Soc. Am. B*, vol. 3, p. 683, 1986.

94. J. D. Bierlein, M. G. Roelofs, J. B. Brown, T. Tohma, and S. Okamoto, "$KTiOPO_4$ blue laser using segmented waveguide structure," *Technical Digest*

of the Topical Meeting on Compact Blue-Green Lasers, PostdeadlinePaper PD7, Optical Society of America, Salt Lake City, Utah, February 10-11, 1994.

95. D. Eger, M. Oron, M. Katz, and A. Zussman, "Very high efficiency of frequency doubling in QPM waveguide of KTP," *Technical Digest of the Topical Meeting on Compact Blue-Green Lasers*, Paper CThB1, Optical Society of America, Salt Lake City, Utah, February 10-11, 1994.

96. D. Eger, M. Oron, M. Katz, and A. Sussman, "Efficient frequency doubling and locking of diode laser light in periodically segmented $KTiOPO_4$ waveguide," *J. Appl. Phys.*, vol. 77 (5), pp. 2205-2207, March, 1995.

97. W. P. Risk, S. D. Lau, and M. A. McCord, "Third-order guided-wave distributed Bragg reflectors fabricated by ion-exchange in $KTiOPO_4$," *IEEE Photon. Lett.*, vol. 6 (3), pp. 406-408, March, 1994.

98. Q. Chen and W. P. Risk, "High-efficiency quasi-phasematched waveguide device in $KTiOPO_4$ fabricated by electric field poling," *Technical Digest of Conference on Lasers and Electro-Optics*, Paper CFA2, Optical Society of America, Baltimore, Maryland, May 21-26, 1995.

99. J. D. Bierlein, Private Communication, Du Pont, Wilmington,Delaware, 1994.

100. P. A. Morris, J. B. Brown, and J. D. Bierlein, "Characteristics of $KTiOPO_4$ waveguides up to high power densities," *Technical Digest of the Topical Meeting on Blue-Green Lasers*, Paper CThB1, Optical Society of America, New Orleans, Louisiana, February 1-4, 1993.

101. F. Laurell, J. B. Brown, and J. D. Bierlein, "Simultaneous generation of UV and visible light in segmented KTP waveguides," *Appl. Phys. Lett.*, vol. 62 (16), pp. 1872-1874, April, 1993.

102. G. Ghosh, "Temperature dispersion in KTP for nonlinear devices," *IEEE Photonics Tech. Lett.*, vol. 7 (1), pp. 68-70, January, 1995.

103. M. M Fejer, G. A. Magel, D. H. Jundt, and R. L. Byer, "Quasi-phase-matched second harmonic generation: tuning and tolerances," *IEEE J. Quantum Electron.*, vol. QE-28 (11), pp. 2631-2654, November, 1992.

104 G. P. Agarwal and N. K. Dutta, *Long-Wavelength Semiconductor Lasers*, von Nostrand Reinhold, New York, 1986.

105. Sony Corp., *Laser Diode Guidebook*, Tokyo, 1992.

106. D. Eger, M. Oron, M. Katz, and A. Zussman, "Highly efficient blue light generation in $KTiOPO_4$ waveguides," *Appl. Phys. Lett.*, vol. 64 (24), pp. 3208-3209, June, 1994.

107. M. J. Jongerius, R. R. Drenten, and R. B. J. Droste, "Blue Second-Harmonic Generation in KTP, $LiNbO_3$, and $LiTaO_3$ Waveguides," *Philips J. Res.*, vol. 46, pp. 231-265, 1992.

108. L. Li and J. J. Burke, "Linear propagation characteristics of periodically segmented waveguides," *Opt. Lett.*, vol. 17 (17), pp. 1194-1196, September, 1992.

109. J. D. Bierlein, *Technical Digest of Quantum Electronics and Laser Science Conference*, vol. 13, p. 42, Optical Society of America, Anaheim, California, May, 1992.

110. Z. Weissmann and A. Hardy, "Modes of periodically segmented waveguides," *J. Lightwave Technol.*, vol. 11 (11), pp. 1831-1838, November, 1993.

111. M. G. Roelofs, A. Suna, W. Bindloss, and J. D. Bierlein, "Characterization of optical waveguides in $KTiOPO_4$ by second harmonic generation," *J. Appl. Phys.*, vol. 76 (9), pp. 4999-5006, November, 1994.

112. D. Marcuse, *Theory of Dielectric Optical Waveguides*, Academic Press, New York, 1974.

113. M. Fukuda, *Reliability and Degradation of Semiconductor Lasers and LEDs*, Artech House, Boston, 1991.

114. Z. Bao, "Focused-ion-beam Micromachined Unstable Resonator Semiconductor Lasers," *Ph.D Dissertation*, Oregon Graduate Institute of Science and Technology, Beaverton, Oregon, 1995.

115. G. H. B. Thompson, "A theory for filamentation in semiconductor lasers including the dependence of dielectric constant on injected carrier density," *Opto-Electronics*, vol. 4, pp. 257-309, 1972.

116. P. A. Kirkby, A. R. Goodwin, G. H. B. Thompson, and P. R. Selway, "Observation of self-focusing in stripe geometry semiconductor lasers and the development of a comprehensive model of their operation," *IEEE J. Quantum Electron.*, vol. QE-13 (8), pp. 705-719, August, 1977.

117. M. L. Tilton, G. C. Dente, and A. H. Paxson, "Mode control of broad area semiconductor lasers using unstable resonators," *Proc. SPIE Laser Diode Technol. Appl. II*, vol. 1219, p. 423, 1990.

118. M. L. Tilton, G. C. Dente, A. H. Paxson, J. Cser, R. K. DeFreez, C. E. Moeller, and D. Depatie, "High power, nearly diffraction-limited output from a semiconductor laser with an unstable resonator," *IEEE J. Quant. Electron.*, vol. QE-27(9), pp. 2098-2108, September, 1991.

119. R. K. DeFreez, Z. Bao, P.D. Carlson, M. K. Felisky, and C. Largent, "High-brightness unstable resonator semiconductor lasers," *Proc. SPIE, Laser Diode Technol. V*, vol. 1850, pp. 75-83, 1993.

120. T. Ikegami, S. Sudo, Y. Sakai, *Frequency Stabilization of Semiconductor Laser Diodes*, Artech House, Boston, 1995.

121. D. Mehuys, S. O'Brien, R. J. Lang, A. Hardy, and D. F. Welch, "5 W, diffraction-limited, tapered-stripe unstable resonator semiconductor laser," *Electon. Lett.*, vol. 30, pp. 1855-1856, October, 1994.

122. S. O'Brien, D. Mehuys, R. J. Lang, and D. F. Welch, "1 W CW, single-frequency, diffraction-limited unstable resonator semiconductor laser with distributed Bragg reflector mirrors," *Electron. Lett.*, vol. 31(3), pp. 203-204, 2 February, 1995.

123. Z. Bao, R. K. DeFreez, P. D. Carlson, C. Largent, C. Moeller, and G. C. Dente, "Spatio-spectral characteristics of a high power, high brightness CW InGaAs/AlGaAs unstable resonator semiconductor laser," *Electron. Lett.*, vol. 29(18), pp. 1597-1599, September, 1993.

124. W. P. Risk, W. J. Koslovsky, S. D. Lau, G. L. Bona, H. Jaeckel, and D. J. Webb, "Generation of 425-nm light by waveguide frequency doubling of a GaAlAs laser diode in an extended-cavity configuration," *Appl. Phys. Lett.*, vol. 63 (23), pp. 3134-3136, December, 1993.

125. R. K. DeFreez, Z. Bao, G. A. Evans, B. W. Baird, and R. S Harris,"Focused-ion-beam micromachined unstable resonator semiconductor lasers," *Proceedings of the Annual Meeting of the Optical Society of America*, Dallas, Texas, October 2-7, 1994.

126. R. Petit, *Electromagnetic Theory of Gratings*, Springer-Verlag, Berlin, 1980.

127. J. D. Bierlein, B. D. Laubacher, J. B. Brown, and C. J. van der Poel, "Balanced phase matching in segmented $KTiOPO_4$ waveguides," *Appl. Phys. Lett.*, vol. 56, p. 1725, 1990.

128. D. Yevick, "A review of recent beam propagation method results in integrated optics, semiconductor laser theory, and fiber optics," *SPIE*, vol. 473, pp. 226-228, 1984.

129. M. Rivera, "A finite difference BPM analysis of bent dielectric waveguides," *J. Lightwave Technol.*, vol. 13 (2), pp. 233-238, February, 1995.

130. B. W. Baird and R. K. DeFreez, "Spatial Mode Characteristics of Potassium Titanyl Phosphate Periodically Segmented Nonlinear Waveguides," *Proceedings of Progress in Electromagnetic Research Symposium*, p. 667, Seattle, Washington, July 24-28, 1995.

131. J. Buus, "The effective index method and its application to semiconductor lasers," *IEEE J. Quantum Electron.*, vol. QE-18, no.7, p. 1083, 1982.

132. P. L. Demers, *MODEIG/II MANUAL*, Version 1.1, David Sarnoff Research Center, Princeton, 1989.

133. M. D. Feit and J. A. Fleck, "Light propagation in graded-index optical fibers," *Appl. Opt.*, vol. 17 (24), pp. 3990-3998, December, 1978.

134. M. D. Feit and J. A. Fleck, "Calculation of dispersion in graded-index multimode fibers by a propagating-beam method," *Appl. Opt.*, vol. 18 (16), pp. 2843-2851, August, 1979.

135. M. D. Feit and J. A. Fleck, "Computation of mode properties in optical fiber waveguides by a propagating beam method," *Appl. Opt.*, vol. 19 (7), pp. 1154-1164, April, 1980.

136. D. Yevick, "Efficient beam propagation techniques," *IEEE J. Quantum Electron.*, vol. QE-26 (1), pp. 109-112, January, 1990.

137. D. Yevick, "New formulations of the matrix beam propagation method: application to rib waveguides," *IEEE J. Quantum Electron.*, vol. QE-25 (2), pp. 221-229, February, 1989.

138. E. E. Kriezis and A. G. Papagiannakis, "A joint finite difference and FFT full vectorial beam propagation scheme," *J. Lightwave Technol.*, vol. 13 (4), pp. 692-700, April, 1995.

139. Y. Chung and N. Dagli, "Explicit finite difference vectorial beam propagation method," *Electron. Lett.*, vol. 27 (23), pp. 2119-2121, 1991.

140. W. P. Huang, C. L. Xu, S. T. Chu, and S. K. Chaudhuri, "The finite-difference vector beam propagation method--Analysis and assessment," *J. Lightwave Technol.*, vol. 10 (3), pp. 295-305, March, 1992.

141. P. L. Liu and B. J. Li, "Full vectorial mode analysis of rib waveguides by iterative Lanczos reduction," *IEEE J. Quantum Electron.*, vol. QE-29 (12), pp. 2859-2863, December, 1993.

142. C. L. Xu, W. P. Huang, J. Chrostowski, and S. K. Chaudhuri, "A full-vectorial beam propagation method for anisotropic waveguides," *J. Lightwave Technol.*, vol. 12 (11), pp. 1926-1931, November, 1994.

143. H.-P. Nolting and R. Marz, "Results of benchmark tests for different numerical BPM algorithms," *J. Lightwave Technol.*, vol. 13 (2), pp. 216-224, February, 1995.

144. W. H. Press, B. P. Flannery, S. A. Teukolsky, and W. T. Vetterling, *Numerical Recipes,* pp. 394-395, Cambridge, Cambridge, 1986.

145. B. Hermansson and D. Yevick, "A propagation beam method analysis of nonlinear effects in optical waveguides," *Opt. Quant. Elect.*, vol.16, pp. 525-534, 984.

146. P. Weitzman and U. Osterberg, "A modified beam propagation method to model second harmonic generation in optical fibers," *IEEE J. Quant. Elect.*, vol. 29, pp. 1437-1443, 1993.

147. H. Masoudi and J. Arnold, "Parallel beam propagation method for the analysis of second harmonic generation," *IEEE Photon. Technol. Lett.*, vol. 7, pp. 400-402, 1995.

148. A. Yariv, *Quantum Electronics*, John Wiley and Sons, 3rd Ed., p. 392, 1985.

149. J. D. Bierlein, Private Communication, DuPont, Wilmington, Delaware, 1994.

150. J. D. Bierlein and M. Roelofs, Private Communication, DuPont, Wilmington, Delaware, 1994.

151. Coherent Inc., *ModeMaster Beam Propagation Analyzer*, Auburn, 1992.

152. M. Sasnett, in *The Physics and Technology of Laser Resonators,* ed. D. R. Hall and P. E. Jackson, Chapter 9, Adam Hilger, Bristol, 1989.

153. R. Tamosaitis, Private Communication, DuPont, Wilmington, Delaware, 1995.

154. W. P. Risk and S. D. Lau, "Distributed-Bragg-reflection properties of segmented KTP waveguides," *Opt. Lett.*, vol. 18(4), pp. 272-274, 15 February 1993.

155. H. Kressel and F. Z. Hawrylo, "Red-light-emitting laser diodes operating CW at room temperature," *Appl. Phys. Lett.,* vol. 28 (10), pp. 598-600, 15 May 1976.

156. G. A. Evans, "Progress Report on Compact Ultraviolet Laser Project," *ESI Internal Report 1194*-03, November 30, 1994.

157. E. S. Kintzer, J. N. Walpole, S. R. Chinn, C. A. Wang, and L. J. Missaggia, "High-power, strained-layer amplifiers and lasers with tapered gain regions," *IEEE Photon. Tech. Lett.*, vol. 5(6), pp. 605-608, June, 1993.

158. J. B. Cser, "Unstable Resonator Semiconductor Lasers Fabricated by Focused Ion Beam Micromachining," *M.S. Thesis*, Oregon Graduate Institute of Science and Technology, Beaverton, Oregon, October, 1990.

159. R. K. DeFreez, J. Puretz, J. Orloff, R. A. Elliott, H. Namba, E. Omura, and H. Namizaki, "Operating characteristics and elevated lifetests of focused-ion-beam micromachined transverse junction stripe lasers," *Appl. Phys. Lett.*, vol. 53(13), pp.1153-1155, 26 September 1988.

160. J. Puretz, R. K. DeFreez, R. A. Elliott, and J. Orloff, "Focused-ion-beam micromachined AlGaAs semiconductor laser mirrors," *Electron. Lett.*, vol. 22, pp.700-702, 19 June 1986.

161. R. K. DeFreez, J. Puretz, R. A. Elliott, J. Orloff, and L. W. Swanson, "CW operation of widely and continuously tunable micromachined-coupled-cavity-diode lasers," *Electron. Lett.*, vol. 22, pp. 919-921, 14 August 1986.

162. J. Puretz, R. K. DeFreez, R. A. Elliott, J. Orloff, and T. L. Paoli, "300 mW operation of a surface-emitting phase-locked array of diode lasers," *Electron. Lett.*, vol. 23, pp.130-131, 29 January 1987.

163. R. K. DeFreez, J. Puretz, R. A. Elliott, G. A Crow, H. Ximen, D. J. Bossert,

G. A. Wilson, and J. Orloff, "Focused-ion-beam micromachined diode laser mirrors," *Proc. SPIE, Laser Diode Technology and Applications*, vol. 1043, pp. 25-35, 1989.

164. R. A. Elliott, R. K. DeFreez, J. Puretz, J. Orloff, and G. A. Crow, "Focused-ion-beam micromachining of diode laser mirrors," *Proc. SPIE., Symposium on Communications Networking in Dense Electromagnetic Environments*, vol. 876, pp. 114-120, January 1988.

165. H. Ximen, R. K. DeFreez, J. Orloff, R. A. Elliott, G. A. Evans, N. W. Carlson, M. Lurie, and D. P. Bour, "Focused ion beam micromachined three dimensional features by means of a digital scan," *J. Vac. Sci. Technol. B*, vol. 8(6), pp. 1361-365, Nov./Dec. 1990.

166. J. Puretz, "A Theoretical and Experimental Study of Liquid Metal Ion Sources and Their Application to Focused Ion Beam Technology," *Ph.D Dissertation*, Oregon Graduate Center (currently Oregon Graduate Institute of Science and Technology), Beaverton, Oregon, December 1988.

167. G. A. Crow, "Focused Ion Beam Micromachining of *Si* and *GaAs* Using *Ga* and *Au* Liquid Metal Ion Sources," *Ph.D. Disssertation*, Oregon Graduate Institute of Science and Technology, Beaverton Oregon, October 1990.

168. H. Ximen, "A Study of Focused Ion Beam Micromachining by Development of a 3-D Computer Simulation and a 3-D Digital Scan Strategy," *Ph.D Dissertation,* Oregon Graduate Institute of Science and Technology, Beaverton, Oregon, September 1990.

169. B. Brown, Private Communication, DuPont, Wilmington, Delaware, 1995.

Appendix A: Computer Codes

```
Program KTPSELL
c     This program computes the indices of refraction as a function
c     of wavelength using the Sellmeier equation and Sellmeier
c     coefficients listed in Table I, Ghosh, PTL, Jan. 1995, pg. 69.

      Real*8 lam,lamlo,lamhi,lamstep
      Real*8 ax,bx,cx,dx,ex,ay,by,cy,dy,ey
      Real*8 az,bz,cz,dz,ez,nx2,ny2,nz2
      Real*8 nx,ny,nz

      write (6,*) "starting wavelength in microns"
      read (6,*) lamlo
      write (6,*) "ending wavelength in microns"
      read (6,*) lamhi
      write (6,*) "wavelength step size in microns"
      read (6,*) lamstep

      open (20,file='sellx.out', status='new')
      open (30,file='selly.out', status='new')
      open (40,file='sellz.out', status='new')

      do 100 lam=lamlo,lamhi,lamstep

       ax=2.0009584          ! These are the Sellmeier coeffs
       bx=1.0011186          ! All values from Ghosh Table I
       cx=.040294037
       dx=1.7740435
       ex=150

       ay=2.0411662
       by=0.9874869
       cy=.043432843
       dy=1.8828437
       ey=150

       az=2.2541202
       bz=1.0539416
       cz=.055303637
       dz=2.2516434
```

```
      ez=150

c     These are the Sellmeier equations for nx, ny, nz
      nx2=ax + (bx/(1.-(cx/(lam**2)))) + (dx/(1.-(ex/(lam**2))))
      ny2=ay + (by/(1.-(cy/(lam**2)))) + (dy/(1.-(ey/(lam**2))))
      nz2=az + (bz/(1.-(cz/(lam**2)))) + (dz/(1.-(ez/(lam**2))))

      nx=sqrt(nx2)
      ny=sqrt(ny2)
      nz=sqrt(nz2)

      write (20,701) lam,nx
      write (30,701) lam,ny
      write (40,701) lam,nz

  100 continue

      close (20)
      close (30)
      close (40)
  701 format (1x,e14.7,1x,e14.7)
      stop
      end
```

```
c      program bpmg7
c*****************************************************************
c This code simulates a periodically segmented KTP nonlinear waveguide.
c It reads the original parameters from data
c file INPUTG.DAT; (1) uses the Paraxial Wave Equation method to model
c the wave propagation inside the waveguide, and incorporates an index
c setting subroutine to pattern the refractive index in the lateral
c and longitudinal dimensions of the waveguide.  Absorbing layers have
c been introduced laterally to dampen reflections from the model boundary.
c Revision History (Start 11/14/94)
c Revised 11/25/94--Incorporate power variance algorithm into main program.
c Revised 11/27/94--Place Tol as input.dat data parameter.
c Revised 11/28/94--Place write statements for nearf.cur and final-fl.cur
c                   after 3000 statement.
c Major revision 1/03/95
c Attempt revision to input top hat field code structure
c 2nd attempt to reivse input top hat field code structure
c Major revision 1/8/95--incorporate absorption algorithm, remove
c                        complex refractive index from FFT algorithm
c Revised 1/12/95--changed output scaling for nearf.cur to read in microns
c Revised 1/13/95--changed input.dat parameter for tophat width to be input
c                  in microns
c Revised 1/14/95--Modify input.dat listing to eliminate unneeded variables
c Revised 1/18/95--Removed unused common blocks,variables, added write after
c                  each pass through period loop to nearf.curve.
c Revised 1/19/95--Remove unused code
c Revised 1/20/95--Change output for prop.dat to scale in microns
c Revised 1/21-1/22/95--Add gaussian field option; change input.dat
c                       variables to all be input in microns.
c Revised 1/24/95--Add field amplitude variable selection to input.dat
c Revised 1/30/95--Change nearf.cur format.  Change initf.cur out to intensity.
c Revised 2/11/95--Change nearf.cur format so z-pos is real.
c Revised 2/23/95--Fixed y3 output variable (changed zz1 to az1).
c Revised 3/12/95--Placed prop step loop control in main (removed from Prop).
c Revised 3/15/95--Modify write nearf.cur to allow control of output dimen.
c Revised 4/7/95--Correct y1 in main.
c Revised 4/11/95--Correct gain term in prop subroutine.
c Revised 4/15/95--Code clean-up.
c Revised 4/19/95--Incorporate prop.dat flag1 in inputz2.dat
c Revised 4/22/95--Place dim. control logic in prop sub for prop.dat
c Revised 5/3/95--Remove top hat init field and power tol code.
c Revised 5/9/95--Remove comment character from write initf to nearf.cur
c*****************************************************************
```

```
      integer nx,nz,zz,mstep,k,lnx,loop,nnn
      integer jj1,jj2,zhi,flag1
      double precision qq1,qq2,qq3,y5
      double precision x(100),off1,off2,abw
      double precision tw,k2
      double precision ndr,ndi,nkr,nki
      double precision rlam,sw,ax,az
      double precision pi,delx,delz,y1
      double precision ss,aww,y3
      double precision abin,rin,fampr,fampi
      double precision rx,ra,r1,g1,w0,ww0
      double precision rlam1,ax1,az1,ss1,sw1
      double complex e(4096),f(4096)
      double complex cpi,b2,p0

      common /name1/delx
      common /name2/nx
      common /name3/nnn
      common /name5/rlam,az
      common /name6/cpi
      common /name9/qq1,qq2,qq3
      common /name11/abw
      common /name12/zz
      common /name13/tw,pi
      common /name14/ndr,nkr,nki
      common /name15/flag1
      common /name16/y1
      common /name17/zhi,jj1,jj2
      common /name18/nz

c*****************************************************************
c     Get the input value for the variables
c*****************************************************************

c open a file to record the in situ output data
      open (2,file='inputg.dat',status='old')
      read (2,*) n
      if (n.le.1) stop
      do 400 j=1,n
      read (2,*) x(j)
 400  continue
c  input wavelength
      rlam1=x(1)
```

```
c  input problem domain
        ax1=x(2)            ! Domain width
        az1=x(3)            ! Guide length
c  input exponential index of the # of lateral steps
        lnx=int(x(4))
c  input # of propagation steps ! e.g. if steps=4 then this index =2
        nz=int(x(5))
c  refractive index in diffused segment
        ndr=x(6)
c  refractive index of KTP
        nkr=x(7)
c  diffused segment length
        ss1=x(8)
c  guide width
        sw1=x(9)
c  input # of round-trips
        loop=int(x(10))
c Imaginary index in diffused region
        ndi=x(11)
c Imaginary index in KTP substrate
        nki=x(12)
c Absorber width on each side of domain--type integer = 10X size in microns
        aww=x(13)
c Gaussian beam waist radius in microns
        ww0=x(14)
c Initial real field amplitude
        fampr=x(15)
c Initial imaginary field amplitude
        fampi=x(16)
c Minimum lateral step # to be written to nearf.cur
        jj1=x(17)
c Maximum lateral step # to be written to nearf.cur
        jj2=x(18)
c Period number at which nearf.cur is written to only each period
        zhi=x(19)
c Flag to open prop.dat (1 for open, default value is not open)
        flag1=x(20)

c Conversion from microns to cm for code use
        rlam=rlam1*1.d-4
        ax=ax1*1.d-4
        az=az1*1.d-4
        ss=ss1*1.d-4
```

```
      sw=sw1*1.d-4

c total number of lateral sampling points
      nx=2**lnx
      tw=nx
c lateral step size
      delx=ax/(1.d0*nx)
c Define absorber width per side of domain in lateral point k-space
      abw=aww/(delx*1.0d4)
c longitudinal step size
      delz=az/(1.d0*(nz))
c Unit conversion for Gaussian input field
      w0=ww0*1.d-4

c Definition of pi and complex pi
      pi=3.14159265359795d0
      cpi=dcmplx(0.d0,pi)

c Point at near lateral edge of diffused region
      qq1=((ax/2)-(sw/2))/delx
c Point at far lateral edge of diffused region
      qq2=((ax/2)+(sw/2))/delx
c Point at rear longitudinal edge of diffused region
      qq3=ss/delz

      mstep=1

      open (20, file='nearf.cur', status='new')
c Logic to open prop.dat if flag1=1 in inputz2.dat
      if (flag1 .eq. 1) then
        open (91, file='prop.dat', status='new')
      endif

c     open (21, file='final-fld', status='new')
c     open (72, file='ginitf.cur', status='new')
c     open (73, file='initf.cur', status='new')

c Set the initial field

c This is the gaussian initial field code

      do 10 k=1,nx
      k2=k*ax*1.d4/nx
```

```
          p0=dcmplx(fampr,fampi)
          rx=(nx/2-k)
          ra=dabs(rx)
          r1=ra*ax/nx
          g1=(-0.1d1*r1*r1)/(w0*w0)
          b2=dcmplx(g1,0.d0)
c         e(k)=p0       ! Check line for debug
          e(k)=p0*cdexp(b2)
c         write (72,7006) k2,e(k)

c Set initial field equal to gaussian input field
                  f(k)=e(k)

          off2=f(k)*dconjg(f(k))  ! Define output intensity

c         write (73,7006) k2,off2   ! Write statement for ginitf.cur

c Write statement for nearf.cur for initial field
          y5=0.
          if  ((k.ge.jj1) .and. (k.le.jj2)) then
                  write (20,7005) y5,k2,off2
          endif

 10    continue


c       Starting propagation through waveguide

 2500   do 120  zz=1,loop

     do 110 nnn=1,nz
     y1=(nnn*delz*1.0d4) + ((zz-1)*az1) ! Convert back to z-coord for output
     y3=y1

c propagating through the segment period !
     call prop(f,rin,abin,ax,nx,nz)

c exit the code after output data after completing inputg.dat
c specified number of periods

 3000   do 750, k=1,nx
          xx=k*delx*1.0d4
          off1=f(k)*dconjg(f(k))
```

```
c This is the step/loop # control for write statement for nearf.cur

        if ((zz.lt.zhi) .and. (k.ge.jj1)
     +  .and. (k.le.jj2)) then
          write (20,7005) y3,xx,off1
        else if ((zz.ge.zhi) .and. (nnn.eq.nz) .and. (k.ge.jj1)
     +  .and. (k.le.jj2)) then
          write (20,7005) y3,xx,off1
        endif

 750   continue
 110   continue
 120   continue

        close(2)       ! close inputg.dat
        close(20)      ! close nearf.curve
c       close(21)      ! close final_fld.curve
c       close(72)      ! Gaussian initial field curve
c       close(73)      ! Selected inital field curve
        if (flag1 .eq. 1) then
          close(91)      ! close prop.dat if opened
        endif

 7005   format(f6.2,1x,e10.5,1x,e8.3)
c 7006  format(1x,3e16.8)

        stop
        end



                subroutine fft2c (cdata,nn,isign)
c**************************************************
c
c          COOLEY - TUKEY FFT ALGORITHM
c
c Replace DATA by its discrete Fourier transform, if ISIGN is input as
c or replaces DATA by NN times its inverse discrete Fourier transform
c , if ISIGN is input as -1. DATA is a complex array of length NN or,
c equivalently, a real array of length 2*NN. NN NUST be an integer power
c of 2. (This is not checked for).
c
```

```
c Double precision for the trigonometric recurrences
      integer nx,nz,mmax,ll
      double precision wr,wi,wpr,wpi,wtemp,theta
      double precision data(16384)
      double precision tempr,tempi
      double complex cdata(nn)
      common /name2/nx
      common /name18/nz

      do 200 i=1,nn
      ll=2*i
      data(ll-1)=dreal(cdata(i))
      data(ll)=dimag(cdata(i))
 200  continue

      n=2*nn
      j=1

c This is the bit reversal section of the routine

      do 11 i=1,n,2
            if(j.gt.i) then

c Exchange the two complex numbers

                  tempr = data(j)
                  tempi = data(j+1)
                  data(j)= data(i)
                  data(j+1) = data(i+1)
                  data(i) = tempr
                  data(i+1) = tempi
                 endif
                 m = n/2
 1          if ((m.ge.2).and.(j.gt.m)) then
                        j = j-m
                        m = m/2
                        go to 1
                 endif
                        j = j+m
 11    continue
                        mmax = 2

c Begin the Danielson-Lanczos section of the routine
```

```
c Outer loop executed log2(nn) times

 2          if (n.gt.mmax) then

c Initialize for the trigonometric recurrence

                    istep = 2*mmax
                    theta = 6.28318530717959d0/(isign*mmax)
                    wpr = -2.d0*dsin(0.5d0*theta)**2
                    wpi = dsin(theta)
                    wr = 1.d0
                    wi = 0.d0
               do 13 m=1, mmax, 2
               do 12 i=m,n,istep
                    j = i+mmax

c This is the Danielson-Lancozs formula:

                    tempr = wr*data(j)-wi*data(j+1)
                    tempi = wr*data(j+1)+wi*data(j)
                    data(j) = data(i)-tempr
                    data(j+1) = data(i+1)-tempi
                    data(i) = data(i)+tempr
                    data(i+1) = data(i+1)+tempi
 12    continue

c Trigonometric recurrence

                    wtemp = wr
                    wr = wr*wpr - wi*wpi +wr
                    wi = wi*wpr+wtemp*wpi+wi
 13    continue
                    mmax=istep
               go to 2
        endif
        ll=1
        do 300 i=1,n,2
        cdata(ll)=dcmplx(data(i),data(i+1))
        ll=ll+1
 300    continue
        return
        end
```

```
      subroutine prop(f,rin,abin,ax,nx,nz)
c**********************************************************************
c This subroutine propagates the field through the waveguide.
c**********************************************************************
      integer k,nx,nz,nnn,iwk,zz,flag1
      integer zhi,jj1,jj2,nz
      double precision x1,y1
      double precision ee,rlam,tw,pi
      double precision delz,rff,rrf,qq1,qq2
      double precision qq3,ax,az,abw
      double precision abin,rin,abx,delx,abxr
      double precision ndr,nkr,nki
      double complex f(4096),g(4096),cpi
      double complex ctmp,gain

      common /name1/delx
      common /name3/nnn
      common /name5/rlam,az
      common /name6/cpi
      common /name9/qq1,qq2,qq3
      common /name11/abw
      common /name12/zz
      common /name13/tw,pi
      common /name14/ndr,nkr,nki
      common /name15/flag1
      common /name16/y1
      common /name17/zhi,jj1,jj2

      iwk=1        ! Replace DATA by its discrete Fourier transform
      delz=az/(nz*1.d0)

c multiply by + or - to center the fft
        rrf=1.d0
        do 30 k=1,nx
         f(k)=f(k)*rrf
         rrf=-rrf
30    continue

c fft the field
      call fft2c(f,nx,iwk)

c propagate the field a distance dz
```

```
      do 40 k=1,nx/2
      abb=tw-abw
      if ((nnn .le. qq3) .and. (k .ge. qq1)
     +    .and. (k .le. qq2)) then
                        rin=ndr
      else if (k .le. abw) then
                        rin=nkr
      else if (k .ge. abb) then
                        rin=nkr
      else
                        rin=nkr
      endif

      ee=(k-(nx/2)-1.d0)*1.d0/ax
      x1=k*delx*1.0d4    ! Scale lateral output to microns for prop.dat

c This is the 1st step/loop # control for write statement for prop.dat

      if ((zz.lt.zhi) .and. (k.ge.jj1) .and. (flag1 .eq. 1)
     +  .and. (k.le.jj2)) then
        write (91,7008) y1,x1,rin
      else if ((zz.ge.zhi) .and. (nnn.eq.nz) .and. (k.ge.jj1)
     +  .and. (k.le.jj2) .and. (flag1 .eq. 1)) then
        write (91,7008) y1,x1,rin
      endif

      ctmp=cdexp(-cpi*rlam*delz*ee*ee/rin)
      g(k)=f(k)*ctmp

 40   continue

      do 41 k=(nx/2)+1,nx
      abb=tw-abw
      if ((nnn .le. qq3) .and. (k .ge. qq1)
     +    .and. (k .le. qq2)) then
                        rin=ndr
      else if (k .le. abw) then
                        rin=nkr
      else if (k .ge. abb) then
                        rin=nkr
      else
                        rin=nkr
      endif
```

```
      ee=(k-(nx/2)-1.d0)*1.d0/ax
      x1=k*delx*1.0d4 ! Scale lateral output to microns for prop.dat

c This is the 2nd step/loop # control for write statement for prop.dat

      if ((zz.lt.zhi) .and. (k.ge.jj1) .and. (flag1 .eq. 1)
     +  .and. (k.le.jj2)) then
        write (91,7008) y1,x1,rin
      else if ((zz.ge.zhi) .and. (nnn.eq.nz) .and. (k.ge.jj1)
     +  .and. (k.le.jj2) .and. (flag1 .eq. 1)) then
        write (91,7008) y1,x1,rin
      endif

      ctmp=cdexp(-cpi*rlam*delz*ee*ee/rin)
      g(k)=f(k)*ctmp
 41   continue

c inverse fft the field
      do 50 k=1,nx
        f(k)=dconjg(g(k))
 50   continue
      call fft2c(f,nx,iwk)
      do 60 k=1,nx
      f(k)=dconjg(f(k))/nx
 60   continue

c multiply again by + or - to center the fft
       rff=1.d0

      do 80  k=1,nx

      abb=tw-abw
      if ((nnn .le. qq3) .and. (k .ge. qq1)
     +   .and. (k .le. qq2)) then
                    rin=ndr
      else if (k .le. abw) then
                    rin=nkr
      else if (k .ge. abb) then
                    rin=nkr
      else
                    rin=nkr
      endif
```

```
        abc=abw+1.0d-1    ! Logic fix for precision error in 16th place
        if (k .le. abc) then
                        abin=nki
        else if (k .ge. abb) then
                        abin=nki
        else
                        abin=0.d0
        endif

        x1=k*delx*1.0d4    ! Scale lateral output to microns for prop.dat
c Define the complex gain for field change due to absorption at each step
        abx=-2.0d0*pi*abin*rin/rlam
c added by Rick 4/10/95
        abxr=2.0d0*pi*rin/rlam
        gain=dcmplx(abx,abxr)
c       y2=int(y1)
c       write (91,7008) y2,x1,rin,abin ! 3rd prop.dat write statement
c calculate the field change for each step
        f(k)=rff*f(k)*cdexp(gain*delz)

c back transform previous multiplication by + or -
        rff=-rff

 80     continue

 7008   format(f6.2,1x,e10.5,1x,e8.3)
        return
        end
```

```
20
0.385d0          Wavelength (microns)
204.8d0          Full domain width (microns)
2.81d0           Waveguide period length (microns)
11               Exponential index of 2 for # of lateral points (e.g. 2 sup 10)
56               # of propagation steps
1.998d0          Real refractive index in diffused segment
1.983d0          Real refractive index in KTP substrate
1.405d0          Diffused segment length (microns)
4.0d0            Diffused segment guide width (microns)
37               # of periods to propagate through
0.d0             Imaginary index of diffused region (not implemented in BPMG7)
5.d-3            Imaginary index of absorbing barrier
4.0d1            Absorber width (microns)
1.99d0           Input gaussian beam waist radius (microns)
0.707106781d0    Initial real field amplitude
0.707106781d0    Initial imaginary field amplitude
994              Minimum lateral step # written to nearf.cur
1054             Maximum lateral step # written to nearf.cur
40               Period # at which nearf.cur is written to once per period
0                Flag to open prop.dat (1=open; default=closed)
```

```
c      program b8shg.for
c*****************************************************************
c This code simulates a periodically segmented KTP nonlinear
c waveguide.  It reads the original parameters from data
c file INPUTshg.DAT; (1) uses the Paraxial Wave Equation method
c to model the wave propagation inside the waveguide, and
c incorporates an index setting subroutine to pattern the
c refractive index in the lateral and longitudinal dimensions
c of the waveguide.  Absorbing layers have been introduced
c laterally to dampen reflections from the model boundary.
c Revised 9/5/95--Changed e,f,f2 arrays to size 2048.
c Revised 10/08/95--Incorporate index loop in gen SHG section.
c*****************************************************************
      integer nx,nz,zz,mstep,k,lnx,loop,nnn
      integer jj1,jj2,zhi,flag1
      double precision qq1,qq2,qq3,y5
      double precision x(100),off1,off2,off12,abw
      double precision tw,k2,off22
      double precision ndr,nkr,ndr2,nkr2,nki,ndi
      double precision sw,ax,az
      double precision pi,delx,delz,y1
      double precision ss,aww,y3
      double precision fampr,fampi,power
      double precision rx,ra,r1,g1,w0,ww0,w02,ww02
      double precision rlam1,rlam2,ax1,az1,ss1,sw1
      double precision def,d33,deff
      double precision rin1,rin2,delk,pwrcnv1,pwrcnv2
      double precision totpwr1,totpwr2,pwrcnv3
      double complex e(2048),f(2048),f2(2048)
      double complex cpi,b2,p0,c1,c2
      double complex texp1,texp2,tempf1,tempf2
      common /name1/delx
      common /name2/nx
      common /name3/nnn
      common /name5/rlam1,rlam2,az
      common /name6/cpi
      common /name9/qq1,qq2,qq3
      common /name11/abw
      common /name12/zz
      common /name13/tw,pi
      common /name14/ndr,nkr,ndr2,nkr2,nki
      common /name15/flag1
      common /name16/y1
```

```
      common /name17/zhi,jj1,jj2
      common /name18/nz
      common /name19/def,d33,deff
      common /name20/rin1
      common /name21/rin2
c*****************************************
c     Get the input value for the variables
c*****************************************
      open (2,file='inputshg.dat',status='old')
      read (2,*) n
      if (n.le.1) stop
      do 400 j=1,n
      read (2,*) x(j)
 400  continue
c  input wavelength
      rlam1=x(1)
c  input problem domain
      ax1=x(2)  ! Domain width
      az1=x(3)  ! Period length
c  input exponential index of the # of lateral steps
      lnx=int(x(4))
c  input # of propagation steps in a period
      nz=int(x(5))
c  refractive index in diffused segment at fund. lam.
      ndr=x(6)
c  refractive index of KTP at fund. lam.
      nkr=x(7)
c  refractive index in diffused segment at SH lam.
      ndr2=x(8)
c  refractive index of KTP at SH lam.
      nkr2=x(9)
c  diffused segment length
      ss1=x(10)
c  guide width
      sw1=x(11)
c  input # of periods for propagation
      loop=int(x(12))
c Imaginary index in diffused region
      ndi=x(13)
c Imaginary index in KTP substrate
      nki=x(14)
c Absorber width on each side of domain
      aww=x(15)
```

```
c Fundamental Gaussian beam waist radius in microns
      ww0=x(16)
c Second harmonic Gaussian beam waist radias in microns
      ww02=x(17)
c Power coupled into guide in Watts
      power=x(18)
c Initial imaginary field amplitude
      fampi=x(19)
c Minimum lateral step # to be written to nearint*.cur
      jj1=x(20)
c Maximum lateral step # to be written to nearint*.cur
      jj2=x(21)
c Period number at which nearint*.cur is written to only each period
      zhi=x(22)
c Flag to open prop.dat (1 for open, default value is not open)
      flag1=x(23)
c D33 in undiffused region in units of m/V
c includes free space permitivity
      d33=x(24)
c Average or effective D coefficient in diffused region (m/V)
c includes free space permitivity
      def=x(25)
c Conversion from microns to meters for code use
      rlam1=rlam1*1.d-6
      rlam2=rlam1/2.0d0
      ax=ax1*1.d-6
      az=az1*1.d-6
      ss=ss1*1.d-6
      sw=sw1*1.d-6
c total number of lateral sampling points
      nx=2**lnx
      tw=nx
c lateral step size
      delx=ax/(1.d0*nx)
c Define absorber width per side of domain in lateral point k-space
      abw=aww/(delx*1.0d6)
c longitudinal step size
      delz=az/(1.d0*(nz))
c Unit conversion for Gaussian input field
      w0=ww0*1.0d-6
      w02=ww02*1.0d-6
c Definition of pi and complex pi
      pi=3.14159265359795d0
```

```
      cpi=dcmplx(0.d0,pi)
c Point at near lateral edge of diffused region
      qq1=((ax/2)-(sw/2))/delx
c Point at far lateral edge of diffused region
      qq2=((ax/2)+(sw/2))/delx
c Point at rear longitudinal edge of diffused region
      qq3=ss/delz
      mstep=1
      open (20, file='nearint1.cur', status='new')
      open (19, file='nearint2.cur', status='new')
      open (23, file='totpwr1.cur', status='new')
      open (24, file='totpwr2.cur', status='new')
c Logic to open prop.dat if flag1=1 in inputshg.dat
      if (flag1 .eq. 1) then
        open (91, file='prop.dat', status='new')
      endif
c     open (21, file='final-fld', status='new')
       open (72, file='ginitint.cur', status='new')
c Set the initial fundamental field
c This is the gaussian initial fundamental field code
       do 10 k=1,nx
       k2=k*ax*1.d6/nx
c Conversion of incident power to gaussian amplitude
       fampr=21.899*dsqrt(power/ndr)/w0
       p0=dcmplx(fampr,fampi)
       rx=(nx/2-k)
       ra=dabs(rx)
       r1=ra*ax/nx
       g1=(-0.1d1*r1*r1)/(w0*w0)
       b2=dcmplx(g1,0.d0)
       e(k)=p0*cdexp(b2)
c Set initial field equal to gaussian input field
            f(k)=e(k)
       off2=f(k)*dconjg(f(k))  ! Define output intensity
c Exclude very small numbers from output file
       if (off2 .LT. 1e-20) then
       off2=0.0
       endif
       write (72,7006) k2,off2  ! Write for ginitint.cur
c Write initial field to nearint1,2.cur
      y5=0.0d0
      off22=0.0d0
c     write (20,7005) y5,k2,off2
```

```
c      write (19,7005) y5,k2,off22
 10    continue
c Initialize rin1, rin2, deff
        rin1=ndr
        rin2=ndr2
        deff=def
c Starting propagation through waveguide
        do 120  zz=1,loop  ! loop is # of periods
        do 110 nnn=1,nz   !  nz is # of steps in period
c Convert back to z-corrd. for output
     y1=(nnn*delz*1.0d6) + ((zz-1)*az1)
     y3=y1
c
c *******************************************************
c Generate SH and deplete fundamental
c *******************************************************
c

        do 1011 k=1,nx
        abb=tw-abw
        if ((nnn .le. qq3) .and. (k .ge. qq1)
   +      .and. (k .le. qq2)) then
                        rin1=ndr
                        rin2=ndr2
                        deff=-1.d0*def
        else if (k .le. abw) then
                        rin1=nkr
                        rin2=nkr2
                        deff=d33
        else if (k .ge. abb) then
                        rin1=nkr
                        rin2=nkr2
                        deff=d33
        else
                        rin1=nkr
                        rin2=nkr2
                        deff=d33
        endif


        delk=4*(rin2-rin1)/rlam1

        c2=-1.0d0*cpi*deff/(rlam2*rin2)
```

```
        texp2=cdexp(cpi*delk*delz)
        tempf2=c2*f(k)*f(k)*texp2*delz
        f2(k)=f2(k)+tempf2

        c1=-1.0d0*cpi*deff/(rlam1*rin1)
        texp1=cdexp(-1.0d0*cpi*delk*delz)
        tempf1=c1*f2(k)*dconjg(f(k))*texp1*delz
        f(k)=f(k)+tempf1

 1011   continue
c ******************************************************
c End generate SH and deplete fundamental
c ******************************************************
c
c propagate through segment
      call prop(f,ax,nx,nz)
      call prop2(f2,ax,nx,nz)
         pwrcnv1=rin1*1.3275d-07
         pwrcnv2=rin2*1.3275d-07
         pwrcnv3=1.0d4*dsqrt(pi/2)*w0*delx
         pwrcnv4=1.0d4*dsqrt(pi/2)*w02*delx*(w02**2/w0**2)
         totpwr1=0.0d0
         totpwr2=0.0d0
         do 750, k=1,nx
         xx=k*delx*1.0d6
c Intensity output in Watts/cm^2
         off1=pwrcnv1*f(k)*dconjg(f(k))
         off12=pwrcnv2*f2(k)*dconjg(f2(k))
c Total output power in Watts
         totpwr1=totpwr1+off1
         totpwr2=totpwr2+off12
c This is the step/loop # control for write to nearint1.cur
         if ((zz.lt.zhi) .and. (k.ge.jj1)
     +   .and. (k.le.jj2)) then
           write (20,7005) y3,xx,off1
           write (19,7005) y3,xx,off12
         else if ((zz.ge.zhi) .and. (nnn.eq.nz) .and. (k.ge.jj1)
     +   .and. (k.le.jj2)) then
           write (20,7005) y3,xx,off1
           write (19,7005) y3,xx,off12
         endif
 750   continue
         totpwr1=totpwr1*pwrcnv3
```

```
      totpwr2=totpwr2*pwrcnv4
      write(23,7007)y3,totpwr1
      write(24,7007)y3,totpwr2
 110  continue
 120  continue
      close(2)  ! inputshg.dat
      close(20) ! nearint1.curve
      close(19) ! nearint2.curve
c     close(21) ! final_fld.curve
      close(72) ! Gaussian initial field curve
      close(23) ! total fundamental power
      close(24) ! total S.H. power
      if (flag1 .eq. 1) then
       close(91) ! close prop.dat if opened
      endif
 7005 format(f7.2,1x,f7.2,1x,e10.4)
 7006 format(1x,3e16.8)
 7007 format(f7.2,1x,e14.8)
      stop
      end
            subroutine fft2c (cdata,nn,isign)
c*************************************************************
c          COOLEY - TUKEY FFT ALGORITHM
c Replace DATA by its discrete Fourier transform, if ISIGN
c is input as or replaces DATA by NN times its inverse
c discrete Fourier transform, if ISIGN is input as -1. DATA
c is a complex array of length NN or, equivalently, a real
c array of length 2*NN. NN NUST be an integer power of 2.
c (This is not checked for).
c*************************************************************
      integer nx,nz,mmax,ll
      double precision wr,wi,wpr,wpi,wtemp,theta
      double precision data(16384)
      double precision tempr,tempi
      double complex cdata(nn)
      common /name2/nx
      common /name18/nz
      do 200 i=1,nn
      ll=2*i
      data(ll-1)=dreal(cdata(i))
      data(ll)=dimag(cdata(i))
 200  continue
      n=2*nn
```

```
      j=1
c This is the bit reversal section of the routine
      do 11 i=1,n,2
            if(j.gt.i) then
c Exchange the two complex numbers
             tempr = data(j)
             tempi = data(j+1)
             data(j)= data(i)
             data(j+1) = data(i+1)
             data(i) = tempr
             data(i+1) = tempi
            endif
            m = n/2
 1        if ((m.ge.2).and.(j.gt.m)) then
                  j = j-m
                  m = m/2
                  go to 1
            endif
                  j = j+m
 11   continue
                  mmax = 2
c Begin the Danielson-Lanczos section of the routine
c Outer loop executed log2(nn) times
 2        if (n.gt.mmax) then
c Initialize for the trigonometric recurrence
                  istep = 2*mmax
                  theta = 6.28318530717959d0/(isign*mmax)
                  wpr = -2.d0*dsin(0.5d0*theta)**2
                  wpi = dsin(theta)
                  wr = 1.d0
                  wi = 0.d0
            do 13 m=1, mmax, 2
            do 12 i=m,n,istep
                  j = i+mmax
c This is the Danielson-Lancozs formula:
                  tempr = wr*data(j)-wi*data(j+1)
                  tempi = wr*data(j+1)+wi*data(j)
                  data(j) = data(i)-tempr
                  data(j+1) = data(i+1)-tempi
                  data(i) = data(i)+tempr
                  data(i+1) = data(i+1)+tempi
 12   continue
c Trigonometric recurrence
```

```
                    wtemp = wr
                    wr = wr*wpr - wi*wpi +wr
                    wi = wi*wpr+wtemp*wpi+wi
 13   continue
                    mmax=istep
              go to 2
       endif
       ll=1
       do 300 i=1,n,2
       cdata(ll)=dcmplx(data(i),data(i+1))
       ll=ll+1
 300   continue
       return
       end
       subroutine prop(f,ax,nx,nz)
c*******************************************************
c This subroutine propagates the fund. field thru step
c*******************************************************
       integer k,nx,nz,nnn,iwk,zz,flag1
       integer zhi,jj1,jj2,nz
       double precision x1,y1
       double precision ee,rlam1,rlam2,tw,pi
       double precision delz,rff,rrf,qq1,qq2
       double precision qq3,ax,az,abw
       double precision rin1,abx,delx,abxr
       double precision ndr,nkr,ndr2,nkr2,nki
       double precision def,d33,deff
       double precision abb,abc,abin
       double complex f(2048),g(2048),cpi
       double complex ctmp,gain
       common /name1/delx
       common /name3/nnn
       common /name5/rlam1,rlam2,az
       common /name6/cpi
       common /name9/qq1,qq2,qq3
       common /name11/abw
       common /name12/zz
       common /name13/tw,pi
       common /name14/ndr,nkr,ndr2,nkr2,nki
       common /name15/flag1
       common /name16/y1
       common /name17/zhi,jj1,jj2
       common /name19/def,d33,deff
```

```
      common /name20/rin1
      iwk=1  ! Replace DATA by its discrete Fourier transform
      delz=az/(nz*1.d0)
c multiply by + or - to center the fft
        rrf=1.d0
        do 30 k=1,nx
         f(k)=f(k)*rrf
         rrf=-rrf
 30   continue
c fft the field
      call fft2c(f,nx,iwk)
c propagate the field a distance dz
      do 40 k=1,nx/2
      abb=tw-abw
      if ((nnn .le. qq3) .and. (k .ge. qq1)
     +    .and. (k .le. qq2)) then
                    rin1=ndr
                    deff=-1.d0*def
      else if (k .le. abw) then
                    rin1=nkr
                    deff=d33
      else if (k .ge. abb) then
                    rin1=nkr
                    deff=d33
      else
                    rin1=nkr
                    deff=d33
      endif
      ee=(k-(nx/2)-1.d0)*1.d0/ax
c Scale lateral output to microns for prop.dat
      x1=k*delx*1.0d6
c This is the 1st control for write statement for prop.dat
      if ((zz.lt.zhi) .and. (k.ge.jj1) .and. (flag1 .eq. 1)
     +  .and. (k.le.jj2)) then
        write (91,7008) y1,x1,rin1
      else if ((zz.ge.zhi) .and. (nnn.eq.nz) .and. (k.ge.jj1)
     +  .and. (k.le.jj2) .and. (flag1 .eq. 1)) then
        write (91,7008) y1,x1,rin1
      endif
      ctmp=cdexp(-cpi*rlam1*delz*ee*ee/rin1)
      g(k)=f(k)*ctmp
 40   continue
      do 41 k=(nx/2)+1,nx
```

```
      abb=tw-abw
      if ((nnn .le. qq3) .and. (k .ge. qq1)
     +    .and. (k .le. qq2)) then
                    rin1=ndr
                    deff=-1.0d0*def
      else if (k .le. abw) then
                    rin1=nkr
                    deff=d33
      else if (k .ge. abb) then
                    rin1=nkr
                    deff=d33
      else
                    rin1=nkr
                    deff=d33
      endif
      ee=(k-(nx/2)-1.d0)*1.d0/ax
c Scale lateral output to microns for prop.dat
      x1=k*delx*1.0d6
c This is the 2nd control for write statement for prop.dat
      if ((zz.lt.zhi) .and. (k.ge.jj1) .and. (flag1 .eq. 1)
     +  .and. (k.le.jj2)) then
        write (91,7008) y1,x1,rin1
      else if ((zz.ge.zhi) .and. (nnn.eq.nz) .and. (k.ge.jj1)
     +  .and. (k.le.jj2) .and. (flag1 .eq. 1)) then
        write (91,7008) y1,x1,rin1
      endif
      ctmp=cdexp(-cpi*rlam1*delz*ee*ee/rin1)
      g(k)=f(k)*ctmp
 41   continue
c inverse fft the field
      do 50 k=1,nx
        f(k)=dconjg(g(k))
 50   continue
      call fft2c(f,nx,iwk)
      do 60 k=1,nx
      f(k)=dconjg(f(k))/nx
 60   continue
c multiply again by + or - to center the fft
       rff=1.d0
      do 80 k=1,nx
      abb=tw-abw
      if ((nnn .le. qq3) .and. (k .ge. qq1)
     +    .and. (k .le. qq2)) then
```

```
                rin1=ndr
                deff=-1.0d0*def
        else if (k .le. abw) then
                rin1=nkr
                deff=d33
        else if (k .ge. abb) then
                rin1=nkr
                deff=d33
        else
                rin1=nkr
                deff=d33
        endif
        abc=abw+1.0d-1    ! Logic fix for precision error
        if (k .le. abc) then
                abin=nki
        else if (k .ge. abb) then
                abin=nki
        else
                abin=0.d0
        endif
c Scale lateral output to microns for prop.dat
        x1=k*delx*1.0d6
c Define the complex gain for field change due to
c absorption at each step
        abx=-2.0d0*pi*abin*rin1/rlam1
c added by Rick 4/10/95
        abxr=2.0d0*pi*rin1/rlam1
        gain=dcmplx(abx,abxr)
c      y2=int(y1)
c 3rd prop.dat write statement
c       write (91,7008) y2,x1,rin1,abin
c calculate the field change for each step
         f(k)=rff*f(k)*cdexp(gain*delz)
c back transform previous multiplication by + or -
         rff=-rff
 80    continue
 7008  format(f6.2,1x,e10.5,1x,e8.3)
        return
        end
        subroutine prop2(f2,ax,nx,nz)
c*******************************************************
c This subroutine propagates the S.H. field thru a step
c*******************************************************
```

```
      integer k,nx,nz,nnn,iwk,zz,flag1
      integer zhi,jj1,jj2,nz
      double precision y1
      double precision ee,rlam1,rlam2,tw,pi
      double precision delz,rff,rrf,qq1,qq2
      double precision qq3,ax,az,abw
      double precision abin,rin2,abx,delx,abxr
      double precision ndr,nkr,ndr2,nkr2,nki
      double precision def,d33,deff
      double precision abb,abc
      double complex f2(2048),g(2048),cpi
      double complex ctmp,gain
      common /name1/delx
      common /name3/nnn
      common /name5/rlam1,rlam2,az
      common /name6/cpi
      common /name9/qq1,qq2,qq3
      common /name11/abw
      common /name12/zz
      common /name13/tw,pi
      common /name14/ndr,nkr,ndr2,nkr2,nki
      common /name15/flag1
      common /name16/y1
      common /name17/zhi,jj1,jj2
      common /name19/def,d33,deff
      common /name21/rin2
      iwk=1  ! Replace DATA by its discrete Fourier transform
      delz=az/(nz*1.d0)
c multiply by + or - to center the fft
        rrf=1.d0
        do 301 k=1,nx
         f2(k)=f2(k)*rrf
         rrf=-rrf
 301    continue
c fft the field
      call fft2c(f2,nx,iwk)
c propagate the field a distance dz
      do 401 k=1,nx/2
      abb=tw-abw
      if ((nnn .le. qq3) .and. (k .ge. qq1)
     +    .and. (k .le. qq2)) then
                    rin2=ndr2
                    deff=-1.0d0*def
```

```
      else if (k .le. abw) then
                  rin2=nkr2
                  deff=d33
      else if (k .ge. abb) then
                  rin2=nkr2
                  deff=d33
      else
                  rin2=nkr2
                  deff=d33
      endif
      ee=(k-(nx/2)-1.d0)*1.d0/ax
      ctmp=cdexp(-cpi*rlam2*delz*ee*ee/rin2)
      g(k)=f2(k)*ctmp
401   continue
      do 411 k=(nx/2)+1,nx
      abb=tw-abw
      if ((nnn .le. qq3) .and. (k .ge. qq1)
     +   .and. (k .le. qq2)) then
                  rin2=ndr2
                  deff=-1.0d0*def
      else if (k .le. abw) then
                  rin2=nkr2
                  deff=d33
      else if (k .ge. abb) then
                  rin2=nkr2
                  deff=d33
      else
                  rin2=nkr2
                  deff=d33
      endif
      ee=(k-(nx/2)-1.d0)*1.d0/ax
      ctmp=cdexp(-cpi*rlam2*delz*ee*ee/rin2)
      g(k)=f2(k)*ctmp
411   continue
c inverse fft the field
      do 501 k=1,nx
        f2(k)=dconjg(g(k))
501   continue
      call fft2c(f2,nx,iwk)
      do 601 k=1,nx
      f2(k)=dconjg(f2(k))/nx
601   continue
c multiply again by + or - to center the fft
```

```
      rff=1.d0
      do 80  k=1,nx
      abb=tw-abw
      if ((nnn .le. qq3) .and. (k .ge. qq1)
     +    .and. (k .le. qq2)) then
                  rin2=ndr2
                  deff=-1.0d0*def
      else if (k .le. abw) then
                  rin2=nkr2
                  deff=d33
      else if (k .ge. abb) then
                  rin2=nkr2
                  deff=d33
      else
                  rin2=nkr2
                  deff=d33
      endif
      abc=abw+1.0d-1    ! Logic fix for precision error
      if (k .le. abc) then
                  abin=nki
      else if (k .ge. abb) then
                  abin=nki
      else
                  abin=0.d0
      endif
c Define the complex gain for field change due to
c absorption at each step
      abx=-2.0d0*pi*abin*rin2/rlam2
c added by Rick 4/10/95
      abxr=2.0d0*pi*rin2/rlam2
      gain=dcmplx(abx,abxr)
c     y2=int(y1)
c calculate the field change for each step
      f2(k)=rff*f2(k)*cdexp(gain*delz)
c back transform previous multiplication by + or -
      rff=-rff
 80   continue
      return
      end
```

```
 25
0.7350d0      Wavelength (microns)
102.4d0       Full domain width (microns)
2.80d0        Waveguide period length (microns)
10            Exponential index of 2 for # of lateral points (e.g. 2 sup 10)
56            # of propagation steps
1.856d0       Real refractive index in diffused segment fund. lam.
1.846d0       Real refractive index in KTP substrate fund. lam.
1.990d0       Real refractive index in diffused segment SH lam.
1.980d0       Real refractive index in KTP substrate SH lam.
1.4d0         Diffused segment length (microns)
4.0d0         Diffused segment guide width (microns)
50            # of periods to propagate through
0.d0          Imaginary index of diffused region (not implemented in BPMshg)
5.d-3         Imaginary index of absorbing barrier
4.0d1         Absorber width (microns)
2.4004d0      Fundamental Gaussian beam waist radius (microns)
1.9880d0      S.H. Gaussian beam waist radius (microns)
0.5d0         Power coupled into guide (Watts)
0.0           Initial imaginary field amplitude
482           Minimum lateral step # written to nearf.cur
542           Maximum lateral step # written to nearf.cur
1             Period # at which nearf.cur is written to once per period
0             Flag to open prop.dat (1=open; default=closed)
13.7d-12      d33 in units of m/V
13.7d-12      deff in units of m/V
```

```
      Program Gauss
c     This program computes the Gaussian beam radius and diameter as a
c     function of z-propagation distance from an input value of the beam
c     waist radius.

      Real*8  w,w0,lam,x,xlo,xhi,xstep,xlomm,xhimm
      Real*8  xstepmm,xout,p1,p2,p3,pi,dia

      pi=3.141592653

      write (6,*) "input wavelength in microns"
      read (6,*) lam
      write (6,*) "beam waist radius in microns"
      read (6,*) w0
      write (6,*) "starting x-position (waist pos=0) in mm"
      read (6,*) xlomm
      xlo=xlomm*1000.
      write (6,*) "ending x-position in mm"
      read (6,*) xhimm
      xhi=xhimm*1000.
      write (6,*) "x step size in mm"
      read (6,*) xstepmm
      xstep=xstepmm*1000.

      open (20,file='gauss.out', status='new')

      do 100 x=xlo,xhi,xstep

       p1=(lam*x)/(pi*(w0**2))        ! Define parameter for calc
       p2=p1**2
       p3=(w0**2)*(1. + p2)
       w=sqrt(p3)
       dia=2.*w
       xout=x*.001
       write (20,701) xout,dia

  100  continue
      write (6,*) xlo,xhi,xstep
      write (6,*) xout,dia
      close (20)
  701  format (1x,e9.4,1x,e9.4)
      stop
      end
```

Untapered URSL Parameters--Mathcad

M = URSL magnification,
R = curved mirror radius of curvature,
W1 = is the output nearfield aperture width,
W2 = is the rear (HR) gain region width,
RSC = depth of Siegman source from curved mirror,
RFC = depth of Siegman source from flat (output) mirror,
RSCn = apparent depth Siegman source from curved mirror,
RSFn = apparent depth of Siegman source from flat (output) mirror,
A = top-view, cross-sectional area of FIBM mirror,
Depth = depth of FIBM mirror from top epi layer,
Vol = volume of material to be removed to fabricate curved mirror,
Sag = center depth of the FIBM mirror from the original facet position,

(all spatial units in microns)

$W1 := 245$ 200 Micron Output Aperture

$M := 2.0, 2.1 .. 3.5$ $L := 500$ $n := 3.3$ $Depth := 10$ $buffer := 0$

$$R(M) := \frac{4 \cdot M \cdot L}{(M-1)^2} \qquad RSC(M) := \frac{2 \cdot M \cdot L}{M-1} \qquad RSF(M) := \frac{(M-1) \cdot L}{M-1}$$

$$RSCn(M) := \frac{RSC(M)}{n} \qquad RSFn(M) := \frac{RSF(M)}{n} \qquad MAG(M) := M$$

$$W2(M) := W1 \qquad xu(M) := \frac{W2(M)}{2} + buffer \qquad xl(M) := -xu(M)$$

$$facet(M) := \sqrt{R(M)^2 - xu(M)^2} \qquad A(M) := \int_{xl(M)}^{xu(M)} \left(\sqrt{R(M)^2 - x^2} - facet(M)\right) dx$$

$$Vol(M) := Depth \cdot A(M) \qquad Sag(M) := R(M) - facet(M) \qquad XM(M) := 2 \cdot xu(M)$$

$$RV2FXU(M) := \sqrt{\frac{RSF(M)^2 + (1 - n^2) \cdot xu(M)}{n^2}}$$

MAG(M)	R(M)	RSC(M)	RSF(M)	RSCn(M)	RSFn(M)	RV2FXU(M)
2	4000	2000	1500	606	455	454
2.1	3471	1909	1409	579	427	427
2.2	3056	1833	1333	556	404	404
2.3	2722	1769	1269	536	385	384
2.4	2449	1714	1214	519	368	368
2.5	2222	1667	1167	505	354	353
2.6	2031	1625	1125	492	341	341
2.7	1869	1588	1088	481	330	330
2.8	1728	1556	1056	471	320	320
2.9	1607	1526	1026	463	311	311
3	1500	1500	1000	455	303	303
3.1	1406	1476	976	447	296	296
3.2	1322	1455	955	441	289	289
3.3	1248	1435	935	435	283	283
3.4	1181	1417	917	429	278	278
3.5	1120	1400	900	424	273	273

MAG(M)	Sag(M)	W2(M)	XM(M)	A(M)	Vol(M)
2	1.9	245	245	306	3065
2.1	2.2	245	245	353	3532
2.2	2.5	245	245	401	4013
2.3	2.8	245	245	451	4505
2.4	3.1	245	245	501	5008
2.5	3.4	245	245	552	5520
2.6	3.7	245	245	604	6040
2.7	4	245	245	657	6567
2.8	4.3	245	245	710	7101
2.9	4.7	245	245	764	7641
3	5	245	245	819	8186
3.1	5.3	245	245	874	8737
3.2	5.7	245	245	929	9292
3.3	6	245	245	985	9851
3.4	6.4	245	245	1041	10415
3.5	6.7	245	245	1098	10982

BIOGRAPHICAL SKETCH

Brian Baird received the B.S. degree in Physics from University of Oregon in 1980 and the M.S. in Physics from University of Washington in 1984. He has conducted many laser and optics research studies as either a researcher or principal investigator for the last fourteen years. His research programs have emphasized the application of semiconductor lasers as optical pump sources for solid state lasers and nonlinear optical waveguides and applications of diode-pumped solid state lasers in materials processing. His areas of research include: diode-pumped solid state lasers; Q-switched solid state lasers; spatially-coherent high-power semiconductor lasers; nonlinear optical waveguides; applications of lasers in photodynamic therapy; and laser processing of electronics materials. For the last eight years, he has been employed by Electro Scientific Industries where he currently holds the position of Senior Engineer. At Electro Scientific Industries, he has been responsible for the development of diode-pumped solid state lasers for integration in laser processing systems used in the repair of dynamic random access memories and in laser trimming of hybrid electronics. Previously, he held the position of Research Engineer at Lockheed Aeronautical Systems Company. At Lockheed, he participated in the research and development of the optical avionics components of the YF-22.

In 1991, he entered the Ph.D program in Applied Physics at Oregon Graduate Institute of Science and Technology. His dissertation research was conducted on unstable resonator semiconductor lasers, nonlinear optical waveguides, and the requirements for their integration to form compact visible and near ultraviolet laser sources suitable for applications ranging from optical recording, photodynamic therapy, and materials processing. After five years of effort, he completed all requirements towards his degree in 1997.

Dr. Baird is a member of the Optical Society of America. He is the author or co-author of seven contributed conference publications and six patents. A listing of the papers he contributed to during his stay at Oregon Graduate Institute may be found below.

(1) R. K. DeFreez, Z. Bao, G. A. Evans, B. W. Baird, and R. S. Harris, "Focused-ion-beam micromachined unstable resonator semicondcutor lasers," *Proceedings of the Annual Meeting of the Optical Society of America*, Dallas, Texas, October 2-7, 1994.

(2) B. W. Baird and R. K. DeFreez, "Spatial mode characteristics of potassium titanyl phosphate periodically segmented nonlinear waveguides," *Proceedings of Progress in Electromagnetic Research Symposium*, Seattle, Washington, July 24-28, 1995.

(3) B. W. Baird and R. K. DeFreez, "Spatial modes of potassium titanyl phosphate periodically segmented nonlinear waveguides in the near infrared and near ultraviolet," *Proceedings of the Annual Meeting of the Optical Society of America*, Portland, Oregon, September 10-15, 1995.

(4) B. W. Baird, R. K. DeFreez, and E. M. Freden, "High excited ion density effects on the effective fluorescence lifetime in Q-switched solid state lasers," *OSA TOPS on Advanced Solid-State Lasers,* vol. 1, pp. 582-584, Optical Society of America, 1996.

(5) B. W. Baird and R. K. DeFreez, "Optical characterization of periodically segmented KTP waveguides for second harmonic generation in the near ultraviolet," *Proceedings of the Oregon Academy of Sciences*, Eugene, Oregon, March, 1996.

(6) B. W. Baird and R. K. DeFreez, "Beam propagation method modeling of second harmonic generation in periodically segmented potassium titanyl phosphate waveguides," *Technical Digest of Conference on Lasers and Electro-Optics*, Optical Society of America, Anaheim, California, June 3-7, 1996.

(7) B. W. Baird, R. K. DeFreez, G. A. Evans, and J. Kirk, "Single frequency high power core grating unstable resonator semiconductor laser," accepted for presentation at *Conference on Lasers and Electro-Optics (CLEO '97)*, Optical Society of America.

(8) B. W. Baird and R. K. DeFreez, "Method and apparatus for efficient operation of a solid-state laser optically pumped by an unstable resonator semiconductor laser," *U.S. Patent* No. 5,260,963, November 9, 1993.

(9) B. W. Baird and R. K. DeFreez, "High-power, compact, diode-pumped, tunable laser," *U.S. Patent* No. 5,317,447, May 31, 1994.

(10) B. W. Baird and R. K, DeFreez, "Laser system and method employing a nonimaging concentrator," *U.S. Patent* No. 5,323,414, June 21, 1994.

(11) B. W. Baird and R. K. DeFreez, "Optical frequency-converting medium pumped by unstable resonator semiconductor laser," *U.S. Patent* No. 5,559,824, September 24, 1996.